MULTINUCLEAR NMR SPECTROSCOPY METHODS FOR THE STUDY OF STRUCTURE AND DYNAMICS IN SOLID-STATE ELECTROLYTES FOR LITHIUM ION BATTERIES

MULTINUCLEAR NMR SPECTROSCOPY METHODS FOR THE STUDY OF STRUCTURE AND DYNAMICS IN SOLID-STATE ELECTROLYTES FOR LITHIUM ION BATTERIES

BY

T. LEIGH SPENCER NOAKES, H.B.SC.

A Thesis Submitted to the School of Graduate Studies in Partial Fulfillment of the Requirements for the Degree Doctor of Philosophy

McMaster University

McMaster University DOCTOR OF PHILOSOPHY (2013) Hamilton, Ontario (Chemistry)

TITLE: Multinuclear NMR Spectroscopy Methods for The Study of Structure and Dynamics in Solid-State Electrolytes for Lithium Ion Batteries

AUTHOR: T. Leigh Spencer Noakes, B. Sc. (The University of Toronto)

SUPERVISOR: Professor Gillian R. Goward

NUMBER OF PAGES: xxv, 236, A21

ABSTRACT

This thesis evaluates several solid-state NMR spectroscopy approaches to studying lithium ion dynamics in solid-state electrolytes. With the goal of reducing the risks associated with current liquid electrolytes, solid-state electrolytes provide non-flammable materials that are also stable against attack by cathode and anode materials. Solid-state NMR spectroscopy offers a versatile method to determine structural details and can also provide information about ion mobility in solid-state electrolytes. Challenges involved in the study of solid-state electrolytes include the difficulty in distinguishing between ^{6,7}Li resonances due to the small chemical shift range of diamagnetic lithium species. Also, many of these materials tend to exhibit ion conduction in a single crystallographic site, while at the same time long T_1 relaxation times create lengthy experiment times. The NMR methods selected in this thesis aim to circumvent some of these issues in order to determine structural and dynamic properties in solid-state electrolytes. Several different electrolytes have been examined including $LaLi_{0.5}Fe_{0.2}O_{2.09}$ and related materials, which exhibit intricate structural properties. ^{139}La NMR spectroscopy, in combination with ^{7}Li MAS NMR spectroscopy, was used to determine the nature of this disorder. In addition, studies of the quadrupolar framework ^{87}Rb nucleus, which take advantage of its large electric field gradient, have been used to indirectly probe the activation energy for Ag^+ ion hopping in the solid-state silver ion electrolyte $RbAg_4I_5$. Alternatively, heteronuclear dipolar coupling between ^{6}Li and ^{7}Li has been used to qualitatively compare lithium ion hopping rates in $Li_6BaLa_2M_2O_{12}$ (M = Ta, Nb) using ^{6}Li{^{7}Li}-REDOR NMR studies. Finally, T_2 relaxation studies have been used to probe ion dynamics in $Li_3V_2(PO_4)_3$ and $LiVO_3$ in order to determine if this is a viable method to study dynamics in this class of materials.

TABLE OF CONTENTS

List of Tables

List of Figures

List of Abbreviations and Symbols

NMR	Nuclear Magnetic Resonance
ssNMR	Solid-State Nuclear Magnetic Resonance
I	Nuclear spin quantum number (observed spin)
S	Nuclear spin quantum number (non-observed spin)
GHG	Greenhouse Gas
μ_N	Nuclear magnetic moment
γ_N	Nuclear gyromagnetic ratio
g_N	Nuclear g factor
β_N	Nuclear magneton
$\hbar$	Reduces Planck's Constant
$\boldsymbol{B_0}$	External magnetic field strength
ω_0	Larmor frequency
$\mathcal{H}$	Hamiltonian
m_α	High energy state in Zeeman splitting
m_β	Low energy state in Zeeman splitting

ΔE	Energy difference
k	Boltzmann constant
ω_{RF}	Strength of radiofrequency pulse
Ω	Radiofrequency offset
r_{ij}	Distance between two nuclei, *i* and *j*
θ	Angle of separation
MAS	Magic Angle Spinning
B_1	Applied magnetic field
T_1	Longitudinal nuclear relaxation (spin-lattice relaxation)
T_2	Transverse nuclear relaxation (spin-spin relaxation)
M_Z	Magnetization aligned along the z-axis
M_{XY}	Magnetization in the xy-plane
CSA	Chemical Shift Anisotropy
CPMG	Carr-Purcell-Meiboom-Gill
FID	Free Induction Decay
SNR	Signal-to-noise ratio

T_r	Length of rotor period
N_c	Number of rotor periods
eQ	Nuclear electric quadrupole moment
EFG	Electric Field Gradient
ω_Q	Quadrupole splitting parameter
δ	Chemical shift
η	Asymmetry parameter
C_Q	Quadrupolar coupling (also represented by χ)
α, β, γ	Euler Angles
Ω	Span
κ	Skew
$f(I)$	Spin dependent factor
P_2, P_4	Legendre polynomials
RF	Radiofrequency
WURST	Wideband Uniform-Rate Smooth Truncation
D_{ij}	Dipolar coupling constant between nuclei i and j

μ_0	Permeability of free space
REDOR	Rotational Echo Double Resonance
SEDOR	Spin Echo Double Resonance
M_2	Dipolar second moment
EXSY	Exchange Spectroscopy
μ_A	Redox potential at anode
μ_C	Redox potential at cathode
σ	Chemical shielding
E_g	Band gap
V	Volt
Z	Atomic number
ppm	Parts per million
FWHM	Full-Width at Half-Maximum
E_A	Activation energy
DSC	Differential Scanning Calorimetry
PXRD	Powder X-Ray Diffraction

eV	Electron volts
EXPRESS	Exchange Program for Relaxing Spins
DFT	Density Functional Theory
CPMAS	Cross Polarization Magic Angle Spinning
P	Slope of REDOR curve

Chapter 1: Introduction to Solid-State Electrolytes for Lithium Ion Batteries

1.1. Thesis Layout

This thesis describes the use of solid-state nuclear magnetic resonance (NMR) techniques to evaluate structure and dynamics of ion conductors. Particular attention is paid to the use of alternative methods of studying ion dynamics in solid-state electrolyte materials, such as the study of quadrupolar nuclei as well as the use of heteronuclear dipolar coupling measurements, which are both sensitive to ion dynamics. Garnet-like lithium-containing materials are the main focus of this collection of work and many of the materials studies in this thesis fall into the category of electrolyte material for lithium ion batteries and conduct lithium ions. Several model materials have been studied in order to establish novel methods used in this thesis.

Chapter 1 describes the motivation for the work outlined throughout this thesis, with an overview of lithium ion batteries and the current materials used. Properties of electrolyte materials are described with a focus on their behaviour within a lithium ion battery. Chapter 2 introduces the foundations of the NMR spectroscopic techniques used throughout this thesis and also describes the pulse sequences used. This chapter focuses largely on the details of studying quadrupolar nuclei and also the determination of heteronuclear dipolar coupling. Chapter 3 marks the beginning of the experimental section, and focuses on the structure of the complex family of garnet-like material $LaLi_{0.5}Fe_{0.2}O_{2.09}$ and its derivatives, which vary in La, Li and Fe content. ^{7}Li and ^{139}La

NMR spectroscopy were used to identify the structural disorder present in this family of materials. Some of the challenges of using these techniques are outlined in this chapter. Model materials La_2O_3, $La(OH)_3$, $LaNbO_4$, $LaAlO_3$, $Li_7La_3Zr_2O_{12}$, and La_3NbO_7 were studied in order to become familiar with the challenges associated with performing and understanding ^{139}La NMR spectroscopy. In addition, the solid-state electrolyte $Li_{3x}La_{(2-x)/3}TiO_3$ was studied in order to assess the contribution of disorder in this material to the featureless ^{139}La NMR spectrum. Chapter 4 presents the solid-state Ag^+ ion electrolyte and describes the use of ^{87}Rb NMR spectroscopy to measure the activation energy of Ag^+ ion hopping. This chapter also outlines some of the limitations of studying the mobile species in solid-state electrolyte materials, and suggests an alternative method to assess ion dynamics. As a framework element, Rb is in a unique environment, in which it does not take part in ion dynamics, but is sensitive to the motion of Ag^+ ions in close proximity. By taking advantage of this sensitivity, measurements of the ^{87}Rb NMR spectral line shape as a function of temperature were used to calculate the activation energy for lithium ion hoping. Chapter 5 introduces $Li_6BaLa_2M_2O_{12}$ (M = Ta, Nb), solid-state lithium ion electrolyte materials. Rotational echo double resonance (REDOR) NMR spectroscopic experiments are used to qualitatively compare lithium ion dynamics in these two materials. This method offers yet another method to study dynamics in materials that pose a challenge when the mobile ion is studied directly using NMR spectroscopy. Chapter 6 presets the study of ^6Li and ^7Li T_2 relaxation in $Li_3V_2(PO_4)_3$. T_2 relaxation can be used to measure the activation energy of lithium ion hopping provided that the inverse of the T_2 (in Hz) is on the same order of magnitude as the lithium ion

hopping rate. This technique becomes useful for systems in which ion motion occurs within a single crystallographic site. Although REDOR studies have been useful in similar situation, their use is limited to situations in which the rate of ion hopping is on the same order of magnitude as the ^{6}Li-^{7}Li dipolar coupling. In instances where this method fails, temperature dependent T_2 analysis provides another sensitive method to study ion dynamics. Chapter 7 provides a summary of the projects discussed in this thesis, as well as a future outlook for this work.

1.2. Motivation for Studying Lithium Ion Batteries

Development of alternative energy sources and energy storage is essential to reducing the amount of greenhouse gases (GHGs) currently in the atmosphere. One of the methods of achieving this is to reduce the amount of hydrocarbon-based fuel consumed by the automotive industry. The transportation sector is responsible for ~13.1 % of greenhouse gas (GHG) emissions worldwide. This amounts to 5 billion tonnes of CO_2 per year throughout the world.[1] In addition, automobiles contribution to particulate air pollution, which contributes to many respiratory conditions, especially in densely populated regions. Moreover, with political instability in many oil-rich regions, the dependence on oil for transportation is a challenging issue.[1]

Lithium ion batteries (LIBs) are used as light-weight, portable energy storage devices. Currently, many small electronic devices, such as cellular phones and laptops make use of this technology to minimize the total weight of the device. ***Figure 1.1*** shows a comparison of different battery systems with respect to their gravimetric and volumetric

energy densities.[2] The success of LIBs in the electronics industry has lead to the extension of this technology into the automotive industry by providing energy storage devices for hybrid and electric vehicles (HEVs and EVs, respectively). The use of lithium ion batteries in automotive vehicles would reduce GHGs due to the burning of gasoline, by allowing clean forms of energy, such as solar or wind, to provide fuel for the automotive industry.

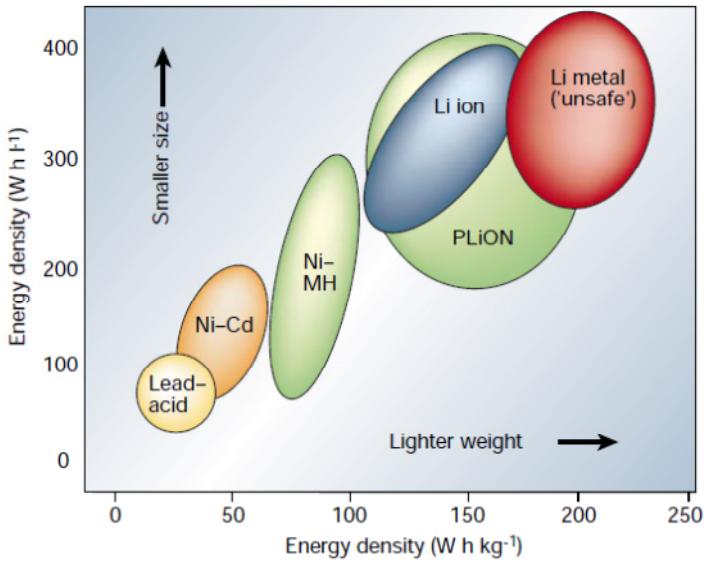

Figure 1.1. Comparison of gravimetric and volumetric densities of different battery types.[2] This figure was published in (Tarascon, J. M.; Armand, M., Issues and challenges facing rechargeable lithium batteries. *Nature* **2001,** 414, (6861), 359-367) and was reproduced with permission from the Nature Publishing Group.

Some of the targets set by researchers in order to develop LIBs that can be used commercially in the automotive industry include: the need for fast charging batteries; reversibility in battery cycling; high energy density; stability against electrolyte combustion. Research has focused extensively on the material components of the battery,

with each component made individually. The development of these components allows the tailoring of materials properties to suit specific criteria.[3]

1.3. Design of a Lithium Ion Battery

A standard LIB is composed of a cathode, an anode and an electrolyte. During electrochemical cycling lithium ions move from one electrode to another through the electrolyte, while electrons are passed through the circuit. Lithium ions are inserted into or extracted from the electrodes (intercalated or deintercalated, respectively). It is essential that the electrodes have good lithium ion conductivity as well as good electrical conductivity. Conversely, the electrolyte must be ionically conductive but electrically resistive. ***Figure 1.2*** shows a schematic figure of a discharging battery, where lithium is being extracted from the $LiCoO_2$ cathode and inserted into the graphite anode, moving through the electrolyte. Simultaneously, electrons travel from the cathode to the anode via the circuit to power a device.

The current cathode material in many lithium ion batteries is lithium cobalt oxide, $LiCoO_2$, while the anode is porous graphite. The electrolyte is usually an ionic salt, typically lithium hexafluorophosphate, $LiPF_6$, dissolved in an organic solvent such as ethylene carbonate-dimethyl carbonate, EC-DMC.[1] There has been a significant effort in recent years to create a battery with optimal cycling properties and a higher energy density than the previous commercial standard.[3] This has resulted in the design of materials with more reversible insertion and extraction of lithium for the cathode and

anode, as well as the development of electrolytes that are capable of withstanding high voltage windows, thus enabling higher power output.

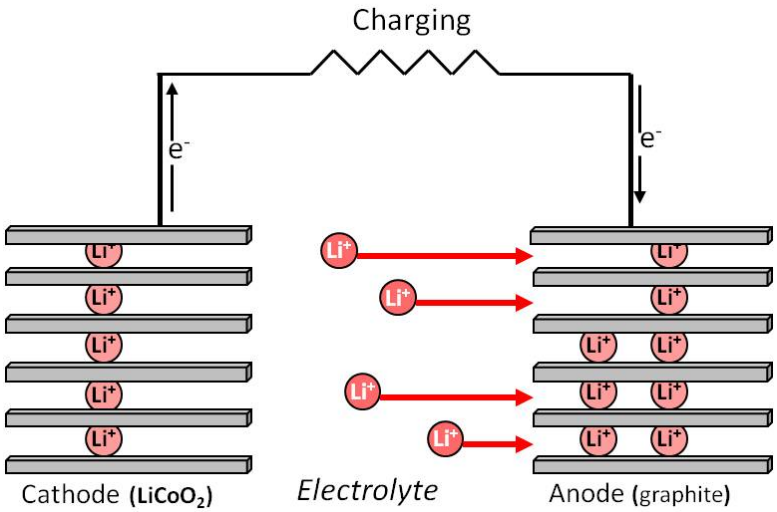

Figure 1.2. A standard lithium ion battery performing a discharge. Lithium ions are extracted from the positive electrode, $LiCoO_2$, and inserted into the graphite negative electrode through the electrolyte; while at the same time electrons move from the positive electrode to the negative electrode through the circuit. If the battery were in the charging phase, the electrons and lithium ions would move in the opposite direction shown in the figure.

Ultimately, fast and reversible ionic mobility is required. Thus, efforts to design better materials have also resulted in creative methods to study ionic motion in these materials. Solid-state nuclear magnetic resonance (NMR) has played an important role, with the unique ability to study the mobile lithium ions directly.[4-7] This technique has been used to study cathode, anode and solid-state electrolyte materials. The end result of these studies is generally the determination of an ionic hopping rate or activation energy for lithium ion hopping, which can be used to determine the viability of a particular material before it is put into a cell.

1.4. Electrolyte Stability

The safety of lithium ion batteries hinges on the stability of the battery components under electrochemical cycling. Some of the most common degradation processes occur within the electrolyte and also as a result of the reactions that can occur between the electrolyte and the electrode materials.

1.4.1. Safety Concerns

Lithium ion batteries used for automotive application store a large amount of energy and are expected to run reversibly under a wide temperature range, sometimes with fast charge and discharge. Under these taxing conditions it is essential for a user to rely on the stability of these batteries. Within the battery, both the oxidizer (cathode) and fuel (anode) are contained in close proximity, which is a strategy not used widely in energy storage devices.[8] It is thus the responsibility of the electrolyte and separator to prevent reactions between the electrode species, which can be violent. The electrolyte must be able to withstand the extreme oxidation and reduction potentials at the anode and cathode, respectively.

Dendrite formation is perhaps the most common safety concern in a lithium ion battery. This occurs when lithium is plated onto the surface of an anode or cathode instead of being inserted into a material, such as graphite. This layer can form if the rate of charge/discharge is too fast to allow the lithium insertion process.[9-11] If lithium deposition is significant, the formation of long spikes of lithium metal can create a short

circuit in the battery when the cathode and anode come into electrical contact. If there is a flammable organic liquid electrolyte, this can pose a hazard, as it may ignite.

Lithium metal is known to be reactive to air and moisture. The reaction between lithium metal and water produces hydrogen in an exothermic reaction, and can cause a fire. Any puncture of a lithium ion battery that contains lithium metal, as an electrode or as a side product of electrochemical cycling, can potentially cause a fire. Several instances of battery related fires have been reported: in 2006 there was a recall on Dell laptops due to safety issues with batteries, and in 2013 there was an incident involving the ignition of a lithium ion battery on a Boeing airplane. These safety issues are a source of concern in the battery community and as a result there has been great effort to create electrolyte materials that are more stable and unreactive to attack by the cathode and anode.[12]

1.4.2. Current Liquid Electrolytes

Several classes of electrolyte species have been considered for use in lithium ion batteries. The most common are liquid organic electrolytes, in which an ionic salt is dissolved. Alternatively, several ionic liquid electrolytes have been sampled, which also make use of a lithium-containing ionic salt, such as the salt $LiBF_4$ in the ionic liquid EMI-BF_4. Many liquid electrolytes are flammable, with the exception of the pure ionic liquid electrolytes, and all of them react chemically with the electrodes to form a SEI.[3, 13]

The most commonly used electrolyte material is $LiPF_6$ in EC-DMC. This mixture is stable up to 4.5 V, and decomposes at higher voltages.[14] The decomposition voltage of

this material limits its use in batteries in which high voltages are accessed and therefore cannot be used in high power batteries.[3] In addition, the SEI that is formed from this material is not permeable to lithium ions and hinders lithium ion intercalation and deintercalation for the cathode and anode, although the presence of EC makes this effect less significant.[15] The formation of unfavourable SEI layers is common when liquid electrolytes are used.

1.4.3. The Solid Electrolyte Interface

The SEI is a layer that forms on the cathode and/or anode as a result of the reaction of a liquid electrolyte with the electrode surface.[16] The SEI is formed on initial charge/discharge of the battery and is the limiting step for lithium ion transport in the battery. Once formed, it stays in place and cannot be removed, and its characterization can be problematic. The SEI is thought to protect the electrodes from further reaction with the electrolyte, even though its presence is sometimes detrimental to the battery performance.[13]

The SEI is composed of products from the electrolyte and the electrodes and the composition is thought to be similar to that of the electrolyte. For example, ether-based electrolytes form Li_2O in the SEI.[17] Some lithium is contained within the layer, and ultimately this reaction decreases the capacity of the battery, since this lithium in no longer available to take place in the electrochemical process. For SEI layers that are penetrable to lithium, the diffusion of lithium through this layer becomes the rate determining step for the intercalation process at the respective electrode. In some cases

the SEI layer is favourable if the lithium ion conduction through the layer is fast.[13] The ideal SEI has the following characteristics:[17]

(1) No electrical conductivity.

(2) High ionic conductivity.

(3) Uniform morphology and chemical composition.

(4) Sufficient adhesion to electrode surface.

(5) Mechanical strength and flexibility to withstand the expansion of the electrode on electrochemical cycling.

(6) Low solubility in electrolyte.

1.4.4. Selection of Electrolytes

Control and prediction of the reactions that may occur between the electrolyte and the electrodes can be done in some cases. One method of controlling unwanted reactions is by consideration of the HOMO/LUMO gap of the electrolyte (the electrolyte window, E_g) as compared to the electrochemical potentials of the cathode and anode. The goal is for the electrolyte not to become reduced at the anode or oxidized at the cathode. This is usually done by controlling the cathode and anode electrochemical potentials, μ_A and μ_C, respectively, such that they fall within the electrolyte window. This requires knowledge of the redox potentials of the transition metal redox pairs in the cathode, with respect to lithium metal (Li^+/Li^0).[3, 9]

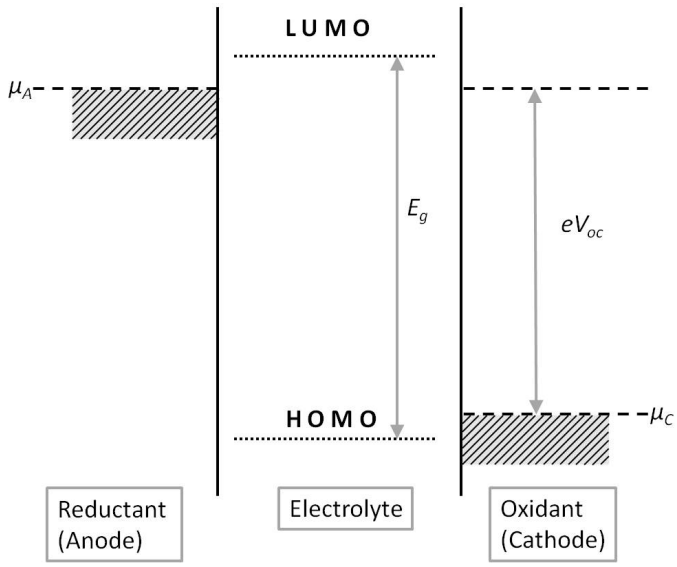

Figure 1.3. Relative energies of the electrolyte window, E_g, and the electrochemical potentials μ_A and μ_C for a liquid electrolyte with solid electrodes. The HOMO and LUMO of the electrolyte are lower and higher in energy than the μ_A and μ_C for a liquid electrolyte, respectively.

Figure 1.3 shows the relative energies of the electrolyte window, E_g, and the electrochemical potentials μ_A and μ_C for a liquid electrolyte with solid electrodes when there is no reaction between the electrolyte and electrodes. If μ_A is above the lowest unoccupied molecular orbital (LUMO) of the electrolyte, this will result in the reduction of the electrolyte unless the reaction between the anode and the electrolyte becomes blocked by the formation of a SEI. Subsequently, oxidation of the electrolyte will occur at the cathode if the μ_C is below the highest occupied molecular orbital (HOMO) of the electrolyte, unless a SEI is formed. In the case of a solid-state electrolyte, the LUMO and HOMO are replaced by the conduction band (CB) and the valence band (VB), respectively, in ***Figure 1.3***.[3, 9, 18]

1.5. Solid-State Electrolytes

Solid-state electrolytes are chosen as they may overcome many of the safety challenges associated with lithium ion batteries. In addition to being non-flammable, many solid-state electrolytes are unreactive with the cathode and anode materials, and therefore prevent SEI and dendrite formation.[12, 15] Solid-state electrolytes can be divided into three categories:[18]

1) Crystalline electrolytes
2) Glass electrolytes
3) Polymer electrolytes

This thesis focuses primarily on crystalline electrolytes, specifically the measurement of ion conduction within these materials. In particular, there is significant interest in those with a garnet-like structure, which will be discussed in further detail.

1.5.1. Crystalline Electrolytes

Some crystalline solids are capable of ionic conduction. While most require high temperatures, some can conduct ions even at room temperature, and are known as fast ion conductors. Examples of Ag^+, Cu^+, Tl^+, Li^+, Na^+, K^+, H^+, O^{2-}, and F^- have been shown in the literature. Many contain a mobile ion as well as an immobile sublattice, or framework. There are several mechanisms of ion hopping in these materials, each of which requires a partial occupancy of energetically equivalent sites:[18]

The vacancy migration mechanism describes materials that have partial occupancies, or vacancies, due to some defect in the structure, such as a Schottky defect. These sites would usually be occupied in the ideal crystal structure however, with these defects an ion adjacent to a vacant site can jump into the empty site, leaving an empty space. This forms the foundation of ion conduction in these materials. Alternatively, interstitial migration occurs when a mobile ion hops into a site that would usually be empty in an ideal crystal structure, forming a Frenkel defect. In each of these cases ion hops occur randomly and this behaviour forms the basis of the random walk theory. Each hop is said to be isolated and hopping behaviour can be encouraged through doping. Aliovalent doping is a technique used to introduce interstitials or vacancies, which involves the partial replacement of ions of one type with ions of a different formal charge.[18]

Alternatively, the knock-on mechanism is another mode of ion conduction in which an ion cannot move unless one of the surrounding ions moves first to make space. This is a continuous process that can occur in three dimensions and is an example of cooperative ion migration, which is common in solid-state electrolytes.[18]

Some examples of crystalline solid electrolytes include:

1) Garnet-like structures such as $Li_6BaLa_2M_2O_{12}$ (M = Ta, Nb).[19]
2) NASICON [Na super ion conductor with structure $Na_{1+x}Zr_2(P_{1-x}Si_xO_4)_3$].[20]
3) LISICON [lithium analogues of NASICON: $Li_{2+2x}Zn_{1-x}GeO_4$ and $Li_{3+x}(P_{1-x}Si_x)O_4$].[21]

4) Layered structures such as spinels and β-aluminas.[18]

1.5.2. Glass Electrolytes

Ion conducting glasses, such as the Li^+ conducting Li_2S-SiS_2, have been known for some time, with the presence of Na^+ ion mobility reported in 1884.[22] Thus far, Li^+ and Ag^+ ion conducting glasses have proven to be the most ionically conductive and some are stable within the voltage window of 0 to 5 V.[23] Typical liquid electrolytes are stable between 0.9 and 5.3 V, with organic liquids having a narrower stability window than ionic liquids. Structurally, glasses are similar to the parent liquids from which they are formed, possessing overall significant disorder, with small regions of ordered microstructures. Hopping mechanisms are used to describe ion motion in glass solids.[18, 24]

1.5.3. Polymer Electrolytes

Ion conduction in polymers is achieved either when a conducting salt is added to a flexible polymer host, or when covalently attached charged groups are connected to the polymer, leaving the counter-ion mobile. Conducting polymers form a robust class of material, with flexibility that can withstand the volume changes that occur during electrochemical cycling. These materials are stable within a voltage window of 0 and 5 V at room temperature, and are sometimes used in combination with other electrolytes, such as ionic liquids.[3] The combination of ionic salts in a polymer host was discovered in the 1960's and sparked the development of polymer electrolyte materials.[25] Conduction processes in these materials depend on the dynamics of the polymer host, with a different mechanism from that observed in crystalline and glass electrolytes.[18]

1.6. Assessment of Solid-State Electrolyte Materials

Assessment of potential electrolyte materials requires knowledge of the structure as well as the rate and mechanism of ion mobility. Even though many techniques are available for such analysis, the solid nature of these materials poses a challenge in many of them. In addition, many of the crystalline materials proposed as solid-state electrolytes are synthesized as powdered solids, with very little able to form single crystals. For solid-state electrolytes ions can move in one, two or three dimensions, with 3D ionic motion being the most favourable. The following sections discuss methods used to determine the properties of ion motion in solid-state lithium ion electrolytes.

1.6.1. Structural Determination

Characterization of the structure of powdered solids is typically done using powder X-ray diffraction.[15] Since lithium is a relatively light element, X-ray diffraction is not effective at locating it in the crystal structure, since the small number of electrons results in a small scattering factor for X-rays. Therefore powder X-ray diffraction is generally used to determine the framework structure of solid-state electrolyte materials, which usually consists of heavier elements. In many cases this is enough information to determine if the structure conductions ions in one, two or three dimension by locating channels throughout the framework with sufficient size to allow easy passage of lithium. Identifying the location of the lithium ions can be challenging. In some cases powder neutron diffraction can be used because neutrons have a larger scattering factor for lithium that X-rays, and therefore are more sensitive to the position of lithium atoms in

the crystal structure.[26] However, this technique requires a large amount of material, and is not a routine method of analysis.

1.6.2. Impedance Analysis

Electrical properties of solid-state electrolytes are routinely measured using impedance analysis. This technique measures the ion conductivity through a material in bulk form. The powder is typically pressed into a pellet after which the pellet is sintered and the surfaces are sputtered with an inert material, such as platinum or gold metal. Ionic conductivity is measured by placing the pellet between two electrodes. A voltage is applied and the current that passes through the pellet is measured, as well as the resistance. Ionic conductivity, in S/cm, can be measured as a function of temperature to obtain the activation energy for lithium ion transport through an Arrhenius analysis. This method is widely used to determine the electrical properties of solid-state electrolytes.[18] Drawbacks to this technique include the presence of grain boundary resistance. This can affect impedance measurements and lead to inconsistent results, as the degree of grain boundary resistance is dependent on the preparation technique of the material (grain size, sintering temperature, etc.).[19, 27]

1.6.3. Nuclear Magnetic Resonance Spectroscopy

NMR spectroscopy has the unique ability to observe lithium ions within a material without simultaneously observing other nuclei in the structure. Unlike PXRD, NMR spectroscopy can distinguish between lithium nuclei that are in different chemical environments.[28] This is a distinct advantage and is vital to understand the lithium ion

transport mechanisms in battery materials. In addition, NMR spectroscopy observes lithium within a grain of material and is therefore not susceptible to grain boundary resistance. Using variable temperature techniques, which will be discussed in this thesis, NMR spectroscopy can measure the activation energy for lithium ion hopping for lithium within a grain, and therefore can get an absolute value for the activation energy for lithium ion hopping.[5, 29] In combination with the ability to distinguish between lithium environments, this technique can map out the transport mechanism by determining which lithium crystallographic sites undergo chemical exchange, and identifying the rate of chemical exchange for specific sites.[4]

Although NMR spectroscopy is a powerful technique, there are drawbacks associated with the observation of mobile ion species in solid-state electrolyte materials, which will be discussed in further detail in the experimental sections. For diamagnetic materials, the small chemical shift range limits the resolution of ^{6,7}Li NMR spectra and the long T_1 relaxation time of ^{6,7}Li causes experimental times to be very long. Even more challenging is the fact that in many solid-state electrolyte materials, ionic conduction occurs in a single crystallographic site. This thesis describes the development of NMR spectroscopic methods that aim to circumvent some of the inherent challenges involved in observing Li^+ ion dynamics within solid-state lithium ion electrolytes. The observation of nuclei that compose the framework of the electrolyte materials offers a method to study dynamics in electrolytes. These secondary nuclei are often quadrupolar in nature, and their large electric field gradients make them sensitive to their surrounding environment, with the ability to detect ion hopping nearby. Alternatively, the dipolar coupling between

^{6}Li and ^{7}Li is also sensitive to the motion of lithium ions, and therefore can be used to probe changes in dynamics in solid-state electrolytes. This thesis discusses unique approaches to studying lithium ion motion in solid-state electrolytes, taking advantage of the NMR techniques discussed above. These techniques offer an alternative approach to the analysis of solid-state electrolyte materials for lithium ion batteries, and this thesis shows that these methods can be used effectively to study ion dynamics in solid-state lithium electrolytes.

1.7. References

1. Pollet, B. G.; Staffell, I.; Shang, J. L., Current status of hybrid, battery and fuel cell electric vehicles: From electrochemistry to market prospects. *Electrochimica Acta* **2012,** 84, 235-249.

2. Tarascon, J. M.; Armand, M., Issues and challenges facing rechargeable lithium batteries. *Nature* **2001,** 414, (6861), 359-367.

3. Goodenough, J. B.; Kim, Y., Challenges for Rechargeable Li Batteries. *Chemistry of Materials* **2010,** 22, (3), 587-603.

4. Davis, L. J. M.; He, X. J.; Bain, A. D.; Goward, G. R., Studies of lithium ion dynamics in paramagnetic cathode materials using Li-6 1D selective inversion methods. *Solid State Nuclear Magnetic Resonance* **2012,** 42, 26-32.

5. Davis, L. J. M.; Heinmaa, I.; Goward, G. R., Study of Lithium Dynamics in Monoclinic $Li_3Fe_2(PO_4)_3$ using Li-6 VT and 2D Exchange MAS NMR Spectroscopy. *Chemistry of Materials* **2010,** 22, (3), 769-775.

6. Cahill, L. S.; Chapman, R. P.; Kirby, C. W.; Goward, G. R., The challenge of paramagnetism in two-dimensional Li-6,Li-7 exchange NMR. *Applied Magnetic Resonance* **2007,** 32, (4), 565-581.

7. Cahill, L. S.; Kirby, C. W.; Goward, G. R., Li-6{P-31} rotational-echo, double-resonance studies of lithium ion site dynamics in $Li_3V_2(PO_4)_3$. *Journal of Physical Chemistry C* **2008,** 112, (6), 2215-2221.

8. Doughty, D. a. P., P., E. , A General Discussion of Li Ion Battery Safety. *The Electrochemical Society Interface* 2012, pp 37-44.

9. Goodenough, J. B.; Park, K. S., The Li-Ion Rechargeable Battery: A Perspective. *Journal of the American Chemical Society* **2013,** 135, (4), 1167-1176.

10. Yazami, R.; Touzain, P., A Reversible Graphite Lithium Negative Electrode for Electrochemical Generators. *Journal of Power Sources* **1983,** 9, (3-4), 365-371.

11. Zaghib, K.; Goodenough, J. B.; Mauger, A.; Julien, C., Unsupported claims of ultrafast charging of $LiFePO_4$ Li-ion batteries. *Journal of Power Sources* **2009,** 194, (2), 1021-1023.

12. Thangadurai, V.; Schwenzel, J.; Weppner, W., Tailoring ceramics for specific applications: A case study of the development of all-solid-state lithium batteries. *Ionics* **2005,** 11, (1-2), 11-23.

13. Xu, K., Nonaqueous liquid electrolytes for lithium-based rechargeable batteries. *Chemical Reviews* **2004,** 104, (10), 4303-4417.

14. Guyomard, D.; Tarascon, J. M., High-Voltage Stable Liquid Electrolytes for $Li_{1+X}Mn_2O_4$/Carbon Rocking-Chair Lithium Batteries. *Journal of Power Sources* **1995,** 54, (1), 92-98.

15. Thangadurai, V.; Weppner, W., Investigations on electrical conductivity and chemical compatibility between fast lithium ion conducting garnet-like $Li_6BaLa_2Ta_2O_{12}$ and lithium battery cathodes. *Journal of Power Sources* **2005,** 142, (1-2), 339-344.

16. Peled, E., The Electrochemical-Behavior of Alkali and Alkaline-Earth Metals in Non-Aqueous Battery Systems - the Solid Electrolyte Interphase Model. *Journal of the Electrochemical Society* **1979,** 126, (12), 2047-2051.

17. Dey, A. N., Lithium Anode Film and Organic and Inorganic Electrolyte Batteries. *Thin Solid Films* **1977,** 43, (1-2), 131-171.

18. Bruce, P. G., *Solid State Electrochemistry*. Cambridge University Press: Cambridge, 1995; p 344.

19. Thangadurai, V.; Weppner, W., $Li_6ALa_2Nb_2O_{12}$ (A = Ca, Sr, Ba): A new class of fast lithium ion conductors with garnet-like structure. *Journal of the American Ceramic Society* **2005,** 88, (2), 411-418.

20. Goodenough, J. B.; Hong, H. Y. P.; Kafalas, J. A., Fast Na^+-Ion Transport in Skeleton Structures. *Materials Research Bulletin* **1976,** 11, (2), 203-220.

21. Hong, H. Y. P., Crystal-Structure and Ionic-Conductivity of $Li_{14}Zn(GeO_4)_4$ and Other New Li^+ Superionic Conductors. *Materials Research Bulletin* **1978,** 13, (2), 117-124.

22. Eckert, H.; Zhang, Z. M.; Kennedy, J. H., Glass-Formation in Non-Oxide Chalcogenide Systems Structural Elucidation of Li_2S-SiS_2-Li_I Solid Electrolytes by Quantitative Si-29, Li-6 and Li-7 High-Resolution Solid-State NMR Methods. *Journal of Non-Crystalline Solids* **1989,** 107, (2-3), 271-282.

23. Hayashi, A.; Muramatsu, H.; Ohtomo, T.; Hama, S.; Tatsumisago, M., Improvement of chemical stability of Li_3PS_4 glass electrolytes by adding M_xO_y (M = Fe, Zn, and Bi) nanoparticles. *Journal of Materials Chemistry A* **2013,** 1, (21), 6320-6326.

24. Angell, C. A., Mobile Ions in Amorphous Solids. *Annual Review of Physical Chemistry* **1992,** 43, 693-717.

25. Armand, M., Polymer Solid Electrolytes - an Overview. *Solid State Ionics* **1983,** 9-10, (DEC), 745-754.

26. Cussen, E. J., The structure of lithium garnets: cation disorder and clustering in a new family of fast Li^+ conductors. *Chemical Communications* **2006**, (4), 412-413.

27. Truong, L.; Thangadurai, V., Soft-Chemistry of Garnet-Type $Li_{5+x}Ba_xLa_{3-x}Nb_2O_{12}$ (x=0, 0.5, 1): Reversible H^+ <-> Li^+ Ion-Exchange Reaction and Their X-ray, Li-7 MAS NMR, IR, and AC Impedance Spectroscopy Characterization. *Chemistry of Materials* **2011,** 23, (17), 3970-3977.

28. Cahill, L. S.; Chapman, R. P.; Britten, J. F.; Goward, G. R., Li-7 NMR and two-dimensional exchange study of lithium dynamics in monoclinic $Li_3V_2(PO_4)_3$. *Journal of Physical Chemistry B* **2006,** 110, (14), 7171-7177.

29. Spencer, T. L.; O'Dell, L. A.; Moudrakovski, I.; Goward, G. R., Dynamics of Ag+ Ions in $RbAg_4I_5$ Probed Indirectly via Rb-87 Solid-State NMR. *Journal of Physical Chemistry C* **2013,** 117, (19), 9558-9565.

Chapter 2: Introduction to Solid-State NMR Spectroscopy

2.1. Introduction

Solid-State nuclear magnetic resonance (NMR) spectroscopy is a robust tool that can be used to study structure and dynamics in solid-state electrolytes. Throughout this thesis, solid-state NMR spectroscopy has been employed to study a variety of battery materials and ion conductors with the goal of understanding ion dynamics. This chapter presents the basic theoretical background of the interactions of nuclear spins in a magnetic field, as well as the behaviour of spins following an applied radio frequency pulse. The majority of the nuclei presents in this thesis are of quadrupolar nature, $I < ½$, therefore a description of quadrupolar nuclei will also be presented in this chapter. Heteronuclear dipolar coupling interactions and relaxation phenomena play a significant role in this thesis and will also be described in this chapter.

2.2. Behaviour of Nuclear Spins in a Magnetic Field

2.2.1. Nuclear Spins in an Applied Magnetic Field

A nucleus that possesses both spin and charge has a magnetic moment, $\boldsymbol{\mu}_N$, which is expressed by the following equation, ***Equation 2.1***:[1]

$$\boldsymbol{\mu}_N = \gamma_N \hbar \mathbf{I} = g_N \beta_N \mathbf{I} \qquad 2.1$$

Where γ_N is called the gyromagnetic ratio of the nucleus and has units of rad·sec^{-1}·gauss^{-1} and $\boldsymbol{I}\hbar$ is the spin angular momentum vector. Additionally, the magnetic moment can be expressed in terms of g_N, the nuclear g factor, and β_N, the nuclear magneton. A nucleus is

distinguished from another by the values of g_N and I. Together, $g_N I$ is defined as the scalar magnetic moment, μ_N.

The nuclear spin quantum number, m_I can only have discreet quantized values of $+I...-I$. Protons of the hydrogen atom are the most common nuclei studied by NMR spectroscopy. These nuclei have the value $I = ½$ and may have m_I = -1/2 or +1/2. Under an applied external magnetic field, $\boldsymbol{B_0}$, the magnetic moment, $\boldsymbol{\mu}_N$, of a proton interacts with the magnetic field and the following Hamiltonian in ***Equation 2.2*** can be used to describe the interaction:

$$\mathcal{H} = -\mu_N \cdot \mathbf{B_0} \qquad 2.2$$

Since nuclei have a spin angular momentum, they are known to precess around an externally applied magnetic field, $\boldsymbol{B_0}$. The frequency of this precession is called the Larmor frequency, ω_0, which is a product of the gyromagnetic ratio, γ, of the nucleus and the applied field:

$$\omega_0 = \gamma \boldsymbol{B_0} \qquad 2.3$$

2.2.2. Zeeman Splitting in an External Magnetic Field

With an external magnetic field in the z-direction the interaction between the magnetic moment and the external field can be represented by the following Hamiltonian:

$$\mathcal{H} = -\gamma\hbar \boldsymbol{B_0} I_z = -g_N \beta_N \boldsymbol{B_0} I_z \qquad 2.4$$

I_Z is the allowed component of the nuclear spin in the z-direction and has the value + 1/2 or – 1/2. This separation in energy levels is called the Zeeman splitting. For a large number of spins there is a distribution of spins between the +1/2 and -1/2 states, |α› and

|β›, respectively. The +1/2 state is considered the low energy state, since the values of β_N and g_N are both positive. The nuclear moment of the spins in this state are aligned with the direction of the external magnetic field, $\boldsymbol{B_0}$, which by convention are aligned along the z-axis. In the -1/2 state β_N and g_N are antiparallel. The energy difference (ΔE) between these states is given by ***Equation 2.5***:

$$\Delta E = g_N \beta_N \boldsymbol{B_0} = -\gamma \hbar \boldsymbol{B_0}(m_\beta - m_\alpha) \qquad 2.5$$

Where m_α and m_β represent the high energy and low energy states, respectively. The distribution of spins throughout these states is given by the Boltzmann law where the ratio of spins between the low and high energy states is given by $e^{-\Delta E/kT}$. Where k is the Boltzmann constant and T is the temperature of the system in Kelvin.[1] A schematic diagram of this distribution is shown in ***Figure 2.1***.[1, 2]

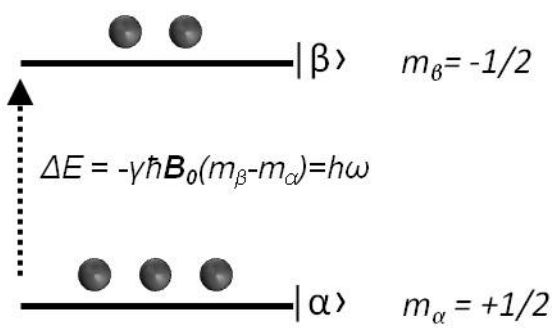

Figure 2.1. Zeeman splitting of nuclear spins in an applied external magnetic field. The energy difference, ΔE, leads to a population difference in the energy levels, |α› and |β›, which is governed by the Boltzmann distribution. ω is the Larmor frequency of the nuclei in this system.

2.2.3. Radiofrequency Pulses

NMR spectroscopic experiments are performed by applying a radiofrequency, RF, pulse to nuclear spins in materials, which places them in an excited state. Relaxation by

the free induction decay (FID) of the spins produces the NMR signal that is detected in an experiment.[2] The RF pulse is an oscillating magnetic field, $\boldsymbol{B_1}$, which is close in frequency to the Larmor frequency of the nucleus of interest. It is applied in the plane perpendicular to the external field, $\boldsymbol{B_0}$, which is conventionally the xy-plane. For a pulse applied along the x-axis with a pulse oscillating at ω_{RF} the following Hamiltonian for a single spin is:[3]

$$\mathcal{H} = \omega_0 I_Z + 2\omega_1 cos\omega_{RF} t\, I_x \qquad 2.6$$

The term $\omega_0 I_Z$ represents the interaction of the spin with the external static magnetic field, and the term $2\omega_1 cos\omega_{RF} t I_x$ represents the interaction with the $\boldsymbol{B_1}$ oscillating field. The frequency of the oscillating $\boldsymbol{B_1}$ field is given by ω_1. In general when pulses are described, the rotating frame is used. The rotating frame is taken at the point of reference of the oscillating spin as it rotates around the z-axis (direction of $\boldsymbol{B_0}$). The rotation occurs at a frequency, ω_{RF}. This causes the Larmor precession to be at (ω_0-ω_{RF}), which is known as the offset, Ω. The translation to the rotating frame removes the time dependence of the applied pulse, and the Hamiltonian becomes time-independent:

$$\mathcal{H} = (\omega_0 - \omega_{RF}) I_Z + \omega_1 I_x = \Omega I_Z + \omega_1 I_x \qquad 2.7$$

For excitation pulses the offset can be ignored when the $\boldsymbol{B_1}$ field strength is much greater than the offset. Therefore we can write the pulse Hamiltonian for an x- and y-pulse as follows:[3]

$$\mathcal{H}_x = \omega_1 I_x \qquad \mathcal{H}_y = \omega_1 I_y \qquad 2.8$$

Many NMR experiments aim to align spins along the xy-plane, after which relaxation occurs within this plane and also towards alignment with the z-axis. This will be discussed in more detail later. The goal is to have the final position of the spins in the xy-plane since when the spins are in this plane they are observable by the receiver coil, which detects magnetization in the x and y directions.

2.2.4. Magic Angle Spinning

Magic angle spinning (MAS) is a technique used in many solid-state NMR spectroscopic experiments to remove line broadening of spectral resonances. In solution NMR spectra, rapid tumbling of molecules averages the molecular orientation dependence which, in solids, causes the broadening associated with chemical shift anisotropy, dipolar coupling, quadrupolar coupling and other orientation dependent effects. In solid-state NMR spectra, these effects are still present and affect the observed line shapes. Many of the features that contribute to line broadening have the term ($3cos^2\theta$-1) in their respective Hamiltonians, such as that for heteronuclear dipolar coupling:[4, 5]

$$\mathcal{H}_D = -\frac{\mu_0}{4\pi}\frac{\gamma_i\gamma_j\hbar}{r_{ij}^3}(3cos^2\theta - 1) \qquad 2.9$$

When θ = 54.74°, the term ($3cos^2\theta$-1) is equal to 0. In NMR spectroscopy, for a powdered sample, crystallites can be averaged to 54.74° by physically spinning a solid sample in a rotor at 54.74° with respect to the external magnetic field, $\boldsymbol{B_0}$. 54.74° is the Magic Angle. Faster spinning results in more effective averaging. At this point the fastest achieved spinning speed is 110 kHz, but speeds around 30 kHz are more widely used. In

general, to obtain faster spinning, smaller rotors, and thus less material, must be used.[5] It should be noted that with smaller coils, the sensitivity per mass of sample increases.[6]

When the spinning of the sample is less (in Hz) than the spectral width of the observed spectrum, the signal is divided into frequency bins, which are separated by the spinning speed. This results in spinning sidebands, which appear as peaks in the NMR spectrum. ***Figure 2.2*** shows an example of the ^{79}Br spectrum under static and under MAS conditions. The broad ^{79}Br signal at the bottom is narrowed by MAS to reveal a sharp peak (single most intense peak in the spectrum). In addition to the isotropic resonance, in the MAS spectrum there are also a series of spinning sidebands which extend much further than the expected width of the central transition seen in the static sample. These spinning sidebands are in fact signal from the satellite transitions that arise as a result of the ^{79}Br quadrupolar transitions, as it has spin 3/2. These are not visible in the static spectrum as they are very broad and lie along the baseline. A discussion of quadrupolar nuclei will be given in section 2.3.

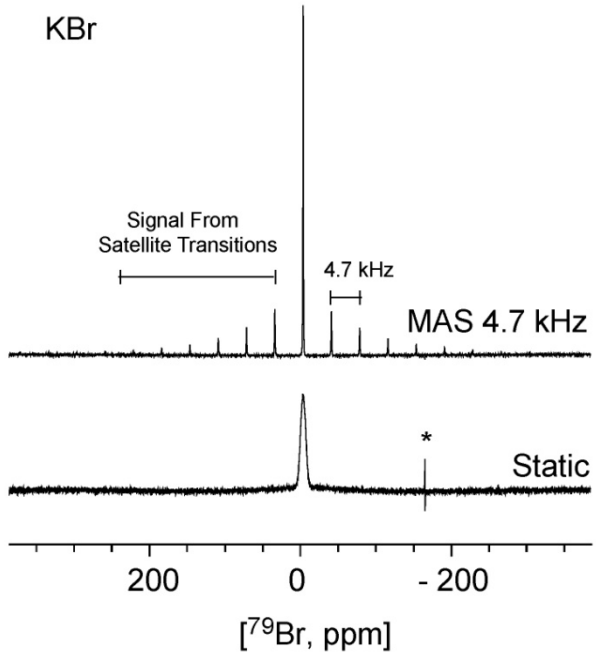

Figure 2.2. Bottom: Static; and Top: MAS (4.7 kHz) spectra of ^{79}Br in KBr. The signal from the central transition can be seen in the static spectrum as a single broad resonance. In the MAS spectrum it is the most intense peak in the center of the spectrum. In addition to the central transition, the MAS spectrum also shows signal form the satellite transitions, which are not visible in the static spectrum, as they are very broad and lie along the baseline. * Indicates an artifact.

2.2.5. Nuclear Spin Relaxation

Nuclear spins in a magnetic field naturally align with the axis of the external field, $\boldsymbol{B_0}$. As a result, when a $\boldsymbol{B_1}$ pulse is applied for a time the spins naturally tend to relax to their equilibrium position, aligned with the external field. Generally spin relaxation following an applied pulse occurs in two modes: Spin-lattice relaxation, also known as longitudinal, or T_1, relaxation; and spin-spin relaxation, also known as transverse, or T_2, relaxation. Relaxation occurs as a result of fluctuations in the local magnetic field at the nucleus. The main contributions in solids are shielding anisotropy, dipolar coupling and the quadrupolar interaction, where applicable.[4]

2.2.5.1. Spin-Lattice Relaxation

The spin-lattice relaxation time constant, T_1, is the time associated with the relaxation of spins from the xy-plane to the z-axis after an applied $\boldsymbol{B_1}$ pulse. This is an exponential relaxation where the magnetization along the z-axis, M_z, returns from 0 to the original value at equilibrium, M_Z^{eq} and is governed by the following equation:[2]

$$M_Z = M_Z^{eq}(1 - e^{-\frac{t}{T_1}}) \qquad 2.10$$

T_1 is governed by the local environment around the nucleus of interest. Structural as well as dynamic properties within a material can have a significant effect on T_1. Some of the most common contributions to the total relaxation (T^{-1}_{1T}) in solids are dipolar coupling (T^{-1}_{1D}), chemical shift anisotropy (T^{-1}_{1CSA}) and quadrupolar coupling (T^{-1}_{1Q}):[7]

$$T_{1T}^{-1} = T_{1D}^{-1} + T_{1CSA}^{-1} + T_{1Q}^{-1} \qquad 2.11$$

T_1 is a limiting factor in experimental time where integration is concerned. In order to obtain spectral resonances that represent the true relative quantity of nuclei in different environments, an experiment must be performed after a wait period of five times T_1. For many materials this is not an extended period, however, lithium ion electrolytes tend to have a very long T_1 relaxation time. Immobile lithium sites can have T_1 on the order of 10 minutes. Factors that contribute to this are the lack of relaxation mechanisms due to high symmetry, which remove contributions from quadrupolar and chemical shift anisotropy. In this thesis, nuclei within the same material have exhibited vastly different T_1 relaxation times due in part to differences in local environment, but also due to differences in ion

mobility. Furthermore, the great difference in T_1 for different crystallographic environments is evidence that there is no chemical exchange between sites. This will be discussed in more detail in upcoming chapters. ***Figure 2.3*** illustrates the T_1 relaxation after a pulse.

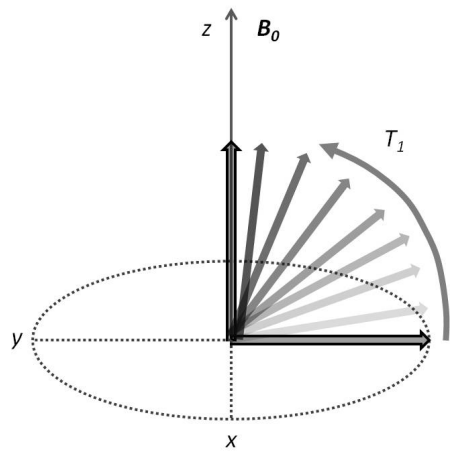

Figure 2.3. Spin-lattice relaxation after a pulse is applied, placing the magnetization in the xy-plane.

2.2.5.2. Spin-Spin Relaxation

The spin-spin relaxation time constant, T_2, is the time associated with the relaxation of spins in the xy-plane. After a $\boldsymbol{B_1}$ pulse directs nuclear spins into the xy-plane, the spins spread into the plane under various influences, such as chemical shift anisotropy, dipolar coupling and quadrupolar coupling. After a time, T_2, the vector average of all of the spins becomes 0. This is treated as an exponential decay, where the magnetization in the xy-plane ($\boldsymbol{M_{XY}}$) returns to 0 from its maximum value ($\boldsymbol{M_0}$) after a pulse onto the xy-plane:[2]

$$M_{XY}(\tau) = M_0[\exp\left(-\frac{\tau}{T_2}\right)] \qquad 2.12$$

As in the case of spin-lattice relaxation, spin-spin relaxation also has many contributing factors. In many cases, the relaxation cannot be represented by a single exponential decay. ***Figure 2.4*** illustrates the T_2 relaxation in the xy-plane after a pulse is applied. The length of T_2 relaxation is usually shorter than the T_1 relaxation and can be as short as tens of microseconds, but in the case of mobile solutions the rapid exchange present causes $T_1 = T_2$.[2] The free induction decay (FID) measured by NMR is a manifestation of T_2, known as T_2*. T_2* is the time taken for the NMR signal to decay to 1/e of its original value and it is generally shorter than T_2 because the presence magnetic field inhomogeneities increases the relaxation rate. The line width of the NMR spectral resonance is governed by T_2* and can be given by $1/\pi T_2$* (for the lineshape of a sample in solution), where a shorter value of T_2* results in a broader line width.[2, 4]

Two different methods can be used to measure T_2 relaxation: the Carr-Purcell-Meiboom-Gill (CPMG)[8] pulse sequence; and a series of Hahn-echo[9] experiments with different delay times. The CPMG experiment is the most commonly used method to determine the T_2 of a nucleus, and it consists of an excitation pulse followed by a delay time and then a series of echoes which refocus the spin vectors.[8] Signal is acquired after each refocusing pulse and therefore the collection of data occurs rapidly, since many acquisitions occur within a single experiment. The pulse sequence is shown in ***Figure 2.5*** along with a typical CPMG FID, where the signal is separated into several echoes. T_2 is measured by plotting the intensity of the peak of the echoes as a function of time and

using ***Equation 2.12*** to extract the T_2 constant.[8, 10] It should be noted that when collecting a spectrum using the CPMG pulse sequence, the signal is separated into spikelets, which are separated by the inverse of π-pulse separation. The collection of multiple echoes also causes an increase in the signal-to-noise ratio (SNR).[4]

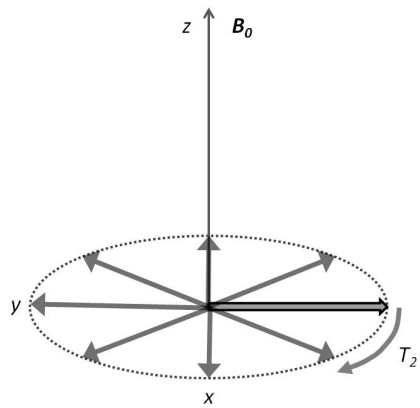

Figure 2.4. Spin-spin relaxation after a pulse is applied, which places the magnetization in the xy-plane.

The Hahn-echo experiment is collected as a series of separate experiments in which the echo delay and refocusing time are systematically increased (τ_1 and τ_2, respectively in ***Figure 2.5*** (c)). The intensity of the spectral peak in each experiment is measured and plotted as a function of the total echo time (total time between the $^{\pi}/_{2}$ excitation pulse and the beginning of data collection) to obtain the T_2 using ***Equation 2.12***.[9]

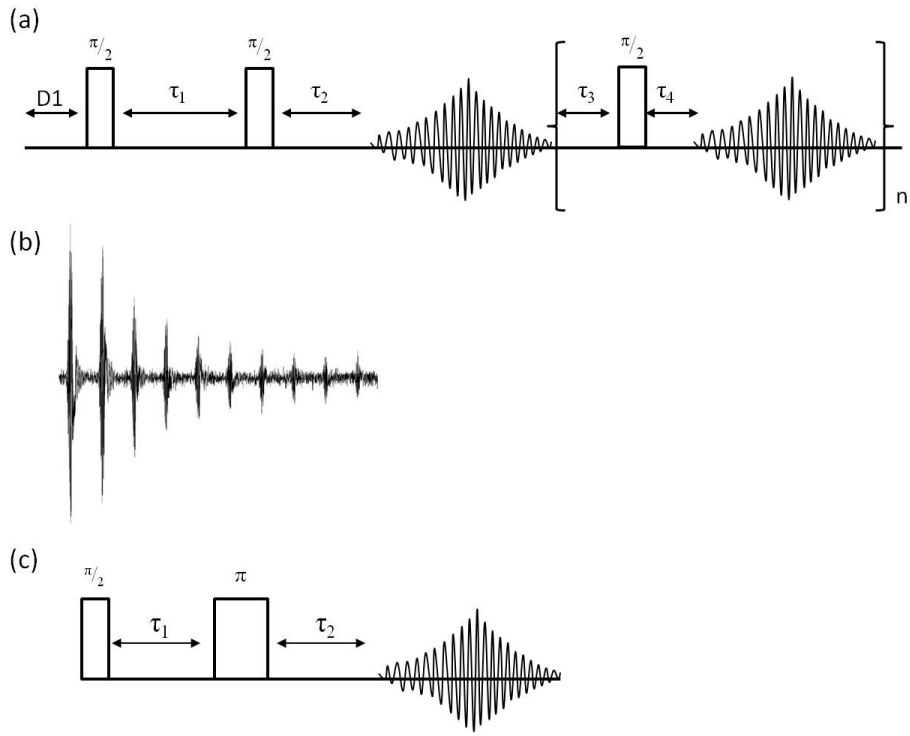

Figure 2.5. NMR experiments used to measure T_2 relaxation. (a) The CPMG pulse sequence; (b) a typical FID resulting from a CPMG experiment; (c) the Hahn-echo pulse sequence, where τ_1 and τ_2 are changed systematically in a series of experiments in order to observe the signal decay as a function of the total echo time.

2.3. Solid-State NMR of Quadrupolar Nuclei

Nuclei with a spin number greater that 1/2, quadrupolar nuclei, are subject to a nuclear electric quadrupole moment, *eQ*. The value of *Q* can be positive or negative, and is measured in m^2, with the magnitude determined by the charge distribution in the nucleus, which is non-spherical. This is a nuclear property and does not depend on environment. The corresponding values of *Q* are listed later in ***Table 2.1***. The quadrupole moment couples with the electric field gradient, EFG (***eq***), which is a product of the surrounding electron environment. The quadrupolar interaction is large, and in many

cases dominates the NMR spectrum. In general this relationship makes the NMR lineshape of quadrupolar nuclei very interesting, and sensitive to surrounding environments.[4] In this thesis quadrupolar nuclei have played a significant role in the determination of structural and dynamic properties of lithium ion conductors.

2.3.1. Energy Level Splitting in a Magnetic Field

Nuclei with a spin greater than 1/2 have different energy transitions than their spin-1/2 counterparts. In addition to the Zeeman splitting shown in ***Figure 2.1***, quadrupolar nuclei can also have first-order and second-order contributions from the quadrupolar interaction. This is illustrated for a spin-3/2 nucleus in ***Figure 2.6***.[11] For this system, there are two satellite transitions present: (-3/2 ↔ -1/2) and (+3/2 ↔ +1/2). Only the satellite transitions are affected by the first-order quadrupolar interaction, while the central transition (-1/2 → +1/2 transition) remains unaffected. However, if the quadrupolar interaction is large enough, i.e. significant when compared to the Zeeman interaction, all transitions are affected by the second-order quadrupolar interaction. This includes the central transition, which exhibits an orientation dependence in the quadrupolar shift and EFG for single crystals, and is therefore known to display very interesting lineshapes for powder samples, which will be discussed in section 2.3.3.[4]

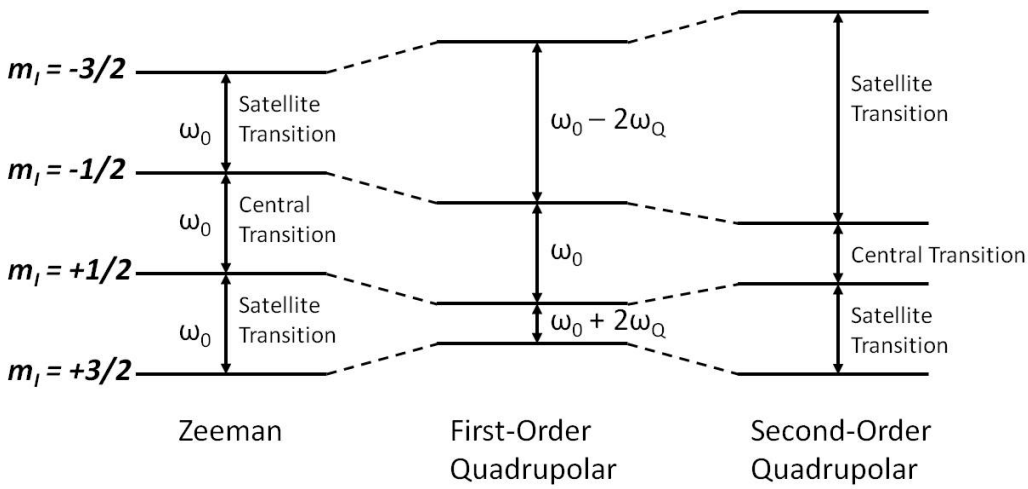

Figure 2.6. Energy-levels for a spin-3/2 nucleus in an external magnetic field. The Zeeman, as well as first- and second-order quadrupolar interactions is shown. ω_0 represents the Larmor frequency of the spin, while ω_Q represents the quadrupolar splitting parameter.[11]

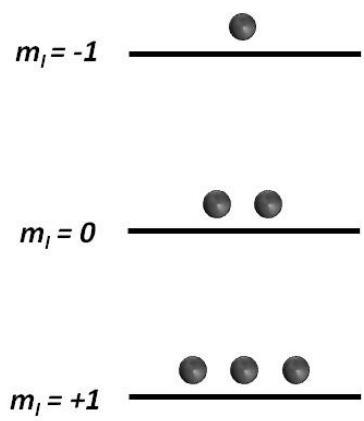

Figure 2.7. Energy level diagram for a spin-1 nucleus under Zeeman splitting.

The situation for a spin-1 nucleus is slightly different. ***Figure 2.7*** shows the energy transitions for a spin-1 nucleus under Zeeman splitting. Unlike the half-integer spins, this nucleus has no central transition, but has two satellites. This gives rise to interesting spectra and can be very useful, in particular, the satellite transitions are known to be sensitive to chemical properties, such as mobility.[5]

2.3.2. Quadrupolar Parameters

There are two parameters that are usually used to characterize the quadrupolar interaction. These are used to characterise the magnitude of the traceless tensor, $\boldsymbol{q}$, which is a component of the EFG. The quadrupolar coupling constant, C_Q (also known as χ), is proportional to the EFG anisotropy and is expressed in Hz (***Equation 2.13***); while the dimensionless asymmetry parameter, η, is defined according to the magnitude of the three components of the tensor, $\boldsymbol{q}$, where $q_{ZZ} \geq q_{YY} \geq q_{ZZ}$ (***Equation 2.14***). Both the shape of the central transition and the separation of the satellite transitions are affected by these parameters. The specific effects on the quadrupolar line shapes will be discussed in the following section.[4]

$$C_Q = \frac{e^2 Q q_{ZZ}}{h} \qquad 2.13$$

$$\eta = \frac{q_{YY} - q_{XX}}{q_{ZZ}} \qquad 2.14$$

In addition to the quadrupolar interaction there can be a contribution from shielding asymmetry and anisotropy. If this interaction is on the same order as the quadrupolar interaction there are several other terms that must be considered. The presence of shielding can influence the shape of the central transition depending on the span, Ω (in ppm); skew, κ (dimensionless); and isotropic shift, δ_{iso} (in ppm) (Herzfeld-Berger convention). In addition, the orientation of the CSA tensor with respect to the EFG tensor also affects the shape of the NMR resonance. Three Euler angles, α, β, and γ are used to describe this orientation.[5] Chapters 3 and 4 of this thesis will describe the use of these

parameters to answer questions about structure and dynamics in various ion-conducting materials.

Overall there are eight parameters that can be used to describe the shape of the central transition of a quadrupolar nucleus that is affected by a second-order quadrupolar interaction: C_Q, η, Ω, κ, δ_{iso}, α, β, γ. This makes simulating a quadrupolar line shape quite challenging, and often *ab initio* calculations are performed to aid in the determination of these parameters. In addition, some knowledge of the structure and how it might influence the line shape is very important. In the following section the relationship between structure and quadrupolar line shapes will be discussed.

2.3.3. Quadrupolar Line Shapes

For powdered samples, the shape of the central transition powder pattern can be very useful for structural determination. In addition, elements with larger EFGs are more sensitive to the surrounding environment. This sensitivity allows for the detection of dynamic processes. If shielding is not considered, the main contribution to the quadrupole line shape for the central transition of a powdered sample is the magnitude of its anisotropy and its asymmetry parameter (deviation from cylindrical symmetry), which can be described by the parameters C_Q and η.

The quadrupole coupling constant, C_Q, affects the width of the NMR spectrum. The larger the value of C_Q, which can range from Hz to MHz, the broader the powder pattern for the central transition. The satellite transitions can be very broad and are not usually observed for nuclei with large values of C_Q, since in many cases they appear along the

baseline, as in the ^{79}Br spectra in ***Figure 2.2***. ***Figure 2.8*** shows the changes in a simulated spectrum for a nuclei with spin-7/2, while $\eta = 0$, i.e. axially symmetric. The value of C_Q is increased by lower symmetry of directly bonded atoms. Larger values of C_Q result in a broader spectrum. For spins in a more spherical environment, C_Q is smaller and the spectral width is narrower.[12]

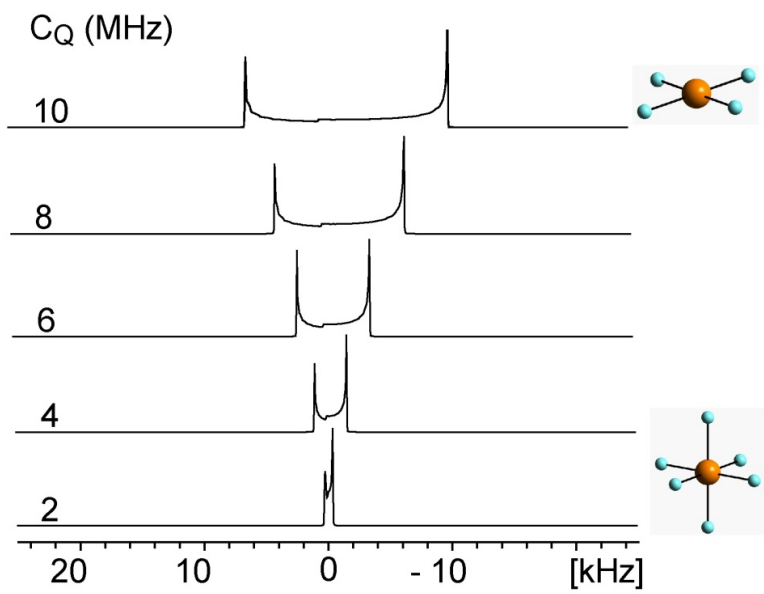

Figure 2.8. Simulated central transition for a spin-7/2 system under axial symmetry. C_Q ranges from 2 MHz to 10 MHz. A larger C_Q is observed for systems with non-spherical directly bonded atoms, while a small C_Q is observed for a more spherical geometry.

While the value of C_Q (in Hz) stays constant with the external magnetic field, the effect on the spectral width varies inversely to the strength of the external field (in ppm). When the interaction of CSA is considered, measuring spectra at different fields is extremely helpful, since this interaction scales proportionally to the field. This allows the simulation of two line shapes at different fields to obtain the same spectral parameters and ultimately results in a more accurate measurement of the quadrupolar parameters.

The asymmetry parameter, η, ranges from 0 to 1 and affects the line shape of the central transition in a quadrupolar powder pattern. ***Figure 2.9*** shows the line shape dependence for quadrupolar nuclei with spin-7/2. When $\eta = 0$ the line shape is said to be axial. The outer features, called singularities, are at the ends of the spectral shape. A value of $\eta = 0$ results from long range order in a crystal system, in particular, when there is a symmetry axis of 3-fold rotation or some higher symmetry element that runs directly thought the nucleus of interest. This is very useful for structural analysis in solids, where crystal symmetry is a key consideration. For lower symmetry cases, η has some value between 0 and 1. The positions of the singularities vary considerably as η increases.

Magic angle spinning is used in many cases in solid-state NMR to obtain highly resolved spectra which are averaged to the isotropic shift. For quadrupolar line shapes this is not as easily done. The resonance frequency for an axially symmetric system ($\eta = 0$) can be represented by ***Equation 2.15***, where ω_0 is the Larmor frequency, $f(I)$ is the spin-dependent factor, given in ***Equation 2.16***, θ is the angle of a crystallite with respect to $\boldsymbol{B_0}$, and P_2 and P_4 are the Legendre polynomials shown in ***Equations 2.17*** (a) and (b).[4]

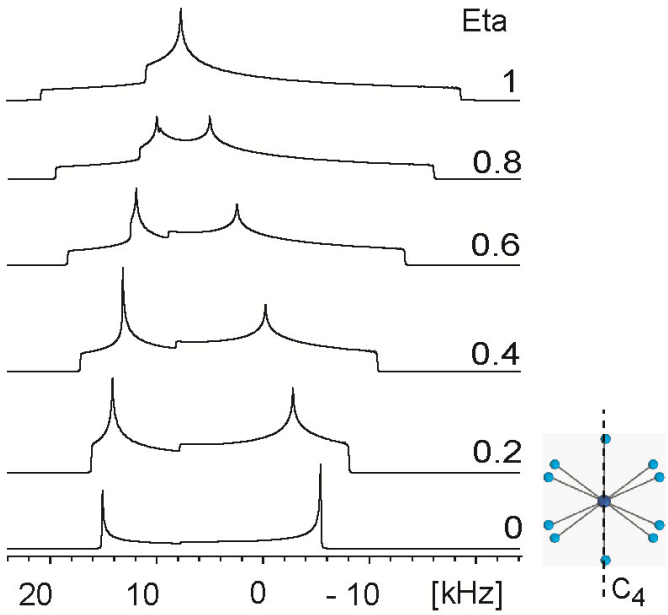

Figure 2.9. Variation of η from 0 to 1 in a simulated spectrum for a spin-7/2 system. The inset shows a crystallographic position with a C_4 symmetry axis passing through the nucleus of interest, creating a value of $\eta = 0$.

$$\nu = -\frac{C_Q^2}{\omega_0} f(I)[\frac{3}{10} + \frac{6}{7}P_2(cos\theta) - \frac{81}{70}P_4(cos\theta)] \qquad 2.15$$

$$f(I) = \frac{2I+3}{(4I)^2(2I-1)} \qquad 2.16$$

$$P_2(cos\theta) = \frac{1}{2}(3cos^2\theta - 1) \qquad 2.17(a)$$

$$P_4(cos\theta) = \frac{1}{8}(35cos^4\theta - 30cos^2\theta + 3) \qquad 2.17(b)$$

MAS removes contributions to the line shape that are described by ($3cos^2\theta$-1) terms, such as P_2. However, ***Equation 2.15*** contains two angle-dependent terms, only one of which is affected by the averaging of ($3cos^2\theta$-1) to 0 by MAS. This means that when quadrupolar nuclei are spun at the magic angle some residual line shape remains. When

the quadrupolar interaction is large enough, spinning sidebands from the second order quadrupolar interaction can be observed. In such cases, static spectra are easier to use. ***Figure 2.10*** illustrates the effect of MAS on a spin-7/2 system with C_Q = 10 MHz and $\eta = 0$ in a pair of simulated spectra. In order for this change in line shape under MAS the sample spinning speed must be 3 to 4 times the width of the static line shape. This is challenging in many cases, since spectra that result from large quadrupolar couplings are much broader than the current MAS rates.

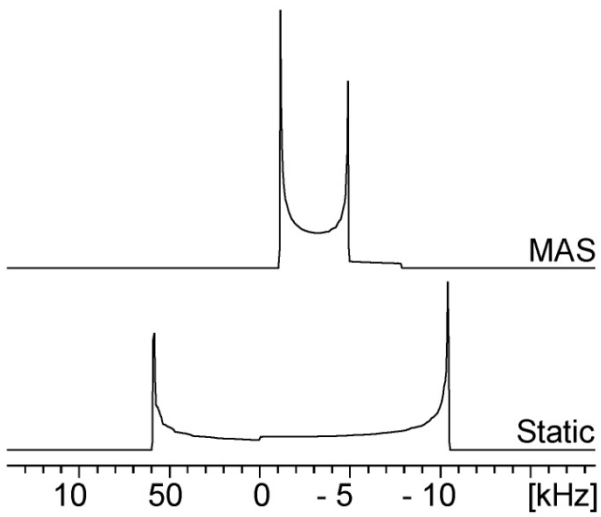

Figure 2.10. Simulations of static and MAS spectra for a spin-7/2 system with C_Q = 10 MHz and $\eta = 0$.

Equations 2.15 and ***2.16*** bring to light some interesting properties of quadrupolar lineshapes: The center of gravity of the powder line shape for the central transition is calculated from the first term in ***Equation 2.15***: ($-3C_Q^2 f(I)/10\nu_0$). Also, if the term *f(I)* is considered, the larger the spin term (I = 3/2, 5/2, ...), the smaller the value of *f(I)*. This means that for systems with similar coupling constants the second-order quadrupolar

effects, such as line broadening, are less significant for spins with a larger nuclear spin number.[4]

2.3.4. Dynamics and Quadrupolar Nuclei

Quadrupolar nuclei with large EFGs are sensitive to their surrounding chemical environments. This makes these nuclei sensitive to dynamic processes that occur on a timescale that is on the same order of magnitude as the width of the NMR spectral resonance. Specific types of exchange processes affect the quadrupolar line shape of the central transition differently. Work by Schurko *et al.* has pointed out that for different types of motion, the rate of exchange has predictable influences on the shape of the central transition powder patter. ***Figure 2.11*** shows simulations which shows the changes in quadrupolar line shape, as well as first-order shielding anisotropy, as a function of hopping rate for several different types of molecular-reorientation-motion.[13]

Other authors have reported changes in quadrupolar line shape to explain the ionic transport motion in materials. van Wüllen *et al*. have used ^{17}O NMR to study motion in the lithium ion conductor $LiCF_3SO_3$. In each of these cases the motion reported was rotational, as seen in ***Figure 2.11.*** In the case of $LiCF_3SO_3$ there is rotation of CF_3 and SO_3 groups in addition to lithium ion motion.[14] Prof. R. L. Vold *et al*. have developed software to calculate such motion: EXPRESS is a program written to model quadrupolar line shapes as a function of motion. This will be discussed in more detail in Chapter 4 of this thesis.

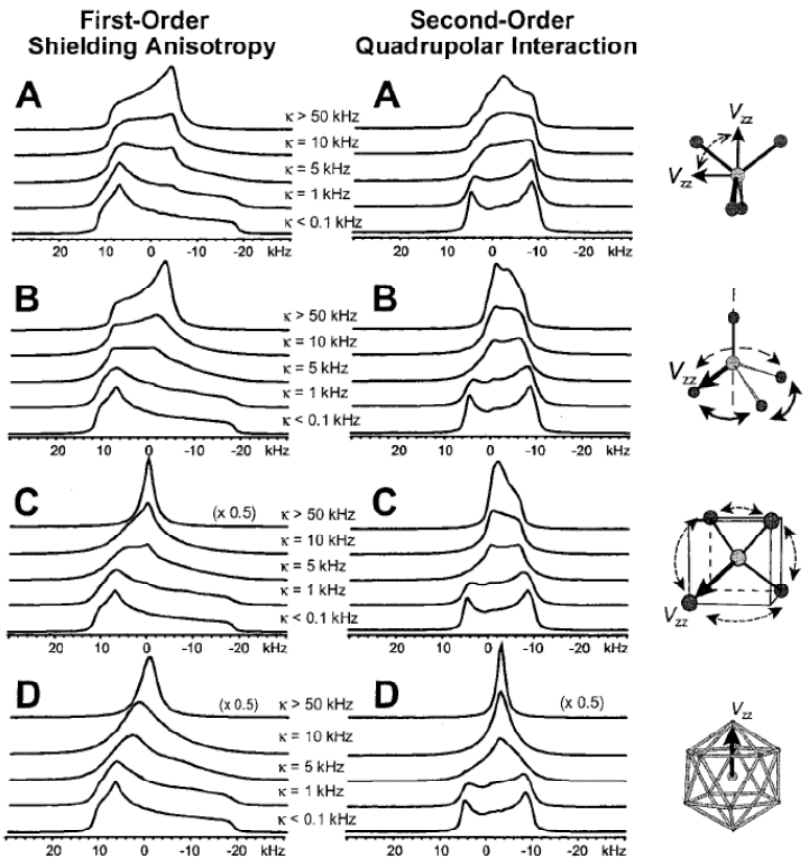

Figure 2.11. Dependence of second-order quadrupolar line shape and first-order shielding anisotropy on dynamic processes. This figure was reproduced from work done by Shurko *et al*.[13] Reprinted with permission from (Schurko, R. W.; Wi, S.; Frydman, L. *Journal of Physical Chemistry A,* **2002,** 106, (1), 51-62.) Copyright 2002 American Chemical Society.

2.3.5. Measurement of Quadrupolar Line Shapes

Quadrupolar nuclei behave differently from their spin-1/2 counterparts under excitation with a $\boldsymbol{B_1}$ pulse. While the flip angle (orientation of the nuclear vector after $\boldsymbol{B_1}$ excitation pulse with respect to $\boldsymbol{B_0}$) of a spin-1/2 nucleus has a sinusoidal dependence on pulse length, quadrupolar nuclei have several different conditions for flip angle dependence, which depend on the size of the quadrupolar coupling in relation to the RF

excitation frequency (RF).[12] Note that the RF nutation frequency is derived from the nutation curve obtained from the liquid reference. The conditions are as follows:

1) When C_Q << RF the nutation frequency is the same as the RF frequency. This is the same as the spin-1/2 case and the relationship is sinusoidal.
2) When C_Q >> RF the nutation frequency scales by a constant (I + ½), known as the Rabi factor, and is still sinusoidal.[4] This means a pulse calibrated on a solution sample, where $C_Q = 0$ is not appropriate to be used for a solid sample with C_Q >> 0, and instead the calibrated pulse length must be divided by (I + ½) for solids.
3) When C_Q ~ RF the nutation behaves in a non-sinusoidal fashion.[12, 15, 16]

In many cases when observing a quadrupolar nucleus with a single pulsed experiment, a very short pulse length is used, commonly < 45° (for the solid quadrupolar central transition). This is to ensure that if there are several resonances with different C_Q's all are excited equally. ***Figure 2.12*** illustrates the dependence of the intensity of the central transition on pulse length for a variety of situations in which the ratio of ω_Q/ω_{rf} (C_Q/RF) is changed for a spin-5/2 system. It can be seen that for small pulse lengths, where ($\sin\theta \sim \theta$) (x-axis) that the excitation of all systems is that same. This interesting dependence has inspired several intensive studies involving nutation spectroscopy.[15-18]

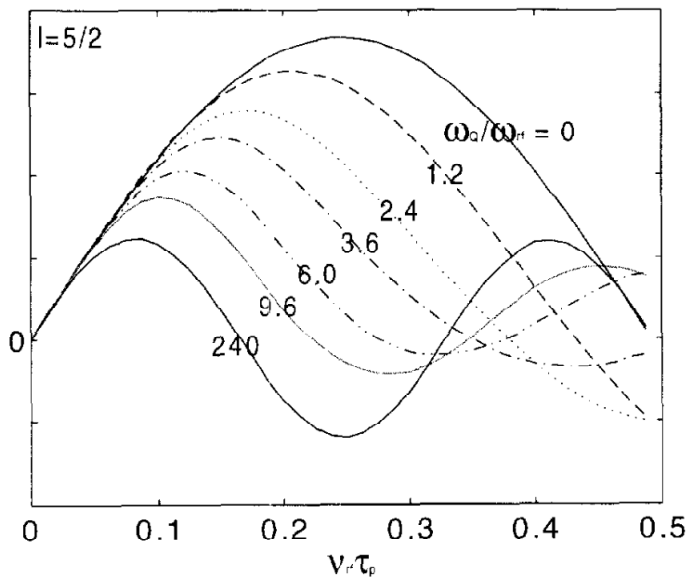

Figure 2.12. Dependence of intensity of central transition on pulse length for several cases where the ratio of the quadrupolar coupling to the RF frequency is varied [ω_Q/ω_{rf} (C_Q/RF)]. This figure was produced by A. P. M. Kentgens.[12] Reprinted from publication title (Kentgens, A. P. M., A practical guide to solid-state NMR of half-integer quadrupolar nuclei with some applications to disordered systems. *Geoderma* **1997,** 80, (3-4), 271-306) with permission from Elsevier.

2.3.5.1. Solid-Echo and WURST-Echo, and WURST-QCPMG Pulse Sequences

Several different NMR spectroscopy pulse sequences are used to collect ultra-wideline NMR spectra (hundreds of kHz MHz in spectral width). There are a number of considerations, in particular, the signal intensity is spread through such a wide range that the signal to noise ratio is very low. For quadrupolar nuclei with resonances that are too broad for MAS to be effective the solid-echo, WURST-echo, and WURST-QCPMG (Quadrupolar Carr-Purcell Meiboom-Gill) pulse sequences are perhaps the most widely used for the observation of powder pattern of the quadrupolar central transition.[19, 20] The

WURST techniques can excite a broad bandwidth, and QCPMG techniques allow the collection of NMR spectra in a small amount of time. ***Figure 2.13*** shows these pulse sequences.[10] Each pulse sequence is a type of "echo", meaning that there is an initial excitation pulse followed by a delay and then another pulse, which re-focuses the spin vectors ("refocusing pulse").[3] The traditional Hahn-echo uses a $^{\pi}/_{2}$ excitation pulse followed by a refocusing π-pulse.

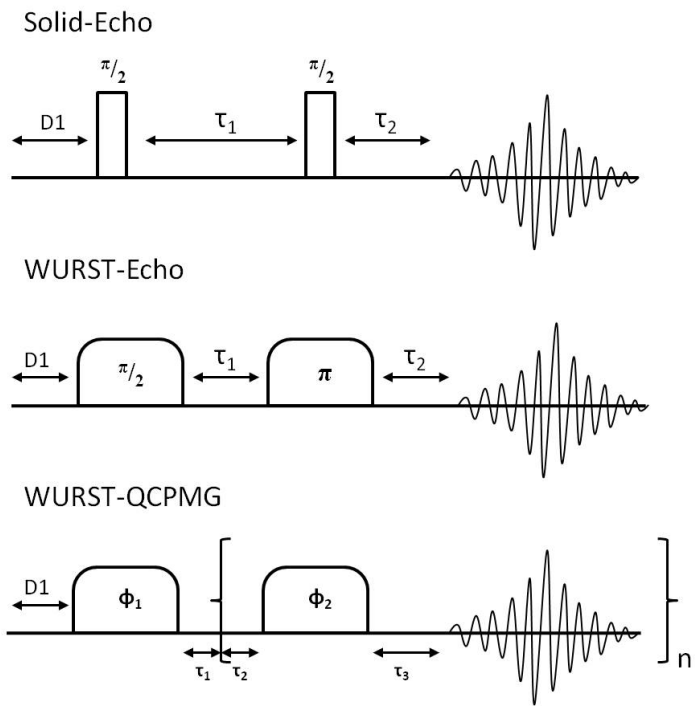

Figure 2.13. Solid-echo, WURST-echo and WURST-QCPMG pulse sequences.[10, 19, 20]

The solid-echo pulse sequence uses two $^{\pi}/_{2}$-pulses with high power and a relatively small bandwidth (when compared to the WURST pulse) that can excite the full central transition of nuclei with small C_Q, such as ^{27}Al or ^{87}Rb. For larger C_Q this pulse sequence can be used, but several spectra must be recorded in which the excitation frequency

(transmitter frequency) is moved systematically for each experiment such that when the experiments are combined the full spectral width of the resonance had been excited. This frequency stepping allows the collection of wide spectra in pieces, which must be added or overlaid to find the shape of the full spectrum.[21, 22] Alternatively, the application of frequency-swept non-adiabatic WURST (Wideband Uniform-Rate Smooth Truncation) pulses allow a wide sweep width to be sampled in the same experiment allowing the collection of very broad spectra (sometimes reaching 2 MHz) in a single experiment.[19, 20, 23, 24] Frequency-swept non-adiabatic pulses are low power pulses in which the transmitter frequency is swept over a large bandwidth exciting a wide sweep width, larger than that of a typical hard pulse.[24]

WURST pulses can be applied in the solid-echo pulse sequence, to make the WURST-echo pulse sequence, or used to modify the QCPMG pulse sequence. The WURST pulse is applied by sweeping the transmitter through a range of frequencies at low power, while simultaneously modifying the phase of the pulse.[20] The original CMPG pulse sequence begins by exciting the spins in a system using a 90° pulse (***Figure 2.5*** (a)). This is then followed by a series of refocusing 180° pulses which are combined with signal acquisition after each pulse. As mentioned above, this allows rapid signal collection and is very efficient.[25] The WURST-QCPMG experiment is shown in ***Figure 2.13***, where the original CPMG pulse sequence has been modified to include WURST pulses instead of hard pulses. When the WURST-QCPMG pulse sequence is applied the resulting spectrum is made up of spikelets, as in the CPMG experiment discussed above. ***Figure 2.14*** shows a comparison of these three pulse sequences when applied to ^{139}La in

$LaNbO_4$ at 21.1 T. The experimental time for the WURST-QCPMG is much shorter than that of the other echo techniques, since multiple acquisitions are recorded in a single experiment and the resulting signal is concentrated in spikelets. In ***Figure 2.14*** the solid-echo and WURST-echo experiments took ~ 34 minutes to collect, while the WURST-QCPMG was collected in 4 minutes.

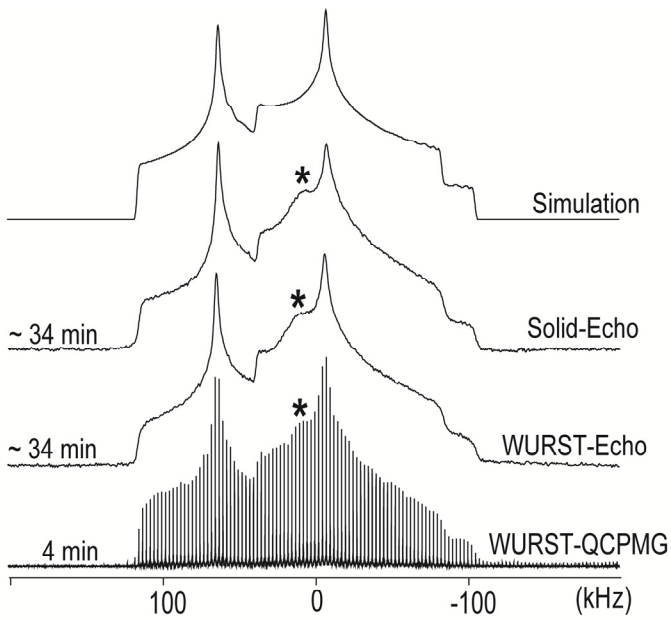

Figure 2.14. Solid-echo, WURST-echo and WURST-QCPMG spectra of ^{139}La in $LaNbO_4$ at 21.1 T.[26] * represents a small impurity. Here C_Q = 36 ±2 MHz, η = 0.44 ± 0.05, δ_{iso} = 295 ± 25 ppm, Ω = 255 ± 10 ppm, κ = 0.40 ± 0.04, α = 90 ± 5°, β = 50 ± 5°, γ = 270 ± 10°. A simulation performed using WSolids software is shown at the top.

2.3.5.2. Line Shape Simulations and *Ab Initio* Calculations

In addition to the collection of wide-line spectra, the simulation of line shapes is an important aspect of studying quadrupolar nuclei. As mentioned earlier, there are potentially eight parameters that contribute to the line shape observed for quadrupolar

nuclei when shielding is considered. This means that it is essential to simulate these spectra (acquired at multiple fields, if possible) in order to extract the parameters. Several programs have been developed for spectral simulation including: WSolids[27] and DMFit[28] software. These programs allow a user to input the parameters for a lineshape and refine these parameters against an experimentally obtained spectrum. Refinement may be done by hand or iteratively through the software. ***Figure 2.14*** (top) shows the simulation of the ^{139}La NMR spectrum of $LaNbO_4$ performed in WSolids software. The positions of the singularities are the most significant fitting feature. This includes the sharp central features as well as the steps, seen at low frequency in ***Figure 2.14***.

Ab initio calculations play an important role in the determination of the parameters that contribute to the NMR line shape. Density functional theory (DFT) calculations can provide information about these parameters and software such as CASTEP have been used widely to perform such calculations.[29] To perform CASTEP calculation a crystallographic information file (.cif) is input into the software and the program calculates the EFG and shielding parameters, which can be used to determine the NMR line shape parameters. Often, this is used in combination with simulation programs in which the parameters are entered and a comparison is made between the calculated parameters and the experimentally obtained parameters. For cases in which it is very difficult to simulate a line shape, such as instances in which there are several NMR line shapes, *ab initio* calculations can provide initial information about the line shapes and simulations can be performed.[30] CASTEP software has limitations on the information that

can be entered. Systems with unpaired electrons, such as paramagnetic or metallic systems, pose a problem. Also, partial occupancies can be problematic.

In some instances it is necessary to determine the Euler angles (α, β, γ), which relate the orientation of the CSA tensor with respect to the EFG tensor. The Euler angles can provide important information used to describe the crystal structure. In particular, systems with complex dynamics can be understood by evaluating the Euler angles.[31, 32] In spectral simulations using WSolids of DMFit software, several Euler angles may result in the same line shape. NMR parameters of a nucleus are heavily dependent on the crystal structure of the system and DFT calculation can provide information about the tensor orientations such that the true Euler angles can be calculated.

This thesis focuses heavily on the use of quadrupolar nuclei to study structure and dynamics in ion conductors. In some cases, such as the ^{6,7}Li NMR spectra, the quadrupolar parameters are small and do not contribute to the spectral interpretation; while in other cases, such as the ^{139}La spectra, the quadrupolar contribution plays a significant role. Quadrupolar nuclei are sensitive probes of structure and dynamics in solids. Although collection and interpretation of NMR spectra is not trivial, in many cases it is the only way to answer specific questions about a system. Modifications of traditional pulse sequences, such as CPMG, have improved the sensitivity towards quadrupolar nuclei, as in the WURST-QCMPG pulse sequence. In addition, high field NMR magnets and the development of *ab initio* calculation software has made the interpretation of NMR spectra less challenging.

2.4. Dipolar Coupling in NMR Spectroscopy

Dipolar coupling is a phenomenon that occurs between a pair of spins and is due to the dipole moments of the two spins, $\boldsymbol{\mu}_j$ and $\boldsymbol{\mu}_k$. This is a "through space" interaction, the magnitude of which depends on the distance between the spins. Dipolar coupling manifests itself in solid-state NMR spectra as homogeneously broadened line shapes, which can usually be narrowed using MAS, since the interaction is dependent on the term, ($3cos^2\,\theta$-1). Researchers have used the distance dependence of heteronuclear dipolar coupling to determine structural characteristics of materials.

The Hamiltonian for the heteronuclear dipolar coupling between a spin pair is given above in ***Equation 2.9***, from which the dipolar coupling constant (in frequency units, Hz) can be extracted:[4]

$$D_{jk} = \gamma_j \gamma_k \left(\frac{h}{4\pi^2}\right)\left(\frac{\mu_0}{4\pi}\right) r_{jk}^{-3} \qquad 2.18$$

where r_{jk} is the distance between a single pair of nuclei. The gyromagnetic ratios of ^{7}Li and ^{6}Li are 103.96 x 10^6 rad/sT [16.55 MHz/T] and 39.37 x 10^6 rad/sT [6.27 MHz/T], respectively. Therefore, for a pair of heteronuclear lithium nuclei that are separated by 3 Å, the dipolar coupling constant is 1598 Hz. In this thesis (Chapter 5) the dipolar coupling between ^{6}Li and ^{7}Li is extensively studied in solid state electrolytes. The dipolar coupling constant can range from 100 to 10000 Hz for a single heteronuclear pair of lithium nuclei, depending on the distance between them. However, the translation of the dipolar coupling value for a single pair of nuclei to that of several pairs is not

straightforward. In addition, the dipolar coupling interaction is anisotropic, and depends on the angle between the external magnetic field and the vector connecting a spin pair.

2.4.1. Measurement of Dipolar Coupling

Several experiments can be used to measure dipolar coupling in solids. Rotational Echo Double Resonance (REDOR) and Spin Echo Double Resonance (SEDOR) are two pulse sequences which can be used to measure heteronuclear dipolar coupling.[5, 33, 34] Each of these experiments uses a Hahn-echo to observe a nucleus, while the other dipolar coupled nucleus is perturbed systematically.

2.4.1.1. REDOR NMR Spectroscopy

The REDOR NMR experiment uses a rotor-synchronized pulse sequence, which can measure the heteronuclear dipolar coupling between a pair of spins. In the experiment a Hahn-echo is applied to the observed spin (*I*), while the other spin (*S*) is perturbed by a series of π-pulses. ***Figure 2.15*** shows the REDOR pulse sequence with the observed spin, *I* and perturbed spin, *S* (*S* is not observed). For a single resonance, the resulting experiment compares the intensity of the *I* spin with and without pulses applied to the *S* channel. By convention, the intensity of the *I* channel is called S (not in italic), and the initial intensity of the Hahn-echo (on the *I* channel) with no pulses applied to the S channel is called S_0, and is compared to the intensity of the resonance when pulses are applied to the *S* channel in the following relation:

$$(S_0 - S)/S_0 \qquad 2.19$$

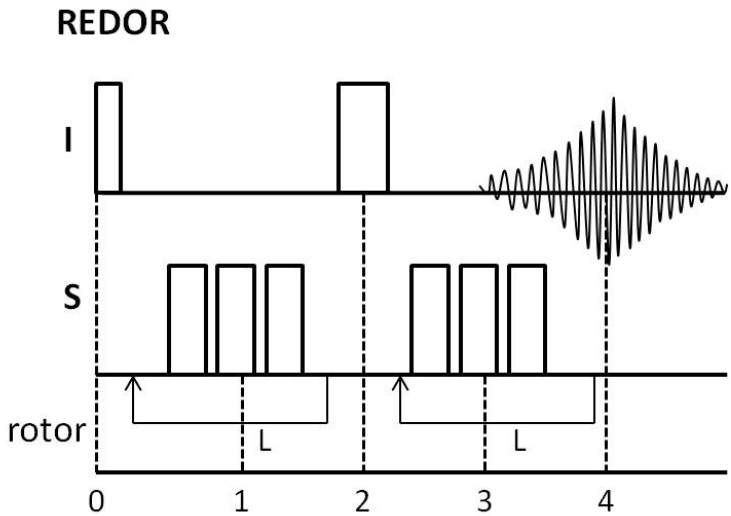

Figure 2.15. The REDOR NMR experiment. Spin *I* is observed using a Hahn-echo experiment, while spin *S* is perturbed using a series of rotor-synchronized π-pulses.

The ratio in ***Equation 2.19*** is plotted as a function of echo time, which can be calculated from the number of rotor periods used in given experiment. This results in a curve with a slope that depends on the magnitude of the heteronuclear dipolar coupling of spins *I* and *S*.[35] Extracting the dipolar coupling from the resulting curve is done using numerical simulations in software packages, such as SPINEVOLUTION.[36] The application of this method will be discussed in detail in Chapter 5 of this thesis.

A typical REDOR experiments for an isolated *I-S* system are illustrated in ***Figure 2.16*** (a)**.** The intensity on *I* channel decreases with the increase in number of pulses applied on the *S* channel as a result of *I-S* dipolar coupling. Two sets of data can be extracted for this experiment. If only the S_0 intensity is plotted there is an exponential decay with time, which is a result of T_2 relaxation. If S is plotted as a function of time the slope of the resulting curve is due to the dipolar coupling in combination with T_2 decay and oscillates around 0, as in ***Figure 2.16*** (b). The

separation of S and S_0 allows the measurement of T_2 decay form the REDOR experiment. The REDOR curve is calculated as $(S_0\text{-}S)/S_0$ and is shown in ***Figure 2.17***.

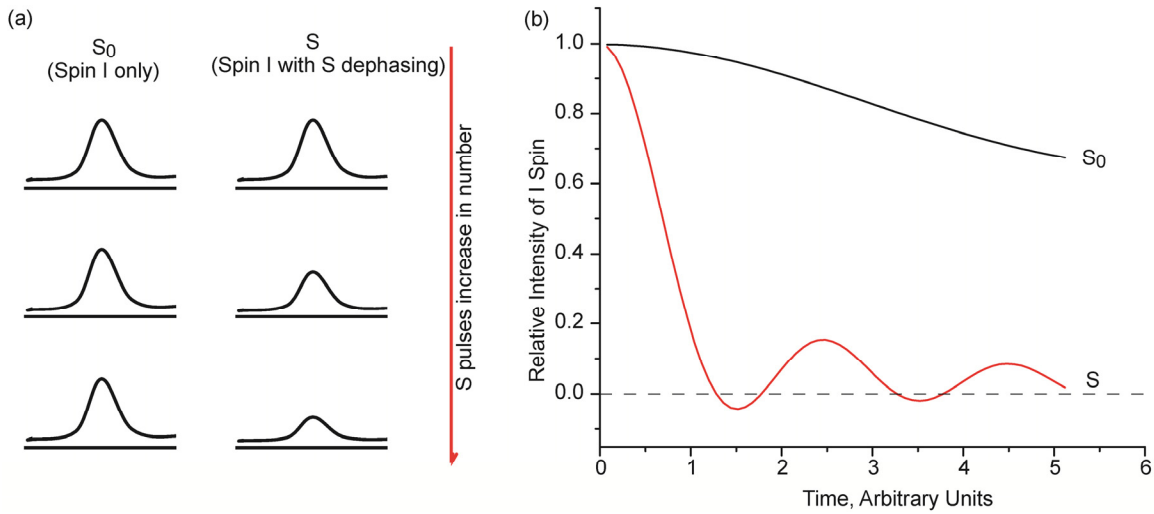

Figure 2.16. (a) Illustration of the peak intensities for a single resonance during the REDOR experiment, separated into S and S_0 peaks. (b) Plot of S and S_0 intensities as a function of time.

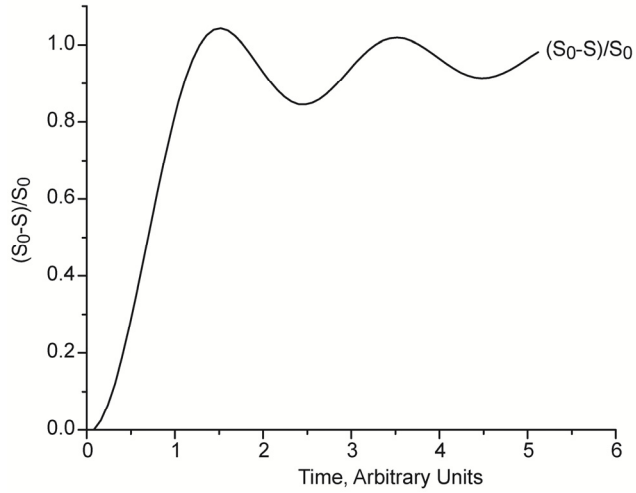

Figure 2.17. Typical REDOR curve for an isolated 2-spin system.

For a multiple spin system, the S_0 curve does not result in an oscillation around 0. Instead there is a smooth exponential decay which plateaus at 0 for both S and S_0 curves, as shown in ***Figure 2.18***. This results in the ^{6}Li{^{7}Li}-REDOR curves shown for LiCl in ***Figure 2.20***.

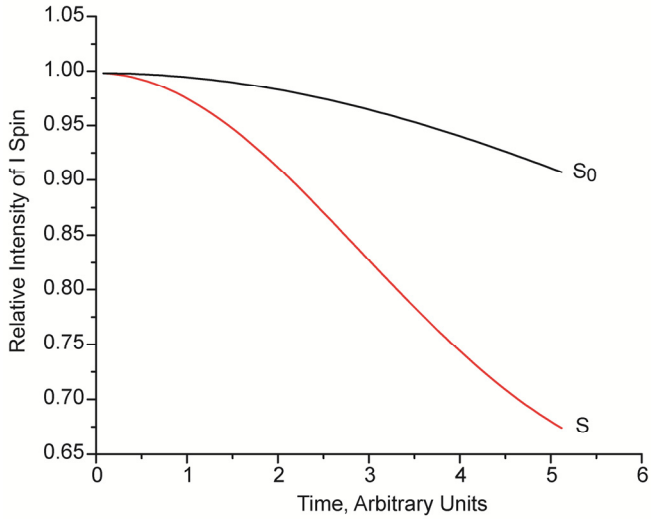

2.18. S and S_0 curves for a multi-spin system, with more than one pair of I and S spins.

If T_2 decay plays a significant role and the rate of T_2 relaxation is greater than the dipolar coupling, then this dominates the REDOR experiment. In this case, the curves corresponding to the S and S_0 signals are approximately equal, as shown in ***Figure 2.19***. When this occurs, the calculated REDOR curve $(S_0\text{-}S)/S_0$ appears as noise, since the values of $(S_0\text{-}S)$ are approximately 0 for the entire range. This will been shown for the case of $Li_3V_2(PO_4)_3$ in Chapter 6 of this thesis where no ^{6}Li{^{7}Li}-REDOR curve is observed.

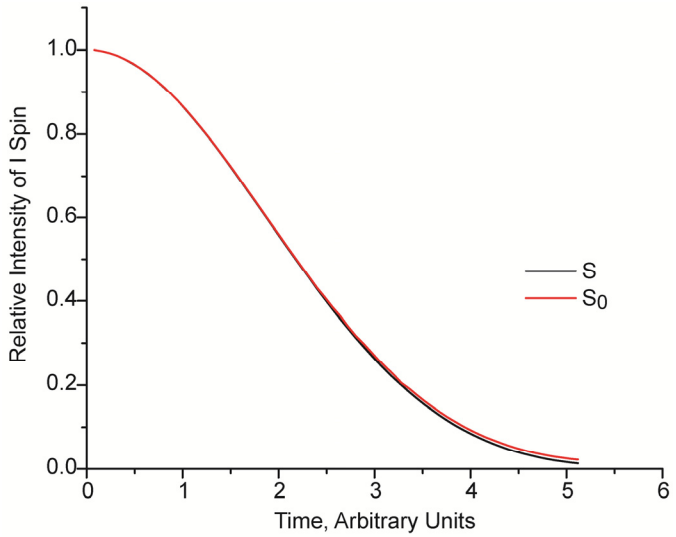

Figure 2.19. S and S_0 curves for a system in which T_2 relaxation dominates, and dipolar coupling does not contribute significantly to the shapes of the curves.

2.4.1.2. The Application of REDOR NMR Spectroscopy

Initial REDOR studies focused on materials which contained a single pair of heteronuclear spins.[34] A prime example of this is in organic materials which can be labeled with isotopes to include a single pair of ^{15}N and ^{13}C. The REDOR experiment results in a curve with a slope that depends on the distance between the ^{15}N-^{13}C spin pair and thus the experiment can be used to determine the distance between this pair of nuclei.

When solid-state materials are considered, the isotope labeling of a single pair is not possible because of the nature of the infinitely repeating lattice. Therefore a REDOR experiment of such a material results in a curve that is dependent on the relative orientations of all spins involved. To illustrate the dependence of the REDOR curve on the distribution and orientation of spin pairs ***Figure 2.20*** (a) shows an example of the

^{6}Li{^{7}Li}-REDOR curves that were experimentally observed for LiCl along with the SPINEVOLUTION simulation of the ^{6}Li{^{7}Li}-REDOR curve for a single ^{6}Li-^{7}Li pair.

LiCl is a highly ordered material with no partial occupancies existing on the Li crystallographic sites. The simulation was based on data presented by Levin'sh et al., which have a Li-Li internuclear distance of 3.627 Å. A representation of the crystal structure is shown in ***Figure 2.20*** (b). A comparison of the experimental and simulated REDOR curves show that the predicted curve for the single Li-Li pair is has a more shallow slope than any of the experimental curves. This is because on observing ^{6}Li, only a single ^{7}Li contributes to the dipolar coupling. As a result, the internuclear Li-Li distance can be directly correlated to the ^{6}Li-^{7}Li dipolar coupling and therefore to the slope of the REDOR curve. When the experimentally observed curves are considered, there are multiple ^{7}Li spins in the system that all contribute to the dipolar coupling experienced by the observed ^{6}Li spin. Thus, there is a trend in this data, which shows that the more ^{7}Li present, as in the red curve (7% ^{6}Li and 92% ^{7}Li), the steeper the slope of the resulting ^{6}Li{^{7}Li}-REDOR curve. Conversely, the less ^{7}Li present, as in the green curve (90% ^{6}Li and 10% ^{7}Li), the more shallow the resulting slope is.

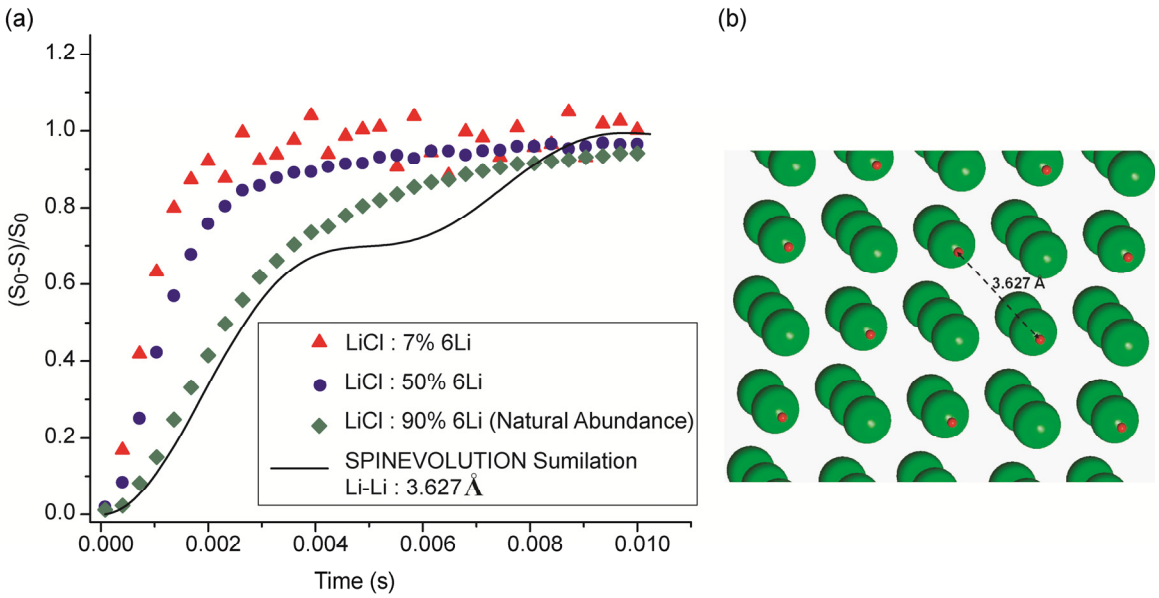

Figure 2.20.(a) Experimentally observed ^{6}Li{^{7}Li}-REDOR curves of LiCl with 90%, 50% and 7% ^{6}Li content in red, blue and green, respectively. For comparison the black line shows the SPINEVOLTUION simulation of a ^{6}Li{^{7}Li}-REDOR curve for a single ^{6}Li-^{7}Li pair with a distance of 3.627 Å, as reported be *Levinsh et al*. (b) Representation of LiCl showing a Li-Li internuclear distance of 3.627 Å.[37] Li is shown as red sphere, while the Cl is shown as green spheres.

This example illustrated some of the considerations that must be acknowledged when interpreting experimental REDOR data for solid-state systems. Therefore, for solid-state materials in which there is a distribution of spin pairs, the extraction of a single dipolar coupling value from a REDOR curve is not trivial, since multiple spin pairs contribute to the observed dipolar coupling. In this case the dipolar second moment, M_2, as shown in ***Equation 2.20***, can be used to describe the REDOR curve.[35, 38] The use of M_2 analysis will be discussed further in Chapter 5 of this thesis. The value of M_2 can be calculated, if the crystal structure of the material of interest is known, by summing all spin pairs involved in the heteronuclear dipolar coupling. The calculated value can be used to predict the REDOR curve for the heteronuclear system. If the crystal structure is now

known, simulating the REDOR curve using M_2 as a variable allows the determination of M_2, which can give information about the magnitude of heteronuclear dipolar coupling in a system, particularly when compared to that of similar systems.[35, 38]

$$M_2^{hetero} = \frac{4}{15}\left(\frac{\mu_0}{4\pi}\right)^2 \gamma_I^2 \gamma_S^2 \hbar^2 S(S+1) \sum_S r_{IS}^{-6} \qquad 2.20$$

Where S is the spin number for the non-observe spin, r_{IS} is the internuclear distance between I and S and all other variables are defined above.

Measurement of heteronuclear dipolar coupling extends past structural considerations, as it can give information about dynamics in a material. Rapid ion motion reduces the heteronuclear dipolar coupling between mobile species. Therefore, the slope of the REDOR curve can be used to indicate the presence of dynamics.[38] In this thesis changes in the slope of the REDOR curve as a function of temperature have been used for the first time to assess ion hopping in lithium ion battery materials. This method provides an excellent tool to study materials in which dynamics occurs in a single crystallographic site. Chapter 5 of this thesis will discuss how REDOR NMR can be used to study ^{6}Li-^{7}Li dipolar coupling as a function of temperature to probe dynamics in solid-state lithium ion electrolyte materials.

2.5. Choice of Nuclei Studied in This Thesis

This thesis focuses on the study of solid-state electrolyte materials for lithium ion batteries. Mobile species ^{6}Li and ^{7}Li can be studied directly by NMR spectroscopy in many cases, but the assessment of dynamics has been challenging due to the poor site

resolution and small spectral width inherent in diamagnetic lithium materials.[39] Instead, nuclei found in the framework of these materials can be studied. These include quadrupolar nuclei such as ^{139}La, which can be sensitive to the mobility of lithium ions.

The nuclei studied in this thesis are summarized in ***Table 2.1*** along with their respective Larmor frequencies at 11.7 T and 21.1 T, since these are the most common magnetic field used in this thesis. Also included in ***Table 2.1*** are the values of the quadrupole moment and nuclear spin for the relevant nuclei. For comparison, information is also included for ^{1}H.

Table 2.1: Table of nuclei considered in this thesis

Nucleus	Larmor Frequency at 11.7 T (MHz)	Larmor Frequency at 21.1 T (MHz)	Quadrupole Moment, *Q* (fm^2)	Nuclear Spin	Natural Abundance
^{7}Li	194.370	349.825	-4.01	3/2	92.58
^{6}Li	73.600	132.464	-0.0808	1	7.42
^{139}La	70.647	127.149	20.0	7/2	99.91
^{87}Rb	163.645	294.527	13.35	3/2	27.85
^{1}H *	500.130	900.130	0	1/2	99.98

* ^{1}H was not studied in this thesis, but has been included for comparison.

The combination of nuclei studied throughout this thesis has contributed to a variety of methods used to examine the structural and dynamic properties of battery materials. In most endeavors the goal has been to determine lithium ion hopping rates or the activation energy for lithium ion hopping. However, structural complexity has played a role in several studies, and the use of multinuclear NMR studies has proven to be very insightful in these cases. Together, these nuclei have provided a range of options to answer specific

questions regarding the structural and dynamic properties of each system discussed in this thesis.

2.6. Summary

This chapter outlines some of the fundamental concepts and experiments that will be called upon throughout this thesis. Solid-state NMR spectroscopic techniques have been used extensively throughout this work, with quadrupolar nuclei measured almost exclusively. The use of quadrupolar properties of some nuclei has been vital in the study of the materials discussed in Chapters 3, 4, and 5. In these cases the large electric field gradients have provided sensitive probes of the surrounding environment, and created a method to study structural and dynamic properties. Additionally, dipolar coupling has played a significant role in the analysis of lithium ion mobility in several solid-state electrolytes. Chapter 5 discusses the use of REDOR NMR experiments to study dipolar coupling in lithium ion electrolytes. Finally, T_2 relaxation phenomena have provided an alternative method to study ion dynamics, which will be discussed in Chapter 6.

A variety of methods have been employed in this thesis to study several battery materials. The methods discussed were used in order to circumvent some of the challenges related to the use of more traditional methods of studying dynamics in battery materials. Two of the main challenges are the poor site resolution of ^{6,7}Li in diamagnetic materials; and ion conduction occurring in a single crystallographic site. Multinuclear NMR studies have taken advantage of the large electric field gradient of quadrupolar nuclei or the heteronuclear dipolar coupling experienced by mobile species. These experiments have allowed the successful determination of structural and dynamic

properties of the lithium ion electrolyte materials studies in this thesis. By approaching the study of ion dynamics in novel ways these techniques provide tools to answer questions about structure and dynamics in a wide variety of materials, in particular, those that are difficult to study using traditional NMR methods.

2.7. References

1. A. Carrington, A. D. M., *Introduction to Magnetic Resonance with Application to Chemistry and Chemical Physics*. Harper and Row, Publishers: New York, 1967.

2. Levitt, M. H., *Spin Dynamics*. John Wiley and Sons Ltd.: West Sussex, 2001; p 686.

3. Keeler, J., Lecture Notes. In Cambridge, 1998.

4. Apperley, D. C., Harris, R. K., Hodgkinson, P., *Solid-State NMR: Principles and Practice*. Momentum Press: New York, 2012; p 276.

5. Duer, M. J., *Introduction to Solid-State NMR Spectroscopy.* Blackwell Science, Oxford, UK: 2004; p 349.

6. McNeill, S. A.; Gor'kov, P. L.; Struppe, J.; Brey, W. W.; Long, J. R., Optimizing ssNMR experiments for dilute proteins in heterogeneous mixtures at high magnetic fields. *Magnetic Resonance in Chemistry* **2007,** 45, S209-S220.

7. Dong, R. Y., NMR Relaxation Rates. *Elsevier* **1999,** Reproduced From Vol.2, 1568-1575.

8. S. Meiboom, D. G., Modified Spin-Echo Method for Measuring Nuclear Relaxation Times. *The Review of Scientific Instruments* **1958,** 29, (8), 688-691.

9. Hahn, E. L., Spin Echoes. *Physical Review* **1950,** 80, (4), 580-594.

10. Perras, F. A.; Viger-Gravel, J.; Burgess, K. M. N.; Bryce, D. L., Signal enhancement in solid-state NMR of quadrupolar nuclei. *Solid State Nuclear Magnetic Resonance* **2013,** 51-52, 1-15.

11. Ashbrook, S. E., Recent advances in solid-state NMR spectroscopy of quadrupolar nuclei. *Physical Chemistry Chemical Physics* **2009,** 11, (32), 6892-6905.

12. Kentgens, A. P. M., A practical guide to solid-state NMR of half-integer quadrupolar nuclei with some applications to disordered systems. *Geoderma* **1997,** 80, (3-4), 271-306.

13. Schurko, R. W.; Wi, S.; Frydman, L., Dynamic effects on the powder line shapes of half-integer quadrupolar nuclei: A solid-state NMR study of XO_4- groups. *Journal of Physical Chemistry A* **2002,** 106, (1), 51-62.

14. van Wullen, L.; Hildebrandt, L.; Jansen, M., Cation mobility and anion reorientation in lithium trifluoromethane sulfonate, $LiCF_3SO_3$. *Solid State Ionics* **2005,** 176, (15-16), 1449-1456.

15. Spencer, T. L., Goward, G. R., Bain, A. D., Exact calculation of the response of a quadrupolar nucleus to radiofrequency irradiation. *Can. J. Chem.* **2011**.

16. Spencer, T. L.; Goward, G. R.; Bain, A. D., Complete description of the interactions of a quadrupolar nucleus with a radiofrequency field. Implications for data fitting. *Solid State Nuclear Magnetic Resonance* **2013,** 53, 20-26.

17. Kentgens, A. P. M., Off-resonance nutation nuclear magnetic resonance spectroscopy of half-integer quadrupolar nuclei. *Progress in Nuclear Magnetic Resonance Spectroscopy* **1998,** 32, 141-164.

18. Kentgens, A. P. M.; Lemmens, J. J. M.; Geurts, F. M. M.; Veeman, W. S., Two-Dimensional Solid-State Nutation Nmr of Half-Integer Quadrupolar Nuclei. *Journal of Magnetic Resonance* **1987,** 71, (1), 62-74.

19. Bhattacharyya, R.; Frydman, L., Quadrupolar nuclear magnetic resonance spectroscopy in solids using frequency-swept echoing pulses. *Journal of Chemical Physics* **2007,** 127, (19), 194503-1 - 194503-8.

20. O'Dell, L. A.; Schurko, R. W., QCPMG using adiabatic pulses for faster acquisition of ultra-wideline NMR spectra. *Chemical Physics Letters* **2008,** 464, (1-3), 97-102.

21. Sindorf, D. W.; Bartuska, V. J., Wide-Line NMR-Spectroscopy in Solids Using Variable Frequency Pulses. *Journal of Magnetic Resonance* **1989,** 85, (3), 581-585.

22. Kennedy, M. A.; Vold, R. L.; Vold, R. R., Stepped-Frequency Nmr-Spectroscopy. *Journal of Magnetic Resonance* **1991,** 92, (2), 320-331.

23. Massiot, D.; Farnan, I.; Gautier, N.; Trumeau, D.; Trokiner, A.; Coutures, J. P., Ga-71 and Ga-69 Nuclear-Magnetic-Resonance Study of Beta-Ga_2O_3 - Resolution of 4-Fold and 6-Fold Coordinated Ga Sites in Static Conditions. *Solid State Nuclear Magnetic Resonance* **1995,** 4, (4), 241-248.

24. Tannus, A.; Garwood, M., Adiabatic pulses. *Nmr in Biomedicine* **1997,** 10, (8), 423-434.

25. Larsen, F. H.; Jakobsen, H. J.; Ellis, P. D.; Nielsen, N. C., Sensitivity-enhanced quadrupolar-echo NMR of half-integer quadrupolar nuclei. Magnitudes and relative orientation of chemical shielding and quadrupolar coupling tensors. *Journal of Physical Chemistry A* **1997,** 101, (46), 8597-8606.

26. Spencer, T. L.; Ramzy, A.; Thangadurai, V.; Goward, G. R., Structural Complexity and Electrical Properties of the Garnet-Type Structure $LaLi_{0.5}Fe_{0.2}O_{2.09}$

Studied by (7)Li and (139)La Solid State NMR Spectroscopy and Impedance Spectroscopy. *Chemistry of Materials* **2011,** 23, (12), 3105-3113.

27. Eichele, K., Wasylishen, R. E., WSolids1. *WSolids1, Dalhousie University and University of Tuebingen* **2010**.

28. Massiot, D.; Fayon, F.; Capron, M.; King, I.; Le Calve, S.; Alonso, B.; Durand, J. O.; Bujoli, B.; Gan, Z. H.; Hoatson, G., Modelling one- and two-dimensional solid-state NMR spectra. *Magnetic Resonance in Chemistry* **2002,** 40, (1), 70-76.

29. Clark, S. J.; Segall, M. D.; Pickard, C. J.; Hasnip, P. J.; Probert, M. J.; Refson, K.; Payne, M. C., First principles methods using CASTEP. *Zeitschrift Fur Kristallographie* **2005,** 220, (5-6), 567-570.

30. Carlier, D.; Menetrier, M.; Grey, C. P.; Delmas, C.; Ceder, G., Understanding the NMR shifts in paramagnetic transition metal oxides using density functional theory calculations. *Physical Review B* **2003,** 67, (17).

31. Spencer, T. L.; O'Dell, L. A.; Moudrakovski, I.; Goward, G. R., Dynamics of Ag^+ Ions in $RbAg_4I_5$ Probed Indirectly via Rb-87 Solid-State NMR. *Journal of Physical Chemistry C* **2013,** 117, (19), 9558-9565.

32. O'Dell, L. A.; Schurko, R. W.; Harris, K. J.; Autschbach, J.; Ratcliffe, C. I., Interaction Tensors and Local Dynamics in Common Structural Motifs of Nitrogen: A Solid-State N-14 NMR and DFT Study. *Journal of the American Chemical Society* **2011,** 133, (3), 527-546.

33. Gullion, T.; Schaefer, J., Rotational-Echo Double-Resonance Nmr. *Journal of Magnetic Resonance* **1989,** 81, (1), 196-200.

34. Gullion, T., Introduction to rotational-echo, double-resonance NMR. *Concepts in Magnetic Resonance* **1998,** 10, (5), 277-289.

35. Puls, S. P.; Eckert, H., Spatial distribution of lithium ions in glasses studied by Li-7{Li-6} spin echo double resonance. *Physical Chemistry Chemical Physics* **2007,** 9, (30), 3992-3998.

36. Veshtort, M.; Griffin, R. G., SPINEVOLUTION: A powerful tool for the simulation of solid and liquid state NMR experiments. *Journal of Magnetic Resonance* **2006,** 178, (2), 248-282.

37. Levin'sh, A. F., Straumanis, M. E., Karlson, K., Praezisionsbestimmung von Gitterkonstanten hygroskopischer Verbindungen (Li Cl, Na Br). *Zeitschrift fuer Physikalische Chemie, Abteilung B: Chemie der Elementarprozesse, Aufbau der Materie* **1938,** 40, 146-150.

38. Koller, H.; Kalwei, M., Studying ionic motion in tetrahydroxoborate sodalite by second moment analysis using Na-23{B-11} rotational echo double resonance data. *Journal of Physical Chemistry B* **2004,** 108, (1), 58-63.

39. Xu, Z.; Stebbins, J. F., Li-6 Nuclear-Magnetic-Resonance Chemical-Shifts, Coordination-Number and Relaxation in Crystalline and Glassy Silicates. *Solid State Nuclear Magnetic Resonance* **1995,** 5, (1), 103-112.

Chapter 3: Structural Analysis of Garnet-Type $LaLi_{0.5}Fe_{0.2}O_{2.09}$ and Related Materials Using ^{7}Li and ^{139}La Solid-State NMR Spectroscopy

3.1. Introduction

This chapter discusses the work done toward understand the structure of the cathode material $LaLi_{0.5}Fe_{0.2}O_{2.09}$ and related materials. This study has used a combination of ^{7}Li and ^{139}La NMR spectroscopic techniques to investigate the nature of the disorder found in $LaLi_{0.5}Fe_{0.2}O_{2.09}$ and its structural derivatives. In addition, PXRD and transmission electron microscopy (TEM) have been used to support the structural analysis. The study began with the consideration of model La-containing oxide materials using ^{139}La NMR spectroscopy, which highlights some of the benefits and challenges of using ^{139}La NMR techniques. In model materials a correlation was made between the observed NMR powder patterns and the crystal structure. The nature of any disorder in the second coordination sphere of lanthanum in these model materials has also been studied and linked to features in the ^{139}La NMR spectra. This has been further extended to the analysis of battery materials and used to unveil structural information about the lanthanum-containing battery materials.

Components of this work were published in the *Canadian Journal of Chemistry* and *Chemistry of Materials.* Initial manuscripts were prepared by the current author, Leigh Spencer, The content was reproduced with the permission of:

(1) The *Canadian Journal of Chemistry* (**89**, *1105-1117*, 2001) with co-authors E. Coomes, E. Ye, V. Terskikh, A. Ramzy, V. Thangadurai, and G. R. Goward. ©2008 Canadian Science Publishing.

(2) *Chemistry of Materials* (23, 3105-3113, 2011) with co-authors A. Ramzy, V. Thangadurai and G. R. Goward. Copyright 2011 American Chemical Society.

^{139}La NMR Spectroscopic data at 21.1 T and 11.7 T were collected at the National Ultra-high Field Facility for Solids at the National Research Council in Ottawa under the supervision of Dr. Victor Terskikh and Dr. Eric Ye. The reminder of the work was collected at McMaster University. All spectral processing was done at McMaster University under the supervision of Prof. Gillian Goward.

^{6,7}Li magic angle spinning solid-state NMR is a useful non-destructive tool to study the structures of battery materials, as well as their lithium ion dynamics; however in the absence of any paramagnetic interactions, both ^{6}Li and ^{7}Li suffer from poor chemical shift resolution and long T_1 relaxation times. Of the two, ^{6}Li is somewhat preferable, as it has smaller line widths in NMR spectral peaks. This is due to the reduction of the homonuclear dipolar coupling of this lower gamma nucleus.[1, 2] In addition to electrolytes, cathode materials, aimed at replacing the currently used $LiCoO_2$, are highly sought after.[3-5] They often contain paramagnetic centers that provide unpaired electrons, which allow the lithium centers in the materials to have short T_1 relaxation times, and an expanded chemical shift range.[3, 6] ^{6,7}Li MAS NMR, along with powder X-ray diffraction, provides a powerful tool to study the structure, as well as the nature of lithium ion dynamics in lithium ion battery materials.[2]

Many of the garnet structures proposed thus far for these applications contain significant amounts of lanthanum, an NMR active nucleus with spin 7/2. Thus, ^{139}La NMR may be a valuable tool in the structural analysis of these, and other related materials.[2, 7, 8] In particular, ^{139}La NMR is capable of detecting atomic-level disorder in materials that contain atomic substitution within different crystallographic sites.[9, 10]

In this study we report the synthesis, structure, electrical transport properties of Fe-based garnet-related structures $LaLi_{0.5}Fe_{0.2}O_{2.09}$, $La_{0.94}Li_{0.69}Fe_{0.2}O_{2.09}$, and $LaLi_{0.75}Fe_{0.14}O_{2.09}$ together with ^{7}Li and ^{139}La solid-state NMR spectral characterization. The parent garnet-like $LaLi_{0.5}Fe_{0.2}O_{2.09}$ was first prepared by Mazza in 1985.[11-13] It has been shown to conduct lithium ions as well as electrons, and has a redox couple between Fe^{3+} and Fe^{4+}. It is therefore a potential material for use as a cathode in Li ion batteries.[12] Although this material has not been cycled electrochemically, it can be expected that there will be a high voltage plateau, such as that found for the Fe^{3+}/Fe^{4+} couple in $Li[Fe_yMn_{2-y}]O_4$ at ~5 V.[14] As such, it would be viable in the context of all-solid-state Li ion cells, with the possibility of incorporating a complementary garnet structured solid-state electrolyte.[15]

The theoretical fully occupied parent compound for this series of structures is $La_{1.1}Li_{0.5}Fe_{0.31}O_{2.5}$.[12] It has been determined that this compound does not exist in this fully occupied state, but rather has a series of partial occupancies present. These are distributed over the compound and are found in varying amounts on each atomic position, except that of Li.[12] In particular, the vacancies reported on the Fe sites at (0, 0, 0) and (0.25, 0.25, 0.25) are significant, as will be discussed further in this work. This structure opens the

possibility of Li ion dynamics, via vacancy-mediated conductivity. Moreover, our studies provide evidence, for the first time, of Li-Fe substitution in these garnet structures. Precedent for this is seen in the $LiFePO_4$ phase, where such anti-site defects have been shown to create channel-blocking iron centers in this one dimensional (1D) Li ion conductor.[16]

3.2. Challenges of ^{139}La NMR Spectroscopy

Although ^{139}La is an NMR active nucleus with high natural abundance, 99.91%, and many materials significant to the development of materials science contain large amounts of lanthanum, ^{139}La NMR is not performed routinely.[17-19] This is mainly due to the many difficulties associated with the collection and interpretation of the NMR spectra, as outlined in Chapter 2 of this thesis. The EFG-dominated spectra of ^{139}La are very broad, which makes low-field NMR measurements quite difficult. Nevertheless, it has been shown that ^{139}La NMR spectroscopy is sensitive to the symmetry elements of lanthanum containing structures. Resulting spectral line shapes are heavily dependent on the asymmetry parameter η (defined in ***Equation 2.13***) and the quadrupolar coupling constant C_Q (defined in ***Equation 2.14***), which are known to vary according to the elements of symmetry present at the nucleus of interest.[20]

La_2O_3, $Li(OH)_3$, $LaNbO_4$, $LaAlO_3$, $Li_3La_2Zr_2O_{12}$ and La_3NbO_7 serve as model materials for the study of lanthanum-containing lithium battery materials. The collection and interpretation of ^{139}La NMR spectra will be discussed in detail in the Results and Discussion section. Crystalline $LaNbO_4$, $Li(OH)_3$, LaAlO3 and La_2O_3 are highly ordered compounds, which show no sign of disorder in their crystal structures.[21, 22] In all of these

materials, lanthanum is surrounded only by oxygen in the first coordination sphere. In each case, the ^{139}La spectrum is a clear representation of a single ^{139}La crystallographic site. In addition to these four model materials, several other model materials have been examined. $Li_7La_3Zr_2O_{12}$ and La_3NbO_7 are also highly ordered lanthanum-containing oxides. In contrast to the materials mentioned above, these two materials each contain two distinct crystallographic sites, making the interpretation of ^{139}La NMR spectra challenging. These materials have been studied to determine the quadrupolar parameters, C_Q and η in order to compare the experimentally determined parameters to those calculates by *ab initio* quantum chemical calculations. This collection data sets for of model materials provides a variety of different lanthanum environments which share the fact that lanthanum is surrounded by oxygen in its first coordination sphere. In contrast to the well ordered model materials, the electrochemical materials $LaLi_{0.5}Fe_{0.2}O_{2.09}$ and $Li_{3x}La_{(2/3)-x}TiO_3$ ($x \leq 0.03 \leq 0.063$) are known to show disorder in the form of atomic distribution on particular crystallographic sites, which occurs as a result of vacancies present in the materials.[12, 23]

The garnet-like structure $LaLi_{0.5}Fe_{0.2}O_{2.09}$ is a potential cathode material for lithium ion batteries. The structure contains iron centers, which provide unpaired electrons that reduce the T_1 relaxation times of lithium that is in close proximity to the iron centers.[12] $LaLi_{0.5}Fe_{0.2}O_{2.09}$ was first prepared by Mazza *et al.*, and it was thought that the lithium in this compound occupied a single crystallographically unique site, while the lanthanum is distributed between two crystallographic sites, each with the lanthanum surrounded by

oxygen in the first coordination sphere.[12] The source of disorder in this compound will be discussed later in this work.

$Li_{3x}La_{(2/3)-x}TiO_3$ ($x \leq 0.03 \leq 0.063$) is a potential electrolyte material for lithium ion batteries and does not contain paramagnetic centers.[23] The disorder in this compound is attributed to the distribution of Li, La, and a vacancy, which can randomly occupy the same crystallographic site.[23] In all of the materials mentioned, lanthanum is surrounded only by oxygen in the first coordination sphere. Thus, the ^{139}La NMR spectra can be compared directly to relate the lineshape of the spectra to the environment of the lanthanum in the respective crystal structures.

Crystallographic information for each of the model compounds is shown in ***Table 3.1***, which presents the space groups, La–O bond distances, and elements in the second coordination sphere. In addition, the lanthanum environments for La_2O_3, $La(OH)_3$, $LaNbO_4$, $Li_{3x}La_{(2/3)-x}TiO_3$, and $LaLi_{0.5}Fe_{0.2}O_{2.09}$ are illustrated in ***Table 3.2***. For each structure, lanthanum is shown in its oxygen environment as well as in its second coordination sphere environment. Together, a suite of reference structures were studied using ^{139}La NMR spectroscopy, for comparison to the electrochemical materials of interest.

Table 3.1: Crystallographic data for the materials studied in Chapter 3.

Material	Space Group	La	O-Coordination	La-O Bond Range(Å)	2nd CS*	Ref.
$LaNbO_4$	*I 2/c*	La-1	8	2.5 - 2.6	La, Nb	21
La_2O_3	*P -3 m 1*	La-1	7	2.4 - 2.8	La	22
$La(OH)_3$	*P 6 3/m*	La-1	9	2.6 – 2.8	La	24
$Li_{3x}La_{(2/3)-x}TiO_3$	*P m m m*	La-1	12	2.7 - 2.8	La, Ti	23
		La-2	12	2.7 - 2.8	La, Ti	
$LaLi_{0.5}Fe_{0.2}O_{2.09}$	*I m 3 m*	La-1	10	2.5 – 2.7	La, Fe	This Work
		La-2	9	2.3 - 2.7	La, Fe	This Work
$LaAlO_3$	*R -3 c*	La-1	12	2.5-2.8	La, Al	25
$Li_7La_3Zr_2O_{12}$	*I 4₁ / a c d*	La-1	6	1.6-2.6	Li, Zr	26
$Li_7La_3Zr_2O_{12}$	*I 4₁ / a c d*	La-2	-	-	Li, Zr	26
La_3NbO_7	C m c m	La-1	10	1.9-2.8	La, Nb	27
La_3NbO_7	C m c m	La-2	6	1.9-2.9	La, Nb	27

The space group, La coordination number for each La site, La-O bond distance range, and the second coordination environment are shown. 2nd CS = second coordination sphere.*

Table 3.2: The lanthanum environments in materials studied in Chapter 3.

Material	Oxygen Environment	Second Coordination Sphere
$LaNbO_4$	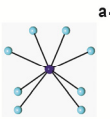	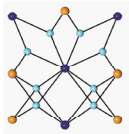
La_2O_3	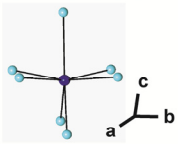	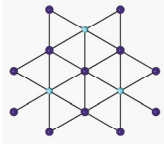
$La(OH)_3$	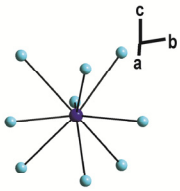	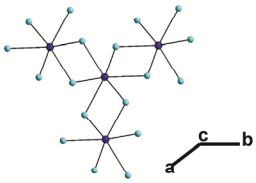
$Li_{3x}La_{(2-x)/3}TiO_3$ La-1	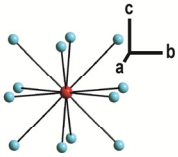	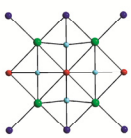
$Li_{3x}La_{(2-x)/3}TiO_3$ La-2	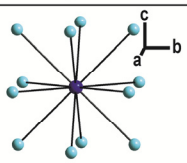	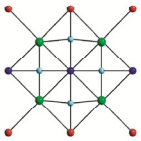
$LaLi_{0.5}Fe_{0.2}O_{2.09}$ La-1	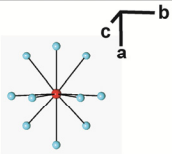	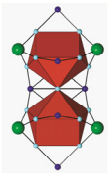
$LaLi_{0.5}Fe_{0.2}O_{2.09}$ La-2	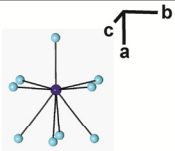	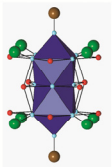

Legend

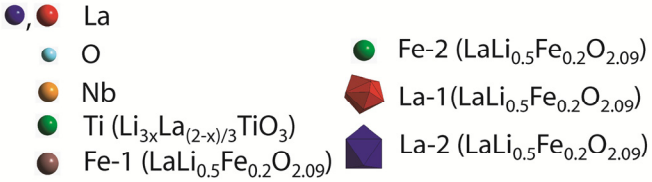

Lanthanum is represented by a dark blue (La-2) or red (La-1) sphere. In the $LaLi_{0.5}Fe_{0.2}O_{2.09}$ structure, lanthanum is also represented by corresponding polyhedra, for clarity, as lanthanum lies in a complex environment. In addition, oxygen is represented by light blue spheres; niobium, by orange spheres; titanium by green spheres; in $LaLi_{0.5}Fe_{0.2}O_{2.09}$ a distinction is made between iron that participates in a distribution (green spheres) with lithium, and iron that does not (brown spheres). The details of the distribution are discussed in the text. All crystallographic figures were prepared in XtalDraw software.[28]

3.3. Experimental

3.3.1. Sample Preparation

La_2O_3 and $LaAlO_3$ were purchased from Sigma-Aldrich. La_2O_3 was exposed to air in ambient conditions to produce $La(OH)_3$. To produce La_2O_3 void of $La(OH)_3$ impurity, the purchased sample was heated at 900 °C for 24 h.[29] $LaNbO_4$ and La_3NbO_7 were obtained from the National Ultra-High Facility for Solids and was prepared elsewhere by a co-precipitation from $NbCl_5$ and $La(NO_3)_3$ by NH_3 with subsequent calcination at 800 °C.[30] To prepare $Li_{3x}La_{(2/3)-x}TiO_3$ ($0.03 \leq x \leq 0.063$), stoichiometric amounts of La_2O_3, Li_2CO_3, and TiO_2 were mixed. The mixture was ball milled and heated at 500 °C. This process was repeated with temperatures of 800 and 1150 °C. A pellet was then pressed and annealed at 1350 °C to create the final product.[31] By comparing the experimental powder X-ray diffraction data to that reported by Ibarra *et al*., it has been determined that the content of lithium in the structure is consistent with the desired stoichiometry.[23]

$LaLi_{0.5}Fe_{0.2}O_{2.09}$, $La_{0.94}Li_{0.69}Fe_{0.2}O_{2.09}$, and $LaLi_{0.75}Fe_{0.14}O_{2.09}$ were synthesized by members of the Thangadurai group according to the procedure found in (*Chem. Mater.* **23**, 3105-3113, *2011*). Powder X-ray diffraction (Cu KR, 40 kV, 40 mA)) was employed for phase confirmation. $Li_7La_3Zr_2O_{12}$ was synthesized according to the procedure found in (Journal of Solid State Chemistry, **182**, 2046-2052, *2009*).

3.3.2. Solid-State NMR Spectroscopy Measurements

3.3.2.1. ^{7}Li NMR Spectroscopy Measurements

^{7}Li MAS NMR was collected at 11.7 T (Larmor frequency, 194.4 MHz) on a Bruker Avance I 500 NMR spectrometer with an external reference of 1 M LiCl solution,

at 0 ppm, having a 90° pulse length of 4 μs at 1.25 dB with a nutation frequency of 62.5 kHz. A 2.5mm probe was used, with a rotor spinning speed of 20 kHz, and solid-state ^{7}Li MAS spectra were collected using a 1 μs (π/8) pulse, with a relaxation delay of 20 s. This short pulse was used to accommodate the very long T_1 of the diamagnetic resonance at 0 ppm. T_1 relaxation measurements were performed at 21.1 T for ^{7}Li in $La_{0.94}Li_{0.69}Fe_{0.2}O_{2.09}$. An inversion recovery pulse sequence was used, with a variable delay list of 16 values. A recycle delay of 30 s was used in the first experiment; and a recycle delay of 450 s was used in the second experiment. The experiment was performed twice to account for the great differences in T_1 relaxation properties of the lithium sites in the material.

3.3.2.2. ^{139}La NMR Spectroscopy Measurements

Experiments at 21.1 T (Larmor frequency, 127.1 MHz), were carried out using a Bruker Avance II 900 NMR spectrometer and were performed with stationary samples using a home-built single-channel probe with a 5 mm i.d. solenoid coil. An external reference of a 1 M solution of $LaCl_3$ (0 ppm) was used, for which a 180° pulse had a pulse length of 16.0 μs at 3.30 dB, with a nutation frequency of 31.25 kHz. Depending on the sample, one of two pulse sequences was used: WURST-echo or WURST-QCPMG. Typically in the WURST-QCPMG experiments, 50 ms WURST pulses were applied and swept across a range of 1 MHz at a rate of 20 MHz/ms, with an RF power of 10 kHz. The spikelet-separation was set to be 2.5 kHz at 21.1 T and 5.0 kHz at 11.7 T. The number of echoes in a QCPMG train ranged from 32 to 64. Recycle delays of 0.2 – 0.5 s were found

sufficient for complete relaxation in most samples. From 1 000 to 40 000 transients were accumulated, depending on the sample.

^{139}La NMR spectra were also acquired at 11.7 T (Larmor frequency, 70.6 MHz) on a Bruker Avance III 500 NMR spectrometer using a 5 mm solenoid Bruker H/X probe. WURST pulse conditions were similar to those at 21.1 T. A number of spectra were obtained using a $\pi/2$–$\pi/2$ quadrupolar-echo pulse sequence, employing a 2 ms central-transition selective $\pi/2$ pulse, with RF power of 30 kHz. From 2 000 to 4 000 transients were accumulated. NMR spectral simulation was performed using WSolids in most cases.[32] DMFit[33] or QuadFit[34] programs were used for disordered systems. Uncertainties were determined statistically by performing several simulations of each spectrum.

3.3.3. Computational Methods

Quantum chemical calculations of the ^{139}La EFG and chemical shielding, CS, tensors were performed with available crystallographic data for La_2O_3,[22] $La(OH)_3$,[24] and $LaNbO_4$.[21] Calculations of $LaAlO_3$, $Li_7La_3Zr_2O_{12}$ and La_3NbO_7 focused on the EFG alone and were used to determine the values of C_Q and η. The original structure for $La(OH)_3$ did not contain hydrogen atoms. Before calculations, hydrogen atoms were placed in the expected positions, and the crystal structure was fully geometrically optimized. The CASTEP NMR program[35, 36] in the Accelrys Materials Studio 4.4 environment was utilized to carry out *ab initio* plane-wave density functional theory (DFT) calculations.[37-41]

3.4. Result and Discussion

3.4.1. ^{139}La NMR Spectroscopy of Model La-Containing Materials

$LaNbO_4$: In the first model compound, $LaNbO_4$, lanthanum contains only oxygen in its first coordination sphere. It has a monoclinic structure in space group *I2/c*. There is only one crystallographically unique lanthanum site in this compound, and one niobium site. Lanthanum is coordinated to eight oxygen atoms within 2.6 Å, with a La-O bond distance range of 2.5 – 2.6 Å. The shortest La-O contact is 2.5 Å, and the highest element of symmetry for La is a 2-fold rotational axis.[21] The minimum distance between La and Nb is 3.7 Å, and the minimum distance between La and another La atom is 3.9 Å.[21] Static solid-state NMR measurements were taken at 11.7 T, and compared to those taken at 21.1 T to illustrate many of the challenges of ^{139}La solid-state NMR. Static spectra collected for $LaNbO_4$ using three different pulse sequences, quadrupolar-echo, WURST-QCPMG, and WURST-echo, are compared in ***Figure 3.1***.

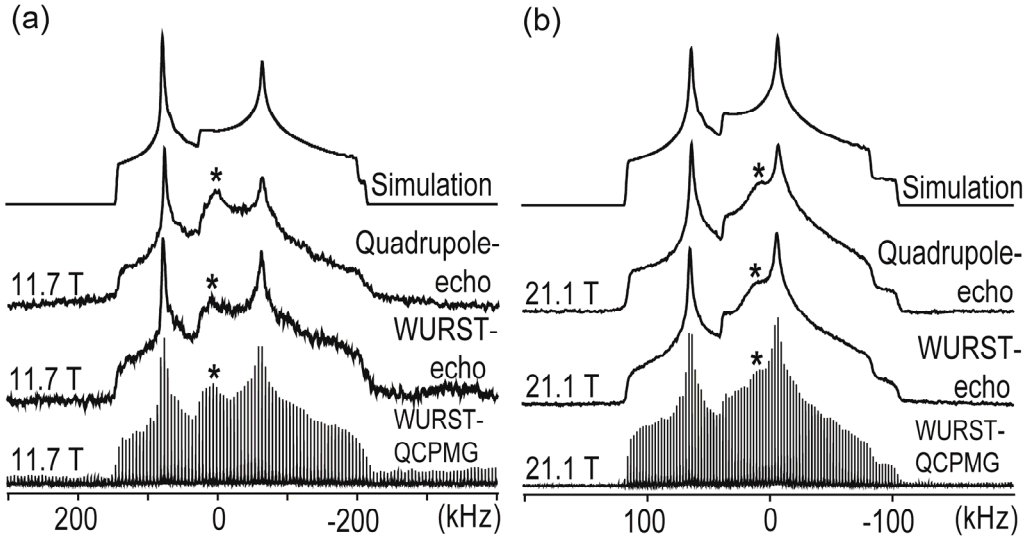

Figure.3.1. ^{139}La WURST-QCPMG, WURST-echo, and Quadrupole-echo NMR spectra of $LaNbO_4$ taken at (a) 21.1 T and (b) 11.7 T. * indicates a minor impurity in the sample. Simulations were performed using WSolids software.

This simple example already fully illustrates some of the difficulties in obtaining high-quality ^{139}La NMR spectra for solid state samples. Even at 11.7 T the static line-width for this sample is in excess of 300 kHz. When the more traditional quadrupolar-echo pulse sequence is applied, the resulting spectrum shows a line shape with attenuated intensity for outer discontinuities, compared with the simulated spectrum. This distortion is due to the limited excitation bandwidth of the rectangular $\pi/2$ pulse (2 μs). Near to the edge of the excitation bandwidth the intensity of the excitation profile decreases significantly, resulting in the spectrum with attenuated intensity on its outer edges. To obtain a more accurate line shape using the quadrupolar-echo pulse sequence it is often necessary to record several spectra with different central frequency offsets and then to add them together.[42, 43] The WURST-echo approach affords much broader excitation bandwidth, so that the same spectrum can be correctly recorded using only a single

central frequency offset in the same amount of time (***Figure 3.1***).[44] In systems with sufficiently long T_2 relaxation times, the WURST-QCPMG approach[45] delivers all the advantages of WURST in providing broadband excitation now combined with significantly improved signal-to-noise. Due to spikelet spacing in QCPMG the finer details of the line shape are sometime lost. Furthermore, we found that for disordered battery materials studied in this work the T_2 relaxation times are rather short, which does not favour the use of the QCPMG method. Thus, the technique of choice in this work was the WURST-echo pulse sequence.

Simulations of the NMR spectra of $LaNbO_4$ collected at 11.7 T and 21.1 T reveal a C_Q of 34 MHz ± 2 MHz, and η of 0.51 ± 0.05. It should be noted here that only first-and second-order quadrupolar interactions are considered. Collecting the ^{139}La spectrum at two different magnetic fields allowed for the identification of a small impurity, marked with (*) in ***Figure 3.1***. Contributions from quadrupolar interaction as well as CSA were considered, and the span, skew and Euler angles, defined throughout this work as the angles that relate the CSA axis system to the EFG axis system, were determined to be 420 ppm ± 10 ppm, 0.33 ± 0.05, $\alpha = 90\,° \pm 10\,°$, $\beta = 27\,° \pm 3\,°$, $\gamma = 270\,° \pm 10\,°$, respectively, and are in agreement with values predicted by CASTEP calculations.[35] $LaNbO_4$ provides a good example of a system with complex NMR parameters that were difficult to simulate, and illustrates the advantage of using calculation software for NMR interpretation. CASTEP calculations proved to be extremely beneficial in the simulation of the $LaNbO_4$ spectra obtained at 11.7 T and 21.1 T, providing a starting point for the

simulation of values of C_Q, η, the span, skew, and Euler angles. The values produced by CASTEP for this compound and others are shown in ***Table 3.3***.

The second coordination sphere of La in $LaNbO_4$ contains both La and Nb, as shown in ***Table 3.2***. The value of η obtained by simulation of the experimental spectra is 0.51 ± 0.05. Since the highest rotational symmetry element present is a 2-fold rotational axis, which lies along the b-axis of the crystal, the experimental simulation is not sufficient to predict the respective orientation of $\boldsymbol{V_{ZZ}}$, the principle component of the EFG tensor. However, this information can be achieved by first principle calculations which have been performed using CASTEP. The theoretically predicted orientation of the EFG tensor for $LaNbO_4$, with respect to the crystal axes, is shown in ***Figure 3.2*** (a), along with those of La_2O_3 (b) and $La(OH)_3$ (c).

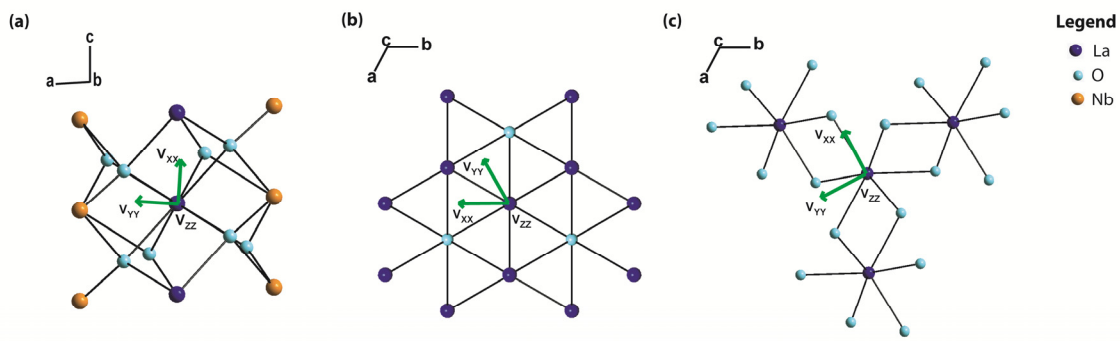

Figure 3.2. EFG tensor orientations for **(a)** $LaNbO_4$**, (b)** La_2O_3, and **(c)** $La(OH)_3$. In each case $\boldsymbol{V_{zz}}$ is directed out of the page, while $\boldsymbol{V_{xx}}$ and $\boldsymbol{V_{yy}}$ lie in the a-b plane of the crystal axes. Tensor orientations are shown by green arrows. Calculations of the EFG tensor orientations were performed in CASTEP. La is represented by dark blue spheres, O is represented by light blue spheres, and Nb is represented by orange spheres.

^{139}La NMR powder patterns are known to be very sensitive to the environment surrounding La, often displaying high values of C_Q, as large as 105 MHz,[46] for cases in

which La has a non-spherical environment. In the case of $LaNbO_4$, the crystallographic parameters do not show disorder or partial occupancies in either the niobium or lanthanum positions, suggesting that the structure itself is ordered. This is consistent with the observed ^{139}La NMR spectrum which clearly shows a typical powder pattern for highly ordered samples with high crystalline symmetry. (The sensitivity of quadrupolar nuclei, such as lanthanum, is to the symmetry of the oxygen environment, as well as the complexity of the second coordination sphere).[46, 47]

La_2O_3 : The second model compound, La_2O_3, is known to form a trigonal lattice structure with space group *P-3m1*, in which the lanthanum atoms are surrounded by seven oxygen atoms within 2.8 Å with the La-O bond distance in the range of 2.4 – 2.8 Å. This structure is shown in ***Table 3.2***, and the corresponding ^{139}La NMR spectra, collected at 11.7 T and 21.1 T are shown in ***Figure 3.3*** (a) and (b). The spectra are dominated by the quadrupolar interactions, and at 11.7 T the full spectral width is about 600 kHz. Yet even at this field it was possible to acquire this spectrum with only a single central frequency offset using the WURST-echo pulse. Since the second-order central transition quadrupolar line width scales inversely with the field, the same spectrum recorded at 21.1 T is only about 300 kHz broad. Not only is it easier to obtain the correct line at the higher magnetic field, but the signal-to-noise is also significantly improved which will become important when studying battery samples with lower lanthanum content. Another advantage of recording ^{139}La NMR spectra at 21.1 T is the fact that the chemical shielding interactions are proportional to the external magnetic field and the quadrupolar interactions are inversely proportional to the external magnetic field, which facilitates the extraction of information

about the chemical shielding interaction at higher magnetic fields.[48] In the La_2O_3 example (***Figure 3.3*** (a) and (b)), note how the singularity in the middle of the powder pattern moves to higher frequency in the high-field spectrum. The position of this singularity is directly related to the magnitude of CSA interactions, and the shift becomes more pronounced at higher magnetic field, allowing accurate quantification of CSA interactions.

The crystallographic lanthanum environment in La_2O_3 is simple, in that the major influence on lanthanum is its surrounding oxygen environment, with there being no lanthanum within 4.00 Å. Lanthanum sits in a pseudo-octahedral environment with six of the oxygen atoms, while the seventh oxygen is directly above this octahedral system. The distance between lanthanum and the seventh oxygen is 2.555 Å. This non-spherical environment contributes to a lanthanum NMR spectrum with a large quadrupolar coupling constant, C_Q, of 59.0 MHz ± 0.5 MHz. Simulations of ^{139}La NMR measurement, shown in ***Figure 3.3,*** also reveal an asymmetry parameter, η, of 0.00 ± 0.05. This agrees with the work of Bastow, in which the ^{139}La NMR of La_2O_3 was recorded at 9.4 T, although no CSA contribution to the ^{139}La NMR spectrum was reported.[10] Nevertheless, in our ^{139}La NMR spectrum, in addition to EFG contributions, there is a contribution from the CSA, and the simulated spectrum produces a span of 500 ppm ± 10 and a skew of -1 ± 0.1 with α = 150 º ± 30 º , β = 90 º ± 10 º, and γ = 180 º ± 10 º. These values were obtained by the simulation of NMR spectra collected at 21.1 T and 11.7 T. The asymmetry parameter, η = 0, arises from the axially symmetrical EFG tensor, which is the result of the 3-fold rotational axis of the La_2O_3 crystal structure, which lies along the c-

axis.[22] The values obtained for C_Q and η by simulating the ^{139}La NMR spectrum are supported by the values obtained through theoretical calculations using CASTEP: C_Q = 56 MHz and η = 0. In addition CASTEP calculated a span of 260 ppm, a skew of -0.44, and Euler angles α = 150 º, β = 88 º, and γ = 180 º. These are shown in ***Table 3.3***. The corresponding EFG tensors, as predicted by CASTEP, are shown with relation to the crystal axis in ***Figure 3.2*** (b).[35] It is clear that the major EFG tensor component, $\boldsymbol{V}_{zz}$, is oriented along the c-axis of the crystal, which has 3-fold rotational axis that passes through the center of the La atom. This supports experimental finding of η being 0.00 ± 0.05, with the axial line shape evident in the ^{139}La NMR spectra.

For comparison, the ^{139}La NMR spectra of $La(OH)_3$ in La_2O_3 that was produced by exposing La_2O_3 to air in ambient conditions were measured at 21.1 T, ***Figure 3.3*** (c).[29] The $La(OH)_3$ impurity is clearly visible in the ^{139}La NMR of the exposed sample.[29] (To obtain the pure La_2O_3 sample, the exposed sample was heated in air at 900 ºC for 24 hours.) At first the identity of the central $La(OH)_3$ line shape was not known. Simulation of the NMR spectrum obtained at 21.1 T shows that the peak representing the La-impurity was found to have a C_Q of 22.0 MHz ± 0.5 MHz, and an η of 0.00 ± 0.05, with a span of 80 ± 7 ppm, skew of 0, and α = 90 º ± 30 º, β = 10 º ± 10 º, γ = 0 º ± 10 º. These values are also supported by measurements taken at 11.7 T. By measuring the ^{139}La NMR spectrum of $La(OH)_3$ at 9.4 T, Herreros *et al.*[20] reported that the C_Q and η for this compound are 20.5 ± 0.5 MHz and 0.05 ± 0.05, respectively. From the similarity in the spectra obtained, it was concluded that the second phase present in this compound consisted primarily of $La(OH)_3$.

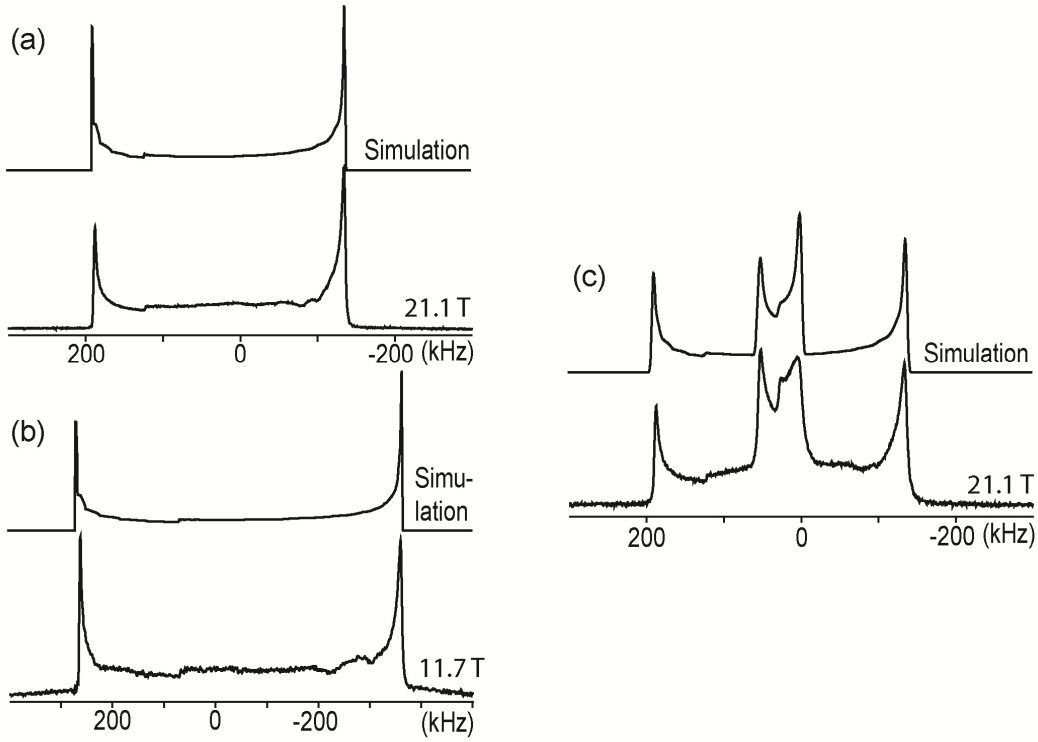

Figure 3.3. ^{139}La NMR spectra of La_2O_3, heated at 900 ºC to remove $La(OH)_3$ impurity: (a) taken at 21.1 T and (b) 11.7 T. (c) ^{139}La WURST-echo NMR spectra at 21.1 T of La_2O_3, exposed to air in ambient conditions. Simulations were performed using WSolids Software.

Further support is given by theoretical predictions, performed in CASTEP. The theoretically predicted values are shown in ***Table 3.3***, along with the experimentally obtained results. $La(OH)_3$ CASTEP predictions result in a C_Q and η of -23.5 MHz and 0.00 respectively, which support the axial shape of the observed spectra. The value of η suggests that the EFG tensor component, $\boldsymbol{V_{zz}}$, lies along the c-axis of the $La(OH)_3$ crystal structure. This is consistent with the crystallographic information, which places $La(OH)_3$ in the space group *P63/m*, and shows that the lanthanum atom lies at the center of a 3-fold rotational axis as well as a 6-fold screw axis, which are both directed along the c-axis of the crystal.[24] ***Figure 3.2*** (c) shows the orientation of the theoretically calculated EFG

tensor of $La(OH)_3$ with respect to the crystal axis. In addition CASTEP produced values of 200 ppm and 0.01 for the span and skew, respectively, with Euler angles of α = 92 º, β = 0 º, and γ = 0 º. Although the theoretically predicted span is larger than that observed, the predicted Euler angles are in good agreement with the observed values. Theoretically predicted and experimentally obtained values are shown in ***Table 3.3***.

$LaAlO_3$, $Li_7La_3Zr_2O_{12}$ and La_3NbO_7: Additional information about the line shapes and ranges of NMR parameters that are typically observed for lanthanum-containing oxides was determined from the study of model materials $LaAlO_3$, $Li_7La_3Zr_2O_{12}$ and La_3NbO_7. In these model lanthanum-containing materials the ^{139}La C_Q ranges from 7.1 ± 0.4 for $LaAlO_3$ to 97 ± 2 in La_3NbO_7 (La-1). A comparison was also made between the experimentally observed and calculated values of C_Q and η. These values were plotted together on two graphs, shown in ***Figure 3.4***. A linear trend was observed for these parameters with slopes of 1.01 ± 0.02 and 0.95 ± 0.04 observed for the C_Q and η, respectively. This trend shows that the CASTEP prediction of these parameters is accurate for these materials.

Like members of the $LaLi_{0.5}Fe_{0.2}O_{2.09}$ family, $Li_7La_3Zr_2O_{12}$ and La_3NbO_7 each have two unique crystallographic sites, making the spectral simulation cumbersome. Collection of the ^{139}La NMR spectra at two magnetic fields, 11.7 T and 21.1 T, allows for the more accurate determination of the spectral parameters, as discussed above. In addition, when attempting to distinguish between multiple resonances, which each have several singularities, simulation at two fields allows these singularities to occur in different position relative to each other making them more distinct. This is a result of the

field dependence of C_Q. ***Figure 3.5*** (a) shows the ^{139}La NMR spectrum of $Li_7La_2Zr_2O_{12}$ at 21.1 T along with the spectral simulation in which each site can be resolved clearly. (b) Compares the ^{139}La NMR spectra of this material collected at 11.7 T and at 21.1 T. Although the signal to noise ratio is smaller for the 11.7 T data, the singularities in the spectrum are separated due to differences in quadrupolar contributions, making them more distinct. The parameters C_Q and η are strong indicators of the structure and local symmetry in lanthanum compounds, and thus ^{139}La NMR is a valuable tool in the study of lanthanum containing compounds.[29]

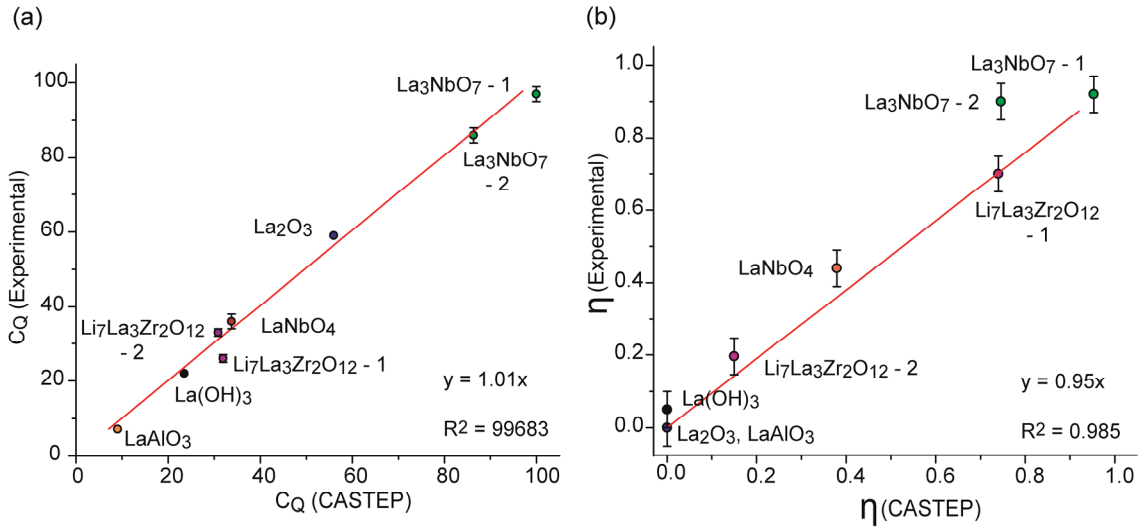

Figure 3.4. Comparison of experimentally observed and calculated values for (a) C_Q and (b) η. A linear trend is observed for both of these parameters, as shown by the slopes of 1.01 ± 0.02 for C_Q and 0.95 ± 0.04 for η.

Table 3.3: Experimental and calculated ^{139}La NMR parameters in model compounds.

Material	Method	C_Q (MHz)	η	δ_{iso} (ppm)	Ω (ppm)	κ	α (°)	β (°)	γ (°)
$LaNbO_4$	Expt.	36 ± 2	0.44 ± 0.05	295 ± 25	255 ± 10	0.40 ± 0.04	90 ± 5	50 ± 5	270 ± 10
	Calc.	33.8	0.38	220 *	490	0.11	90	27	270
La_2O_3	Expt.	59.0 ± 0.4	0.00 ± 0.05	640 ± 10	500 ± 10	-1.0 ± 0.1	150 ± 30	90 ± 10	180 ± 10
	Calc.	56	0.0	378 *	260	0.44	150	88	180
$La(OH)_3$	Expt.	22.0 ± 0.5	0.05 ± 0.02	260 ± 20	80 ± 7	0 ± 0.1	80 ± 7	10 ± 10	0 ± 10
	Calc.	23.5	0.0	301 *	200	0.01	92	0	0
$LaAlO_3$	Expt.	7.1 ± 0.4	0.0 ± 0.05	374.5 ± 0.5	119 ± 2	-1	0 ± 5	90 ± 5	0 ± 5
	Calc.	9.05	0						
$Li_7La_3Zr_2O_{12}$ -1	Expt.	26 ± 1	0.7 ± 0.05	395 ± 5					
	Calc.	31.94	0.74						
$Li_7La_3Zr_2O_{12}$ -2	Expt.	33 ± 1	0.196 ± 0.05	530 ± 5					
	Calc.	30.88	0.15						
La_3NbO_7-1	Expt.	97 ± 2	0.92 ± 0.05	400 ± 10					
	Calc.	99.95	0.953						
La_3NbO_7-2	Expt.	86 ± 2	0.9 ± 0.05	700 ± 10					
	Calc.	86.36	0.746						

*C_Q = quadrupole coupling constant; η = asymmetry parameter; δ_{iso} = isotropic chemical shift; Ω = span; κ = skew; α, β, and γ are the Euler angles. *: the chemical shifts were calculated using δ_{iso} (sample)- δ_{iso} (ref)= σ_{iso} (ref)- σ_{iso} (sample), where δ_{iso} (ref) and σ_{iso} (ref) are experimental chemical shift (0.0 ppm) and calculated chemical shielding (5022 ppm) of aqueous 1.0 M $LaCl_3$, respectively.*[20]

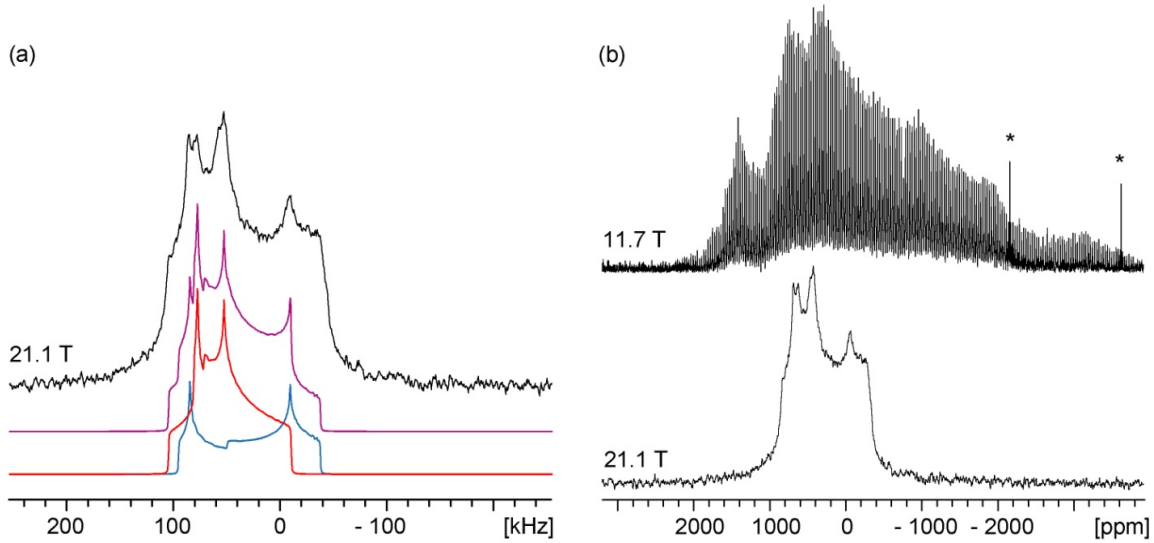

Figure 3.5. ^{139}La spectra of $Li_7La_3Zr_2O_{12}$. (a) Spectrum at 21.1 T (WURST-echo experiment) with spectral simulation, performed in WSolids software. The black line is the observed spectrum; the blue line represents La-1; and the red line represents La-2. (b) Comparison of the ^{139}La NMR spectrum at 21.1 T and 11.7 T. At 11.7 T the spectrum was collected using the WURST-QCPMG pulse sequence.

3.4.2. Structural Analysis of $Li_{3x}La_{(2/3)-x}TiO_3$ Using ^{139}La NMR Spectroscopy

In contrast to the highly ordered model materials discussed above, the fast lithium ion electrolyte material, $Li_{3x}La_{(2/3)-x}TiO_3$, is known to have considerable disorder, which results from the ability of lithium and lanthanum to occupy the same crystallographic site.[23, 31] $Li_{3x}La_{(2/3)-x}TiO_3$ has an orthorhombic, perovskite type structure in space group *Pmm* and consists of corner-shared TiO_6 octahedra, while the lanthanum/lithium is situated between the TiO_6 octahedra.[23] The crystal structure predicts two lanthanum environments, as shown in ***Table 3.2***. Each environment is oxygen rich and in each case La is coordinated to 12 oxygen atoms. La atoms are differentiated by their positions in the unit cell, with La-1 positioned on the corners of the unit cell and La-2 at the center of the

c-axis. In addition, each La site has different La-O bond distances; although all La-O bonds lie in the range of 2.7 - 2.8 Å. Interestingly, the ^{139}La NMR spectrum recorded at two magnetic fields (***Figure 3.6***) shows only one La line shape. This asymmetric line shape, which lacks the usual sharp discontinuities typically observed in quadrupole powder patterns, is skewed to one side and is indicative of substantial quadrupolar interaction. This is due to the disorder in the second coordination sphere of lanthanum which usually results in distribution of the quadrupolar parameters C_Q and η.[9] This distribution also makes C_Q and η for the two sites irresolvable at both magnetic fields (21.1 T and 11.7 T), since there are many sites with different quadrupolar parameters in this sample. Nevertheless, using appropriate simulation tools, many details of this distribution can still be extracted.

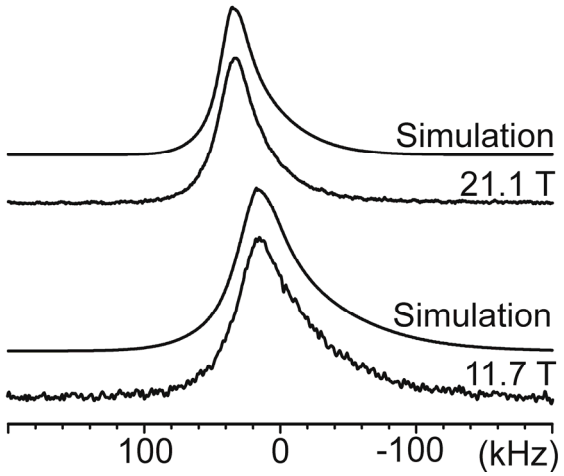

Figure 3.6. ^{139}La WURST-echo NMR spectra of $Li_{3x}La_{(2/3)-x}TiO_3$ collected at 21.1 T (top) and 11.7 T (bottom). Simulations were performed in QuadFit and are shown above each spectrum.

To effectively simulate the spectra in order to extract quadrupolar information, one needs to analyze the contribution of chemical shielding interaction and quadrupolar

coupling interaction in the spectrum. In ***Figure 3.6***, the full width at half height (FWHH) for the spectrum at 11.7 T is 53.5 kHz, while at 21.1 T the FWHH is reduced significantly to 34.0 kHz. This suggests that the spectra are dominated by second order quadrupolar interaction and can be simulated neglecting the potential chemical shielding anisotropy of lanthanum. Using QuadFit,[34] which has the capability of including a distribution in the parameters η and C_Q, the spectra at two fields were simulated accurately by considering the distribution of quadrupolar parameters, with the resulting simulations shown in ***Figure 3.6***. Shown in ***Table 3.4***, the quadrupolar coupling constant of La in $Li_{3x}La_{(2/3)-x}TiO_3$ is ~ 22.5 MHz with a broad distribution of 14.5 MHz, although the asymmetry parameter is 0.75 with a narrow distribution of 0.15. It should be mentioned that almost no line broadening is needed in both simulations, which is expected for this sample, as it is highly crystalline. The extraction of quadrupolar information was also attempted by using the quadrupolar induced shift (QIS) that is inversely proportional to the external magnetic field.[49] ***Equation 3.1*** is valid for a nucleus with I=7/2.

$$\delta_{CG} - \delta_{iso} = -2551.02\left(\frac{C_Q^2}{\omega_0^2}\right)\left(1 + \frac{\eta^2}{3}\right) \tag{3.1}$$

Where δ_{CG} is the center of gravity of the peak, δ_{iso} is the isotropic chemical shift, ω_0 is the Larmor frequency, C_Q is the quadrupolar coupling constant and η is the asymmetry. 2551.02 is a constant, which varies with the spin, I, of the nucleus of interest. The measured centers of gravities of peaks at 11.7 T and 21.1 T are 67 ppm and 217 ppm, respectively. Using the ***Equation 3.1***, one can obtain the δ_{iso} = 284 ± 8 ppm, as shown in ***Table 3.4***. However, C_Q and η cannot be determined unambiguously using this method.

Since η has the range of 0 to 1, the minimum and the maximum values of C_Q can still be determined, which are 17.8 MHz and 20.5 MHz, respectively. Although as can be seen in ***Table 3.4***, the QuadFit and the QIS calculation give very similar isotropic chemical shifts and quadrupolar coupling constants, one should notice that the QIS calculation does not allow the determination of the distribution of C_Q and η, owing to the fact that the QIS calculation considers only the position of centre of gravity, not the overall line shape. The minimum and the maximum values of C_Q are not the actual distributions of C_Q, but the values corresponding to the minimum and the maximum values of the asymmetry parameter. Both spectra can be simulated with a single site without considering the distribution of C_Q and η as well, although a very large line broadening value was necessary. The results are also presented in ***Table 3.4*** for comparison. It can be seen that the simple simulation without distributions of C_Q and η gives results close to the previous methods. This may be due, coincidently, to the high asymmetry parameter of this particular sample. It has been shown previously that a featureless line shape such as the spectra shown in ***Figure 3.6*** could result from a very low asymmetry but with broad distribution of quadrupolar parameters.[50]

The distribution of quadrupolar parameters obtained above can be explained by analyzing the second coordination sphere of La in the crystal structure, which contains lanthanum, lithium, and a vacant site in a disordered distribution.[23, 31] Lanthanum is in a highly symmetric environment according to the surrounding oxygen atoms, which form a cube-like arrangement around the La atoms. The highest symmetry element present is a 2-fold rotational axis, which passes through both La-1 and La-2, which agrees with $\eta \neq 0$. It

should be noted here that there are several possible structure of lithium lanthanum titanate materials.[51, 52] Powder X-ray diffraction was used to determine that the present structure was in fact $Li_{3x}La_{(2/3)-x}TiO_3$ ($0.03 \leq x \leq 0.063$).[23] ^{139}La NMR also proved to be a very useful technique to support the XRD data. This technique was able to differentiate the present structure from other possible structures based on the differences in symmetry elements present for the La sites. Other lithium lanthanum titanate structures are of higher symmetry and most contain rotational exes, either 3- or 4-fold, that run through La. The non-zero η obtained for the present structure by simulating the NMR spectrum obtained for this material confirmed that it was the correct structure, which has only 2-fold rotational symmetry passing through each La site. Although disorder certainly plays a role in the observed ^{139}La NMR spectrum, the spectral simulations still suggest a non-zero value of η. For situations in which the spectral width is small there is the possibility of using multiple-quantum magic angle spinning (MQMAS) NMR experiments to separate the contributions from chemical shielding and quadrupolar coupling. However, the line width here is too broad to apply this method.

The lithium atoms, as well as vacant sites, in this structure are known to substitute lanthanum in its crystallographic sites, displacing a stoichiometric amount of the lanthanum from the crystal structure.[23, 31] This means that for each lanthanum atom in its original place in the crystal structure, the surrounding environment is disordered by the substitution of lanthanum for lithium, or a vacant site, in the second coordination sphere. This disordered lanthanum environment is present in the same context for both lanthanum sites, which leads to the featureless ^{139}La NMR spectra of $Li_{3x}La_{(2/3)-x}TiO_3$ at both fields.

The CASTEP NMR calculations were performed for this compound and the results are presented in ***Table 3.4***. The $Li_{3x}La_{(2/3)-x}TiO_3$ sample represents a certain challenge for CASTEP NMR calculations due to significant disorder in cationic positions, as disorder or partial site occupancies are not implemented in the CASTEP code. Nevertheless, calculations for three models structures which best represent the true $Li_{3x}La_{(2/3)-x}TiO_3$ structure have been attempted. The results are summarized in the ***Table 3.4***. In the first model structure, both sites, La-1 and La-2, were fully occupied, while there was no Li present. Even though there is significant charge imbalance, the CASTEP results allow the discrimination of two La sites, and obtained C_Q and η values are reasonably close to those found experimentally. In the second model structure, the La-1 site was fully occupied with La, and the La-2 site was fully occupied with Li. The third structure has the site occupations inversed, the La-1 site was fully occupied with Li, and the La-2 site was fully occupied with La. As can be seen in ***Table 3.4***, for these three model structures, the CASTEP calculated C_Q values are in the same general range as found in experiments.

3.4.3. Structural Analysis of $LaLi_{0.5}Fe_{0.2}O_{2.09}$ and Related Materials

3.4.3.1. Powder X-Ray Diffraction and Transmission Electron Microscopy

The garnet-like structure, $LaLi_{0.5}Fe_{0.2}O_{2.09}$, considered as a potential cathode material for lithium ion batteries, has a cubic structure in space group *Im3m*.[12] Related materials were prepared by varying the amount of Li, La and Fe in the structures. The PXRD pattern shows the formation of single-phase garnet-like structure for

$LaLi_{0.5}Fe_{0.2}O_{2.09}$, $La_{0.94}Li_{0.69}Fe_{0.2}O_{2.09}$, and $LaLi_{0.75}Fe_{0.14}O_{2.09}$ and the observed line match with parent compound $LaLi_{0.5}Fe_{0.2}O_{2.09}$, as reported by Mazza in 1985.[11-13] A TEM image of $LaLi_{0.5}Fe_{0.2}O_{2.09}$ indicates a highly crystalline structure, with d-spacing of 0.40 nm, and is shown in ***Figure 3.7***. Similar TEM analysis was performed for the other investigated materials.

Table 3.4: Experimental and calculated ^{139}La NMR parameters in battery materials.

Material	Method	La	δ_{iso} (ppm)	C_Q (MHz)	η
$\mathbf{Li_{3x}La_{(2/3)-x}TiO_3}$	Calc.[1]	La-1	-	25.4	0.5
		La-2	-	18.3	0.43
	Calc.[2]	La-2	-	34.7	0.70
	Calc.[3]	La-1	-	17.9	0.49
	Expt.[4]	-	284 ± 5	19.2 ± 1.3	
	Expt.[5]	-	260 ± 20	22.5 ± 0.5	0.75 ± 0.1
	Expt.[6]	-	270 ± 10	17.0 ± 2.0	0.9 ± 0.1
$\mathbf{LaLi_{0.5}Fe_{0.2}O_{2.09}}$	Expt.	La-1	510 ± 40	56.0 ± 1.0	0.05 ± 0.05
		La-2	290 ± 30	29.0 ± 2.0	0.6 ± 0.1

1. *CASTEP, structure with two La sites, La-1 and La-2*
2. *CASTEP, structure with one La site (La-2). The La-1 site has been replaced with Li (Li-1).*
3. *CASTEP, structure with one La site (La-1). The La-2 site has been replaced with Li (Li-2).*
4. *Calculated using QIS (see text).*
5. *Spectra were fitted using QuadFti with distributions for both C_Q (14.5 MHz) and η (0.15).*
6. *Spectra were fitted using DMFit with a single site.*

Rietveld refinement on the powder X-ray diffraction pattern using GSAS was also performed, shown in ***Figure 3.8*** for $LaLi_{0.5}Fe_{0.2}O_{2.09}$.[53] There is a small peak in the PXRD at 30º, which is due to a small Li_2O impurity.[54] ***Table 3.5*** lists the Rietveld refinement structure parameters of $LaLi_{0.5}Fe_{0.2}O_{2.09}$ for comparison and is consistent with literature.[13-15] Powder X-ray diffraction is known to be insensitive to Li, therefore, it can be expected that ^{7}Li NMR would give a more accurate measurement of the Li environments in this sample.

It should be noted that the crystal structure for $LaLi_{0.5}Fe_{0.2}O_{2.09}$ (also written as $La_{32}Li_{16}Fe_{6.4}O_{67}$), reported by Mazza et al.,[12] contains partial occupancy on each site, including the oxygen sites. The occupancies for the oxygen sites vary from 40 to 89 %. This is different from the stoichiometry obtained experimentally in this work through powder X-ray diffraction, which is $La_{1.125}Li_{0.5}Fe_{0.30}O_3$ (also written as $La_{36}Li_{16}Fe_{9.4}O_{96}$). This is slightly different from the stoichiometry reported in the literature and contains full occupancy for all elements, except for Fe, as shown in ***Table 3.5***. For the purpose of consistency the literature stoichiometry is used in this work. In each case the reported stoichiometry is based on the lanthanum content of the parent material ($La_{32}Li_{16}Fe_{6.4}O_{67}$), i.e. the total stoichiometric portion of each element is divided by 32. This is also in keeping with the method used in the literature for $LaLi_{0.5}Fe_{0.2}O_{2.09}$ and related materials.

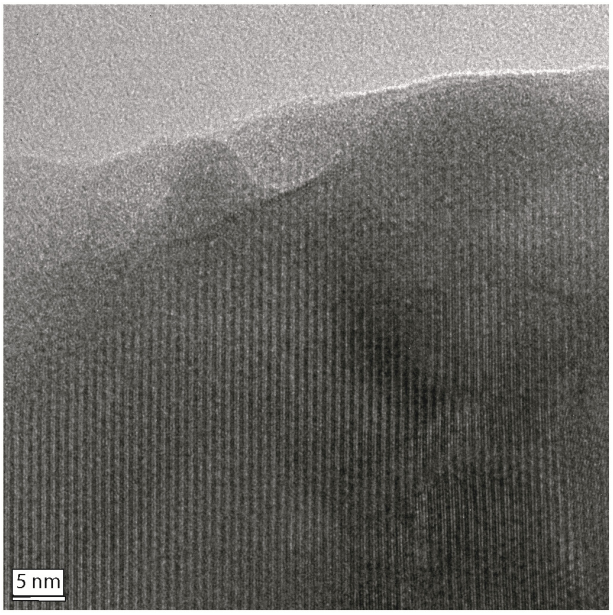

Figure 3.7. Typical TEM image of $LaLi_{0.5}Fe_{0.2}O_{2.09}$. The image was taken on an FEI Titan 80-300 equipped with image aberration corrector operated at 300kV. TEM analysis showed a single phase, with a high degree of crystallinity.

Table 3.5: Rietveld refinement structural parameters for $LaLi_{0.5}Fe_{0.2}O_{2.09}$.

Atom	X	Y	Z	Multiplicity	Occupancy
La-1	0.00000	0.30431(8)	0.30431(8)	24	1.0000
La-2	0.34548(8)	0.00000	0.00000	12	1.0000
Fe-1	0.00000	0.00000	0.00000	2	1.0000
Fe-2	0.25000	0.25000	0.25000	8	0.9305
O-1	0.36471(1)	0.36471(1)	0.20633(5)	48	1.0000
O-2	0.25000	0.50000	0.00000	12	1.0000
O-3	0.13908(1)	0.50000	0.00000	24	1.0000
O-4	0.00000	0.13059(1)	0.00000	12	1.0000
Li	0.15894(4)	0.15894(4)	0.15894(4)	16	1.0000

Note: For the $LaLi_{0.5}Fe_{0.2}O_{2.09}$ in space group I m 3 m, $a = b = c = 12.2032 \pm 0.0002$ Å; $\alpha = \beta = \gamma = 90$ °; $\chi^2 = 2.5$.

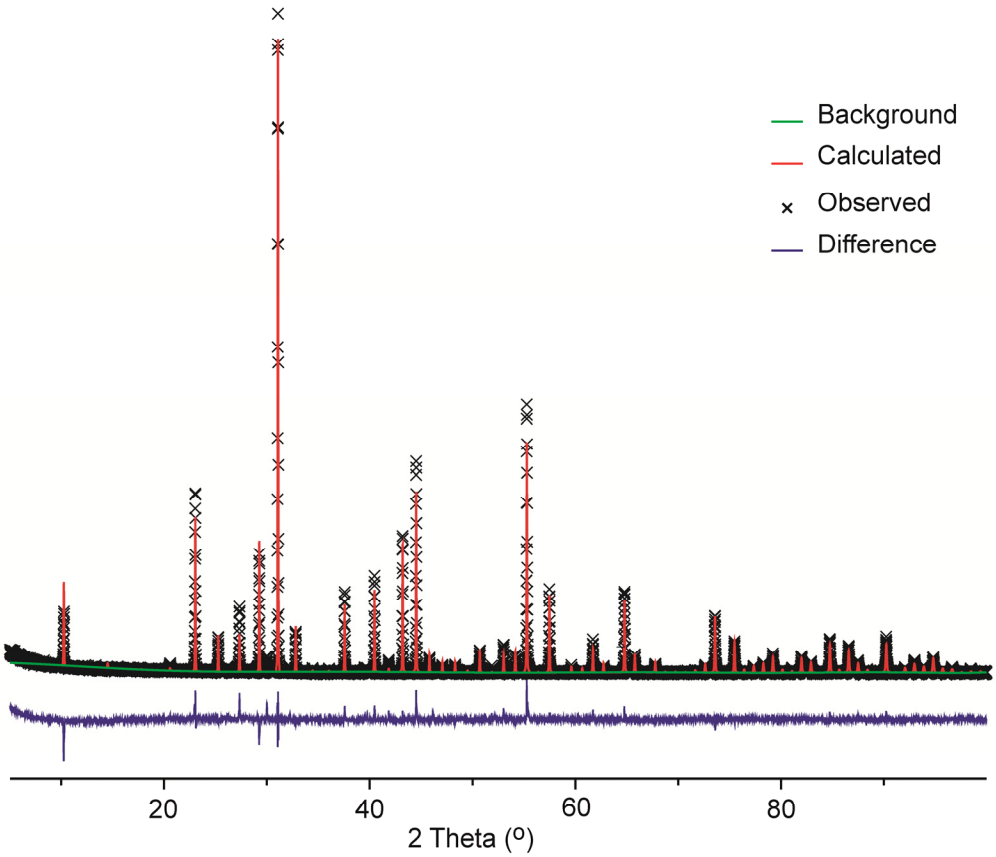

Figure 3.8. GSAS Rietveld refinement output for $LaLi_{0.5}Fe_{0.2}O_{2.09}$. Parameters used for the refinement were taken from the literature.[12] χ^2 was found to be 2.5.

Different combinations of the positions of Li and Fe were attempted in the Rietveld refinement of the resulting PXRD data and it was found that there is a potential for Li to partially occupy the Fe site at (0.25, 0.25, 0.25). Occupancy of the (0, 0, 0) Fe site by Li was not found as a solution by the software, suggesting that there is only Li substitution on the (0.25, 0.25, 0.25) Fe site. ***Figure 3.9*** shows an image of the unit cell of $LaLi_{0.5}Fe_{0.2}O_{2.09}$ for a situation in which there is a total substitution of Fe for Li on the (0.25, 0.25, 0.25) site. This is the extreme case, and it is more likely that a partial

replacement of Fe by Li occurs on this site. This rearrangement accounts for one additional Li site in the crystal structure.

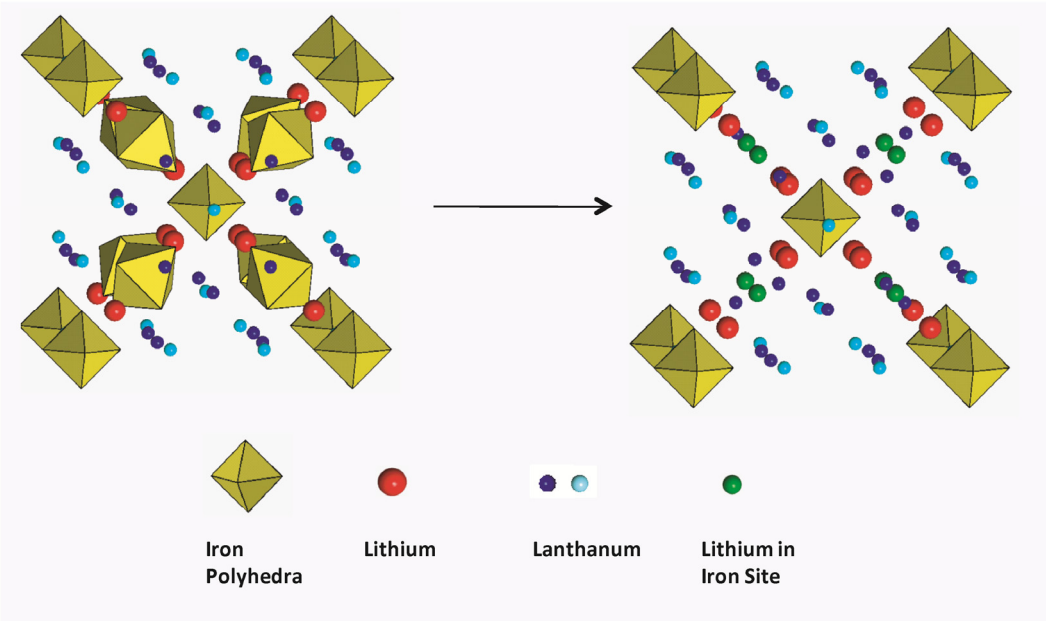

Figure 3.9. Right: Xtal Draw image of $LaLi_{0.5}Fe_{0.2}O_{2.09}$.[28] This is a cubic structure in space group *Im-3m*, with cell length 12.231 Å. Left: Xtal Draw image of structure in which all of the Fe (0.25, 0.25, 0.25) sites have been replaced by Li, shown as the green spheres.

The $LaLi_{0.5}Fe_{0.2}O_{2.09}$ structure is known to have partial occupancies, some of which exist on the iron (0.25, 0.25, 0.25) site (green spheres in ***Figure 3.9***).[12] A vacancy may also exist on the Li site, since it is possible for the Li to move onto a vacant Fe site, and thus be replaced by the vacancy. This introduces the possibility of a distribution of Li sites, in which different Li environments are created by having different proximities to Fe, and therefore the unpaired electrons that are found on Fe in this system.

3.4.3.2. ^{7}Li NMR Spectral Analysis

Initial studies performed using ^{7}Li MAS NMR at 11.7 T indicated that the material may contain structural disorder. Previous studies determined that the compound had one crystallographically unique lithium site, two lanthanum sites and two iron sites. This number of lithium sites, however, is not supported by ^{7}Li MAS NMR performed at 11.7 T, shown in ***Figure 3.10***. The lithium peaks represent a set of paramagnetic peaks between ~ 4 ppm and ~ 25 ppm, and a set of diamagnetic peaks at ~ 0 ppm. Here, the lithium peak that has a higher chemical shift is known to have the most paramagnetic character. This is supported by T_1 measurements which show that these peaks have T_1 relaxation values of ~ 11 ms, while the diamagnetic peaks have T_1 relaxation times greater than 100 s. The lithium atoms represented by the paramagnetic peaks are likely to be closest to one or more iron sites, while the peak at the lowest chemical shift has the least paramagnetic character due to its greater distance from iron, and thus unpaired electrons in the structure.[3, 6]

The different lithium environments arise from the ability of lithium to occupy vacant sites found on the Fe-2 site at (0.25,0.25, 0.25), which is supported by PXRD analysis.[16] This Li/Fe substitution is a significant source of disorder in this structure, with the existence of vacant sites on the original Li sites as well as the Fe-2 sites, in which Li substitution occurs. This means that the compound contains a “variable” site, which may be occupied by Li, Fe, or a vacancy.[12] The variability of this site produces a distribution of lithium sites, which is responsible for the unique ^{7}Li MAS NMR spectrum.

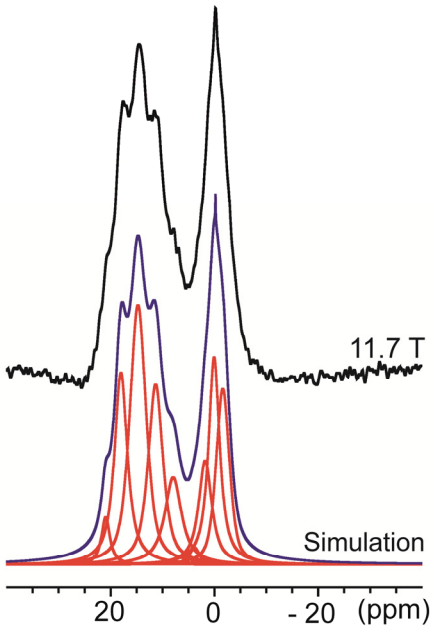

Figure 3.10. ^{7}Li MAS NMR of $LaLi_{0.5}Fe_{0.2}O_{2.09}$, collected at 11.7 T, with MAS 20 kHz.

A comparison of the ^{7}Li MAS NMR spectra of the $LaLi_{0.5}Fe_{0.2}O_{2.09}$ family shows that there is some similarity in the lithium environments in these materials. In particular, each spectrum consists of paramagnetic and diamagnetic regions which are each made up of several different resonances, as shown in ***Figure 3.11***. However, the relative contribution from these regions is different for each material.

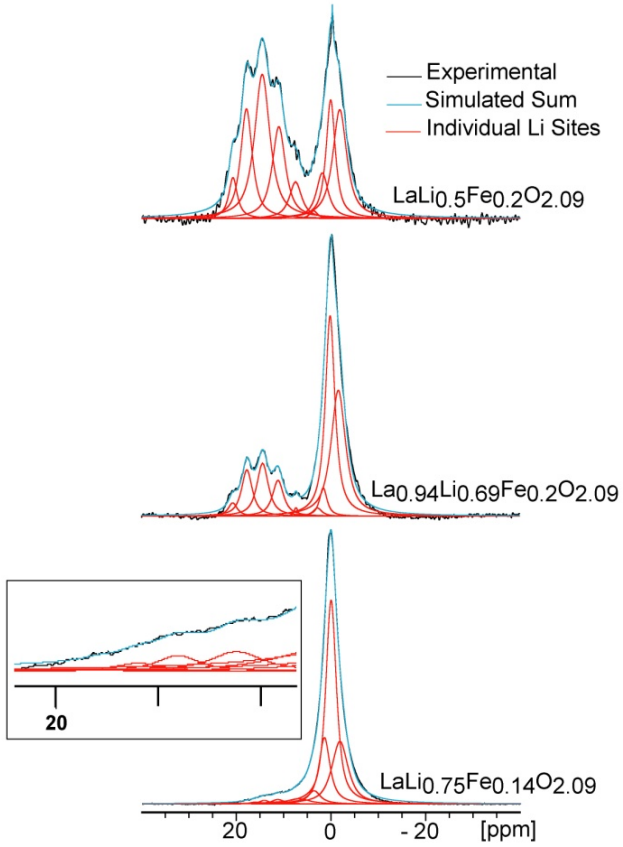

Figure 3.11. ^{7}Li MAS NMR of $LaLi_{0.5}Fe_{0.2}O_{2.09}$ (top) collected at 11.7 T, with a spinning speed of 20 kHz. This shows multiple peaks that represent different Li sites in the sample, with line fit analysis performed in TopSpin 2.1 software, where the lineshapes have a mixture of Gaussian and Lorentzian contributions. The experimental spectrum is shown in black, while the simulated sites are shown in red and their sum is shown in blue. Above, the ^{7}Li MAS NMR of $La_{0.94}Li_{0.69}Fe_{0.2}O_{2.09}$, and $LaLi_{0.75}Fe_{0.14}O_{2.09}$ are shown when measure under the same conditions as $LaLi_{0.5}Fe_{0.2}O_{2.09}$. Line fit analysis was performed with the same number of peaks contributing to the spectrum. The full peak analysis is shown in ***Table 3.6***.

Table 3.6: Line width analysis of ^{7}Li MAS NMR of $LaLi_{0.5}Fe_{0.2}O_{2.09}$, $La_{0.94}Li_{0.69}Fe_{0.2}O_{2.09}$, and $LaLi_{0.75}Fe_{0.14}O_{2.09}$.

$LaLi_{0.5}Fe_{0.2}O_{2.09}$									
Peak Shift (in ppm ±0.5ppm**)**	20.7	17.9	14.5	11	7.5	3.7	1.8	0.1	-1.9
Line Width (in Hz ±20 Hz)	420	570	750	650	610	370	590	450	690
% Contribution (±1%)	25	14	15	5	4	1	17	12	6
$La_{0.94}Li_{0.69}Fe_{0.2}O_{2.09}$									
Peak Shift (in ppm ±0.5ppm**)**	20.6	17.6	14.3	11.1	7.3	2.7	1.5	0.1	-1.7
Line Width (Hz)	440	520	570	540	190	430	370	470	710
% Contribution (±1%)	11	7	9	1	2	1	32	34	4
$LaLi_{0.75}Fe_{0.14}O_{2.09}$									
Peak Shift (in ppm ±0.5ppm**)**	18.2	16	14.2	11.4	7.1	3.7	1.5	0.1	-1.8
Line Width (Hz) ±20 Hz	290	510	450	570	1070	630	550	520	800
% Contribution (±1%)	0.8	1.0	0.4	3	0.1	4	24	50	17

From the ^{7}Li MAS NMR taken at 11.7 T, the distribution of sites, ranging in chemical shift from ~ 20 ppm to ~ -1 ppm, is shown in ***Table 3.6***. The possibility of this array of Li sites being caused by the effect of Li coupling to La was ruled out when the Li spectrum of this material was studied at a higher magnetic field, 21.1 T. The spacing of the peaks is equal in units of ppm at both fields, while the spacing in Hz is different. This is consistent with NMR peaks that are separated due to chemical shift alone,[55] thereby indicating the presence of several unique local environments of lithium ions. In addition to a complex NMR spectrum, this compound shows interesting ^{7}Li T_1 relaxation. The ^{7}Li NMR spectral peaks represent two groups of Li environments with different magnetic properties: paramagnetic and diamagnetic, as indicated by the large difference in values of T_1, for different peaks that were observed in NMR spectra. T_1 measurements $La_{0.94}Li_{0.69}Fe_{0.2}O_{2.09}$ were analyzed separately in two regions. The site at 14.5 ppm has a short T_1, 11.45 ± 0.06 ms, suggesting that it is paramagnetic in nature. This may be due to its proximity to an Fe atom in the compound, since Fe contains unpaired electrons and will contribute to the paramagnetic nature of nearby Li sites.[3] The Li site at ~ 0 ppm has a very long T_1, > 10.9 x 10^4 ms, suggesting that it is diamagnetic, and comparatively far from Fe atoms, and unpaired electrons.

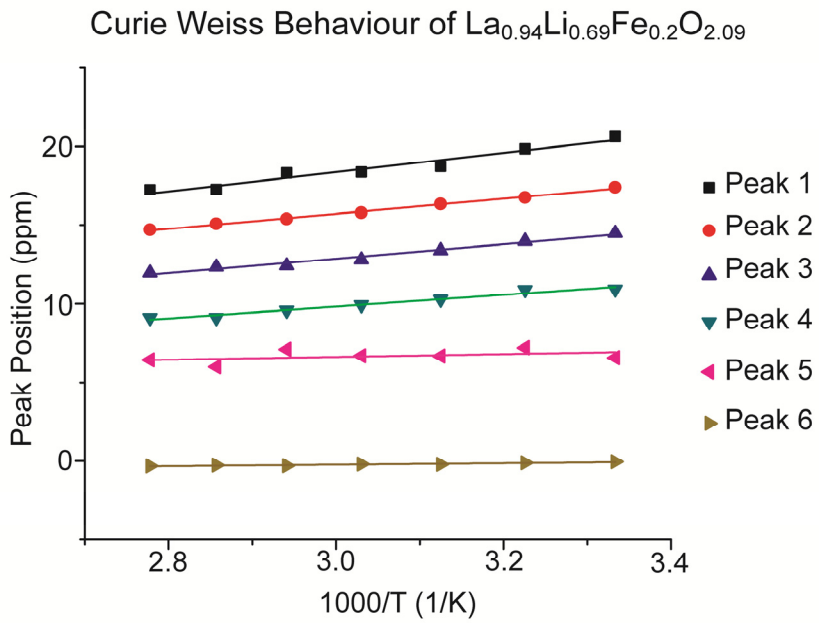

Figure 3.12. Curie Weiss behaviour of peaks in ^{7}Li NMR spectrum of $La_{0.94}Li_{0.69}Fe_{0.2}O_{2.09}$. Peaks are numbers form highest frequency to lowest frequency. Peak 6 represents the center of gravity of the diamagnetic peaks at ~0 ppm.

Figure 3.11 (b) shows the ^{7}Li MAS NMR of $LaLi_{0.5}Fe_{0.2}O_{2.09}$, $La_{0.94}Li_{0.69}Fe_{0.2}O_{2.09}$, and $LaLi_{0.75}Fe_{0.14}O_{2.09}$. It is evident that the ^{7}Li spectrum of each compound includes an array of paramagnetic peaks. Line fit analysis was performed for each of these spectra, and is shown in ***Table 3.6***. It appears that a distribution of paramagnetic peaks exists in each sample, with ratio of diamagnetic to paramagnetic peaks varying throughout the samples as the stoichiometry is varied. In particular, as the Li content is increased stoichiometrically, the contribution of the diamagnetic region increases with respect to the paramagnetic region. $LaLi_{0.75}Fe_{0.14}O_{2.09}$ has the smallest contribution from the paramagnetic region, while the parent material has the largest.

Figure 3.12 shows the chemical shift trends for each of the lithium peaks in the ^{7}Li MAS NMR spectrum of $La_{0.94}Li_{0.69}Fe_{0.2}O_{2.09}$, as a function of temperature. The steeper slope of the data with higher chemical shifts is consistent with the expected Curie Weiss behaviour of the peaks experiencing paramagnetic interactions, arising from the temperature dependence of the magnetic susceptibility.[56] This supports the differences observed in the T_1 values obtained by NMR for ^{7}Li, with the smallest T_1 observed for peaks that show the most significant temperature dependence. The unexpected number of ^{7}Li NMR resonances observed brought to light the possibility of substitution of Li onto the Fe lattice sites, which can be used to justify the range of chemical shifts observed. Where the PXRD analysis accounted for a total of two Li sites, the ^{7}Li NMR spectra reveals many more Li environments, potentially resulting from a higher level of disorder in the environment surrounding the Li ions. Separation of the spectral resonances based on paramagnetic character allows some insight into the differentiation of the Li environments.

Atomic distributions are known to occur in a variety of compounds, with well known crystal structures.[57] Studies performed on compounds containing atomic-level distribution usually focus on an element, which is sensitive to the components of its first coordination sphere. Modification of the first coordination sphere of the observed element through different chemical syntheses can change the NMR spectra obtained for the element of interest, and thus the distribution of the elements in the first coordination sphere is mapped through the NMR analysis of different compounds of similar chemical structure.[57] The garnet-like structure $LaLi_{0.5}Fe_{0.2}O_{2.09}$ exhibits a distribution of Li

environments that is seen in the ^{7}Li MAS NMR. This system is unusual because the distribution of Li environments is seen in the ^{7}Li environments themselves, as opposed to a secondary nucleus in the first coordination sphere.

3.4.3.3. ^{139}La NMR Spectral Analysis

To better understand the nature of the lithium distribution in the $LaLi_{0.5}Fe_{0.2}O_{2.09}$ family of material, ^{139}La NMR was used to assign the La sites and to study their environments. There are two crystallographically unique La sites in this material: La-1 is coordinated to ten O atoms, while having La-O bond distances in the range of 2.5 - 2.7 Å; La-2 is coordinated to nine O atoms with La-O bond distances in the range of 2.3 – 2.7 Å. ^{139}La NMR collected at 21.1 T, shown in ***Figure 3.13***, supports the crystallographic data, and shows evidence of two lanthanum environments.

Simulations of the NMR data, show that La-2 has a C_Q of 56 MHz ± 1 MHz, and η of 0.05 ± 0.05. This large C_Q suggests that La-2 is in a more non-spherical environment with respect to the surrounding oxygen as compared to La-1. In addition, La-2 contains little disorder in the second coordination sphere. Crystallographic information shows that the La-2 site lies on an axis of 4-fold rotation, and 4-fold roto-inversion, which is aligned with the c-axis of the crystal.[12] This high level or rotational symmetry is responsible for the experimentally obtained value of η, 0.05 ± 0.05.

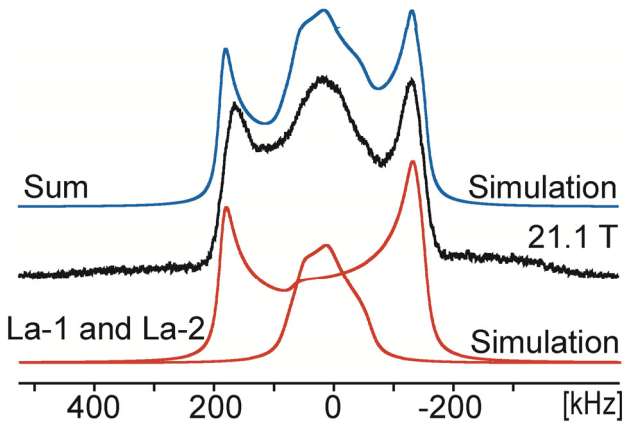

Figure 3.13. ^{139}La static NMR of $LaLi_{0.5}Fe_{0.2}O_{2.09}$. The spectrum was collected at 21.1 T using a WURST-echo pulse sequence.[44] Simulation was done using DMFit software.[33] The simulation shows the ^{139}La spectrum consisting of two peaks. The wider peak, La-2, has a C_Q of 56 ± 1 MHz, and η of 0.05 ± 0.05. The peak in the center of the spectrum, La-1, represents a distribution of lanthanum sites. Details are discussed in the main text.

By comparison, simulations of NMR spectra in ***Figure 3.13*** show that La-1 has a C_Q of 29 MHz ± 2 MHz and a η of 0.6 ± 0.1, suggesting that La-1 is in a more spherical oxygen environment, and yet in a position of lower symmetry than La-2, since the highest symmetry element present for La-1 is a 2-fold rotational axis. The low symmetry of this site is responsible for the large observed values of η, 0.6 ± 0.1, which is considerably different from that of La-2. A considerable amount of line broadening was necessary to simulate this peak, which may be an indication that the NMR parameters of the La-1 site cannot be described by a single set of values of C_Q or η, or rather that there is a distribution of C_Q and/or η for this particular site, similar to that seen in $Li_{3x}La_{(2/3)-x}TiO_3$.

^{139}La static NMR was also used to probe the distribution in the $LaLi_{0.5}Fe_{0.2}O_{2.09}$ family of materials further. Measurements were taken using the WURST-QCPMG pulse sequence in which two resonances were observed for each material. The resonances each

had very different quadrupole parameters, as shown in ***Figure 3.13***, which is consistent with the ^{139}La NMR study of the parent material. The ^{139}La static solid-state NMR spectra of $LaLi_{0.5}Fe_{0.2}O_{2.09}$, $La_{0.94}Li_{0.69}Fe_{0.2}O_{2.09}$, and $LaLi_{0.75}Fe_{0.14}O_{2.09}$ are shown in ***Figure 3.14*** (a), (b) and (c), respectively.[45]

The optimization of EFG and CSA parameters was sufficient to obtain reasonable fits of the experimental ^{139}La spectra. The application of line broadening was necessary, and the values used were different for the two La sites. More line broadening was used in the simulation of La-1, which is closer to the variable Li/Fe/vacant site than La-2. We attribute the necessary line broadening to be primarily the result of the distribution of quadrupole parameters, which results from the distribution of Li, Fe and a vacant site. In addition, there is likely some broadening that is a result of a paramagnetic influence of Fe on the La line shape in this material. This is expected to be more significant for La-1 than La-2, and is consistent with the experimental spectra.

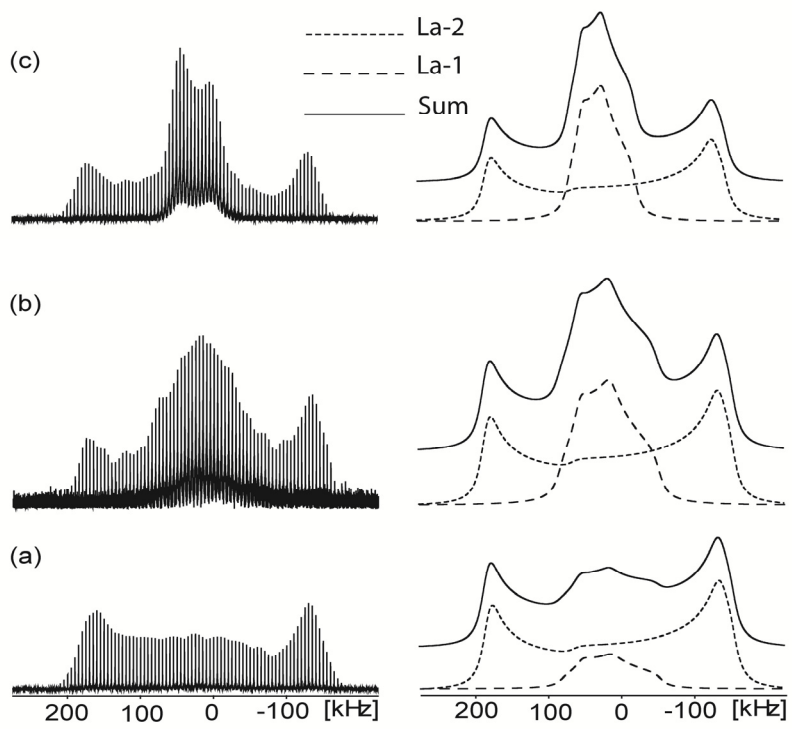

Figure 3.14. ^{139}La static solid-state NMR of (a) $LaLi_{0.5}Fe_{0.2}O_{2.09}$, (b) $La_{0.94}Li_{0.69}Fe_{0.2}O_{2.09}$, and (c) $LaLi_{0.75}Fe_{0.14}O_{2.09}$. Spectra were acquired at 21.1 T using the WURST-QCPMG pulse sequence.[45] Simulations were performed using DMFit software.[33]

When the spectra obtained for $LaLi_{0.5}Fe_{0.2}O_{2.09}$ in ***Figure 3.9*** and ***3.12*** are compared, there is a noticeable difference in the peak in the center of the spectrum. This is due to the sensitivity of the WURST-QCPMG pulse sequence to differences in the T_2 relaxation of the different sites. The center peak (C_Q = 29 MHz ± 2 MHz), with a longer T_2 value than the broader peak (C_Q = 56 MHz ± 1 MHz), is attenuated, with the possibility of some of the features of the quadrupole powder pattern being suppressed. This is not the case when this spectrum is observed with the WURST-echo pulse sequence, where the central line shape is clearly visible. Using this pulse sequence, the intensities of the two peaks are more indicative of the relative stoichiometric amounts of

each La site in the sample and therefore the WURST-echo pulse, ***Figure 3.9***, sequence is preferred for this sample. However, due to the much longer acquisition time it was not feasible to obtain a WURST-echo measurement for each material, and thus the WURST-QCPMG sequence was used instead.

These spectra in ***Figure 3.14*** are consistent with that of the parent material in ***Figure 3.13*** and outline two La sites in each material, as shown in the simulations. One of these sites is common to all of these materials, and is responsible for a broad, axial site with a C_Q of 56 ± 1 MHz and asymmetry parameter, η of 0.05 ± 0.05, while the other peak, which is superimposed on the first, changes throughout the samples and appears to represent a La site that changes, depending on the composition of the sample.[58] On examination of the crystal structure of the material, ***Figure 3.15***, it is evident that one of the La sites (La-2) is far from the variable site at (0.25, 0.25, 0.25) which is occupied by Li, iron or a vacancy (4.485 Å), while the other (La-1) is close to the variable site at (0.25, 0.25, 0.25) (3.206 Å). This means that variation in the La NMR between samples is likely due to this variable site at (0.25, 0.25, 0.25). The differing occupancy of this site creates different La environments through the changing of the electric field gradient of the La atom, which is very sensitive to its environment.[46] The broad NMR line shape that is indicative of axial symmetry represents La-2 and is consistent with a single La site that is in a non-spherical oxygen environment, which lies on the axis of a 4-fold rotation and a 4-fold rotoinversion.[58] The narrower line shape of La-1 is due to the lack of symmetry, specifically, less than 3-fold rotational symmetry. Simulation of the NMR spectra revealed that La- has a C_Q of 29 MHz ± 2 MHz and an asymmetry parameter, η of 0.6 ±

0.1.[58] The simulation of this site in the parent material involved a considerable amount of Gaussian line broadening, which is an indication that this is not a single site, but a distribution of lanthanum sites with a variation in the values of C_Q and η.

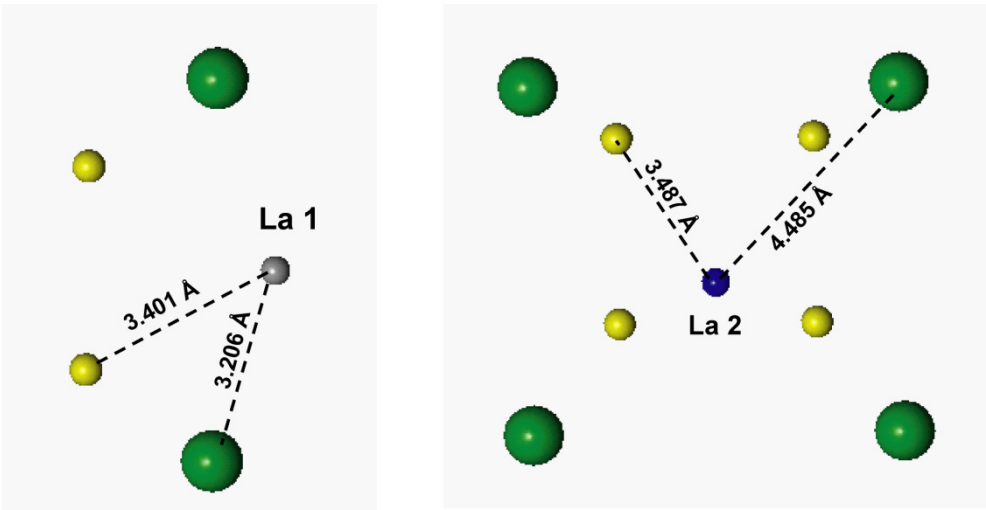

Figure 3.15. La-1 and La-2 crystallographic environments. Green spheres represent Fe-2, which may be replaced by Li or a vacancy; yellow spheres represent Li; the grey sphere represents La-1 (Left); and the blue sphere represents La-2 (Right). Left: La-1, with a distance of 3.206 Å to Fe-2. Right: La-2. Images were created in XtalDraw.[28] Distances between La and Fe/Li have been included in each case within 5 Å.

3.4.3.4. Structural Analysis Based on NMR Spectral Results

This complex family of materials can be further examined by considering the different possible lithium environments present. Using the measured ^{139}La and ^{7}Li NMR spectra, along with crystallographic data, the Li sites found in the ^{7}Li spectra can be tentatively assigned with the following assumptions:

1. Li peaks will be more resolved and have a higher chemical shift if the respective Li site is close to iron.

2. Li peaks will have a chemical shift close to 0 ppm, if the respective Li is far from iron.

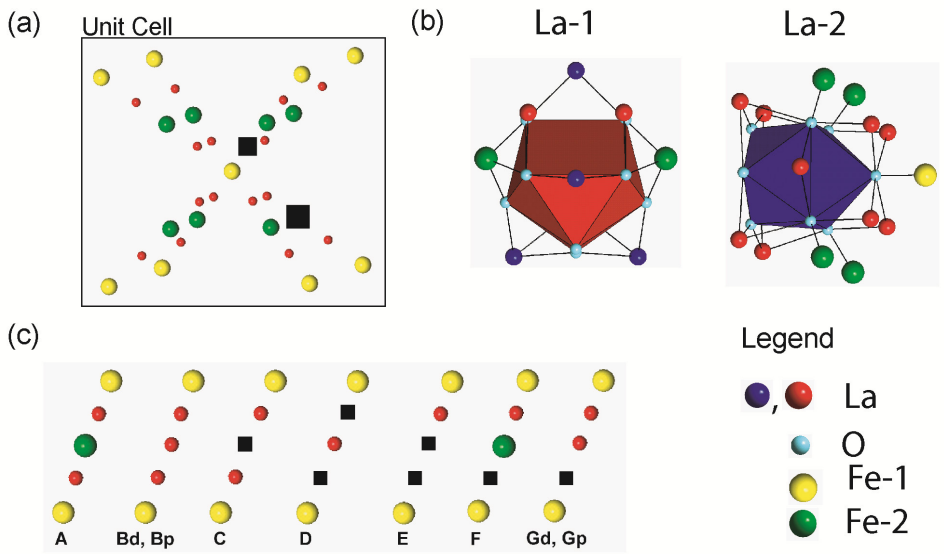

Figure 3.16. (a) $LaLi_{0.5}Fe_{0.2}O_{2.09}$ unit cell showing possible positions of vacancies. The positions of La-1 and La-2 are not shown here for clarity. Black squares represent potential vacancies in the cell. Small red spheres represent Li. (b) Polyhedra representing the La-1 and La-2 local environments in the crystal structure. (c) A through G represent the potential distributions of Li, iron and a vacant site showing half of the body diagonal of the unit cell in the Left of this figure. The legend presented can be applied to (a), (b) and (c). The full unit cell of this material is shown in ***Figure 3.9***, including the placement of the La atoms in the unit cell.

By considering the configurations in ***Figure 3.16*** it can be deduced that some configurations (B and G) contribute more than one Li environment and thus multiple peaks in the ^{7}Li NMR spectrum. By comparison, in configuration A, with no Li substituting Fe-2, the two Li atoms are chemically and magnetically equivalent and likely to have a strong paramagnetic character since the Li ions are surrounded by two Fe ions on each side. However in configuration B there are two 'types' of Li present: the Li atoms

close to the Fe-1 site (yellow spheres) will have a more paramagnetic nature due to their proximity to the iron, whereas the Li in the center of the configuration is farther from iron, and will have a more diamagnetic nature. Thus configuration B will contribute two peaks to the ^{7}Li NMR spectrum. With this consideration, the combination of all of these configurations in any compound will contribute nine peaks in the ^{7}Li NMR spectrum. This is consistent with what is seen in the ^{7}Li MAS NMR spectra, shown in ***Figure 3.10*** and ***Figure 3.11***, which show multiple lithium sites for each of the materials.When the ^{7}Li MAS NMR of these materials is considered, it is not immediately obvious that the distribution of the Li, iron and vacancy is changing throughout the materials. However, when the ^{7}Li MAS NMR spectra are combined with the ^{139}La NMR spectra, the change in the materials as their stoichiometric composition varies becomes evident. As the Li/Fe ratio increases in the samples, the diamagnetic peak in the ^{7}Li MAS NMR increases, this is possibly due to the filling of vacant sites in the (0.25, 0.25, 0.25) position. This site-filling has a dramatic effect on the EFG of La-1, and this is seen as a change in the ^{139}La NMR spectral line shape, where the central peak changes in appearance.

It should be noted here that the ^{7}Li MAS NMR spectral peak assignment is a complicated endeavor, and it is possible that there are more permutations of the atomic distribution than indicated here. The aim here is not to specifically assign the peaks in the NMR spectra, but to illustrate the complexity of this material, and understand how this atomic distribution relates to the ionic and electronic conductivity of the materials.

3.4.4. Electrochemical Cycling of $LaLi_{0.5}Fe_{0.2}O_{2.09}$

In order to determine the nature of the electrochemically active lithium in this material a coin cell was made with $LaLi_{0.5}Fe_{0.2}O_{2.09}$ as the cathode material. Electrochemical cycling was performed at a cycling rate of C/100. ***Figure 3.17*** shows the electrochemical curve, which began in the discharge phase and has a single plateau at ~ 3.2 V. Only ~ 30% of the lithium was extracted before the charging cycle began, leaving 70 % remaining. The red X in ***Figure 3.17*** shows where the cycling was stopped and the cathode was extracted.

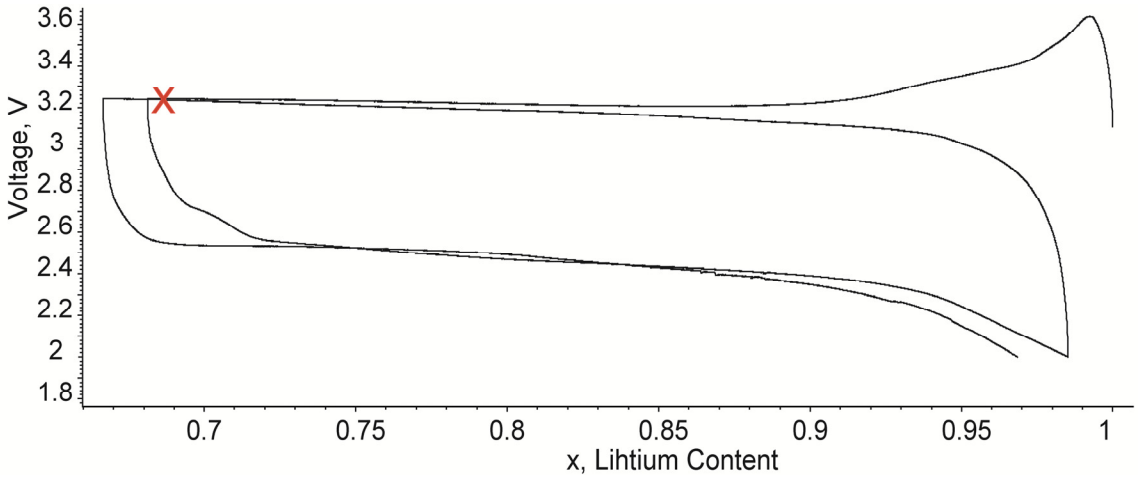

Figure 3.17. Electrochemical curve of $LaLi_{0.5}Fe_{0.2}O_{2.09}$. The curve shows a single plateau at ~3.2 V. The red X represents the point at which the cell was stopped and the cathode extracted.

^{7}Li MAS NMR spectra were obtained before electrochemical cycling, and then after the cycling process. The sample was washed with propylene carbonate to remove any excess electrolyte. ***Figure 3.18*** shows the resulting ^{7}Li MAS NMR. The pristine material clearly shows a combination of diamagnetic and paramagnetic resonances, while the cycled sample only contains a diamagnetic region. This indicates that the electrochemical

cycling has removed the paramagnetic lithium centres, suggesting that the paramagnetic lithium ions take part in the electrochemical process, while the diamagnetic lithium ions do not.

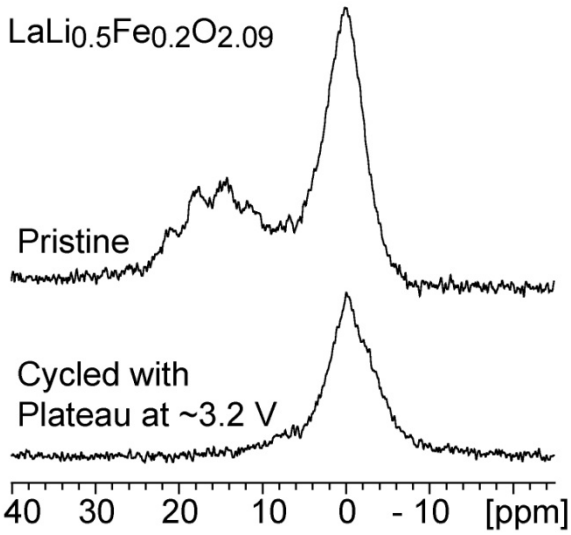

Figure 3.18. ^{7}Li MAS NMR of pristine and cycled $LaLi_{0.5}Fe_{0.2}O_{2.09}$. The cycled sample does not show the collection of paramagnetic resonances that are present in the pristine material, indicating that these resonances take part in the electrochemical cycling process.

The fact that only 30% of the lithium in this material takes part in the electrochemical process indicates that this material is not an efficient battery material, since majority of the lithium is not active. In addition, the high content of heavy lanthanum means that the material has a low gravimetric energy density. Moreover, the theoretical capacity (calculated from the number of active redox centres) of this material was found to be a mere 16 mAh/g, while a more competitive material, $LiFePO_4$ has a theoretical capacity of 170 mAh/g.

Although this material displays intricate structural behaviour that is heavily dependent on stoichiometry, further work to assess its use as a battery material was not pursued due to the poor theoretical capacity and cycling capabilities.

3.5. Conclusion

This work has compared the ^{139}La static solid-state NMR spectra of the model materials La_2O_3, $La(OH)_3$, $LaNbO_4$, $LaAlO_3$, $Li_7La_3Zr_2O_{12}$, and La_3NbO_7 to the spectra of potential lithium ion battery materials $Li_{3x}La_{(2/3)-x}TiO_3$ and $LaLi_{0.5}Fe_{0.2}O_{2.09}$. The model materials have provided a collection of typical ^{139}La NMR line shapes as well as a range of quadrupolar parameters in order to understand what is generally expected of the ^{139}La NMR of lanthanum-containing oxides.

The $LaLi_{0.5}Fe_{0.2}O_{2.09}$ family of compounds has been studied using ^{7}Li MAS and ^{139}La static solid-state NMR. The model materials represent structures in which the ^{139}La environments are well-defined and are not in close proximity to atomic-level disorder. In contrast, $Li_{3x}La_{(2/3)-x}TiO_3$ and $LaLi_{0.5}Fe_{0.2}O_{2.09}$ each show instances of atomic-level disorder, which can be detected by ^{139}La NMR. Theoretical calculations performed in CASTEP were supportive of results obtained through experiments simulations. This information can be used to indicate the presence of disorder in the second coordination sphere around a specific lanthanum site, which manifests itself as a distribution of experimental values of C_Q and η for a lanthanum site in close proximity to a source of disorder.

^{7}Li MAS NMR is very sensitive to Li environments, and can be used to distinguish between very different Li environments, and the combination of ^{7}Li MAS NMR and ^{139}La

NMR is a powerful tool for evaluating such complex structures. It has been shown that the combination of these two very different NMR techniques is useful for the structural evaluation of complex materials such as the $LaLi_{0.5}Fe_{0.2}O_{2.09}$ family of materials. These materials consist of a collection of Li sites, which form as a result of Li and Fe switching positions within the crystal structure. The ^{7}Li NMR spectral analysis is the first indication of this behaviour, and it supported by ^{139}La NMR spectroscopy and PXRD. Knowing the structure of these compounds is the first step to uncovering the mechanism of Li ion dynamics in these materials and understanding the process of Li migration through vacancy-mediated conductivity.

Electrochemical cycling has shown that the paramagnetic lithium ions take part in the electrochemical process, while the diamagnetic lithium ions remain unchanged. Although there is potential to use this material as a cathode for lithium ion batteries, poor theoretical capacity prevents this material from being competitive in the field.

3.6. References

1. O'Callaghan, M. P.; Powell, A. S.; Titman, J. J.; Chen, G. Z.; Cussen, E. J., Switching on fast lithium ion conductivity in garnets: The structure and transport properties of $Li_{3+x}Nd_3Te_{2-x}Sb_xO_{12}$. *Chemistry of Materials* **2008,** 20, (6), 2360-2369.

2. van Wullen, L.; Echelmeyer, T.; Meyer, H. W.; Wilmer, D., The mechanism of Li-ion transport in the garnet $Li_5La_3Nb_2O_{12}$. *Physical Chemistry Chemical Physics* **2007,** 9, (25), 3298-3303.

3. Lee, Y. J.; Wang, F.; Grey, C. P., Li-6 and Li-7 MAS NMR studies of lithium manganate cathode materials. *Journal of the American Chemical Society* **1998,** 120, (48), 12601-12613.

4. Cahill, L. S.; Chapman, R. P.; Britten, J. F.; Goward, G. R., Li-7 NMR and two-dimensional exchange study of lithium dynamics in monoclinic $Li_3V_2(PO_4)_3$. *Journal of Physical Chemistry B* **2006,** 110, (14), 7171-7177.

5. Davis, L. J. M.; Heinmaa, I.; Goward, G. R., Study of Lithium Dynamics in Monoclinic $Li_3Fe_2(PO_4)_3$ using Li-6 VT and 2D Exchange MAS NMR Spectroscopy. *Chemistry of Materials* **2010,** 22, (3), 769-775.

6. Cahill, L. S.; Chapman, R. P.; Kirby, C. W.; Goward, G. R., The challenge of paramagnetism in two-dimensional Li-6,Li-7 exchange NMR. *Applied Magnetic Resonance* **2007,** 32, (4), 565-581.

7. Cussen, E. J., The structure of lithium garnets: cation disorder and clustering in a new family of fast Li^+ conductors. *Chemical Communications* **2006**, (4), 412-413.

8. Thangadurai, V.; Weppner, W., $Li_6ALa_2Ta_2O_{12}$ (A=Sr, Ba): Novel garnet-like oxides for fast lithium ion conduction. *Advanced Functional Materials* **2005,** 15, (1), 107-112.

9. Bastow, T. J.; Mathews, T.; Sellar, J. R., Ga-69,Ga-71 and La-139 NMR characterisation of $LaGaO_3$ and $La_{1-x}Sr_xGa_{1-x}Mg_xO_{3-x}$. *Solid State Ionics* **2004,** 175, (1-4), 129-133.

10. Bastow, T. J., La-139 Nuclear-Magnetic-Resonance Characterization of La2o3 and $La_{1-x}Sr_xMO_3$ Where M=Cr, Mn or Co. *Solid State Nuclear Magnetic Resonance* **1994,** 3, (1), 17-22.

11. Abbattista, F.; Mazza, D.; Vallino, M.; Gazzano, M., A New Structure in the La-Li-Fe-O System. *Journal of the Less-Common Metals* **1988,** 144, (2), 311-319.

12. Mazza, D.; Abbatista, F.; Vallino, M.; Ivaldi, G., Structure of a New Cubic Phase in the La-Li-Me-O System. *Journal of the Less-Common Metals* **1985,** 106, (2), 277-285.

13. Hyooma, H.; Hayashi, K., Crystal-Structures of La3li5nb2o12, La3li5ta2o12. *Materials Research Bulletin* **1988,** 23, (10), 1399-1407.

14. Ohzuku, T.; Ariyoshi, K.; Takeda, S.; Sakai, Y., Synthesis and characterization of 5 V insertion material of $Li[Fe_yMn_{2-y}]O_4$ for lithium-ion batteries. *Electrochimica Acta* **2001,** 46, (15), 2327-2336.

15. Thangadurai, V.; Schwenzel, J.; Weppner, W., Tailoring ceramics for specific applications: A case study of the development of all-solid-state lithium batteries. *Ionics* **2005,** 11, (1-2), 11-23.

16. Chen, J.; Wang, S.; Whittingham, M. S., Hydrothermal synthesis of cathode materials. *Journal of Power Sources* **2007,** 174, (2), 442-448.

17. Lo, A. Y. H.; Sudarsan, V.; Sivakumar, S.; van Veggel, F.; Schurko, R. W., Multinuclear solid-state NMR spectroscopy of doped lanthanum fluoride nanoparticles. *Journal of the American Chemical Society* **2007,** 129, (15), 4687-4700.

18. Ishida, K.; Nakai, Y.; Kitagawa, S.; Kamihara, Y.; Hirano, M.; Hosono, H., As-75 and La-139 NMR studies on $LaFeAs(O_{1-x}F_x)$. *Physica B-Condensed Matter* **2009,** 404, (19), 3089-3094.

19. Nakai, Y.; Ishida, K.; Kamihara, Y.; Hirano, M.; Hosono, H., Spin dynamics in iron-based layered superconductor $(La_{0.87}Ca_{0.13})FePO$ revealed by P-31 and La-139 NMR studies. *Physical Review Letters* **2008,** 101, (7), 077006-1 - 077006-4.

20. Herreros, B.; Man, P. P.; Manoli, J. M.; Fraissard, J., Solid-State La-139 Nmr Investigation of Lanthanum-Exchanged Y-Zeolites. *Journal of the Chemical Society-Chemical Communications* **1992**, (6), 464-466.

21. Vullum, F.; Nitsche, F.; Selbach, S. M.; Grande, T., Solid solubility and phase transitions in the system $LaNb_{1-x}Ta_xO_4$. *Journal of Solid State Chemistry* **2008,** 181, (10), 2580-2585.

22. Marsella, L.; Fiorentini, V., Structure and stability of rare-earth and transition-metal oxides. *Physical Review B* **2004,** 69, (17), 172103-1 - 172103-4.

23. Ibarra, J.; Varez, A.; Leon, C.; Santamaria, J.; Torres-Martinez, L. M.; Sanz, J., Influence of composition on the structure and conductivity of the fast ionic conductors $La_{2/3-x}Li_{3x}TiO_3$ (0.03 <= x <= 0.167). *Solid State Ionics* **2000,** 134, (3-4), 219-228.

24. Djerdj, I.; Garnweitner, G.; Su, D. S.; Niederberger, M., Morphology-controlled nonaqueous synthesis of anisotropic lanthanum hydroxide nanoparticles. *Journal of Solid State Chemistry* **2007,** 180, (7), 2154-2165.

25. Kojima, T.; Nomura, K.; Miyazaki, Y.; Tanimoto, K., Synthesis of various $LaMO_3$ perovskites in molten carbonates. *Journal of the American Ceramic Society* **2006,** 89, (12), 3610-3616.

26. Awaka, J.; Kijima, N.; Hayakawa, H.; Akimoto, J., Synthesis and structure analysis of tetragonal $Li_7La_3Zr_2O_{12}$ with the garnet-related type structure. *Journal of Solid State Chemistry* **2009,** 182, (8), 2046-2052.

27. Kahnharari, A.; Mazerolles, L.; Michel, D.; Robert, F., Structural Description of La3nbo7. *Journal of Solid State Chemistry* **1995,** 116, (1), 103-106.

28. B. Downs, K. B., Kausil Simmaswamy *XtalDraw*, 2003.

29. Fleming, P.; Farrell, R. A.; Holmes, J. D.; Morris, M. A., The Rapid Formation of $La(OH)_3$ from La_2O_3 Powders on Exposure to Water Vapor. *Journal of the American Ceramic Society* **2010,** 93, (4), 1187-1194.

30. Lapina, O. B.; Khabibulin, D. F.; Romanenko, K. V.; Gan, Z. H.; Zuev, M. G.; Krasil'nikov, V. N.; Fedorov, V. E., Nb-93 NMR chemical shift scale for niobia systems. *Solid State Nuclear Magnetic Resonance* **2005,** 28, (2-4), 204-224.

31. Inaguma, Y.; Chen, L. Q.; Itoh, M.; Nakamura, T.; Uchida, T.; Ikuta, H.; Wakihara, M., High Ionic-Conductivity in Lithium Lanthanum Titanate. *Solid State Communications* **1993,** 86, (10), 689-693.

32. Eichele, K., Wasylishen, R. E., WSolids1. *WSolids1, Dalhousie University and University of Tuebingen* **2010**.

33. Massiot, D.; Fayon, F.; Capron, M.; King, I.; Le Calve, S.; Alonso, B.; Durand, J. O.; Bujoli, B.; Gan, Z. H.; Hoatson, G., Modelling one- and two-dimensional solid-state NMR spectra. *Magnetic Resonance in Chemistry* **2002,** 40, (1), 70-76.

34. Kemp, T. F.; Smith, M. E., QuadFit-A new cross-platform computer program for simulation of NMR line shapes from solids with distributions of interaction parameters. *Solid State Nuclear Magnetic Resonance* **2009,** 35, (4), 243-252.

35. Clark, S. J.; Segall, M. D.; Pickard, C. J.; Hasnip, P. J.; Probert, M. J.; Refson, K.; Payne, M. C., First principles methods using CASTEP. *Zeitschrift Fur Kristallographie* **2005,** 220, (5-6), 567-570.

36. Profeta, M.; Mauri, F.; Pickard, C. J., Accurate first principles prediction of O-17 NMR parameters in SiO_2: Assignment of the zeolite ferrierite spectrum. *Journal of the American Chemical Society* **2003,** 125, (2), 541-548.

37. Pickard, C. J.; Mauri, F., All-electron magnetic response with pseudopotentials: NMR chemical shifts. *Physical Review B* **2001,** 63, (24), 245101-1 - 245101-13.

38. Yates, J. R.; Pickard, C. J.; Mauri, F., Calculation of NMR chemical shifts for extended systems using ultrasoft pseudopotentials. *Physical Review B* **2007,** 76, (2), 024401-1 - 0224401-11.

39. Perdew, J. P.; Burke, K.; Ernzerhof, M., Generalized gradient approximation made simple. *Physical Review Letters* **1996,** 77, (18), 3865-3868.

40. Perdew, J. P.; Burke, K.; Ernzerhof, M., Comment on "Generalized gradient approximation made simple" - Reply. *Physical Review Letters* **1998,** 80, (4), 891-891.

41. Yates, J. R.; Pickard, C. J.; Payne, M. C.; Mauri, F., Relativistic nuclear magnetic resonance chemical shifts of heavy nuclei with pseudopotentials and the zeroth-order regular approximation. *Journal of Chemical Physics* **2003,** 118, (13), 5746-5753.

42. Massiot, D.; Farnan, I.; Gautier, N.; Trumeau, D.; Trokiner, A.; Coutures, J. P., Ga-71 and Ga-69 Nuclear-Magnetic-Resonance Study of Beta-Ga_2O_3 - Resolution of 4-Fold and 6-Fold Coordinated Ga Sites in Static Conditions. *Solid State Nuclear Magnetic Resonance* **1995,** 4, (4), 241-248.

43. Medek, A.; Frydman, V.; Frydman, L., Central transition nuclear magnetic resonance in the presence of large quadrupole couplings: Cobalt-59 nuclear magnetic resonance of cobaltophthalocyanines. *Journal of Physical Chemistry A* **1999,** 103, (25), 4830-4835.

44. Bhattacharyya, R.; Frydman, L., Quadrupolar nuclear magnetic resonance spectroscopy in solids using frequency-swept echoing pulses. *Journal of Chemical Physics* **2007,** 127, (19), 194503-1 - 194503-8.

45. O'Dell, L. A.; Schurko, R. W., QCPMG using adiabatic pulses for faster acquisition of ultra-wideline NMR spectra. *Chemical Physics Letters* **2008,** 464, (1-3), 97-102.

46. Hamaed, H.; Lo, A. Y. H.; Lee, D. S.; Evans, W. J.; Schurko, R. W., Solid-state La-139 and N-15 NMR spectroscopy of lanthanum-containing metallocenes. *Journal of the American Chemical Society* **2006,** 128, (39), 12638-12639.

47. Hamaed, H.; Ye, E.; Udachin, K.; Schurko, R. W., Solid-State Ba-137 NMR Spectroscopy: An Experimental and Theoretical Investigation of Ba-137 Electric Field Gradient Tensors and Their Relation to Structure and Symmetry. *Journal of Physical Chemistry B* **2010,** 114, (18), 6014-6022.

48. Ooms, K. J.; Feindel, K. W.; Willans, M. J.; Wasylishen, R. E.; Hanna, J. V.; Pike, K. J.; Smith, M. E., Multiple-magnetic field La-139 NMR and density functional theory investigation of the solid lanthanum(III) halides. *Solid State Nuclear Magnetic Resonance* **2005,** 28, (2-4), 125-134.

49. Mann, P. P., *Encyclopedia of Analytical Chemistry* **2000**, 12224-12265.

50. Kentgens, A. P. M., A practical guide to solid-state NMR of half-integer quadrupolar nuclei with some applications to disordered systems. *Geoderma* **1997,** 80, (3-4), 271-306.

51. Thangadurai, V.; Shukla, A. K.; Gopalakrishnan, J.; Joubert, O.; Brohan, L.; Tournoux, M., X-ray powder diffraction study of $LiLnTiO_4$ (Ln = La, Nd): a lithium-ion conductor. In *European Powder Diffraction, Pts 1 and 2*, Delhez, R.; Mittemeijer, E. J., Eds. 2000; Vol. 321-3, pp 965-970.

52. Alonso, J. A.; Ibarra, J.; Paris, M. A.; Sanz, J.; Santamaria, J.; Leon, C.; Varez, A.; Fernandez, M. T., Relationship between crystal structure and Li+-conductivity in $La_{0.5}Li_{0.5}TiO_3$ perovskite. In *New Materials for Batteries and Fuel Cells*, Doughty, D. H.; Nazar, L. F.; Arakawa, M.; Brack, H. P.; Naoi, K., Eds. 2000; Vol. 575, pp 337-342.

53. Larson, A. C.; Dreele, R. B. V., General Structure Analysis System (GSAS). *Los Almos National Laboratory Report LAUR 86-748* **1994**.

54. Masaki, N.; Doi, K.; Nasu, S.; Tanifuji, T.; Uchida, K., X-Ray Study of the Coexistence of Rhombohedral and Cubic Li_2O. *Journal of Nuclear Materials* **1979,** 84, (1-2), 341-342.

55. Duer, M. J., *Introduction to Solid-State NMR Spectroscopy.* Blackwell Science, Oxford, UK: 2004; p 349.

56. Grey, C. P.; Lee, Y. J., Lithium MAS NMR studies of cathode materials for lithium-ion batteries. *Solid State Sciences* **2003,** 5, (6), 883-894.

57. Ashbrook, S. E.; Whittle, K. R.; Lumpkin, G. R.; Farnan, I., Y-89 magic-angle spinning NMR of $Y_2Ti_{2-x}Sn_xO_7$ pyrochlores. *Journal of Physical Chemistry B* **2006,** 110, (21), 10358-10364.

58. Spencer, L.; Coomes, E.; Ye, E.; Terskikh, V.; Ramzy, A.; Thangadurai, V.; Goward, G. R., Structural Analysis of Lanthanum-Containing Battery Materials Using ^{139}La Solid-State NMR. *Canadian Journal of Chemistry* **2011**.

Chapter 4: Dynamics of Ag^+ Ions in $RbAg_4I_5$ Probed Indirectly Via ^{87}Rb Solid-State NMR Spectroscopy

4.1. Introduction

This chapter discusses the use of solid-state NMR spectroscopy to measure ionic hopping rates and activation energy in α-$RbAg_4I_5$, a material known to have very high Ag^+ ion conductivity, 0.21 ± 0.06 S/cm.[1, 2] Materials such as α-AgI and α-$RbAg_4I_5$ exhibit high ionic conductivity in part due to extensive disorder that exists within these structures due to partial Ag^+ ion occupancy. Both of these materials contain Ag^+ ions which are distributed over a large number of crystallographic sites. Iodine and rubidium ions create a stable lattice while low activation energy for Ag^+ ion hopping allows the ions to hop between sites easily.[1]

This work was adapted with permission from T. L. Spencer, L. A. O'Dell, I. Moudrakovski, and G. R. Goward, *The Journal of Physical Chemistry C*. Copyright 2013 American Chemical Society. All materials were synthesized at McMaster. ^{87}Rb NMR spectra were collected that the National Ultra-high Field Facility for Solids at the National Research Council in Ottawa and experiments were performed by Dr. Luke O'Dell. ^{109}Ag NMR was also collected at this facility under the supervision of Dr. Igor Moudrakovski. All NMR spectra were processed at McMaster University under the supervision of Prof. Gillian Goward. Initial drafts of the manuscripts were written by the current author, T. L. Spencer.

Understanding the modes of ion motion in fast ion conductors is essential in optimizing the structure and conductivity of solid-state electrolyte materials.[3] Solid-state NMR spectroscopy can be used to observe mobile ions (directly or indirectly), allowing the determination of migration pathways and activation energies of ion hopping between crystallographic sites.[4-6] Diamagnetic electrolyte materials pose a unique set of challenges.[7] Long T_1 relaxation rates and poor site resolution of the mobile species in this class of materials are common factors, and make the observation of the conducting sites challenging, and creative methods must be used to tackle the mechanism of dynamics at the atomic level.[8, 9]

Here, we discuss the use of stationary quadrupolar nuclei with large quadrupolar moments. These are found in the frameworks of solid-state electrolyte structures, and are used to investigate the mobility of conducting ions. Since many of the relevant electrolyte materials contain quadrupolar nuclei in the framework of their crystal structures, we will use the study of Ag^+ ion motion in model material α-$RbAg_4I_5$ to demonstrate that this is an effective way to study the challenging mobile species in solid-state electrolyte systems. This study takes advantage of the NMR powder pattern of large quadrupolar nuclei and their sensitivity to changes in their surrounding environments.[10, 11] Here, ^{87}Rb NMR spectral lineshape changes induced by mobile Ag^+ ions in close proximity to the Rb environments have been used to determine rates of ion hopping as a function of temperature providing an activation energy of Ag^+ ion hopping. In addition to NMR studies, differential scanning calorimetry (DSC) and powder X-ray diffraction (PXRD) have been used to assess the structural stability over the temperature range of NMR

experiments. These techniques have also provided supporting evidence for motional processes observed using NMR methods.

4.1.1. Model Material: α-$RbAg_4I_5$

α-$RbAg_4I_5$ is an Ag^+ conducting electrolyte. The α-phase is cubic with space group *P4₁32*. It contains three Ag crystallographic sites, two I sites and one Rb site.[2] Ionic motion in this phase is complex due to the level of partial occupancies which exist on every Ag site. This partial occupancy allows for ionic transport to take place by the defect mechanism. This material, like many other electrolyte materials, has a stationary framework of elements, which allows mobile Ag^+ to move throughout the structure.

Previous NMR studies of $RbAg_4I_5$ were performed mainly on single crystals, and showed that the material has a specific ionic conductivity of 0.21 ± 0.06 S/cm at room temperature, with an activation energy for ionic hopping of 12.5 ± 0.2 kJ/mol (0.13 eV ± 0.01 eV), within a temperature range of -65 to +57 ^oC.[2, 12-14] These NMR studies included the use of ^{109}Ag and ^{87}Rb solid-state NMR to study the ion mobility in single crystals of $RbAg_4I_5$. The values obtained from T_1 relaxation studies of ^{87}Rb and pulsed magnetic field gradient NMR studies of $^{109,107}Ag$ found the activation energy of Ag^+ ion hopping to agree with those derived from other techniques used.[13, 14] Much of the previous work done on this material has focused on phase changes which occur at lower temperatures, -65 and -97 ^oC, at which the β- and γ- phases form, respectively.[14]

The study of the mobile Ag^+ species in $RbAg_4I_5$ by solid-state NMR is challenging due to the low sensitivity of $^{107,109}Ag$, which comes from its small

gyromagnetic ratio and long T_1 relaxation.[15] ^{87}Rb is relatively facile to study by NMR in comparison to ^{109}Ag. Despite its quadrupolar nature, the higher gyromagnetic ratio of ^{87}Rb and greater sensitivity allows fast collection of NMR spectra. The present study shows that the stationary ^{87}Rb can be used to probe the ionic motion of Ag^+ in the structure. The long-term goal of this research is to extend this method to study lithium ion motion in solid-state lithium ion electrolytes.

Many solid-state electrolytes are synthesized, utilized, and studied as powders. The use of quadrupolar powder patterns of stationary framework elements to study ion dynamics promises to resolve some of the challenges faced in probing ion dynamics in these materials. Primarily, quadrupolar nuclei tend to have short T_1 relaxation times, making NMR experiments faster. In addition, this method allows the study of dynamics in materials in which mobile species exhibit multiple unresolved NMR sites, or materials in which ionic motion occurs through a single crystallographic site. The main goal of our work here is to evaluate the solid-state ^{87}Rb NMR of the powdered polycrystalline solid α-$RbAg_4I_5$, to indirectly probe the ionic hopping rates of Ag^+ ions as a function of temperature. This method takes advantage of the changes in the quadrupolar solid-state NMR powder pattern of the ^{87}Rb (I = 3/2) as a function of Ag^+ dynamics, and thus as a function of temperature. The computational modeling of the ^{87}Rb NMR powder lineshape was used to determine the rate of Ag^+ ion hopping at a series of temperatures in the range of 20 to 250 ^{o}C.

4.1.2. Solid-State ^{87}Rb NMR of α-$RbAg_4I_5$

^{87}Rb is a quadrupolar nucleus with spin, I=3/2. It has a natural abundance of 27.9% and an electric quadrupole moment of 133.5 mb (1mb = 10^{-31} m^2). Many researchers have taken advantage of this nucleus for NMR pulse sequence optimization and NMR technique development, particularly in simple rubidium materials, such as $RbClO_4$ and $RbNO_3$.[16-19] The large quadrupole moment of ^{87}Rb makes ^{87}Rb NMR sensitive to its surrounding environment. Thus, the effect that mobile Ag^+ ions may have on the electric field gradient (EFG) will affect the powder pattern ^{87}Rb NMR lineshape.[13]

The changes in the ^{87}Rb powder pattern were modeled using the EXPRESS I (Exchange Program for Relaxing Spin Systems)[20] software, after the initial lineshape fitting done in WSolids.[21] EXPRESS uses the stochastic Liouville equation for spin density to calculate the lineshapes of quadrupolar nuclei under an EFG tensor that is modulated due to local dynamics. This software has been used to simulate dynamics as Markovian jumps, primarily in rotational systems. These include systems such as the ^{2}H NMR of a rotating methyl group, double axis rotation in a urea inclusion compound, as well as ^{93}Nb undergoing jumps between three sites.[20] The EXPRESS software can simulate a variety of different NMR spectra, including static quadrupolar powder patterns. Other uses in the literature include the simulation of ^{14}N NMR spectra of motional imidazole groups.[11] Here, the EXPRESS software has been used to simulate the ^{87}Rb NMR lineshape for a situation in which Ag^+ ions are moving in close proximity to a

central Rb nucleus. This can be thought of as the Rb moving between different environments, determined by the position of the surrounding Ag^+ ions.

4.2. Experimental

4.2.1. Synthesis of α-$RbAg_4I_5$

α-$RbAg_4I_5$ powdered polycrystalline samples are synthesized by ball milling stoichiometric quantities of RbI (Strem Chemicals, 99 %) and AgI (Strem Chemicals, 99.9%-Ag) for more than 24 hours.[22] PXRD was used for phase confirmation, and Rietveld refinements were performed in GSAS.[23] PXRD was performed on a Bruker D8 powder X-ray diffractometer (Cu $K_{\alpha1}$, 40 kV, 40 mA). Variable temperature PXRD was also employed to monitor phase stability at higher temperatures. For these measurements, a small amount of $K_{\alpha2}$ radiation was collected in addition to the primary $K_{\alpha1}$ radiation. Both $K_{\alpha1}$ and $K_{\alpha2}$ radiation were considered in Rietveld refinements for variable temperature analysis.

4.2.2. ^{87}Rb and ^{109}Ag NMR Spectroscopy

^{87}Rb NMR experiments were performed on a Bruker Avance II 9.7 T wide-bore NMR spectrometer. A Bruker 5 mm static two-channel variable temperature probe was used to collect static powder patterns of ^{87}Rb (130.999 MHz at 9.4 T) in $RbAg_4I_5$ over the temperature range of 20 to 250 ^{o}C. Single pulse excitation was used with a central-transition selective 1μs pulse applied at an RF power of 100 kHz. The power was calibrated on a 1 M RbCl aqueous solution at 0.0 ppm, and for each temperature 2000 transients were collected, with a recycle delay of 1 s.

^{109}Ag NMR experiments were performed on a Bruker Avance I 11.7 T NMR spectrometer using a 4 mm MAS Chemagnetics probe. Static ^{109}Ag (23.274 MHz at 11.7 T) NMR spectra were collected over a temperature range of 18 to 170 ^{o}C. Magic angle spinning (MAS) spectra with a spinning frequency of 8.05 kHz, were also collected within this temperature range, and additionally at -60 ^{o}C. ^{109}Ag has a nuclear spin, I=1/2 and is notorious for having poor sensitivity due to its low Larmor frequency. ^{109}Ag is 48.2% naturally abundant, and is known to have a highly sensitive chemical shift. 1 M $AgNO_3$ was used as a shift reference at -11.2 ppm, with a small amount of relaxation agent, 0.24 M $Fe(NO_3)_3$.[15] For each MAS experiment, 8 transients were collected with a recycle delay of 500 s. For static experiments 48 transients were collected.

4.2.3. Computational Methods

Density functional theory (DFT) quantum chemical calculations of ^{87}Rb in α-$RbAg_4I_5$ were performed using CASTEP software.[24-26] The available crystallographic data from Hull *et al.* was used as a starting point for the calculations.[2] CASTEP carries out *ab initio* plane-wave density functional theory, DFT, calculations in the Accelrys Materials Studio 4.4 environment. Several unit cells were considered with varying Ag occupancy. Modifications were made to the unit cell in order to fulfill the requirements of CASTEP. These include the creation of a primitive super cell, in which there was no partial occupancy or net charge. The construction of these will be discussed in more detail in the discussion. The EFGShield software[27] was used to determine the Euler angles, using the EFG and CSA tensors for ^{87}Rb derived in the CASTEP calculations.

4.3. Results and Discussion

4.3.1. Structural Analysis

Powder X-ray diffraction was used to confirm that a single phase of α-$RbAg_4I_5$ was synthesized. ***Table 4.1*** contains the structural parameters obtained from the Rietveld refinement at room temperature for the α-$RbAg_4I_5$ powder phase, as well as the site occupancy at 180 °C for comparison. There was a minor impurity present, which can be seen at ~40 ^{o} in the PXRD (***Figure 4.1***). Variable temperature PXRD was also performed and confirmed that there was no phase change over the temperature range of 35 – 180 ^{o}C. Only a moderate unit cell expansion from 1406 Å^3 (35 ^{o}C) to 1422 Å^3 (180 ^{o}C) was observed, which was determined through Rietveld refinement with the GSAS software.[23] There were also negligible changes in the Ag site occupancy for all three crystallographic sites. ***Figure 4.1*** (Left) shows the initial X-ray data taken at 35 ^{o}C and 180 ^{o}C. The insert in ***Figure 4.1*** shows an expansion of a portion of the PXRD patterns from 22 to 28 ^{o} to illustrate the changes in the position of reflections as a result of cell expansion in this temperature range. PXRD patterns were collected for the temperatures 35, 100, 130, 140, 150, 160, and 170 ^{o}C and it was found that there was a linear change in the positions of the reflections (***Figure 4.1***), indicating that the cell expansion was uniform as well as very small over the observed temperature range and was not the result of a step-wise structural change affecting the cell size.

Table 4.1: Rietveld refinement of structural parameters for α-$RbAg_4I_5$ at ambient conditions.

Atom	*x*	*y*	*z*	Multiplicity	Occupancy 35 °C	Occupancy 180 °C
Rb	*0.375*	*0.375*	*0.375*	*4*	*1*	*1*
I-1	*0.0292(5)*	*0.0292(5)*	*0.0292(5)*	*8*	*1*	*1*
I-2	*0.125*	*0.180(5)*	*0.430(5)*	*12*	*1*	*1*
Ag-1	*0.530(3)*	*0.242(2)*	*0.813(9)*	*24*	*0.336(2)*	*0.330(5)*
Ag-2	*0.992(2)*	*0.850(6)*	*0.204(3)*	*24*	*0.250(2)*	*0.227(5)*
Ag-3	*0.288(9)*	*0.288(9)*	*0.288(9)*	*8*	*0.161(2)*	*0.150(5)*

Space group: $P4_132$; $a = b = c = 11.202(4)$ Å; $\alpha = \beta = \gamma = 90$ °

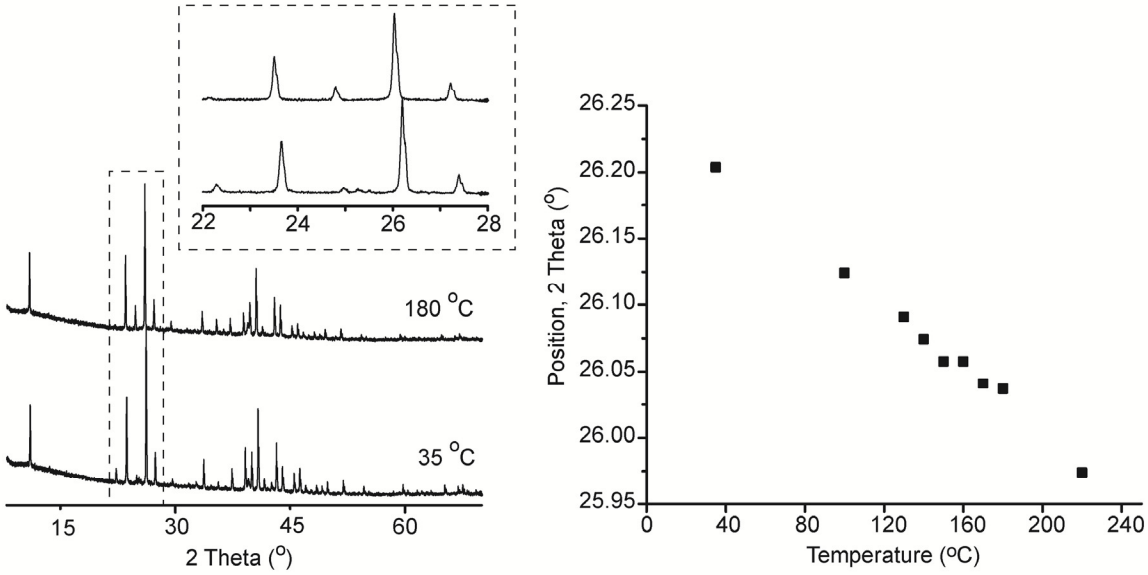

Figure 4.1. Left: Powder X-ray diffraction of α-$RbAg_4I_5$ acquired at 35 °C and at 180 °C. The inset shows that the reflections shift to lower 2° positions at the higher temperature implying an increase in the cell volume from 1406 to 1422 $Å^3$ from 35 to 180 °C, respectively. Right: Position of diffraction peak at ~ 26 ° as a function of temperature. The peak position shows a linear dependence with temperature.

This work, along with previous studies, has used Rietveld refinement to confirm that disordered partial occupancies exist on each of the Ag sites, as shown in ***Table 4.1***.[2] The dilute nature of the Ag^+ ions in this material means that only 16 of 56 potential sites

are occupied within a single unit cell. Ag-3 is particularly sparse, with this work showing 16 % occupancy in this study. Previous work, which included synthesis of a single crystal of α-$RbAg_4I_5$, showed as little as 5 % occupancy of Ag-3. This low occupancy (16 %) results in only one of sixteen Ag sites being occupied as Ag-3 site in a single unit cell. ***Figure 4.2*** shows the unit cell of $RbAg_4I_5$, taking into consideration the disordered partial occupancies in the material. Ag is primarily distributed between the Ag-1 and Ag-2 sites, with each having less than 40% occupancy.

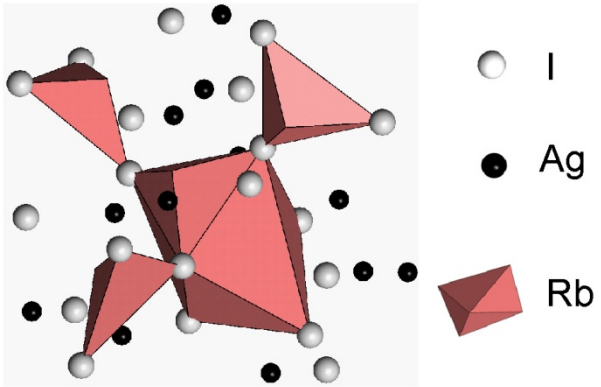

Figure 4.2. Unit cell of $RbAg_4I_5$, including partial occupancy on Ag-1 and Ag-2 sites, and excluding Ag-3, due to its low occupancy. Space group: $P4_132$; $a = b = c =$ 11.202(4) Å; $\alpha = \beta = \gamma = 90$ °

4.3.2. ^{109}Ag NMR Spectroscopy

Solid-state ^{109}Ag NMR of $RbAg_4I_5$ was performed at 11.7 T. A single resonance was observed, which had a chemical shift consistent with that found in the literature, 789 ± 2 ppm at room temperature.[28] ^{109}Ag was found to have a long T_1 relaxation, ~100 s, and therefore experiments were acquired for over 6 hours to average 48 transients. It should be noted that the long T_1 observed from this material is not indicative of poor ionic

mobility, but is likely due to a large difference between the correlation time of ion hopping at the T_1 relaxation time, such that the T_1 is not sensitive to changes in ion hopping rate.[29] In addition, many Ag^+ ion conductors have exhibited the CSA mechanism as the primary mode of relaxation for the mobile Ag^+ species.[15] Variable temperature ^{109}Ag NMR showed that even at -60 ^oC, the three Ag crystallographic sites are not resolvable. This is likely due to peak coalescence as a result of the high ionic conductivity even at this low temperature.

Figure 4.3 (a) shows the ^{109}Ag MAS NMR spectra of $RbAg_4I_5$ at 18 ^oC and -60 ^oC, with an MAS rate of 8.05 kHz. There is little difference in line width or chemical shift between these two spectra. Alternatively, ***Figure 4.3*** (b) shows the static NMR spectra collected between 130 and 170 ^oC, which show no line narrowing, but changes in the chemical shift at a rate of approximately -0.1 ppm/^oC. This is a less dramatic change than was observed by Looser *et al.* for α-$RbAg_4I$ at temperatures below 100 ^oC (-0.5 ppm/^oC).[28] The chemical shift changes here cannot be correlated to Ag^+ mobility with temperature, as the changes observed are likely due to variations in magnetic susceptibility and shielding, which may be in part due to the thermal expansion of the unit cell.[28, 30] Since the ^{109}Ag chemical shift changes observed are not indicative of ionic motion in $RbAg_4I_5$, ^{109}Ag NMR does not offer a straight forward method to assess Ag^+ mobility in this material.[14]

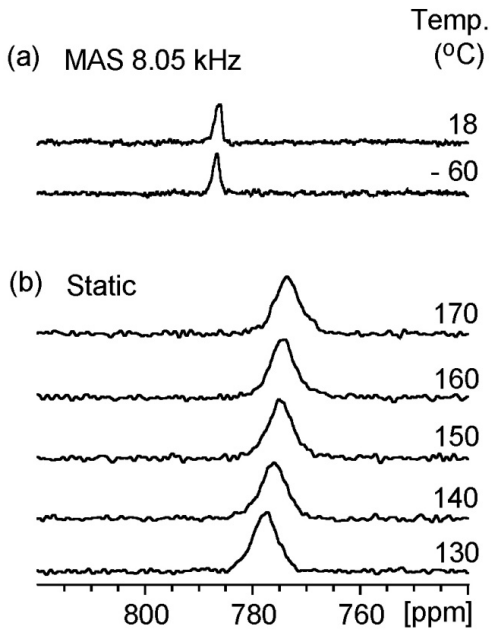

Figure 4.3. Variable temperature ^{109}Ag NMR spectra collected at 11.7 T with (a) MAS 8.05 kHz and (b) Static. Overall, the temperatures range from – 60 °C to 170 °C. Static measurements were not performed at low temperature.

4.3.3. ^{87}Rb NMR Spectroscopy

^{87}Rb is a high sensitivity isotope, commonly studied via solid-state NMR, which has been broadly considered as a "standard" isotope in the development of quadrupolar nuclei solid-state NMR strategies. Here, the properties that make ^{87}Rb an excellent isotope in NMR developments are shown to also make it a viable framework ion, whose solid-state NMR powder lineshape appears to be highly sensitive to changes in the local environment induced by passing Ag^+ ions. Previous studies of α-$RbAg_4I_5$ have included the analysis of changes in the T_1 of ^{87}Rb in single crystals as a function of temperature,[13,

[14] whereas here we have chosen to focus on the changes in the sensitive ^{87}Rb quadrupolar lineshape of the powdered material.

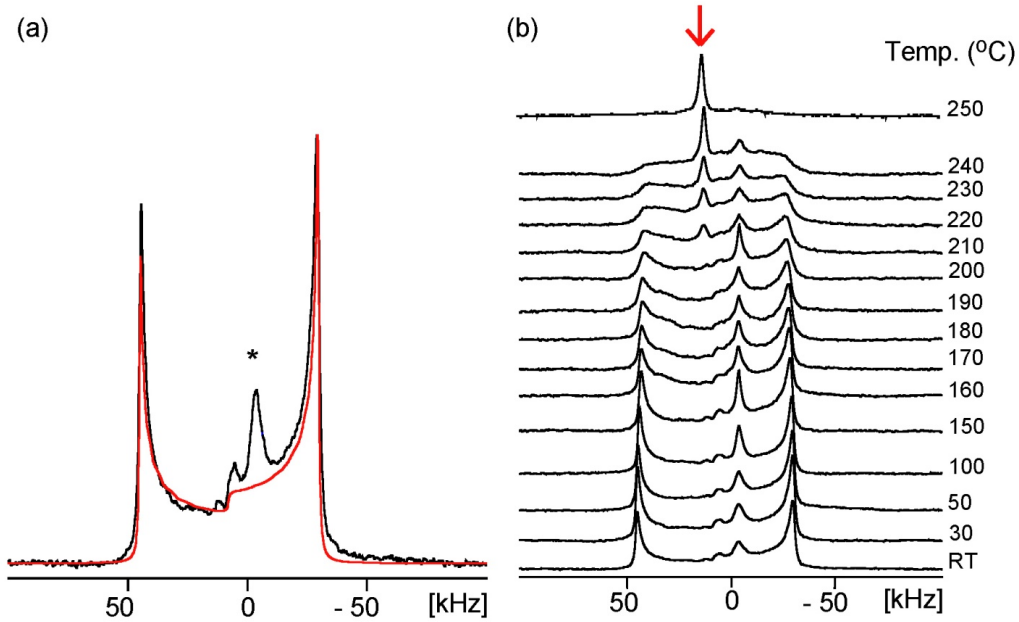

Figure 4.4. ^{87}Rb NMR spectra of $RbAg_4I_5$ at (a) Room temperature, the black line shows the experimental spectrum, and the red line is the simulated lineshape. Spectral simulations resulted in δ_{iso} = 125 ppm, anisotropy = -97 ppm, asymmetry = 0, η_Q = 0, C_Q = 8.25 MHz. * represents a minor impurity (< 10% in ^{87}Rb NMR). The arrow shows isotropic ^{87}Rb chemical shift observed as the sample melts. (b) Variable temperature NMR.

The use of ^{87}Rb as a framework nucleus to probe dynamics is a viable option because of the high content of framework Rb in the structure. Here, variable temperature ^{87}Rb NMR was performed from room temperature (20 °C) until the sample had melted completely, at 250 °C. ***Figure 4.4*** (a) shows the room temperature ^{87}Rb NMR spectrum with the spectral simulation performed in WSolids.[21] The lineshape was described by the following parameters using the Haeberlen convention[31]: δ_{iso} = 125 ppm, anisotropy (Δδ) =

-97 ppm, asymmetry (η_δ) = 0, C_Q = 8.25 MHz, η_Q = 0. ***Figure 4.4*** (b) shows the variable temperature ^{87}Rb NMR spectra from room temperature through the melt transition.

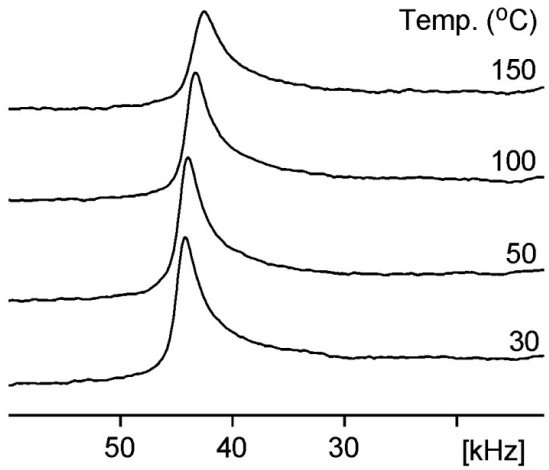

Figure 4.5. The trend of the high frequency discontinuity toward the center of the ^{87}Rb NMR spectrum of α-$RbAg_4I_5$ with increasing temperature as a result of an increase in dynamics of Ag^+ ions at elevated temperatures.

The variable temperature ^{87}Rb NMR shows that the melting begins to occur close to 200 °C, and the sample is fully molten at 250 °C. This is consistent with previous observations.[32] A closer look reveals that the ^{87}Rb NMR lineshape is changing with temperature. More specifically, as the temperature increases, the outer singularities begin to broaden, and decrease in intensity with respect to the center of the spectrum. In addition, there is a trend of the outer singularities to move towards the center of the spectrum. ***Figure 4.5*** shows an expanded portion of the spectrum focusing on the high frequency singularity. These effects do not result from decreasing of the quadrupolar coupling, but rather, they are attributed to an averaging that occurs because of the increasing motion of the Ag^+ ions.

4.3.4. Spectral Simulations in EXPRESS

The changing ^{87}Rb NMR lineshape can be simulated using the EXPRESSsoftware.[20] For accurate determination of Ag^+ ionic hopping rates, it is necessary to define all variables except the ionic hopping rate, such that only Ag^+ mobility is causing changes in the spectral simulation. Many of the necessary variables outlining the powder pattern were obtained from WSolids simulations, as seen in ***Figure 4.4***. However, the Euler angles, which define the relative orientations of the CSA and EFG tensors, can be very difficult to unambiguously establish using only spectral simulations. In addition, EXPRESS requires several sites, or frames, that define the motion in the system. In the case of $RbAg_4I_5$ four Rb sites were defined using different Euler angles, representing the four possible Rb environments with different configurations of Ag^+.

Table 4.2: CSA and EFG site angles used in EXPRESS simulations.

Site	**Site Angles for CSA**			**Site Angles for EFG**		
	α (°)	*β (°)*	*γ (°)*	*α (°)*	*β (°)*	*γ (°)*
1	3.098	10.004	71.743	0	0	0
2	168.998	10.613	124.308	214.552	74.565	177.025
3	141.777	2.555	236.378	205.092	76.856	171.293
4	231.36	11.21	62.39	314.13	80.80	180.56

Site 1: Mixture of Ag-1 and Ag-2; Site 2: Ag-2 only; Site 3: Ag-1 only; Site 4: Ag-1, Ag-2 and Ag-3.

$RbAg_4I_5$ contains three Ag sites, shown in ***Table 4.1***. Ag-1 and Ag-2 have relatively high occupancy, while Ag-3 is sparsely populated, with only 16% occupancy. Four Rb environments were simulated using a unit cell, which approximated the single Rb crystallographic site under four conditions: (1) when a combination of Ag-1 and Ag-2

were occupied; (2) Ag-2 was occupied alone; (3) when Ag-1 was occupied alone; (4) when Ag-1, Ag-2, and Ag-3 were occupied together. Each such combination has the same total amount of Ag present in the cell. DFT calculations performed in CASTEP[24] software were used in combination with EFGShield to calculate the Euler angles which relate EFG and CSA for an individual Rb environment in each Ag configuration associated with the four Rb environments. It should be noted that many combinations of Euler angles may create the same, or very similar, lineshapes, thus theoretical, *ab initio* calculations are necessary to make this important distinction. Knowing the Euler angles was necessary to uniquely describe each Rb environment.

Line shape simulations were performed in EXPRESS with zcw powder averaging using 20000 orientations. To specify the Euler angles relating EFG and CSA, the CSA site angles were set to those calculated in CASTEP and EFGShield; while the EFG site angles were adjusted to relate the principal axis system, PAS, of each of the Rb environments. These angles were calculated by relating the EFG tensor orientations between Rb environments, and allow the Euler angles calculated directly in CASTEP to belong to the same PAS. The relevant angles are summarized in ***Table 4.2***. Here we note that this system is quite different from those typically modeled in EXPRESS. One Rb environment is not mapped onto another by a simple rotation; rather there is an interchanging of the environments due to the jumping movement of Ag in the surroundings, making these four environments inequivalent and not spatial functions of each other. The Euler angles are used to distinguish between the different Rb environments created by the varying distribution of Ag in the system. All other spectral

parameters were held constant during simulations. ***Figure 4.6*** (a) shows an illustration of the four Rb environments with the different Ag populations, while (b) shows the tensor orientations used in the EXPRESS model. The model allows exchange between all four environments outlined in ***Figure 4.6***, including exchange from one environment to itself, i.e. there is exchange between Ag-1 and Ag-2, Ag-1 and Ag-1, as well as Ag-2 and Ag-2.

Several assumptions were made in order to simplify the EXPRESS simulations. Firstly, it was assumed that the values of C_Q and η did not change as a function of temperature. There have been some reported cases in the literature where C_Q has changed with temperature,[33] however it is unlikely that this is the case in this system between room temperature and 100 ºC. Secondly, it was assumed within the EXPRESS simulations that the values of C_Q and η did not vary between the different unit cell models which described the Rb environments based on the Ag occupancy. CASTEP calculations did, however, reveal small differences in C_Q and η through the different Rb environments. It was found that C_Q ranged from 8.2 to 8.7 MHz, while η ranged from 0.1 to 0.2. For the EXPRESS simulations the quadrupolar parameters that were found through the room temperature simulations in WSolids (η_Q = 0, C_Q = 8.25 MHz) were used to represent all of the exchanging sites in the material.

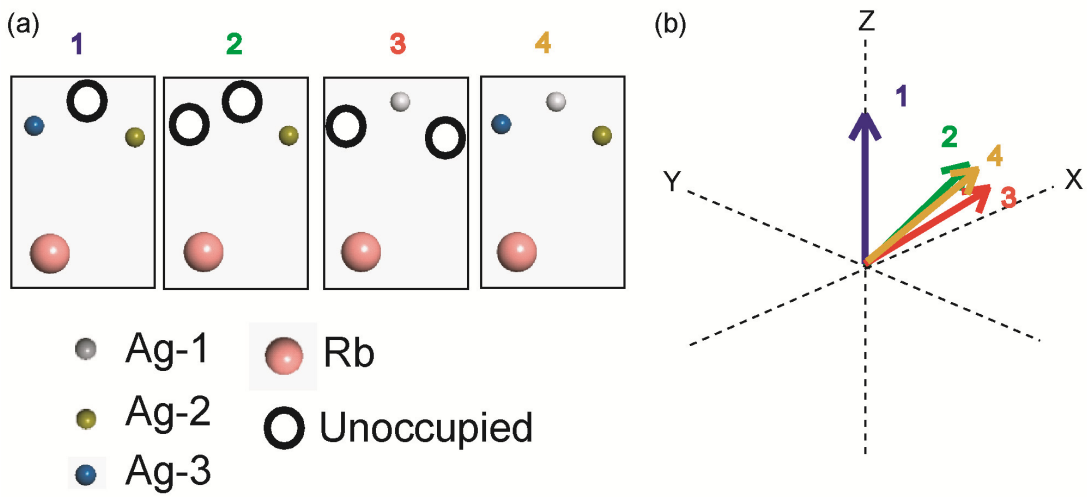

Figure 4.6. (a) Four possible Rb environments considering the occupation of (1) Ag-1 and Ag-2, (2) Ag-2 only, (3) Ag-1 only, and (4) Ag-1, Ag-2 and Ag-3 (b) Relative V_{zz} components of the EFG tensor orientations, 1- 4, obtained using CASTEP calculations for four Rb environments shown in (a).

Simulations in EXPRESS reveal an ionic hopping rate in the range of 7.0 ± 0.5 kHz to 30 ± 2 kHz from 20 to 150 °C, as shown in ***Figure 4.7***. We note that the sensitivity of the ^{87}Rb NMR lineshape to the ion dynamics is governed by the width of the spectrum, ~ 70 kHz. The measured rate of ionic hopping in α-$RbAg_4I_5$ is well within the range of hopping rates observed for other ionic conductors. In the solid-state lithium electrolyte $Li_7La_3Zr_2O_{12}$, Li^+ hopping rates are observed in the range of 1.9 x 10^2 - 4.9 x 10^5 kHz within the temperature window of 52 - 257 °C.[8] Cathode material Li_2VOPO_4 was found to have Li^+ hopping rates in the range of 0.055 - 1.100 kHz in the temperature window 31 to 54 °C.[5]

During the spectral simulation in EXPRESS, we effectively simulated the changing lineshapes up to 100 ^{o}C. The narrowing of the overall lineshape was taken to be the most significant fitting parameter when comparing to experimental NMR spectra. However, above 100 ^{o}C, the lineshapes could no longer be simulated using the current model. The changes in the experimental ^{87}Rb NMR lineshape increased dramatically above ~ 150 ^{o}C, showing a more significant decrease in the intensities of the outer singularities. This change is substantially different than the trends observed up to 100 ^{o}C. This means that careful consideration is necessary to determine at which temperatures the spectra can be effectively described by the Ag^{+} ion motion alone. Although the powder X-ray diffraction does not indicate a phase change at this temperature, there is a possibility that the proximity to the melting point may bring the onset of mobility in the framework elements as they gain kinetic energy, as a result of heating. To confirm that there may be some change that occurs at 150 ^{o}C, DSC, was performed over a temperature range of room temperature to 300 ^{o}C.

Figure 4.8 shows DCS data taken for $RbAg_4I_5$. The sample exhibits significant transitions at 150 ± 1 ^{o}C, 198 ± 1 ^{o}C and 236 ± 1 ^{o}C on heating. Melting occurs at 236 ± 1 ^{o}C, which is close to the temperature, 228 ^{o}C, observed in previous studies.[32] The other two transitions seen in the DCS data are not accounted for in detail in previous studies. From the ^{87}Rb NMR spectra, ***Figure 4.8***, it appears that the onset of melting occurs before the final melting transition at 236 ± 1 ^{o}C. A narrow peak in the ^{87}Rb NMR spectrum begins to appear at 98 ppm (13 kHz), which indicates the presence of the melted sample, and melting is complete by 250 ^{o}C. The onset of this melting occurs before the

final melt, and may account for the thermal transition seen in the DSC at 198 ^{o}C. Although the sample shows a sharp energy change at ~ 150 ^{o}C on cooling, ***Figure 4.8***, the same profile was observed in the DSC when the measurement was repeated on the same sample, using the identical procedure.

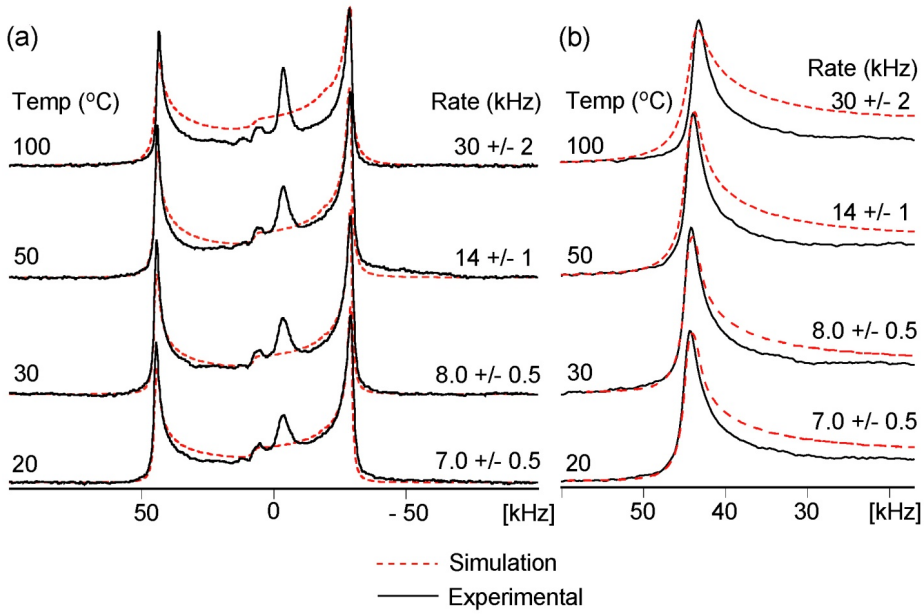

Figure 4.7. EXPRESS simulations of ^{87}Rb NMR spectra of $RbAg_4I_5$ up to 100 ^{o}C. Black, solid lines represent the experimental spectra, while red, dashed lines represent EXPRESS 1.0 simulations. (a) Shows the full spectral width, while (b) shows the high frequency singularity.

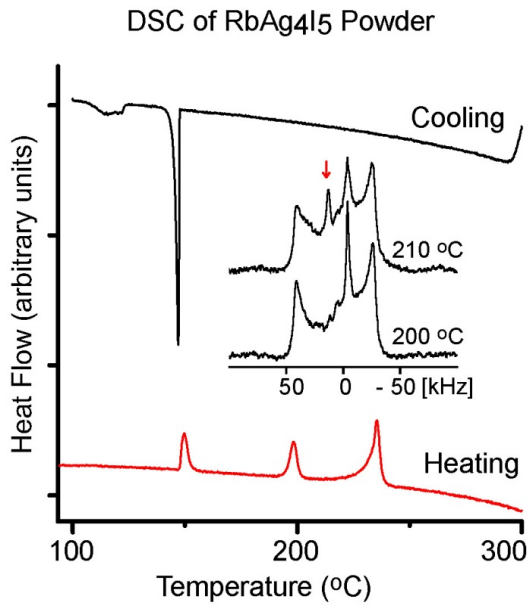

Figure 4.8. DSC data showing transitions occurring in α-$RbAg_4I_5$ between room temperature and 300 ^{o}C. Melting occurs at 236 ± 1 ^{o}C.[32] The upper black line represents the cooling of the sample, and has been offset for clarity, so that a direct comparison of heating and cooling could be made. The inset presents the ^{87}Rb NMR spectra showing onset of melting. The red arrow indicates the peak arising from the melted sample.

The transition seen in the DSC results, ***Figure 4.8***, at 150 ± 1 ^{o}C has been observed previously, but no physical description was made.[32] Interestingly, the ^{87}Rb NMR spectra also begin to exhibit more significant lineshape changes at and above 150 ^{o}C, as shown in ***Figure 4.4***. This observation, combined with the inability to simulate the lineshape using the model that describes Ag^{+} ion hopping alone, indicates that additional dynamic processes are occurring above this temperature. Such effects may include the onset of thermal vibration of lattice elements, Rb and I. The onset of additional dynamics appears to have a sharp initiation, particularly when the shifts of the outer singularities in the ^{87}Rb NMR spectra are considered. ***Figure 4.9*** shows the temperature-dependent

change in position of the low frequency singularity in the ^{87}Rb NMR. Here, a sharp transition can be seen around 150 ^{o}C which highlights the dramatic change in the lineshape of the ^{87}Rb NMR spectra, most likely due to averaging of the electric field gradient (EFG), occurring at this temperature. This sharp transition allows a clear distinction to be made between the temperature range under which the Ag^{+} ionic hopping governs the lineshape, and the temperature at which additional dynamic processes such as the vibrational motion of the lattice elements, Rb and I, contribute to the observed lineshape changes.

Both the DSC data and the ^{87}Rb NMR data point to a transition at 150 ^{o}C, after which a combination of Ag^{+} ion hopping and lattice vibration contribute to dynamics in the α-$RbAg_4I_5$. This transition was undetected by powder X-ray diffraction data, indicating that there is no phase change occurring at 150 ^{o}C. Nevertheless, these different dynamic contributions cannot be separated when they occur together. Thus, in order to assess the Ag^{+} ion motion in the material, only measurements from room temperature to 100 ^{o}C are considered. In this range, Ag^{+} ionic motion is the dominant source of the changes in the ^{87}Rb spectra of α-$RbAg_4I_5$.

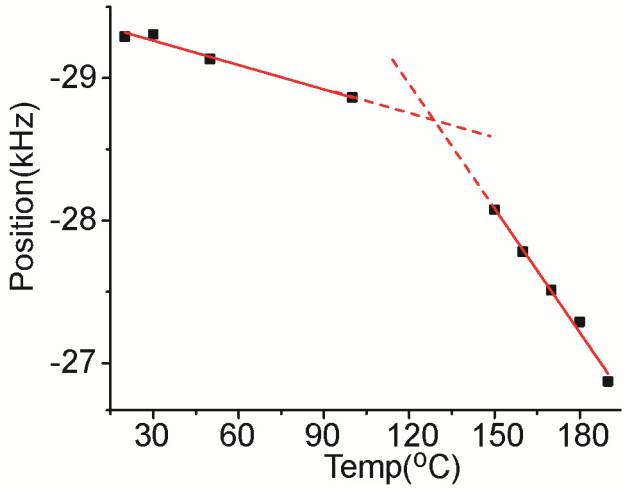

Figure 4.9. Change in the position of low-frequency singularity in the ^{87}Rb NMR spectra of α-$RbAg_4I_5$ as a function of temperature. An abrupt change in the trend can be seen around 150 °C.

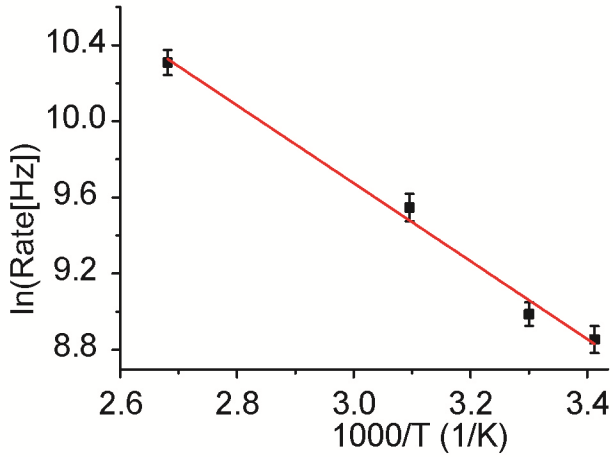

Figure 4.10. Arrhenius analysis of the ionic hopping rate of Ag^+ in polycrystalline powdered α-$RbAg_4I_5$. The slope of the line of best fit results in an activation energy of 17 ± 3 kJ/mol (0.18 ± 0.03 eV) for Ag^+ ion hopping.

Figure 4.10 shows an Arrhenius plot of ln(Rate [Hz]) vs. 1000/T, where the rate is derived from EXPRESS analysis of ^{87}Rb NMR spectra (***Figure 4.7***). From this plot the activation energy for Ag^+ ion hopping was found to be 17 ± 3 kJ/mol (0.18 ± 0.03 eV) for

hopping rates in the range of 7.0 ± 0.5 kHz to 30 ± 2 kHz, over a temperature window from room temperature to 100 ^{o}C. When compared to previously reported data for single crystals of α-$RbAg_4I_5$, the activation energy for Ag^+ ion hopping found here is slightly higher,: 17 ± 3 kJ/mol for the sample synthesized as a powder in this work vs. 12.5 ± 0.2 kJ/mol for the sample synthesized as a single crystal in previous studies.[2, 12, 14] This difference may be attributed to the slight difference in occupation of the Ag sites for materials obtained by different synthesis methods as indicated by PXRD anlaysis.[2] For comparison, a similar simulation was performed considering only sites Ag-1, and Ag-2 (sites 1, 2 and 3 in ***Figure 4.6***). This revealed an activation energy of 15 ± 3 kJ/mol, indicating that even though the content of Ag-3 in the system is small, its presence nevertheless contributes to the overall activation energy of Ag^+ motion.

The ability to extract activation energies as well as rates of ion hopping using the method described above implies the possibility of its extension to a broader range of systems for which single crystals are not available and the mobile species are otherwise challenging to study directly. These systems include solid-state electrolytes for lithium ion batteries. The mobile species in the lattice are Li^+ ions, which have notoriously long T_1 relaxation times.[8] Framework atoms in these systems include heavy nuclei, often with large quadrupole moments, such as ^{139}La, for which it is typical to observe broad quadrupolar NMR powder pattern. For electrochemically relevant oxides, the quadrupolar coupling (C_Q, ^{139}La) ranges from 20 – 60 MHz.[34, 35]

4.3.5. Variable Temperature ^{139}La NMR of $LaLi_{0.62}Fe_{0.17}O_{2.09}$

$LaLi_{0.62}Fe_{0.17}O_{2.09}$ is a potential cathode material for lithium ion batteries, as described in Chapter 3 of this thesis. The study of lithium ion dynamics in this material has been challenging due to the significant overlap of ^{7}Li spectral resonances. Therefore variable temperature ^{139}La NMR was performed at 21.1 T in order to assess the lithium ion mobility. ***Figure 4.11*** shows the ^{139}La NMR spectra between 20 and 200 ºC. The figure shows two distinct ^{139}La sites, which both shows temperature dependence. La-2 has a larger C_Q and a η of 0 and shows singularities at the high and low frequency ends of the lineshape, while La-1 has a smaller C_Q and a η of 0.6 (See Chapter 3 for a full discussion).

Figure 4.11 (a) (left) shows the full spectral line shape, and the right shows the low frequency portion of the La-2 resonance. It is clear that between 20 and 200 ºC the position of the singularity moves toward the center of the spectrum. ***Figure 4.11*** (b) shows the lineshape of La-1 alone, which also exhibits an overall narrowing with increasing temperature in combination with a broadening of the singularities.

The changes in the ^{139}La NMR line shapes with temperature indicate that the lanthanum in sensitive to the increase in lithium ion hopping rate with temperature. In order to assess the lithium ion hopping rate using the method described above (for $RbAg_4I_5$) CASTEP calculations must be used in combination with EFGShield to determine the relative Euler angles that relate the different lanthanum environments that accompany different lithium distributions that occur as a result of dynamics. This

complex structural modeling is not possible for this structure, since the unit cell is greater than 1825 Å, and too large for CASTEP calculations. In addition, the number of lithium environments makes creating a model very challenging. For this reason, simulating ion dynamics in EXPRESS software was not performed.

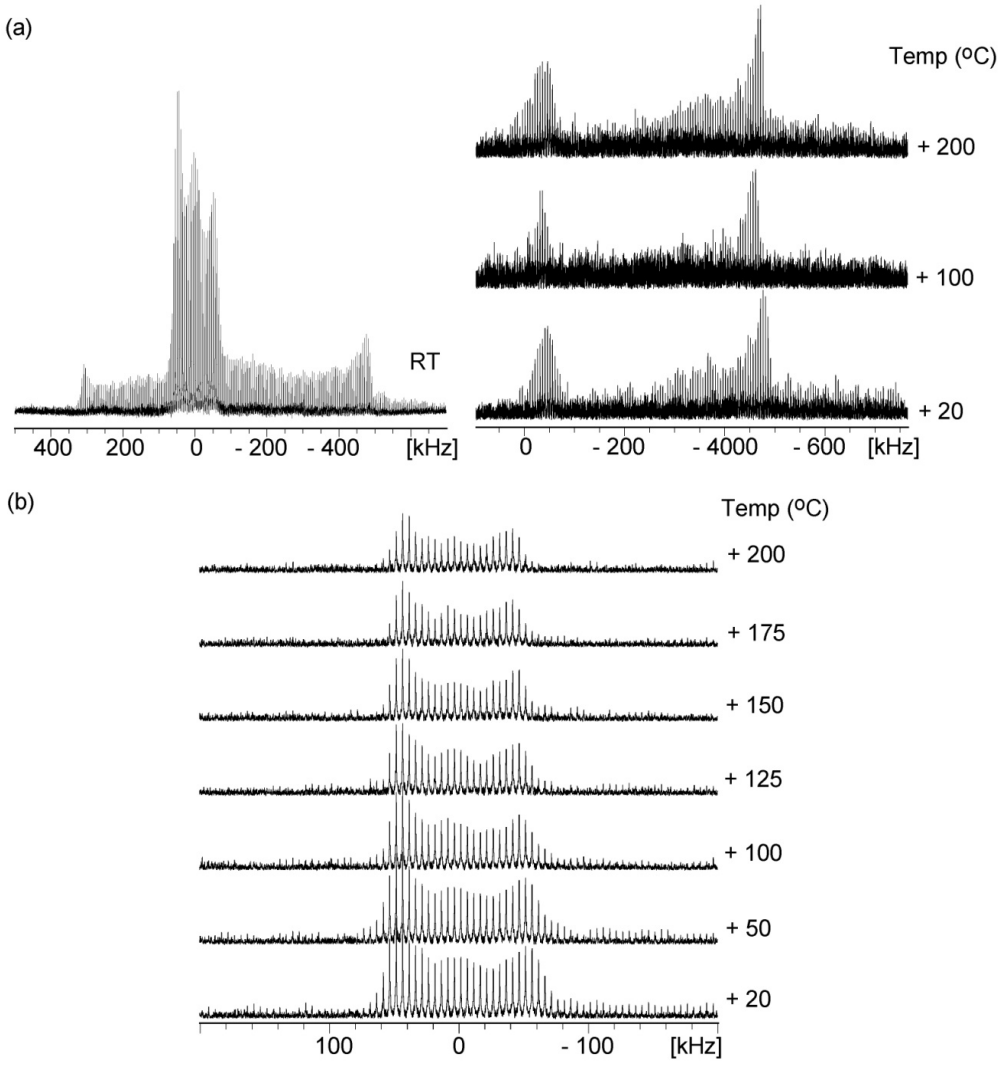

Figure 4.11. (a) ^{139}La NMR spectrum of $LaLi_{0.62}Fe_{0.17}O_{2.09}$ collected at 21.1 T with the La-1 and La-2 line shapes shown. The left shows that full spectrum, while the right shows the low-frequency singularity as a function of temperature. (b) The central line shape of La-1 as a function of temperature between 20 and 200 ºC.

The complexity of the $LaLi_{0.62}Fe_{0.17}O_{2.09}$ system brings to light the limitations of using this method to study ion dynamics in many of the intricate lithium ion battery materials. A small unit cell with well defined occupancy is needed. In addition, the NMR spectrum of the quadrupolar nucleus of interest must also be well defined.

4.4. Conclusion

We have demonstrated that solid-state NMR powder patterns obtained from stationary quadrupolar nuclei can be analyzed to provide an indirect experimental probe of the rates and mechanisms of ion transport. Specifically, we have shown that the rate of Ag^+ ion motion in α-$RbAg_4I_5$ can be determined effectively from the analysis of the ^{87}Rb NMR powder lineshape. This method allows the indirect determination of ionic hopping rates and activations energies for samples that are challenging to study when observing the mobile species directly. The EXPRESS software was utilized in order to include the effects of dynamics in lineshape simulations, resulting in a rate of Ag^+ ion hopping for each ^{87}Rb lineshape considered. With all other variables held constant, the changes in Ag^+ ion hopping rate over a temperature range of room temperature to 100 ^oC, and corresponding hopping rates from 7.0 ± 0.5 kHz to 30 ± 2 kHz, were used to calculate the activation energy of Ag^+ ion hopping, which was found to be 17 ± 3 kJ/mol. Although NMR experiments were performed for temperatures up to 250 ^oC, the Arrhenius analysis was only considered for a limited temperature range reaching 100 ^oC. Above this point there is a sharp onset of thermal vibration of lattice elements, Rb and I, which was identified through the significant change in the slope of the temperature dependant position of the high frequency singularity in the ^{87}Rb NMR powder spectra, as well as by

an accompanying thermal transition observed in the DSC data. In this high temperature range the lattice motion cannot be separated from the effects of Ag^+ ion motion in the ^{87}Rb NMR analysis.

4.5. References

1. Bruce, P. G., *Solid State Electrochemistry*. Cambridge University Press: Cambridge, 1995; p 344.

2. Hull, S.; Keen, D. A.; Sivia, D. S.; Berastegui, P., Crystal structures and ionic conductivities of ternary derivatives of the silver and copper monohalides - I. Superionic phases of stoichiometry MA_4I_5: $RbAg_4I_5$, KAg_4I_5, and KCu_4I_5. *Journal of Solid State Chemistry* **2002,** 165, (2), 363-371.

3. Grey, C. P.; Greenbaum, S. G., Nuclear magnetic resonance studies of lithium-ion battery materials. *Mrs Bulletin* **2002,** 27, (8), 613-618.

4. Cahill, L. S.; Kirby, C. W.; Goward, G. R., Li-6{P-31} rotational-echo, double-resonance studies of lithium ion site dynamics in $Li_3V_2(PO_4)_3$. *Journal of Physical Chemistry C* **2008,** 112, (6), 2215-2221.

5. Davis, L. J. M.; He, X. J.; Bain, A. D.; Goward, G. R., Studies of lithium ion dynamics in paramagnetic cathode materials using Li-6 1D selective inversion methods. *Solid State Nuclear Magnetic Resonance* **2012,** 42, 26-32.

6. Davis, L. J. M.; Heinmaa, I.; Goward, G. R., Study of Lithium Dynamics in Monoclinic $Li_3Fe_2(PO_4)_3$ using Li-6 VT and 2D Exchange MAS NMR Spectroscopy. *Chemistry of Materials* **2010,** 22, (3), 769-775.

7. Cahill, L. S.; Chapman, R. P.; Kirby, C. W.; Goward, G. R., The challenge of paramagnetism in two-dimensional Li-6,Li-7 exchange NMR. *Applied Magnetic Resonance* **2007,** 32, (4), 565-581.

8. Kuhn, A.; Narayanan, S.; Spencer, L.; Goward, G.; Thangadurai, V.; Wilkening, M., Li self-diffusion in garnet-type $Li_7La_3Zr_2O_{12}$ as probed directly by diffusion-induced Li-7 spin-lattice relaxation NMR spectroscopy. *Physical Review B* **2010,** 83, (9).

9. van Wullen, L.; Echelmeyer, T.; Meyer, H. W.; Wilmer, D., The mechanism of Li-ion transport in the garnet $Li_5La_3Nb_2O_{12}$. *Physical Chemistry Chemical Physics* **2007,** 9, (25), 3298-3303.

10. Schurko, R. W.; Hung, I.; Widdifield, C. M., Signal enhancement in NMR spectra of half-integer quadrupolar nuclei via DFS-QCPMG and RAPT-QCPMG pulse sequences. *Chemical Physics Letters* **2003,** 379, (1-2), 1-10.

11. O'Dell, L. A.; Schurko, R. W.; Harris, K. J.; Autschbach, J.; Ratcliffe, C. I., Interaction Tensors and Local Dynamics in Common Structural Motifs of Nitrogen: A Solid-State N-14 NMR and DFT Study. *Journal of the American Chemical Society* **2011,** 133, (3), 527-546.

12. Taralunga, G., Rus, E. M., Structural and Electrochemical Characteristics of RbAg4I5 Solid Electrolyte. *Romanian Journal of Biophysics* **2002,** 12, (3-4), 97-101.

13. Looser, H.; Brinkmann, D.; Mali, M.; Roos, J., The Interdependence of Mobile and Stationary Ions in $RbAg_4I_5$ - an NMR Investigation. *Solid State Ionics* **1981,** 5, (OCT), 485-488.

14. Looser, H.; Mali, M.; Roos, J.; Brinkmann, D., Ag Diffusion Constant in Rbag4i5 and KAg_4I_5 Determined by Pulsed Magnetic Gradient Nmr. *Solid State Ionics* **1983,** 9-10, (DEC), 1237-1240.

15. Penner, G. H., Liu, X., Silver NMR Spectroscopy. *Progress in Nuclear Magnetic Resonance Spectroscopy* **2006,** 46, 151-167.

16. Tang, J. A.; O'Dell, L. A.; Aguiar, P. M.; Lucier, B. E. G.; Sakellariou, D.; Schurko, R. W., Application of static microcoils and WURST pulses for solid-state ultra-wideline NMR spectroscopy of quadrupolar nuclei. *Chemical Physics Letters* **2008,** 466, (4-6), 227-234.

17. Skibsted, J.; Jakobsen, H. J., Variable-temperature Rb-87 magic-angle spinning NMR spectroscopy of inorganic rubidium sails. *Journal of Physical Chemistry A* **1999,** 103, (40), 7958-7971.

18. O'Dell, L. A.; Schurko, R. W., QCPMG using adiabatic pulses for faster acquisition of ultra-wideline NMR spectra. *Chemical Physics Letters* **2008,** 464, (1-3), 97-102.

19. O'Dell, L. A.; Harris, K. J.; Schurko, R. W., Optimized excitation pulses for the acquisition of static NMR powder patterns from half-integer quadrupolar nuclei. *Journal of Magnetic Resonance* **2010,** 203, (1), 156-166.

20. Vold, R. L.; Hoatson, G. L., Effects of jump dynamics on solid state nuclear magnetic resonance line shapes and spin relaxation times. *Journal of Magnetic Resonance* **2009,** 198, (1), 57-72.

21. Eichele, K., Wasylishen, R. E., WSolids1. *WSolids1, Dalhousie University and University of Tuebingen* **2010**.

22. Peng, H., Machida, N., Shigematsu, T., Mechano-chemical Synthesis of $RbAg_4I_5$ and KAg_4I_5 Crystals and Their Silver Ion Conducting Properties. *Journal of the Japan Society of Powder and Powder Metallurgy* **2002,** 49, (2), 69 - 74.

23. Larson, A. C.; Dreele, R. B. V., General Structure Analysis System (GSAS). *Los Almos National Laboratory Report LAUR 86-748* **1994**.

24. Clark, S. J.; Segall, M. D.; Pickard, C. J.; Hasnip, P. J.; Probert, M. J.; Refson, K.; Payne, M. C., First principles methods using CASTEP. *Zeitschrift Fur Kristallographie* **2005,** 220, (5-6), 567-570.

25. Profeta, M.; Mauri, F.; Pickard, C. J., Accurate first principles prediction of O-17 NMR parameters in SiO_2: Assignment of the zeolite ferrierite spectrum. *Journal of the American Chemical Society* **2003,** 125, (2), 541-548.

26. Bonhomme, C.; Gervais, C.; Babonneau, F.; Coelho, C.; Pourpoint, F.; Azais, T.; Ashbrook, S. E.; Griffin, J. M.; Yates, J. R.; Mauri, F.; Pickard, C. J., First-Principles Calculation of NMR Parameters Using the Gauge Including Projector Augmented Wave Method: A Chemist's Point of View. *Chemical Reviews* **2012,** 112, (11), 5733-5779.

27. Adiga, S.; Aebi, D.; Bryce, D. L., EFG Shield - A program for parsing and summarizing the results of electric field gradient and nuclear magnetic shielding tensor calculations. *Canadian Journal of Chemistry-Revue Canadienne De Chimie* **2007,** 85, (7-8), 496-505.

28. Looser, H.; Brinkmann, D., Ag-109 Chemical-Shifts in Some Solid Compounds. *Journal of Magnetic Resonance* **1985,** 64, (1), 76-80.

29. Harris, R. K., *Nuclear Magnetic Resonance Spectroscopy*. Pitman Books Limited: London, 1983; p 249.

30. Jameson, C. J., Theoretical and Physical Aspects of Nuclear Shielding. *Nuclear Magnetic Resonance* **1990,** 19.

31. Haeberlen, U., Academic Press: New York: 1976; Vol. Suppl. 1.

32. Bradley, J. N., Greene, P. D., *Transactions of the Faraday Society* **1967,** 63, 424-430.

33. Schurko, R. W.; Wi, S.; Frydman, L., Dynamic effects on the powder line shapes of half-integer quadrupolar nuclei: A solid-state NMR study of XO_4- groups. *Journal of Physical Chemistry A* **2002,** 106, (1), 51-62.

34. Spencer, T. L.; Ramzy, A.; Thangadurai, V.; Goward, G. R., Structural Complexity and Electrical Properties of the Garnet-Type Structure $LaLi_{0.5}Fe_{0.2}O_{2.09}$ Studied by (7)Li and (139)La Solid State NMR Spectroscopy and Impedance Spectroscopy. *Chemistry of Materials* **2011,** 23, (12), 3105-3113.

35. Spencer, L., Coomes, E., Ye, E., Terskikh, V., Ramzy, A., Thangadurai, V., Goward, G.R., *Canadian Journal of Chemistry-Revue Canadienne De Chimie* **2011,** 89, 1105-1117.

Chapter 5: The Use of ^{6}Li{^{7}Li}-REDOR NMR Spectroscopy to Compare the Ionic Conductivities of Solid-State Lithium Ion Electrolytes

5.1. Introduction

This chapter compares the temperature dependent Li^{+} ion hopping rate in $Li_6BaLa_2M_2O_{12}$ (M = Ta, Nb) using solid-state ^{6}Li{^{7}Li}-REDOR NMR spectroscopy. The slope of the ^{6}Li{^{7}Li}-REDOR curve is highly temperature dependent in these two phases, and a comparison of the changes of the REDOR slopes as a function of temperature has been used to evaluate the Li^{+} ion dynamics. Our results indicate that the Nb phase has a higher overall ionic conductivity in the range of 247 K to 350 K, as well as a higher activation energy for lithium ion hopping than the Ta counterpart. For appropriate relative timescales of the dipolar couplings and ion transport processes, this is shown to be a facile method to compare ion dynamics among similar structures.

This work was prepared for submission on *September 27th, 2013* to the journal *Royal Society of Chemistry Advances* with authors T. L. Spencer, N. W. Plagos, D. H. Brouwer, and G. R. Goward. All ^{6,7}Li NMR spectra were collected and processed at McMaster University under the supervision of Prof. Gillian Goward. Initial drafts of the manuscript were written by the current author, T. L. Spencer.

Solid-state ceramic lithium ion electrolytes withstand a higher voltage window than traditional liquid or polymer electrolytes, which decompose below 5 V and pose a significant fire-risk in traditional lithium ion battery (LIB) cells.[1] Moreover, solid-state ceramic electrolytes show little reactivity with cathode and anode materials where

traditional electrolyte materials are known to form a solid electrolyte interface (SEI), which may be unstable, and consume Li^+, shortening the lifetime of the battery.[1-5] For these reasons, solid-state lithium ion electrolytes provide a method of attaining the stability necessary for batteries to be used in the automotive industry. Within this class of materials, garnet-like ceramic electrolytes exhibit excellent lithium ion conductivity.[4, 6-8] The garnet-like materials $Li_6BaLa_2M_2O_{12}$ (M = Ta, Nb) display among the highest ionic conductivities with the Ta phase having a conductivity of 4 x 10^{-5} S/cm.[9]

Structurally, garnet-like ceramic electrolytes resemble traditional garnets, consisting of an array of large tetrahedrally- and octahedrally-coordinated transition metal cations sharing oxygen corners.[6, 10] Lithium ions also occupy octahedral and tetrahedral sites and there has been disagreement in the literature concerning the number of unique crystallographic lithium sites in this class of materials. Some authors claim that Li is distributed between a single octahedral site and a single tetrahedral site, while others report that there are two octahedral and one tetrahedral sites.[6, 11, 12] Moreover, the exact occupancy of these sites is difficult to quantify, and may substantially impact the conductivity observed. This occupancy issue may be responsible for the differing conductivities observed by groups studying these phases.

Previous studies have made use a combination of powder X-ray diffraction and electron density distribution methods to investigate garnet-like materials. [2-4, 9, 12-15] Results from some authors have shown that for the Ta phase the tetrahedral site, Li-1, is 30 % occupied, while the octahedral site, Li-2, is 42 % occupied. Note that the multiplicities for the Li-1 and Li-2 sites are 24 and 96, respectively, making the contribution from the Li-1

and Li-2 sites 15 % and 85 %, respectively indicating that there is substantially more lithium in the Li-2 site.[14]. At this point similar studies have not yet been performed for the Nb phase, and thus there is no report in the literature of the lithium ion occupancy for this phase. However, efforts have been made to understand the effect of overall lithium content on the ionic conductivity in garnet-like electrolyte materials and several studies have found that an increase in lithium content in the octahedral site can increase the ionic conductivity. [15, 16]

Solid-state nuclear magnetic resonance (ssNMR) has been used in an attempt to assign the relative tetrahedral and octahedral sites.[15-17] In this work we use the assignment proposed by previous authors, in which the garnet-like material $Li_5La_3Nb_2O_{12}$ was studied using ^{6}Li and ^{7}Li MAS NMR spectroscopy. In this study a combination of ^{6}Li{^{7}Li}-Cross Polarization Magic Angle Spinning (^{6}Li{^{7}Li}-CPMAS) NMR and ^{6}Li{^{7}Li}-Cross Polarization MAS-Rotational Double Echo Resonance (^{6}Li-{^{7}Li}-CPMAS-REDOR) NMR was used to determine that of the two observed ^{7}Li spectral resonances the octahedral site was found at +0.7 ppm (^{6}Li NMR spectra), while the tetrahedral site was found at -0.2 ppm.[16]

In addition to the structural assignment of the ^{7}Li NMR spectral sites, it is important to determine which crystallographic site is responsible for ionic motion in this class of materials. Here, we use the assignment determined by previous studies of the garnet structure $Li_{3+x}Nd_3Te_{2-x}Sb_xO_{12}$, in which solid-state ^{7}Li MAS NMR was used to determine that the tetrahedral lithium ions are held tightly in place, while the octahedral lithium ions are held more loosely and are therefore primarily responsible for the ionic

motion in these systems. These results are based on the trend observed when the occupancy of the octahedral site was increased synthetically, which resulted in an increase in ionic conductivity of the material, measured using bulk impedance analysis. High temperature ssNMR studies were performed, which showed no coalescence between the two observed ^{7}Li resonances and therefore the authors concluded that there was no chemical exchange between the two lithium environments and that the octahedral site is responsible for ion motion. The authors noted a significant difference in the T_1 relaxation rates of the two ^{7}Li resonances. The tetrahedral site had a T_1 relaxation which consisted of two components, 15 s and 5 min; while the octahedral site had a T_1 with a single component of 8 ms.[15]

Koller and Kalwei have used the REDOR NMR spectroscopy experiments and second moment, M_2, analysis to consider rotational ion motion in tetrahydroxyborate sodalite. In their work several REDOR experiments were performed: ^{11}B{^{1}H}-REDOR, ^{27}Al{^{11}B}-REDOR and ^{23}Na{^{11}B}-REDOR. The study aimed to determine the nature of ion motion in a sodalite material using REDOR methods to probe re-orientation of anions and sodium motion. This work emphasized the limitation of 1D variable temperature line-narrowing studies for this system and instead made use of the temperature dependence of the observed REDOR curves in combination with M_2 calculations to evaluate the motion in the sodium system. In addition, the authors tackled the contribution of the quadrupole coupling, which is present for several nuclei in the system and can affect the REDOR experiment.[18]

The present work describes a similar method, which uses solid-state $^{6}Li\{^{7}Li\}$-REDOR NMR spectroscopy to qualitatively characterize and compare the lithium ion mobility in the garnet-like structures $Li_6BaLa_2Ta_2O_{12}$ and $Li_6BaLa_2Nb_2O_{12}$.[4, 14, 19] This method can be used to study materials in which chemical exchange occurs between neighbouring lithium ions, which occupy the same site in the crystal structure. In such cases, the use of 2D exchange NMR is not straight-forward, particularly for nuclei which do not possess substantial chemical shielding anisotropy, such as lithium. It is expected that this method can be extended into systems that have previously not been studied using 2D EXSY NMR. The type of motion in this system is different from that studied by Koller *et al.*[18] in that Li ions in $Li_6BaLa_2M_2O_{12}$ (M=Ta, Nb) move via discreet jump between neighbouring sites, and there is no corresponding anion rotation. The complexity of this motion makes modelling the dynamics in this system challenging.

Bulk conductivity measurements of garnet-like materials have included the effect of grain boundary resistance and in some cases, different conductivity values for the same materials have been reported.[4, 9, 14, 20] There has also been some disagreement in the literature regarding the activation energy of lithium ion hopping in $Li_6BaLa_2M_2O_{12}$ (M = Ta, Nb). Authors have reported ionic conductivities and activation energies for the each of these phases, shown in ***Table 5.1***. While the more recent studies ([14, 20]) have referred to the previous studies, there is little discussion of the disagreement observed. Differences in the reported values of activation energy for lithium ion hopping likely result from differences in preparation techniques. Typically for bulk conductivity measurements materials are pressed into a pellet and then sintered. Conductivity measurements are taken

using inert electrodes.[4] Differences in sintering, pelletizing or general setup could potentially lead to slightly different results. Here, we aim to circumvent some of these issues by using solid-state NMR spectroscopic techniques to consider ionic conductivity in these two phases, as this method can be used to probe local ion dynamics without interference from grain boundary resistance.

Table 5.1: Comparing the Li ion conductivity and activation energy of Li ion hopping in $Li_6BaLa_2M_2O_{12}$ (M = Nb and Ta) as obtained from bulk conductivity measurements.

Material	Conductivity, S/cm	Activation Energy, eV	Temperature, °C	Reference
$Li_6BaLa_2\mathbf{Nb}_2O_{12}$	6.0×10^{-6}	0.44	22	4
$Li_6BaLa_2\mathbf{Nb}_2O_{12}$	4.4×10^{-4}	0.35	25	20
$Li_6BaLa_2\mathbf{Ta}_2O_{12}$	1.3×10^{-5}	0.44	25	14
$Li_6BaLa_2\mathbf{Ta}_2O_{12}$	4.0×10^{-5}	0.40	22	9

5.2. Solid-State ^{6,7}Li NMR of Lithium Ion Electrolytes

^{6,7}Li solid-state NMR is a selective and diagnostic tool to probe ionic motion in lithium ion conductors.[21, 22] Differences in the gyromagnetic ratios ($\gamma[^6Li] : \gamma[^7Li] = 1 : 2.64$) and natural isotope abundance (^{6}Li = 7.42%, ^{7}Li = 92.58%) allow for a range of different techniques to be used to study structure and dynamics in lithium battery materials. Many cathode materials for lithium ion batteries have been extensively studied using a combination of ^{6}Li and ^{7}Li solid-state NMR spectroscopy, with paramagnetic contributions creating well resolved lithium sites in a wide chemical shift range (> 1000

ppm).[23-25] Conversely, diamagnetic electrolytes for lithium ion batteries have a small chemical shift range of -5 to +5 ppm, which results in poorly resolved ^{6,7}Li NMR spectral peaks.[26] In addition, it has been shown that garnet-like electrolyte materials conduct lithium ions within a single crystallographic site, and as a result many of the techniques used to study dynamics, such as selective inversion experiments, cannot be applied here.[15, 16, 27, 28] Instead, the change in heteronuclear ^{6}Li-^{7}Li dipolar coupling as a function of temperature is used to probe ionic motion in these materials.

5.3. Rotational Echo Double Resonance Measurements

REDOR NMR spectroscopy is a technique that measures the dipolar coupling between a pair of heteronuclei.[29, 30] This rotor synchronized, double-resonance experiment is traditionally used to determine internuclear distances, making use of the fact that dipolar coupling is related to internuclear distance (*r*), shown in ***Equation 1***.[19, 31]

$$D_{ij} = \hbar\left(\frac{\mu_0}{4\pi}\right)\frac{1}{r_{ij}^3}\gamma_i\gamma_j \qquad (1)$$

Figure 2.15 in Chapter 2 shows the I{S}-REDOR NMR pulse sequence. Spin *I* is observed, while spin *S* is perturbed as a function of the rotor period. The dipolar coupling between the spin pair allows *I* to be affected by the perturbation of the *S* spin. This is examined through the creation of a REDOR curve, which shows the extent of the perturbation as a function of time as the number of pulses on the *S* spins is increased. The REDOR curve is plotted as ($\Delta S/S_0$) vs. the dephasing time. In this case S_0 is the intensity of a reference Hahn-echo experiment measuring the observed *I* spectrum, and ΔS is

difference between the intensity observed in S_0 and that of the corresponding experiment in which there is a dephasing pulse on the *S* channel. The term *S* uses the traditional convention representing the non-observed spin and is not directly related to the term [$\Delta S/S_0$]. The dephasing time is the time allowed for the application of the dephasing pulses on the *S* channel.

The geometry of the spin pairs in a system is an important factor, which affects the outcome of the REDOR experiment. Many REDOR studies of biological materials take advantage of isotopic labeling to ensure that an isolated pair of nuclei creates a single strong dipolar coupling that can be directly measured in a highly selective, readily quantifiable fashion.[32-35] However, the relationship between ^{6}Li and ^{7}Li in solid-state electrolyte materials is more complex, as the control over the enrichment and isolation of single spin pairs in the structure is not possible. Rather, in these materials there are many ^{6}Li and ^{7}Li spin pairs of varying proximity. This is due in part to the fact that in these materials partial occupancy of lithium crystallographic sites is a key factor in ion mobility. Here, the multiple-spin effect must be carefully considered.[36-39] In a system in which there are several spin pairs, a single dipolar coupling between an isolated pair of nuclei is insufficient to describe the system. In this case, each contributing spin pair must be considered if a full quantitative model of the spin system is to be evaluated. For the combination of partial occupancies, and a very large unit cell, this is intractable, and we have focused here on other methods of comparing the dipolar coupling strength in the electrolytes as a function of temperature. These include the use of dipolar second moment, M_2, calculations, and relative scaling of the dipolar curves.

The dipolar second moment is a parameter derived from the summation of all relevant dipolar coupled spin pairs (***Equation 3***) and can be used instead of discrete dipolar couplings to fit Spin-Echo Double Resonance (SEDOR) and REDOR curves (***Equation 2***).[36] Previous studies have effectively used the analysis of the M_2 to describe the results of stationary ^{6}Li{^{7}Li}-SEDOR experiments aimed to study the spatial distribution of lithium ions in the solid electrolyte glasses $(Li_2O)_x(SiO_2)_{1-x}$ and $(Li_2O)_x(B_2O_3)_{1-x}$.[37, 40, 41] For prediction of the SEDOR curves each of the heteronuclear spin pairs were included in the calculation of M_2 (***Equation 3***) and the experiments performed were able to differentiate between the distributions of cations in these two systems. This type of analysis is also valid for REDOR experiments, which make use of magic angle spinning (MAS) to re-focus the heteronuclear dipolar coupling. This method neglects the effect of homonuclear dipolar coupling, as it is usually removed by MAS.[37]

For systems in which there is a distribution in spin geometries, the following equation can be used to simulate the REDOR curve in the short-term limit, where the REDOR curve is geometry-independent:[37]

$$\frac{\Delta S}{S_0} = \frac{4}{3\pi^2}(NT_r)^2 M_2 \qquad (2)$$

$$M_2^{hetero} = \frac{4}{15}\left(\frac{\mu_0}{4\pi}\right)^2 \gamma_I^2 \gamma_S^2 \hbar^2 S(S+1) \sum_S r_{IS}^{-6} \qquad (3)$$

($\Delta S/S_0$), defined earlier, is the intensity of the REDOR curve, N is the number of rotor periods, T_r is the length of a single rotor period, and M_2 is the second moment. In ***Equation 3*** the term *S* is the spin number for the non-observe spin. If M_2 is treated as a

variable in ***Equation 2*** the experimental curve can be simulated with a parabola as a function of M_2 with no prior knowledge of the spin geometry. In this case, M_2 can be determined after simulation of the REDOR curve. This method is useful for situations in which there is disorder resulting in local distributions of spins. General limitations to this method include situations in which there is a significant contribution from homonuclear dipolar coupling in which the I-I chemical shifts are different; this may affect the slope or shape of the REDOR curve. Quadrupolar coupling may also contribute to the shape of the REDOR curve. This is particularly relevant in cases in which satellite transitions are present in the non-observed spin, *I*, and there is concern regarding their contribution to REDOR experiment. ^{7}Li is a prime example as it tends to have a small quadrupolar coupling that can impact the results of the REDOR experiment.[36]

In the previous work performed by Koller *et al*. (discussed earlier) there was a significant contribution from the quadrupolar nature of ^{11}B, ^{23}Na and ^{27}Al. The authors proposed two different equations for the REDOR curve simulated using M_2 analysis:[18]

$$\frac{\Delta S}{S_0} = \frac{1}{\pi^2 S(S+1)} (N_c T_r)^2 M_2 \quad (4)$$

$$\frac{\Delta S}{S_0} = \frac{5}{\pi^2 S(S+1)} (N_c T_r)^2 M_2 \quad (5)$$

Equation 4 describes the REDOR curve for a spin-1/2 system, and is equivalent to ***Equation 2***, when $S = ½$. ***Equation 5*** describes the REDOR curve for a system in which the non-observe spin, *S*, has a spin of $^{3}/_{2}$, and there is excitation of the satellite transitions. The contribution of the quadrupolar interaction to the REDOR curve has been identified

previously, however it is usually not quantitatively considered in the interpretation of REDOR data.[18, 37]

The REDOR curve is dependent not only on the internuclear distance of a single pair of heteronuclei, but also to the dilution of the ^{6}Li and ^{7}Li in the sample. Li-containing materials can be synthesized using differing amounts of ^{6}Li and ^{7}Li precursors, to optimize the heteronuclear dipolar coupling felt by the observed nucleus as well as the signal to noise ratio. The primary focus of our work is the effect of dynamics on ^{6}Li-^{7}Li dipolar coupling and thus on the REDOR curve, since dynamic processes between a pair of nuclei affect the dipolar coupling between them.[38, 42, 43] Here, we have studied the change in the slopes of the ^{6}Li{^{7}Li}-REDOR curve of the electrolyte materials, $Li_6BaLa_2Ta_2O_{12}$ and $Li_6BaLa_2Nb_2O_{12}$ as a function of temperature to determine the difference in ion mobility between the two samples over the temperature range of 247 K to 350 K. After a series of trials with different isotopic enrichments, the materials were found to be ideal with an isotopic ratio of ~ 50% ^{6}Li, which gave the optimal results with respect to the sensitivity of the initial slope of the REDOR curve to changes in experimental conditions.

5.4. Experimental

5.4.1. Synthesis of Lithium Ion Electrolyte Materials: $Li_6BaLa_2M_2O_{12}$ (M = Ta, Nb)

High temperature solid-state synthesis methods were used to prepare $Li_6BaLa_2Ta_2O_{12}$ and $Li_6BaLa_2Nb_2O_{12}$. In each case powder X-ray diffraction was used for phase confirmation, and is shown in Appendix A2, ***Figure A2.1***.

$Li_6BaLa_2Ta_2O_{12}$: Stoichiometric quantities of La_2O_3 (Aldrich, 99.9 %), $Ba(NO_3)_2$ (Aesar, 99+ %), Ta_2O_5 (Aldrich, 99 %), $^6LiOH{\cdot}H_2O$ (synthesized from ^6Li metal), and $LiOH{\cdot}H_2O$ (Anachemia, 98 %) were ground by hand and placed in tube furnace (in air) for 12 hours at 700 ^oC, with heating and cooling ramps of 6 hours each. The mixture was removed, ground again and pelletized. The pellet was sintered in a tube furnace at 900 ^oC for 24 hours, with a heating and cooling ramp of 12 hours each.

$Li_6BaLa_2Nb_2O_{12}$: The synthesis outlined above was followed, using Nb_2O_5 (Aldrich, 99.99 %) in place of Ta_2O_5.

5.4.2. ^{6,7}Li Solid-State NMR Spectroscopy

NMR studies were performed on a Bruker Avance I 500 NMR spectrometer. A Bruker 2.5 mm solid-state triple-resonance probe was used with a MAS rate of 30 kHz. Pulse calibration was performed on a 1 M solution of $^{6,7}LiCl$ (~ 50% ^6Li enriched). For ^6Li a nutation frequency of 54 kHz was applied, while for ^7Li, a nutation frequency of 88 kHz was applied.

^{6}Li{^{7}Li}-REDOR experiments were performed with a sweep width of 50 ppm, with between 32 and 54 transients collected in the indirect dimension. In the direct dimension, between 32 and 64 transients were co-added, depending on the sample sensitivity. The 180° dephasing pulses on ^{7}Li were equivalent to those calibrated on the 1 M solution of LiCl. Temperatures were calibrated using an external chemical thermometer, $Sm_2Sn_2O_7$.[44]

1D ^{6}Li spectra were collected with MAS of 30 kHz. For each spectrum the sample was allowed to relax for > 2700 s before one single-pulse experiment was performed. Only a single transient was collected in each case to ensure that the correct integration was observed for each lithium site.

1D ^{7}Li spectra were collected with no MAS and also with MAS of 5 kHz. 64 transients were collected with a recycle delay of 60 s.

5.4.3. Numerical Simulations of ^{6}Li{^{7}Li}-REDOR Curves

SPINEVOLUTION 3.4.4 software was used to model the ^{6}Li{^{7}Li}-REDOR curve of $Li_6BaLa_2Ta_2O_{12}$ at a low temperature (285 K), where lithium dynamics were found not to contribute to the shapes of the REDOR curves *(vide infra*). Here, we call this the immobile system, since the motion of the lithium ions are slowed to the point at which their motion no longer contributes to the dipolar coupling between pairs of lithium ions.[42] Within the SPINEVOLUTION manual the REDOR experiment is outlined.[45] This was adjusted to include the specific details of the experiment, such as MAS rate, pulse program and the nuclei of interest and is shown in the *Appendix A1*. Simulations included

a single value for the dipolar coupling. Here we call this the effective dipolar coupling, D_{eff}, and it encompasses all effects contributing to the REDOR curve.

Table 5.2: $Li_6BaLa_2M_2O_{12}$ cell parameters and calculated values of M_2.

	$Li_6BaLa_2Ta_2O_{12}$ [14]	**$Li_6BaLa_2Nb_2O_{12}$** [4]
Space group	I a -3 d	I a -3 d
Cell constant (Å)	13.001	12.868
Cell volume (Å^3)	2197.51	2130.75
Li-1, Li-2 Wyckoff positions	24*d*, 96*h*	24*d*, 96*h*
^{6}Li NMR peak area ratio	**Li-1**: 41 ± 5 %	**Li-1**: 25 ± 5 %
	Li-2: 58 ± 5 %	**Li-2** : 75 ± 5 %
Li-1, Li-2 site occupancies	0.830, 0.293	0.494, 0.377
^{6}Li{^{7}Li} Second moment (rad^2 s^{-2})		
^{7}Li in Li-1 and Li-2 sites	2.7×10^7	1.2×10^7
^{7}Li in Li-2 sites only	6.3×10^6	7.8×10^6

^{6}Li{^{7}Li} heteronuclear second moments were estimated for the Ta and Nb phases according to the following procedure. The 1D ^{6}Li NMR spectra (***Figure 5.1*** (b)) were deconvoluted to give the relative peaks areas for the Li-1 and Li-2 sites. The Li-1 and Li-2 site occupancies were then determined from these ratios and the assumption that the number of Li in the chemical formulae was 6 (to maintain charge neutrality), along with the Wyckoff position multiplicity for each site. A disordered structural model was then constructed consisting of a central unit cell and its 26 adjacent unit cells where the Li-1

and Li-2 sites were occupied in a probabilistic manner consistent with their calculated site occupancies. An examination of the crystal structure[14] reveals that the octahedral Li-2 sites occur in symmetry-related pairs separated by only 0.7 Å. Therefore, the structure models did not allow both Li-2 sites in such pairs to be occupied as this would be physically unreasonable. Also, an examination of the crystal structure reveals that each Li-2 site has two Li-1 sites at distances of 1.74 and 2.31 Å. Since the Li-Li distance of 1.74 Å is quite short, when a Li atom was being placed in one of the Li-2 sites within a pair of close symmetry-related sites, the position furthest away from an occupied Li-1 site would be chosen if possible. Once a disordered structural model was constructed, the various Li atoms would be assigned to be ^{6}Li or ^{7}Li in a probabilistic manner consistent with the level of ^{6}Li enrichment (51.45% ^{6}Li). Each ^{6}Li nuclei located in a Li-2 site of the central unit cell was then identified and the distances to ^{7}Li nuclei within 12 Å were calculated (either ^{7}Li nuclei in all Li-1 and Li-2 sites or ^{7}Li nuclei in only Li-2 sites). The second moments were then calculated according to ***Equation 3*** and averaged. This procedure was repeated for 10,000 different disordered structural models and the calculated second moments were averaged again. This procedure was implemented as a *Mathematica* notebook.

5.5. Results and Discussion

Solid-state electrolytes $Li_6BaLa_2Ta_2O_{12}$ and $Li_6BaLa_2Nb_2O_{12}$ are known to exhibit stability against attack by commonly used electrode materials, as well as lithium metal. This property makes these materials promising for use in lithium ion batteries. In order to assess these materials before placing them into the battery it is important to understand

the mechanism of lithium ion conductivity and the effect of temperature on these materials. Here, solid-state ^{6}Li{^{7}Li}-REDOR NMR has been used to compare these two materials by observing the effect of changing temperature on the distance-dependent ^{6}Li-^{7}Li dipolar coupling.

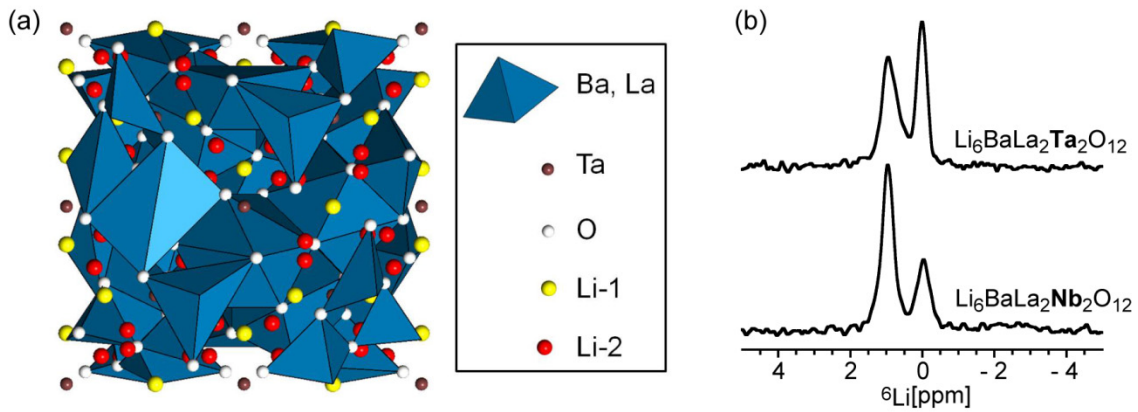

Figure 5.1. (a) Illustrated crystal structure of $Li_6BaLa_2Ta_2O_{12}$. The blue polyhedra represent La and Ba, which share a crystallographic site. The brown spheres represent Ta, and the white spheres represent oxygen; while the yellow and red spheres represen Li-1 (tetrahedral) and Li-2 (octahedral), respectively.[14] The image was created in XtalDraw software.[46] (b) ^{6}Li MAS NMR spectrum of $Li_6BaLa_2Ta_2O_{12}$ with MAS 30 kHz. Recycle delays were > 2700 s and therefore the tetrahedral site at 0 ppm is thought to be fully relaxed.

$^{6,7}Li_6BaLa_2Ta_2O_{12}$ and the corresponding niobium phase were synthesized using high temperature solid-state synthesis methods.[4] The X-ray diffraction patterns of the products showed single-phase, high-purity products, and are in agreement with those reported in the literature.[2] ***Figure 5.1***(a) shows the unit cell of $Li_6BaLa_2Ta_2O_{12}$. These materials are known to have two crystallographic lithium sites, with each having a partial occupancy. The high quality, high resolution ^{6}Li MAS NMR spectra shown in ***Figure 5.1*** (b) easily confirm that there are two sites: Li-1and Li-2, which have chemical shifts of 0

and 1 ppm, respectively. Deconvolution in TopSpin 2.1 software reveal the Li contribution of Li-1 and Li-2 to be 41 ± 5 % and 58 ± 5 %, respectively for the Ta phase; while for the Nb phase the contribution of the Li-1 and Li-2 sites are 25 ± 5 % and 75 ± 5 %. This is significantly different from the contribution of the Li-1 and Li-2 sites predicted for the Ta phase in previous studies, 15 % and 85 %, respectively, as shown previously.

T_1 relaxation analysis of these two sites in each phase has shown that the T_1 for the site at 1 ppm is ~ 12 s, which is at least two orders of magnitude less than the T_1 of the site at 0 ppm. This large difference in T_1 relaxation rate indicates that there is no exchange between the two sites; and also suggests that the site at 1 ppm, with the shorter T_1, is responsible for ion motion.[47] Ionic conductivity in these materials occurs through vacancy-mediated hopping of Li^+ ions, but it is not known to what extent the presence of vacancies affects the rate of ion hopping. ***Table 5.2*** shows a comparison of the cell constants of the Ta and Nb phases. In this work, as in others, Li-1 has been assigned as the tetrahedral site at 0 ppm, while Li-2 is the octahedral site at 1 ppm and is responsible for lithium ion motion.

The relationship between nuclear distance separation and dipolar coupling is well established.[19] Furthermore, the relationship between several heteronuclear spins and their respective separations has been thoroughly described using the dipolar second moment, which is used to analyze experimentally determined REDOR curves.[37, 48, 49] For the electrolyte materials $Li_6BaLa_2M_2O_{12}$ (M = Ta, Nb) there are four effects which influence the shape of the $^6Li\{^7Li\}$-REDOR curves obtained:[38]

(1) Distances between ^{6}Li and ^{7}Li spins.[31]

(2) Distribution: site occupancy and resulting dilution of ^{6}Li and ^{7}Li isotopes (affects Li-Li distances); ^{6}Li/^{7}Li isotope ratio[37]; geometry of lithium pairs.

(3) Dynamics: the hopping rate between crystallographic lithium sites.[43]

(4) Quadrupolar coupling constant of the non-observe *I* spins, in this case ^{7}Li.[18]

While the distances between crystallographic lithium sites can be determined using X-ray diffraction techniques, the lithium ^{6}Li/^{7}Li isotope dilution and any existing partial occupancies make the construction of a model difficult. Garnet-like lithium ion electrolytes have a considerable amount of partial occupancies on each of two crystallographic lithium sites. The materials studied in this work have less than 50% occupancy of each lithium site.[14]

The changes in the slopes of the ^{6}Li{^{7}Li}-REDOR curves of 50% ^{6}Li enriched $Li_6BaLa_2M_2O_{12}$ (M = Ta, Nb) have been studied in order to qualitatively compare lithium ion hopping rates between these two samples over the same temperature range. This was achieved by comparing the slopes of the experimentally observed REDOR curves of the octahedral site, Li-2 at 1 ppm, at different temperatures. The site resolution in the ^{6}Li spectrum, ***Figure 5.1*** (b), allows the separation of the REDOR effect for the two sites. The examination of the REDOR curve of samples where the lithium is immobile with respect to the dipolar coupling is an essential piece of the analysis, since it allows the

determination of the range of temperatures where the slope is sensitive to changes in temperature.

5.5.1. Simulation of the Immobile ^{6}Li{^{7}Li}-REDOR Curve

Second moment calculations as well as numerical simulations for an isolated ^{6}Li/^{7}Li spin pair were used to fit the REDOR curve for the immobile material. This immobile state is achieved by cooling the sample to the point at which only structural characteristics, i.e. distances and distribution of the lithium ions, contribute to the slope of the REDOR curve, and is determined experimentally by decreasing the sample temperature and observing the temperature at which there is no more visible change in the REDOR curve. This point marks the point at which the time-scale of dynamics is much slower than the dipolar coupling between the observed ^{6}Li and the surrounding ^{7}Li. In order to observe a change in the slope of the REDOR curve as a function of temperature the time-scale of the ionic hopping rate must correspond to the dipolar coupling in this system.

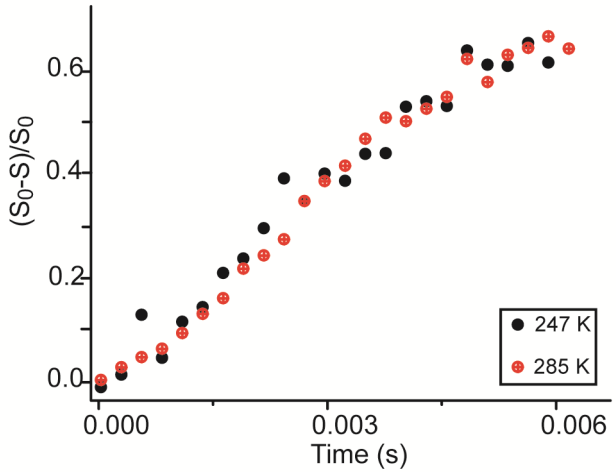

Figure 5.2. ^{6}Li{^{7}Li}-REDOR of $^{6,7}Li_6BaLa_2Ta_2O_{12}$ at 247 K and 285 K. The stability in the slope of the REDOR curve indicates that the lithium ions are immobile with respect to the sensitivity of the REDOR experiment. The only influence on this curve is therefore the stationary crystallographic positions of the lithium ions in the material.

This immobile state was used as a starting point for comparing the REDOR curves at higher temperatures, since at this point the shape of the curve was determined by the positions of the lithium ions alone, with no contribution from dynamics. ***Figure 5.2*** shows the ^{6}Li{^{7}Li}-REDOR curve of $Li_6BaLa_2Ta_2O_{12}$ at 247 K and 285 K. The unchanging slope indicates that at these low temperatures, changes in the hopping rate are no longer detectable by this method and the lithium ions are said to be immobile.

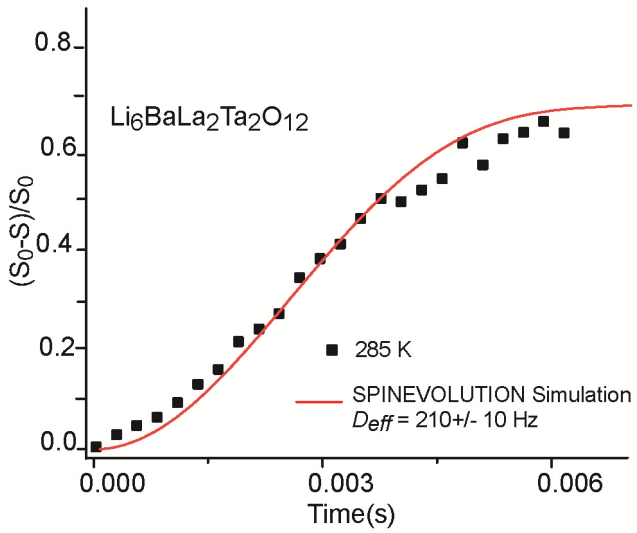

Figure 5.3. Analysis of the $^{6}Li\{^{7}Li\}$-REDOR curve of $Li_6BaLa_2Ta_2O_{12}$ using a simulation of $^{6}Li\{^{7}Li\}$-REDOR in SPINEVOLUTION.

Figure 5.3 shows efforts to use SPINEVOLUTION software to assess the observed $^{6}Li\{^{7}Li\}$-REDOR curves for the immobile Ta phase using a single ^{6}Li-^{7}Li spin pair.[36, 45] Although this is reasonable fit, this is not an accurate representation of the spin system, which consists of many spin pairs. An attempt to re-construct this system in SPINEVOLUTION software was not successful, since the number of spin pairs is too large for standard computational methods. The resulting dipolar coupling is called the effective dipolar coupling, D_{eff}, and is a single value that encompasses the dipolar coupling felt by the ^{6}Li nuclei for all relevant spin pairs. This value can be compared to the isotropic dipolar coupling of a single pair of ^{7}Li and ^{6}Li nuclei. For comparison, at a distance of 3 Å the dipolar coupling has a value of ~ 1.6 kHz, which gives a simulated REDOR curve that is much steeper than the one observed in ***Figure 5.2***. This is a testament of the effect of the partial occupancy in this system on the experimentally observed REDOR curve.

5.5.2. Use of Second Moment Calculations to Evaluate Structure of Ta and Nb Phases

The second moment, M_2, curve was compared to the shape of the ^{6}Li{^{7}Li}-REDOR curves obtained experimentally for the Ta and Nb electrolyte phases. The immobile REDOR curves for these materials are shown in ***Figure 5.4***. The general slopes of these curves are very similar, suggesting that the small differences in the unit cells is insufficient to affect the ^{6}Li-^{7}Li dipolar coupling significantly at these low temperatures. However, when the shape of the curve is considered more closely, the initial slopes seem to differ slightly, with the Nb phase having a slightly steeper initial slope..

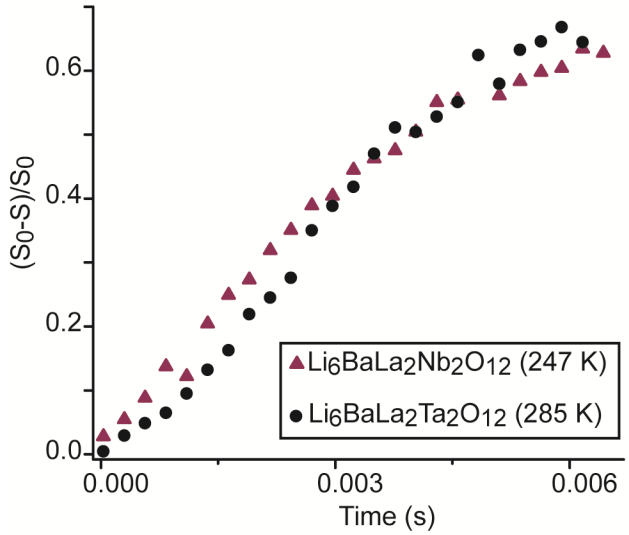

Figure 5.4. ^{6}Li{^{7}Li}-REDOR curves of $Li_6BaLa_2M_2O_{12}$ (M = Ta, Nb). In each case the slope represents a point at which dynamics is no longer a contributing factor, and the lithium ions are immobile with respect to the ^{6}Li-^{7}Li dipolar coupling.

Second moment calculations for these systems were performed in order to assess the possibility of simulating these curves as a function of temperature. Two models were

used to calculate the M_2 values for each material, resulting in a total of four curves shown in ***Figure 5.5*** (a), along with the experimentally observed curves:

1) Second moments were calculated with ^{7}Li nuclei in both Li-1 and Li-2 sites, assuming that all ^{7}Li nuclei contribute to dephasing ^{6}Li nuclei in Li-2 sites in the REDOR experiment.

2) Second moments were calculated with ^{7}Li nuclei in only Li-2 sites, assuming that the ^{7}Li nuclei in the Li-1 sites do not participate in dephasing of ^{6}Li nuclei in Li-2 sites due to their extremely long T_1 relaxation times. Note: this has become a point of concern in this model, since it is not clear what the relation is between T_1 relaxation and dipolar coupling in the REDOR experiment.

As previously mentioned by Koller *et al.*, there are two equations that could be used, along with the appropriate value of M_2, to simulate the shape the REDOR curve. ***Equation 4***, shown earlier, describes a case in which the satellite transitions of the non-observed nucleus, in this case ^{7}Li, are not excited by the NMR experiment. ***Equation 5*** describes a case in which the satellite transitions are excited in the NMR experiment.

From the static NMR spectrum of $Li_6BaLa_2Ta_2O_{12}$ two satellite transitions from the (+1/2 → +3/2) and (-3/2 to →1/2) transitions can be seen in addition to the central transition (-1/2 → +1/2). These appear as shoulders at approximately + 150 ppm and – 150 ppm in ***Figure 5.5*** (b). It is not obvious at the outset whether these satellites contribute to the shape of the observed REDOR curves. However, when M_2 analysis was performed, it was found that the curves that resulted from ***Equation 4*** created a better fit

than those of ***Equation 5***, which would suggest that the satellite transition of ^{7}Li did not have a significant effect on the REDOR experiment.

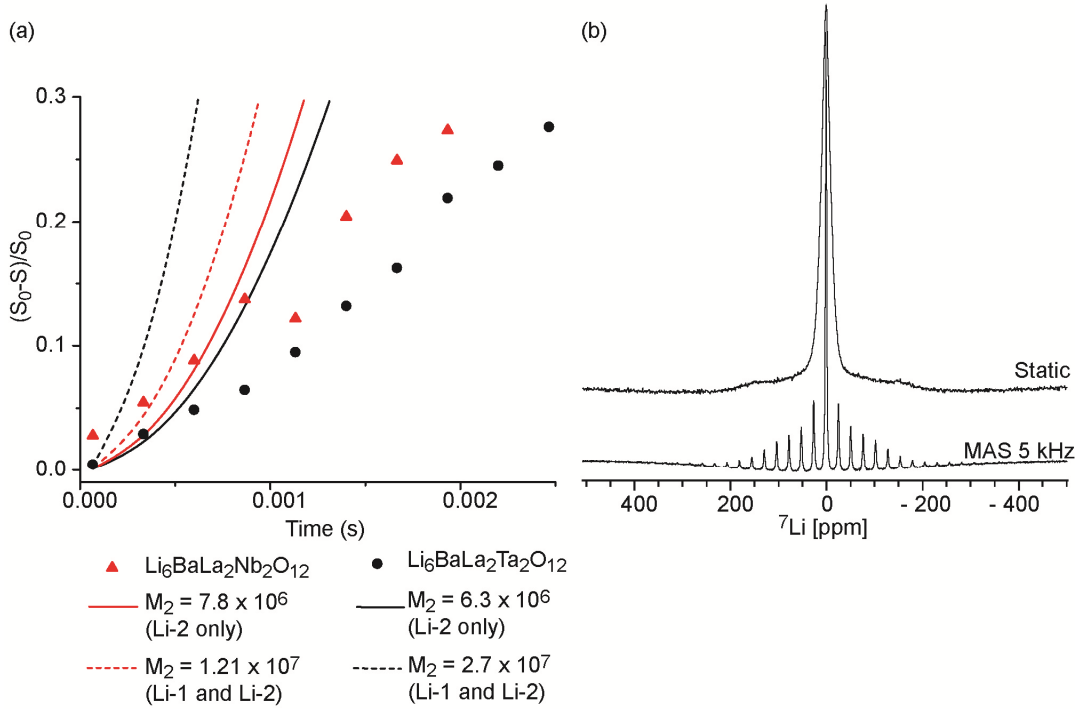

Figure 5.5. (a) M_2 calculations for the Ta and Nb electrolyte phases using ***Equation 4*** for cases in which only Li-2 is occupied, and cases in which Li-1 and Li-2 are occupied in the model structure. (b) ^{7}Li NMR spectra of $Li_6BaLa_2Ta_2O_{12}$ with MAS 5 kHz (bottom) and static (top).

An interesting observation from the M_2 calculations was the difference in the simulated curves for the case in which Li-2 was occupied alone and the case in which both Li-1 and Li-2 were occupied. Experimentally, the ^{6}Li{^{7}Li}-REDOR curves look similar, except that the shape is slightly different for the initial lower values of ([S_0-S]/S_0) on the curve. In this range it would seem that the REDOR curve of the Ta phase has a *more shallow* slope than that of the Nb phase. On performing the M_2 analysis, the opposite trend was observed for the model in which both Li-1 and Li-2 sites were

occupied, dashed lines in ***Figure 5.5*** (a). The M_2 calculations in this case suggest that the slope of the Ta REDOR curve is *larger* than that of the Nb phase. Conversely, when the M_2 analysis is performed and only Li-2 is occupied the order is reversed, the calculations reveal that the slope of the Nb REDOR curve is *larger* than that of the Ta curve. This latter trend is in agreement with the experimental data. This is shown by the solid lines in ***Figure 5.5*** (a).

Overall, the M_2 simulations exhibit a modest representation of the experimentally observed REDOR curves, however, the curves to appear to be in the expected range. Differences between calculated M_2 curves and experimental REDOR curves can be attributed to the contribution from the quadrupole coupling of both ^{6}Li and ^{7}Li, homonuclear dipolar coupling, as well as any disorder in the structure. There could also be residual "rattling" motions within the cages of the octahedral site, where lithium ions vibrate within the octahedral environment. This effect is not temperature dependent, but could contribute to the dipolar coupling between Li pairs, and has been observed previously in ^{7}Li{^{31}P}-REDOR studies of $Li_3V_2(PO_4)_3$.[42]

5.5.3. Examining Dynamics Using the Initial Slope of the ^{6}Li{^{7}Li}-REDOR Curve of $^{6,7}Li_6BaLa_2Ta_2O_{12}$

Here, we have made use of the slope of the initial ^{6}Li{^{7}Li}-REDOR curve of $Li_6BaLa_2Ta_2O_{12}$ for a 50% ^{6}Li enriched sample to describe changes as a function of temperature to indicate the temperature dependence of the lithium ion hopping rate. The initial slope of the REDOR curve has been shown to be independent of sample geometry,

i.e. the relative orientation of lithium ions. Studies of $Li_6BaLa_2Ta_2O_{12}$ show that the REDOR slope is sensitive to changes in temperature and this temperature dependence can be correlated to changes in dynamics in the system. ***Figure 5.6*** shows the effect of temperature on the REDOR curve of $Li_6BaLa_2Ta_2O_{12}$. Increasing the temperature from 285 K, where the sample is immobile, to 350 K shows a steady decrease in the slope of the REDOR curve, which is indicative of an increase in ionic motion within this temperature range, and causes an apparent decrease in the dipolar coupling.

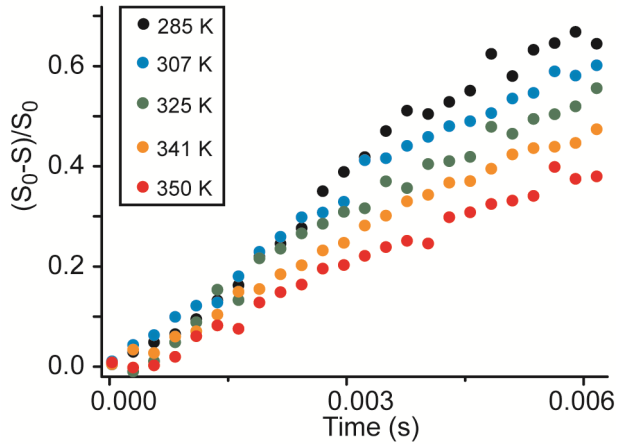

Figure 5.6. Variable temperature $^6Li\{^7Li\}$-REDOR curves of 50 % ^6Li enriched $Li_6BaLa_2Ta_2O_{12}$. Increasing temperature causes a decrease in the slope of the REDOR curve.

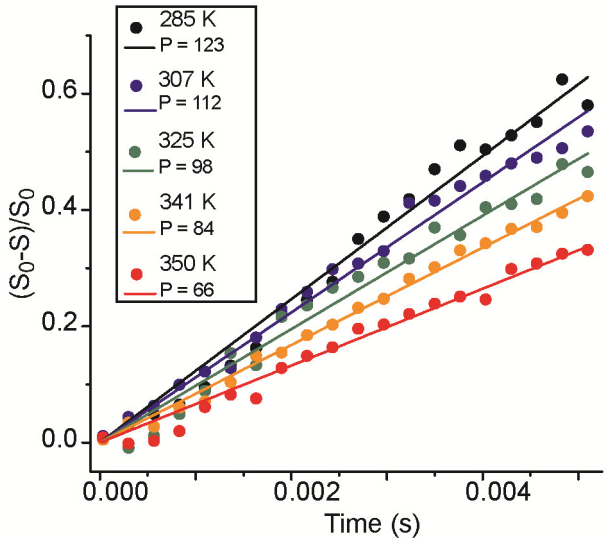

Figure 5.7. Initial slopes, *P*, of the $^{6}Li\{^{7}Li\}$-REDOR curves of $Li_6BaLa_2Ta_2O_{12}$ as a function of temperature. Solid circles represent the experimentally obtained REDOR curves, as in ***Figure 5.6***; while the solid lines represent the lines of best fit. Over the temperature range of 285 K, where the dynamics processes are static, to 350 K *P* ranges from 123 ± 2 s^{-1} to 66 ± 1 s^{-1}.

Figure 5.7 shows the temperature dependent REDOR curves along with the respective slopes, *P*, which begin at a value of 123 ± 2 s^{-1} for the immobile REDOR curve and decreases as the temperature increases. The temperature dependent slopes are summarized in ***Table 5.3***. Here, *P* changes from 123 ± 2 s-^{1} to 66 ± 1 s^{-1} over a temperature range of 285 K to 350 K. Values of *P* can also be used to compare ionic mobility in similar samples where the Li-Li separation is the same, where the only factor affecting the change in the slope of the REDOR curve is a change in ion hopping rate. Here, the slope of the immobile curve is unchanging below 285 K.

Table 5.3: Temperature dependent slopes of $^{6}Li\{^{7}Li\}$-REDOR curves of $Li_6BaLa_2Ta_2O_{12}$ and $Li_6BaLa_2Nb_2O_{12}$.

Temperature (K)	**P (s^{-1}) $Li_6BaLa_2Ta_2O_{12}$**	**Temperature (K)**	**P(s^{-1}) $Li_6BaLa_2Nb_2O_{12}$**
285	123 ± 2	**247**	140 ± 10
307	112 ± 2	**273**	76 ± 3
325	98 ± 2	**294**	33 ± 2
341	84 ± 2	**312**	26 ± 2
350	66 ± 1	**325**	19 ± 1
		332	12 ± 1
		341	10.2 ± 0.5
		350	8.3 ± 0.5

5.5.4. $^{6}Li\{^{7}Li\}$-REDOR Spectroscopy of $^{6,7}Li_6BaLa_2Nb_2O_{12}$

Ion mobility in different materials can be directly compared using $^{6}Li\{^{7}Li\}$-REDOR provided the materials are similar in structure (lithium content, framework structure and Li-Li internuclear distances). A prime use of this method is the comparison of two crystalline materials, which differ only in framework atoms, such as $Li_6BaLa_2Ta_2O_{12}$ and $Li_6BaLa_2Nb_2O_{12}$, where Ta and Nb occupy the same crystallographic sites within in their respective materials. Thus, changes in the slopes of the REDOR curves are attributed to differences in temperature dependent lithium ion

dynamics alone. Minor differences in the shapes of the REDOR curves, shown in ***Figure 5.4***, for these two samples can be attributed to differences in the distribution of lithium ions in these structures. In ***Figure 5.1*** the ^{6}Li MAS NMR spectra show that although the absolute lithium ion content is the same, there is some variation in the lithium ion occupancy between the two sites in the Nb and Ta phases. It seems that the Nb phase has a higher content of Li ions in the octahedral environments, Li-2.

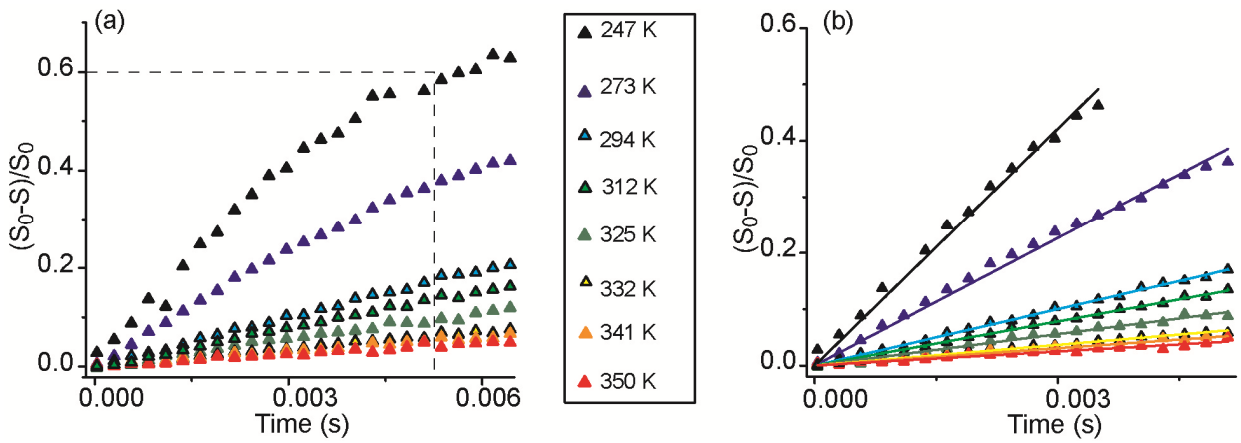

Figure 5.8. (a) ^{6}Li{^{7}Li}-REDOR curves of $Li_6BaLa_2Nb_2O_{12}$ over the temperature range of 247 K, where the sample is immobile, to 350 K. (b) Lines of best fit for each temperature have slopes *P*, which range from 140 ± 10 s^{-1}, for the immobile sample, to 8.3 ± 0.5s^{-1}.

To directly compare the lithium dynamics in this system, the variable temperature ^{6}Li{^{7}Li}-REDOR curves of $Li_6BaLa_2M_2O_{12}$ (M = Ta, Nb) have been considered. ***Figure 5.8*** shows the ^{6}Li{^{7}Li}-REDOR curves for the Nb material obtained over the temperature range of 247 K to 350 K. With increasing temperature the slopes of the REDOR curves change dramatically, particularly at higher temperatures. The temperature dependent slopes are summarized in ***Table 5.3.*** On considering the behaviour of *P*, it is evident that there is a much more significant contribution from dynamics in the Nb

material than for the Ta material. The Nb phase exhibits a slope of 8.3 ± 0.5 s^{-1} at 350 K, while the Ta phase has a slope of only 66 ± 1 s^{-1} at the same temperature as shown in ***Figure 5.7***.

With such different variations in the slopes over the same temperature range it is clear that the ionic motion in the Ta and Nb phases are quite different. While the literature predicts that these materials have differences in ionic conductivity and activation energy, it is unclear to what extent, since this is a point of disagreement. The most recent study of $Li_6BaLa_2Nb_2O_{12}$ reports an ionic conductivity of 4.4 x 10^{-4} S/cm with an activation energy of 0.35 eV.[20] While the most recent study of the Ta phase reports an ionic conductivity of 1.3 x 10^{-5} S/cm and an activation energy of 0.44 eV.[14] Their result would indicate that the Nb phase is an overall better material when considering ionic conductivity and activation energy. The results obtained in this study indicate qualitatively that the Nb phase has an overall higher ionic conductivity at room temperature than the Ta phase due to the smaller value of the slope, *P*, at room temperature.

NMR spectroscopy is capable of observing ionic motion within the particle, and therefore grain boundary resistance does not play a role in the measurement of ion hopping processes, whereas in bulk conductivity measurements, it is difficult to remove the inherent bulk effects. Here, we observe firsthand the importance of using preparation techniques that reduce grain boundary resistance. The NMR spectroscopic data collected here shows that the Nb phase is clearly the better ionic conductor, while previous bulk conductivity measurements have been inconclusive.

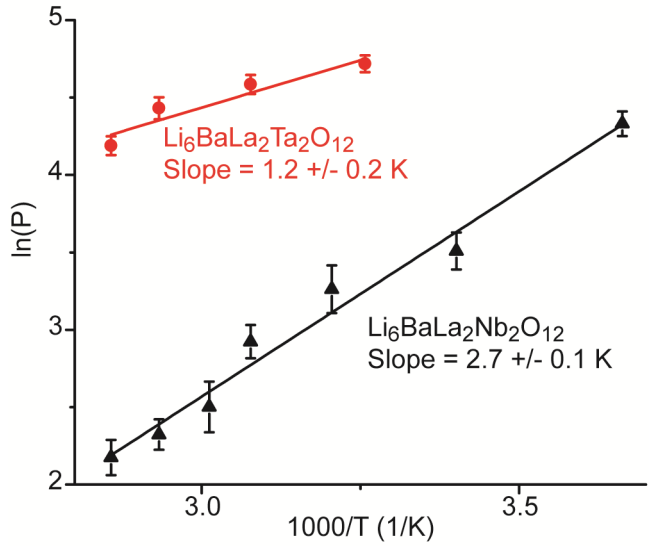

Figure 5.9. Pseudo-Arrhenius analysis of *P* for $Li_6BaLa_2M_2O_{12}$ (M = Ta, Nb). The red circles represent the Ta phase, while the black triangles represent the Nb phase. The slopes are 1.2 ± 0.2 K and 2.7 ± 0.1 K, respectively, for the Ta and Nb phases.

A pseudo-Arrhenius analysis of the changes in *P* for $Li_6BaLa_2M_2O_{12}$ (M = Ta, Nb) was performed and is shown in ***Figure 5.9***. This plot shows that the changes in the slopes of the REDOR curves follow a consistent trend. The slopes of the pseudo-Arrhenius plots show clearly different slopes for the Ta and Nb phases. The Ta phase has a slope of 1.2 ± 0.2 K, while the Nb phase has a steeper slope of 2.7 ± 0.1 K. This indicates that there likely a difference in the activation energy of local lithium ion hopping in these materials within this temperature range, and since the Nb phase shows a more significant temperature dependence it is likely that this material has a higher activation energy for lithium ion hopping. For this analysis, the data points that correspond to the REDOR curves with the lowest temperatures are not considered. The low temperature measurements were not taken to determine the specific temperature (freezing point) at which the slope was no longer temperature dependent, and thus the

slopes corresponding to the lowest temperatures represent a point of convergence of the slopes at low temperatures.

This study is capable of qualitatively determining which of these materials shows a greater response to changes in temperature, and therefore indicates which phase is a better ion conductor at a particular temperature. However, the results do not lead to straight forward quantitative data since the relationship between the changes in *P* and changes in ionic hopping rate are not precisely defined from this method. Note that there is the possibility of using gradient NMR methods (such as pulsed-field gradient NMR) to study diffusion in these materials and subsequently relate this to the values of *P* obtained from the current method. $Li_6BaLa_2Nb_2O_{12}$ appears to have higher ionic conductivity at room temperature. Although the Ta and Nb structures appear to be very similar, it is likely that the difference in the distribution of lithium ions within each structure contributes to differences in ion mobility.

The ^{6}Li MAS NMR spectra in ***Figure 5.1*** (b) show that there is a greater ratio of lithium in the octahedral site in each of the Ta and Nb phases. This site, Li-2, is known to be solely responsible for lithium ion motion in these phases. For the Nb phase, there is significantly more Li in the Li-2 site, while the NMR results show that this phase exhibits higher ionic conductivity at room temperature. These findings suggest that the higher content of lithium in Li-2 in the Nb phase is potentially the cause of the observed higher ionic conductivity in the Nb phase when compared to the Ta counterpart. Although it is not clear from previous studies the extent to which the concentration of lithium in a single

site contributes to the ion hopping rate, this study would suggest that for this material, greater amounts of Li in the octahedral site leads to an increase in the rate of ion hopping.

5.6. Conclusion

Solid-state ^{6}Li{^{7}Li}-REDOR NMR spectroscopy has been used to compare the ionic conductivity in $Li_6BaLa_2M_2O_{12}$ (M = Ta, Nb). ^{6}Li{^{7}Li}-REDOR NMR was used to indirectly study changes in ^{6}Li-^{7}Li dipolar coupling as a function of temperature, which were related to the changes in ion mobility by examining the temperature dependence of slope of the resulting REDOR curve. Higher temperatures increased the ionic mobility for each of the phases, resulting in a shallower slope of the REDOR curve. This occurs as a result of increased mobility at a hopping rate similar to the ^{6}Li-^{7}Li dipolar coupling. The curves were characterised according the slope, *P*. The Nb phase showed a greater change in *P* with increasing temperature, and thus generated a steeper slope in the pseudo-Arrhenius analysis. While this method does not quantitatively measure the ionic hopping rate, it has clearly points out that the Nb material has higher ion hopping rate than the Ta phase at room temperature and above. In addition it is indicated that the Nb phase has a higher activation energy for lithium ion hopping when compared to the Ta counterpart.

The reason for the observed differences in ion conductivity between these two phases is likely the difference in the lithium ion distribution among the two existing crystallographic sites. ^{6}Li MAS NMR spectra have revealed that the Nb phase has a higher content of lithium in the octahedral environment, which is responsible for lithium ion motion.

5.7. References

1. Goodenough, J. B.; Kim, Y., Challenges for Rechargeable Li Batteries. *Chemistry of Materials* **2010,** 22, (3), 587-603.

2. Thangadurai, V.; Weppner, W., Investigations on electrical conductivity and chemical compatibility between fast lithium ion conducting garnet-like $Li_6BaLa_2Ta_2O_{12}$ and lithium battery cathodes. *Journal of Power Sources* **2005,** 142, (1-2), 339-344.

3. Thangadurai, V.; Schwenzel, J.; Weppner, W., Tailoring ceramics for specific applications: A case study of the development of all-solid-state lithium batteries. *Ionics* **2005,** 11, (1-2), 11-23.

4. Thangadurai, V.; Weppner, W., $Li_6ALa_2Nb_2O_{12}$ (A = Ca, Sr, Ba): A new class of fast lithium ion conductors with garnet-like structure. *Journal of the American Ceramic Society* **2005,** 88, (2), 411-418.

5. Nakayama, M.; Kotobuki, M.; Munakata, H.; Nogami, M.; Kanamura, K., First-principles density functional calculation of electrochemical stability of fast Li ion conducting garnet-type oxides. *Physical Chemistry Chemical Physics* **2012,** 14, (28), 10008-10014.

6. Cussen, E. J., The structure of lithium garnets: cation disorder and clustering in a new family of fast Li^+ conductors. *Chemical Communications* **2006**, (4), 412-413.

7. Awaka, J.; Kijima, N.; Hayakawa, H.; Akimoto, J., Synthesis and structure analysis of tetragonal $Li_7La_3Zr_2O_{12}$ with the garnet-related type structure. *Journal of Solid State Chemistry* **2009,** 182, (8), 2046-2052.

8. Buschmann, H.; Dolle, J.; Berendts, S.; Kuhn, A.; Bottke, P.; Wilkening, M.; Heitjans, P.; Senyshyn, A.; Ehrenberg, H.; Lotnyk, A.; Duppel, V.; Kienle, L.; Janek, J., Structure and dynamics of the fast lithium ion conductor "$Li_7La_3Zr_2O_{12}$". *Physical Chemistry Chemical Physics* **2011,** 13, (43), 19378-19392.

9. Thangadurai, V.; Weppner, W., $Li_6ALa_2Ta_2O_{12}$ (A=Sr, Ba): Novel garnet-like oxides for fast lithium ion conduction. *Advanced Functional Materials* **2005,** 15, (1), 107-112.

10. Vosegaard, T.; Byriel, I. P.; Pawlak, D. A.; Wozniak, K.; Jakobsen, H. J., Crystal structure studies on the garnet $Y_3Al_5O_{12}$ by Al-27 single-crystal NMR spectroscopy. *Journal of the American Chemical Society* **1998,** 120, (31), 7900-7904.

11. Thangadurai, V.; Adams, S.; Weppner, W., Crystal structure revision and identification of Li^+-ion migration pathways in the garnet-like $Li_5La_3M_2O_{12}$ (M = Nb, Ta) oxides. *Chemistry of Materials* **2004,** 16, (16), 2998-3006.

12. O'Callaghan, M. P.; Cussen, E. J., Lithium dimer formation in the Li-conducting garnets $Li_{5+x}Ba_xLa_{3-x}Ta_2O_{12}$ ($0 < x <= 1.6$). *Chemical Communications* **2007**, (20), 2048-2050.

13. Murugan, R.; Thangadurai, V.; Weppner, W., Fast lithium ion conduction in garnet-type $Li_7La_3Zr_2O_{12}$. *Angewandte Chemie-International Edition* **2007,** 46, (41), 7778-7781.

14. Awaka, J.; Kijima, N.; Takahashi, Y.; Hayakawa, H.; Akimoto, J., Synthesis and crystallographic studies of garnet-related lithium-ion conductors $Li_6CaLa_2Ta_2O_{12}$ and $Li_6BaLa_2Ta_2O_{12}$. *Solid State Ionics* **2009,** 180, (6-8), 602-606.

15. O'Callaghan, M. P.; Powell, A. S.; Titman, J. J.; Chen, G. Z.; Cussen, E. J., Switching on fast lithium ion conductivity in garnets: The structure and transport properties of $Li_{3+x}Nd_3Te_{2-x}Sb_xO_{12}$. *Chemistry of Materials* **2008,** 20, (6), 2360-2369.

16. van Wullen, L.; Echelmeyer, T.; Meyer, H. W.; Wilmer, D., The mechanism of Li-ion transport in the garnet $Li_5La_3Nb_2O_{12}$. *Physical Chemistry Chemical Physics* **2007,** 9, (25), 3298-3303.

17. Nyman, M.; Alam, T. M.; McIntyre, S. K.; Bleier, G. C.; Ingersoll, D., Alternative Approach to Increasing Li Mobility in Li-La-Nb/Ta Garnet Electrolytes. *Chemistry of Materials* **2010,** 22, (19), 5401-5410.

18. Koller, H.; Kalwei, M., Studying ionic motion in tetrahydroxoborate sodalite by second moment analysis using Na-23{B-11} rotational echo double resonance data. *Journal of Physical Chemistry B* **2004,** 108, (1), 58-63.

19. Gullion, T.; Schaefer, J., Rotational-Echo Double-Resonance Nmr. *Journal of Magnetic Resonance* **1989,** 81, (1), 196-200.

20. Truong, L.; Thangadurai, V., Soft-Chemistry of Garnet-Type $Li_{5+x}Ba_xLa_{3-x}Nb_2O_{12}$ (x=0, 0.5, 1): Reversible H^+ <-> Li^+ Ion-Exchange Reaction and Their X-ray, Li-7 MAS NMR, IR, and AC Impedance Spectroscopy Characterization. *Chemistry of Materials* **2011,** 23, (17), 3970-3977.

21. Lee, Y. J.; Wang, F.; Grey, C. P., Li-6 and Li-7 MAS NMR studies of lithium manganate cathode materials. *Journal of the American Chemical Society* **1998,** 120, (48), 12601-12613.

22. Klett, M.; Giesecke, M.; Nyman, A.; Hallberg, F.; Lindstrom, R. W.; Lindbergh, G.; Furo, I., Quantifying Mass Transport during Polarization in a Li Ion Battery Electrolyte by in Situ Li-7 NMR Imaging. *Journal of the American Chemical Society* **2012,** 134, (36), 14654-14657.

23. Grey, C. P.; Lee, Y. J., Lithium MAS NMR studies of cathode materials for lithium-ion batteries. *Solid State Sciences* **2003,** 5, (6), 883-894.

24. Cahill, L. S.; Chapman, R. P.; Kirby, C. W.; Goward, G. R., The challenge of paramagnetism in two-dimensional Li-6,Li-7 exchange NMR. *Applied Magnetic Resonance* **2007,** 32, (4), 565-581.

25. Davis, L. J. M.; Heinmaa, I.; Goward, G. R., Study of Lithium Dynamics in Monoclinic $Li_3Fe_2(PO_4)_3$ using Li-6 VT and 2D Exchange MAS NMR Spectroscopy. *Chemistry of Materials* **2010,** 22, (3), 769-775.

26. Xu, Z.; Stebbins, J. F., Li-6 Nuclear-Magnetic-Resonance Chemical-Shifts, Coordination-Number and Relaxation in Crystalline and Glassy Silicates. *Solid State Nuclear Magnetic Resonance* **1995,** 5, (1), 103-112.

27. Cahill, L. S.; Chapman, R. P.; Britten, J. F.; Goward, G. R., Li-7 NMR and two-dimensional exchange study of lithium dynamics in monoclinic $Li_3V_2(PO_4)_3$. *Journal of Physical Chemistry B* **2006,** 110, (14), 7171-7177.

28. Davis, L. J. M.; He, X. J.; Bain, A. D.; Goward, G. R., Studies of lithium ion dynamics in paramagnetic cathode materials using Li-6 1D selective inversion methods. *Solid State Nuclear Magnetic Resonance* **2012,** 42, 26-32.

29. Fernandez, C.; Lang, D. P.; Amoureux, J. P.; Pruski, M., Measurement of heteronuclear dipolar interactions between quadrupolar and spin-1/2 nuclei in solids by multiple-quantum REDOR NMR. *Journal of the American Chemical Society* **1998,** 120, (11), 2672-2673.

30. Tran, T. T.; Herfort, D.; Jakobsen, H. J.; Skibsted, J., Site Preferences of Fluoride Guest Ions in the Calcium Silicate Phases of Portland Cement from Si-29{F-19} CP-REDOR NMR Spectroscopy. *Journal of the American Chemical Society* **2009,** 131, (40), 14170-+.

31. Gullion, T., Introduction to rotational-echo, double-resonance NMR. *Concepts in Magnetic Resonance* **1998,** 10, (5), 277-289.

32. Toke, O.; Cegelski, L.; Schaefer, J., Peptide antibiotics in action: Investigation of polypeptide chains in insoluble environments by rotational-echo double resonance. *Biochimica Et Biophysica Acta-Biomembranes* **2006,** 1758, (9), 1314-1329.

33. Jaroniec, C. P.; Tounge, B. A.; Rienstra, C. M.; Herzfeld, J.; Griffin, R. G., Measurement of C-13-N-15 distances in uniformly C-13 labeled biomolecules: J-decoupled REDOR. *Journal of the American Chemical Society* **1999,** 121, (43), 10237-10238.

34. Merritt, M. E.; Christensen, A. M.; Kramer, K. J.; Hopkins, T. L.; Schaefer, J., Detection of intercatechol cross-links in insect cuticle by solid-state carbon-13 and nitrogen-15 NMR. *Journal of the American Chemical Society* **1996,** 118, (45), 11278-11282.

35. Merritt, M. E.; Sigurdsson, S. T.; Drobny, G. P., Long-range distance measurements to the phosphodiester backbone of solid nucleic acids using P-31-F-19 REDOR NMR. *Journal of the American Chemical Society* **1999,** 121, (25), 6070-6071.

36. Bertmer, M.; Eckert, H., Dephasing of spin echoes by multiple heteronuclear dipolar interactions in rotational echo double resonance NMR experiments. *Solid State Nuclear Magnetic Resonance* **1999,** 15, (3), 139-152.

37. Puls, S. P.; Eckert, H., Spatial distribution of lithium ions in glasses studied by Li-7{Li-6} spin echo double resonance. *Physical Chemistry Chemical Physics* **2007,** 9, (30), 3992-3998.

38. Goetz, J. M.; Schaefer, J., REDOR dephasing by multiple spins in the presence of molecular motion. *Journal of Magnetic Resonance* **1997,** 127, (2), 147-154.

39. Celinski, V. R.; Weber, J.; der Gunne, J. S. A., C-REDOR curves of extended spin systems. *Solid State Nuclear Magnetic Resonance* **2013,** 49-50, 12-22.

40. Alam, T. M.; McLaughlin, J.; Click, C. C.; Conzone, S.; Brow, R. K.; Boyle, T. J.; Zwanziger, J. W., Investigation of sodium distribution in phosphate glasses using spin-echo Na-23 NMR. *Journal of Physical Chemistry B* **2000,** 104, (7), 1464-1472.

41. Tsuchida, J.; Schneider, J.; Deshpande, R. R.; Eckert, H., Cation Distribution and Local Order in Mixed Sodium Metaphosphate Glasses. *Journal of Physical Chemistry C* **2012,** 116, (46), 24449-24461.

42. Cahill, L. S.; Kirby, C. W.; Goward, G. R., Li-6{P-31} rotational-echo, double-resonance studies of lithium ion site dynamics in $Li_3V_2(PO_4)_3$. *Journal of Physical Chemistry C* **2008,** 112, (6), 2215-2221.

43. Dupke, S.; Langer, T.; Pottgen, R.; Winter, M.; Passerini, S.; Eckert, H., Structural characterization of the lithium silicides $Li_{15}Si_4$, $Li_{13}Si_4$, and Li_7Si_3 using solid state NMR. *Physical Chemistry Chemical Physics* **2012,** 14, (18), 6496-6508.

44. Grey, C. P.; Cheetham, A. K.; Dobson, C. M., Temperature-Dependent Solid-State Sn-119 MAS NMR of $Nd_2Sn_2O_7$, $Sm_2Sn_2O_7$, and $Y_{1.8}Sm_{0.2}Sn_2O_7$ - Three Sensitive Chemical-Shift Thermometers. *Journal of Magnetic Resonance Series A* **1993,** 101, (3), 299-306.

45. Veshtort, M.; Griffin, R. G., SPINEVOLUTION: A powerful tool for the simulation of solid and liquid state NMR experiments. *Journal of Magnetic Resonance* **2006,** 178, (2), 248-282.

46. B. Downs, K. B., Kausil Simmaswamy *XtalDraw*, 2003.

47. Apperley, D. C., Harris, R. K., Hodgkinson, P., *Solid-State NMR: Principles and Practice*. Momentum Press: New York, 2012; p 276.

48. Gee, B.; Eckert, H., Cation distribution in mixed-alkali silicate glasses. NMR studies by Na-23-{Li-7} and Na-23-{Li-6} spin echo double resonance. *Journal of Physical Chemistry* **1996,** 100, (9), 3705-3712.

49. Causemann, S.; Schonhoff, M.; Eckert, H., Local environment and distribution of alkali ions in polyelectrolyte complexes studied by solid-state NMR. *Physical Chemistry Chemical Physics* **2011,** 13, (19), 8967-8976.

Chapter 6: Analysing Dynamics in Lithium Ion Conductors Using Changes in ^{6,7}Li T_2 Relaxation Times Extracted from REDOR and SEDOR Experiments

6.1. Introduction

NMR spectroscopy is a versatile tool that can be used to study different types of ion dynamics in solid-state materials, which can vary substantially in the respective timescales. A variety of NMR techniques are available, and the choice of method is often governed by its sensitivity to the timescale of dynamic processes. In Chapter 5 of this thesis the use of ^{6}Li{^{7}Li}-REDOR NMR was discussed and it was found that the sensitivity of the REDOR experiment to the ion hopping present in this system was governed by the relative values of the ^{6}Li-^{7}Li dipolar coupling and the rate of ion hopping (each in Hz). In this case, since these values were close in magnitude, the REDOR experiment was useful to observe changes in ion hopping rate as a function of temperature.

In many cases, however, the dipolar coupling between an ion pair is not close in value to the ion hopping rate, and is therefore insensitive to changes in ion hopping rate as a function of temperature. Thus, different NMR techniques must be used in order to sample a wider range of timescales. Another method of probing ion exchange is the use of relaxation measurements as a function of temperature. T_1 and T_2 relaxation experiments have been used widely to study dynamics in a variety of systems.[1] Like the REDOR experiment, the sensitivity of relaxation measurements to dynamic processes is also

limited by the timescales of ion hopping, also known as the correlation time (the inverse of the ion hopping rate) in relation to the T_1 or T_2 relaxation times (in seconds).[2] When these rates are close in value, relaxation measurements become sensitive to changes in ion hopping rates. In some cases, such as the garnet-like materials discussed in Chapter 5 of this thesis, T_1 experiments are not ideal since T_1 relaxation times can be long (> 100 s).

This chapter assesses the use of T_2 relaxation measurements as a function of temperature to evaluate ion hopping in lithium ion conductors. This method of analysis came as a result of the fact that T_2 relaxation measurements are inherent within the REDOR and SEDOR experiments, and this relationship will be discussed later. Some of the details of T_2 relaxation have been discussed in Chapter 2 of this thesis, including the general definition and the NMR experiments typically used to measure T_2 relaxation times. T_2 is sensitive to changes in ion hopping rate, but is also affected by homonuclear and heteronuclear dipolar coupling, as well as many other factors, such as paramagnetic effects.[3] It is not clear at this point if these factors influence the study of dynamic processes using T_2 measurements.

Model materials $Li_3V_2(PO_4)_3$ and $LiVO_3$ have been studied here with the goal of determining the activation energy for lithium ion hopping using T_2 measurements, in order to determine if this is a viable method to study dynamics in these systems. Much of the work here is extracted from initial studies of these materials using REDOR and SEDOR experiments. While previous studies have measured the rate of lithium ion hopping between specific crystallographic sites, the measurement of the ^{6}Li or ^{7}Li T_2 as a function of temperature cannot give exchange information about exchange pairs. Instead

the activation energy for lithium ion hopping can be calculated for processes that occur between sites, without knowledge of which sites participate in the exchange process.

$Li_3V_2(PO_4)_3$ is a paramagnetic cathode materials for lithium ion batteries with three unique crystallographic sites and has previously been studied using ^{7}Li 2D EXSY NMR experiments and ^{6}Li 1D selective inversion NMR experiments.[4, 5] $LiVO_3$ is a diamagnetic cathode material for lithium ion batteries and has two unique crystallographic sites.[6] This material provides a good comparison to the paramagnetic $Li_3V_2(PO_4)_3$ as it contains a number of lithium sites, but does not have a paramagnetic contribution to the T_2. $LiVO_3$ is known to have a Li^+ diffusion coefficient of $10^{-9.5}$ to 10^{-8} cm^2s^{-2}, whereas $Li_3V_2(PO_4)_3$ has a Li^+ diffusion coefficient of 10^{-13} to 10^{-8} cm^2s^{-1} (as calculated from galvanostatic intermittent titration, GITT, electrochemical experiments).[7]

This study arose from initial attempts to evaluate the lithium ion dynamics in $Li_3V_2(PO_4)_3$ using the measurement of the ^{6}Li{^{7}Li}-REDOR curve as a function of temperature, which did not producing the expected results. The REDOR curve did not show a decrease in slope with increasing temperature as expected (Chapter 5). On assumption that there was a contribution from relaxation, the T_2 relaxation was extracted from the REDOR measurement and it was found that this changed dramatically with temperature. It was concluded that the sensitivity of T_2 relaxation to dynamics was due to the Li ion correlation times having values that were closer to the T_2 relaxation times than the inverse of the ^{6}Li-^{7}Li dipolar coupling. Therefore it was hypothesized that measurements of T_2 as a function of temperature would result in an activation energy for

lithium ion hopping that could be compared to previous results in order to determine if this method is a viable tool to study ion dynamics in this system.

6.2. Experimental

6.2.1. Sample Preparation

$Li_3V_2(PO_4)_3$ and $LiVO_3$ were prepared according to the methods outlined by Cahill *et al* and Muller *et al.,* respectively.[8] 50% ^{6}Li enrichment was achieved by using ^{6}Li enriched Li_2CO_3. In each case powder X-ray diffraction (PXRD) was used for phase confirmation as shown in Appendix A3.

6.2.2. ^{6,7}Li NMR Spectroscopy Experiments

REDOR and SEDOR experiments were performed for $LiVO_3$ observing ^{7}Li and dephasing ^{6}Li. For the REDOR experiments 64 slices were collected in the F1 dimension, which resulted in 32 points for the Hahn-echo decay. For ^{6}Li a nutation frequency of 54 kHz was used and for ^{7}Li nutation frequency of 91 kHz was used. For the SEDOR experiments 16 transients were collected with a recycle delay of 30 s, and 32 points were collected in the indirect dimension. The echo delay was set manually, and was optimized to obtain the largest range of points in the resulting SEDOR curve while still defining the features of the curve (this value determines the time between the points in the curve). An echo delay of 6.67 us was found to be optimal for this sample. This delay was used for both the echo delay and the refocusing time and when the time axis was calculated for data processing all of the time between the initial $^{\pi}/_2$ pulse and the signal collection were

considered (echo delay + refocusing time + π-pulse length + dead time). T_2 decay curves were extracted from REDOR and SEDOR data, which will be described later.

T_2 measurements were collected using a series of Hahn-echo experiments in which the delays were varied. ***Figure 6.1*** shows the Hahn-echo pulse sequence. τ_1 and τ_2 were systematically optimized to obtain approximately 32 points which varied as a function of the total echo time (the sum of the echo delay, the refocusing time and the π/2 pulse length). Data was processed by comparing the relative intensity of each experiment to the first. With increasing delay times the relative intensity of the peak of interest decreased exponentially. Data will be shown in the Results and Discussion section.

^{7}Li MAS NMR spectra of $Li_3V_2(PO_4)_3$ were collected using the Hahn-echo pulse sequence with MAS of 25 kHz, in which all 180° pulses were rotor synchronized. The pulse sequence is shown in ***Figure 6.1***. 10240 transients were collected with a recycle delay of 0.2 s. A nutation frequency of 91 kHz was used. The experiments were carried out over the temperature range of 262 K to 335 K, and for each T_2 measurement 14 experiments were performed, which varied in echo delay and refocusing time.

^{6}Li MAS NMR spectra of $Li_3V_2(PO_4)_3$ were collected using a REDOR experiment with MAS of 25 kHz. The relevant pulse sequence is shown in ***Figure 6.2***. 3072 transients were collected with a recycle delay of 0.2 s. 64 slices were collected in the indirect dimension, which resulted in 32 points for the Hahn-echo decay. For ^{6}Li a nutation frequency of 54 kHz was used and for ^{7}Li a nutation frequency of 91 kHz was used. Details of the extraction of T_2 data from the REDOR experiment are given in the

following section. This experiment was repeated as a function of temperature over the range of 262 K to 335 K.

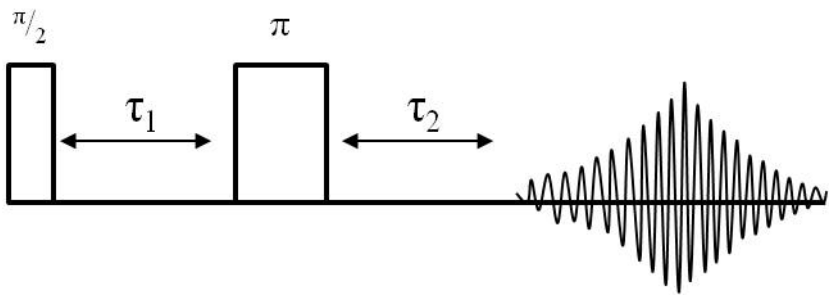

Figure 6.1. Hahn-echo pulse sequence used to measure T_2. A series of Hahn-echo experiments are performed with variation in the echo delay, and refocusing time (τ_1 and τ_2, respectively).

6.2.3. Extraction of T_2 from REDOR and SEDOR Experiments

REDOR and SEDOR experiments are used to measure dipolar coupling between pairs of heteronuclear spins, as discussed in Chapters 2 and 5 in this thesis. Inherent in each of these experiments is the Hahn-echo experiment, which is used to acquire the signal of observed nucleus (*I*). REDOR and SEDOR experiments are performed as a function of dephasing time. In the case of the REDOR experiment, MAS is used and an increasing numbers of rotor periods are combined with pulses on the *S* channel (not observed). In the SEDOR experiment delays are set in the experiment and there is only a single pulse in the S channel. These pulse sequences are shown in ***Figure 6.2***.

REDOR and SEDOR experiments result in curves which are calculated by taking the intensity ratio of a resonance in the form of $(S-S_0)/S_0$, where S is the intensity of the observed resonance, and plotting this as a function of the dephasing time. S_0 is the

intensity of the Hahn-echo with no pulses applied on the *S* channel, and S is the intensity when there are pulses applied on the *S* channel. *S (italic)* is the conventional term for the non-observe spin, and is not related to $(S-S_0)/S_0$, which refers to the intensity of the *I* spin.

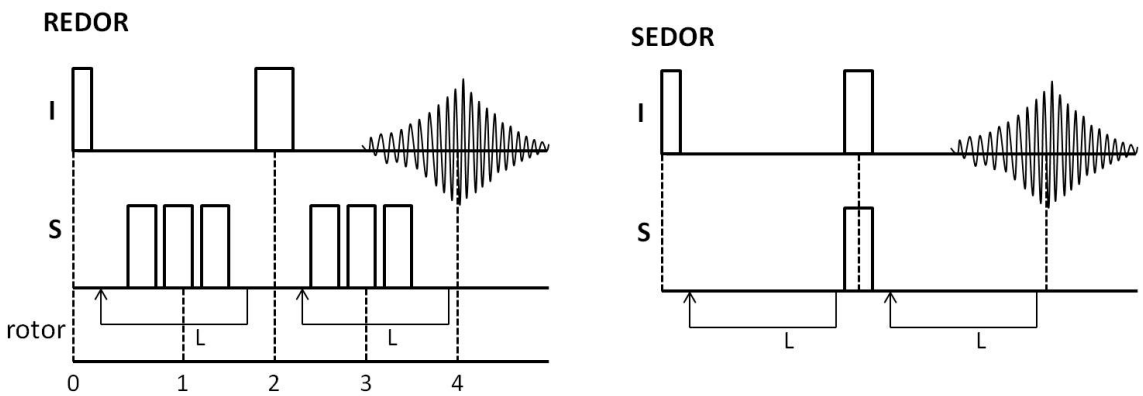

Figure 6.2. REDOR and SEDOR NMR experiments. The REDOR experiment is performed under MAS and is rotor synchronized, while the SEDOR experiment is performed with no MAS. In each experiment the signal of the *I* spin is collected using a Hahn-echo, while the *S* spin is not observed.

T_2 measurements can be extracted from the REDOR and SEDOR experiments by using a different method of data processing. Instead of plotting $(S-S_0)/S_0$ as a function of dephasing time, S/S_1 is plotted as a function of dephasing time, where S_1 is the intensity of the first experiment with the smallest dephasing time. Only the experiments with no pulsing on the *S* spins are included (i.e. the Hahn-echo experiments).

T_2 relaxation is an exponential decay. Therefore the T_2 can be calculated by taking the natural log (ln) of the Hahn-echo signal decay (S/S_1), as in ***Equation 6.1***.

$$M = M_0 \exp\left[\frac{-\tau}{T_2}\right] \qquad 6.1\ (a)$$

$$\ln(M) = \ln(M_0) - [\frac{\tau}{T_2}] \qquad 6.1\ (b)$$

M represents the magnetization in the xy-plane, which is measured by the T_2 experiment, and is represented by the relative intensity of a resonance to the initial intensity (S/S_1). M_0 is a constant, and τ is the total echo time. A plot of $\ln(S/S_1)$ vs. Time (τ) results in a line with a slope of ($-1/T_2$), and therefore $T_2 = -1/(\text{slope})$.

6.3. Results and Discussion

6.3.1. T_2 Relaxation in $LiVO_3$

Lithium vanadium oxide is a potential cathode material for lithium ion batteries, since it conducts both lithium ions and electrons and has a redox active vanadium centre. It has provided an interesting model material for learning the details of the REDOR and SEDOR experiments, and has also proven to be enlightening in terms of the ^{7}Li T_2 analysis. ***Figure 6.3*** shows the ^{7}Li and ^{6}Li MAS NMR spectra of 50% ^{6}Li enriched $LiVO_3$. The two observed lithium resonances are consistent with the two crystallographic lithium environments.[6]

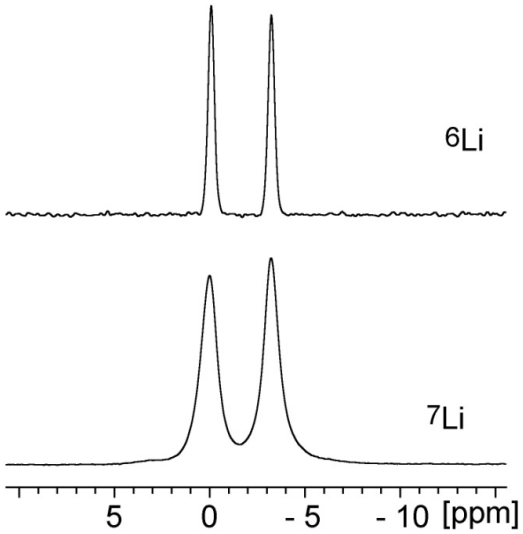

Figure 6.3. ^{6}Li and ^{7}Li MAS NMR spectra of $^{6,7}LiVO_3$. Two lithium resonances at 0.0 ppm (Li-1) and -3.2 ppm (Li-2) are observed. (Labels Li-1 and Li-2 are based on NMR assignment in this work).

REDOR (with MAS) and SEDOR (without MAS) experiments were performed in an attempt to compare the respective curves for these experiments in order to assess any differences that may be observed. Instead, it was found that while the REDOR experiment provided the expected REDOR curve, the SEDOR experiment resulted in scattered points with no visible trend. In order to understand the drastic difference in these very similar experiments, the T_2 relaxation was extracted from each of the respective experiments. ***Figure 6.4*** shows the T_2 relaxation curves for each of the Li sites in the REDOR experiment, and that of the SEDOR experiment (there is only a single broad resonance because the two lithium resonances are not resolved without MAS).

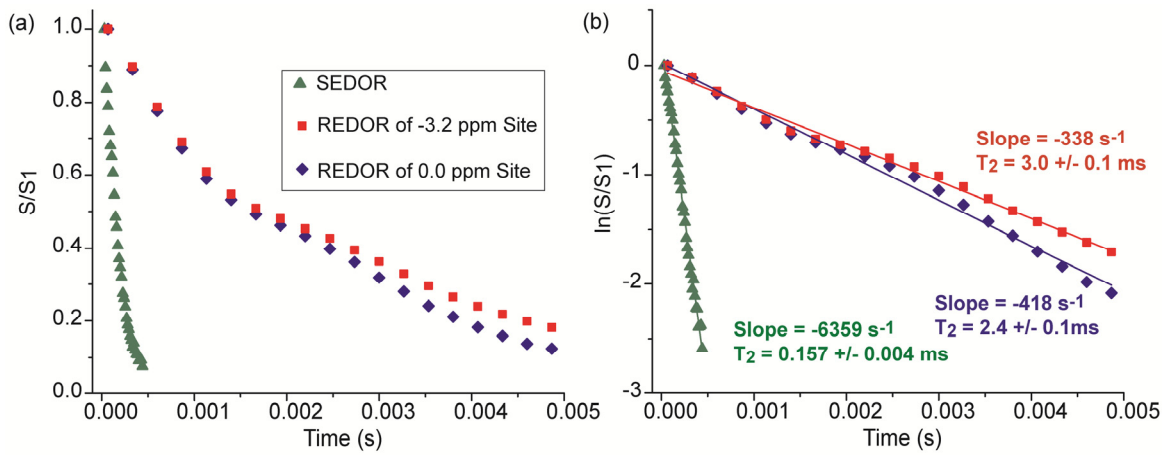

Figure 6.4. (a) T_2 decay of ^{7}Li in $LiVO_3$. This is the intensity of the signal relative to the first spectrum collected. (b) The natural log of the relative intensity of the Hahn-echo decay. The slopes of the best-fit lines are used to calculate the T_2 relaxation times.

The T_2 relaxation times measured for $LiVO_3$ using the REDOR and SEDOR experiments are significantly different. The T_2 of ^{7}Li from the SEDOR experiment is 0.157 ± 0.004 ms, which is an order of magnitude smaller than those observed for the two sites seen in the REDOR experiment, 3.0 ± 0.1 ms and 2.4 ± 0.1 ms, respectively for each site. The most probable cause for this dramatic difference is the fact that in the REDOR experiment the MAS averages the homonuclear and heteronuclear dipolar coupling, which are each contributing factors to the T_2 relaxation. The REDOR experiment refocuses only the heteronuclear dipolar coupling, and thus there is little, if any, contribution of the homonuclear dipolar coupling to the T_2 relaxation. Conversely, in the case of the T_2 extracted from the SEDOR experiment, there is no MAS, and therefore the homonuclear and heteronuclear dipolar couplings contribute to the T_2 relaxation.[9] The differences in the measured T_2 relaxation times points to the fact that there is a significant amount of homonuclear dipolar coupling between ^{7}Li neighbours in this system.

In order for REDOR, SEDOR or T_2 experiments to be sensitive to ion motion the timescale of the measurement must be close to (on the order of magnitude of) the time scale of ion hopping. From T_2 measurements in $LiVO_3$ it can be seen that the processes that will affect T_2 relaxation measurements are of different timescales than those that will affect the REDOR and SEDOR experiments. When REDOR experiments were performed on $LiVO_3$, there was no observable change in the REDOR curves, however, there was a small change in the measured T_2 for both Li sites, which is summarized in ***Table 6.1***.

Table 6.1: Temperature dependent ^{7}Li T_2 of ^{7}Li in $LiVO_3$.

	Li-1 (0.0 ppm)		Li-2 (-3.2 ppm)	
	Slope (s^{-1})	T_2 (ms)	Slope (s^{-1})	T_2 (ms)
300 K	-420 ± 10	2.4 ± 0.1	-340 ± 10	3.0 ± 0.1
350 K	-310 ± 10	3.3 ± 0.1	-280 ± 10	3.7 ± 0.1

6.3.2. T_2 Relaxation in $Li_3V_2(PO_4)_3$

The goal of this project was to extend the work done in Chapter 5, which used REDOR techniques to compare temperature dependent ion hopping rates $Li_6BaLa_2M_2O_{12}$ (M = Ta, Nb), to study a more complex system in which more than one crystallographic site contributed to ion dynamics.[8] The material $Li_3V_2(PO_4)_3$ provided a good test material since the details of ion hopping have been well characterized.[8] The 1D ^{6}Li MAS NMR spectrum of $Li_3V_2(PO_4)_3$ is shown in ***Figure 6.5*** along with an image of the crystal structure. The combination of the NMR and crystallographic assignments results in the following assignment: Li in NMR resonance C of crystallographic site 2 is known as Li_{C2}.

Therefore the three resonances seen in ***Figure 6.5*** are Li_{C2} (124 ppm), Li_{B1} (64 ppm) and Li_{A3} (22 ppm).

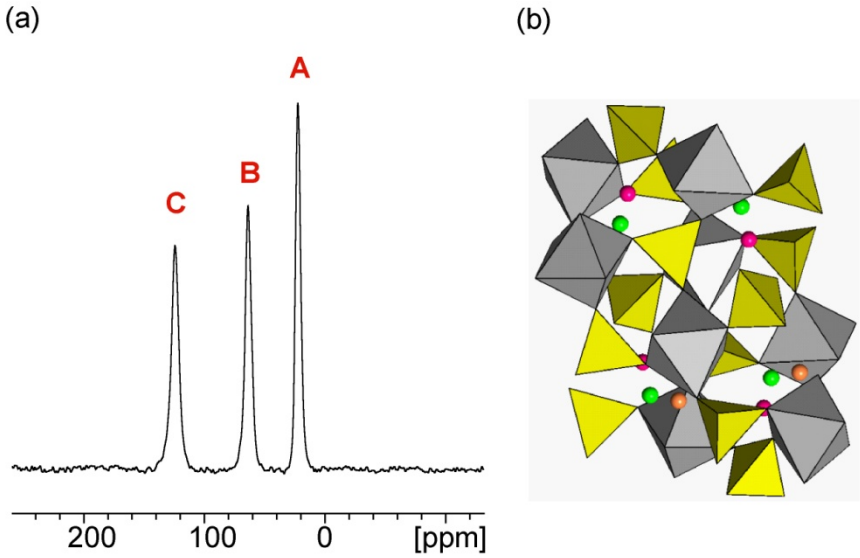

Figure 6.5. (a) ^{6}Li MAS NMR of $Li_3V_2(PO_4)_3$ collected at 262 K with MAS 25 kHz. (b) Drawing of the crystal structure of $Li_3V_2(PO_4)_3$. From the published crystal structure NMR resonances A at 22 ppm, B at 64 ppm, and C at 124 ppm, correspond to the orange, purple and green spheres, respectively (Li-3, Li-1 and Li-2 in the work of Yin *et al.*), giving resonances Li_{C2}, Li_{B1}, and Li_{A3} in order of high to low frequency in the NMR spectrum.[8, 10] Grey polyhedra represent vanadium centres and yellow polyhedra represent phosphorus centres.

^{6}Li{^{7}Li}-REDOR NMR was performed within the temperature range of 262 K to 335 K. The resulting REDOR curves have very shallow slopes as well as significant scatter in the points. As a result, obtaining an accurate measurement of each slope was not possible. ***Figure 6.6*** shows the temperature dependent REDOR curves for Li_{C2}, along with that of $LiVO_3$ for comparison. Previous studies have shown that an increase in temperature increases the rate of dynamic processes, and in general causes a decrease in the slope of the REDOR curve.[11] It is clear that there is no significant change in the

$Li_3V_2(PO_4)_3$ data with temperature, and the shallow slope indicates that the presence of dynamics with hopping rates faster than the ^{6}Li-^{7}Li dipolar coupling in this sample.

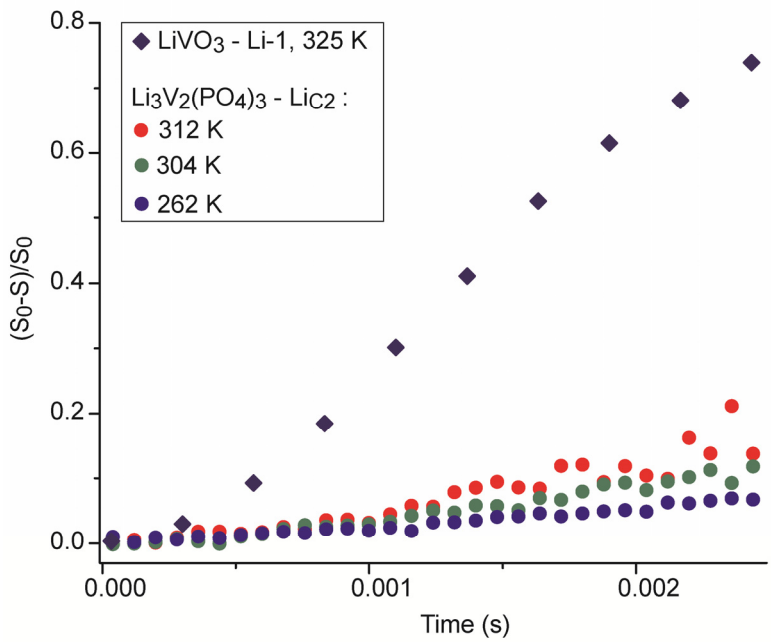

Figure 6.6. ^{6}Li{^{7}Li}-REDOR NMR of $Li_3V_2(PO_4)_3$ at site Li_{C2} between 262 K and 312 K compared to $LiVO_3$ Li-1 at 325 K. There $Li_3V_2(PO_4)_3$ REDOR curves are very shallow in comparison to that of $LiVO_3$, and there is little distinguishable change with temperature.

T_2 relaxation can be a limitation in the REDOR experiment. Significant changes in the T_2 of the observed ^{6}Li dominate the experiment and do not allow the observation of the changes in dipolar coupling. If spins in the observed *I* channel relax during the pulse sequence then the sensitivity of the experiment to the small changes that are caused by the ^{6}Li-^{7}Li dipolar coupling are not observed. During the REDOR experiment the ratio $(S_0-S)/S_0$ defines the REDOR curve. However, the value of S_0 comes from a Hahn-echo experiment. ***Figure 6.7*** shows Hahn-echo decay (the ratio S/S_1 , where S_1 is the spectral intensity of the first Hahn-echo experiment and S represent subsequent Hahn-echo experiments with no pulses on the ^{7}Li channel) for ^{6}Li in $Li_3V_2(PO4)_3$ in site Li_{C2}. It is

evident that the T_2 is changing with temperature, since the curves produced over this temperature range vary dramatically. There is little scatter or noise in the resulting curves, unlike those of the REDOR experiments.

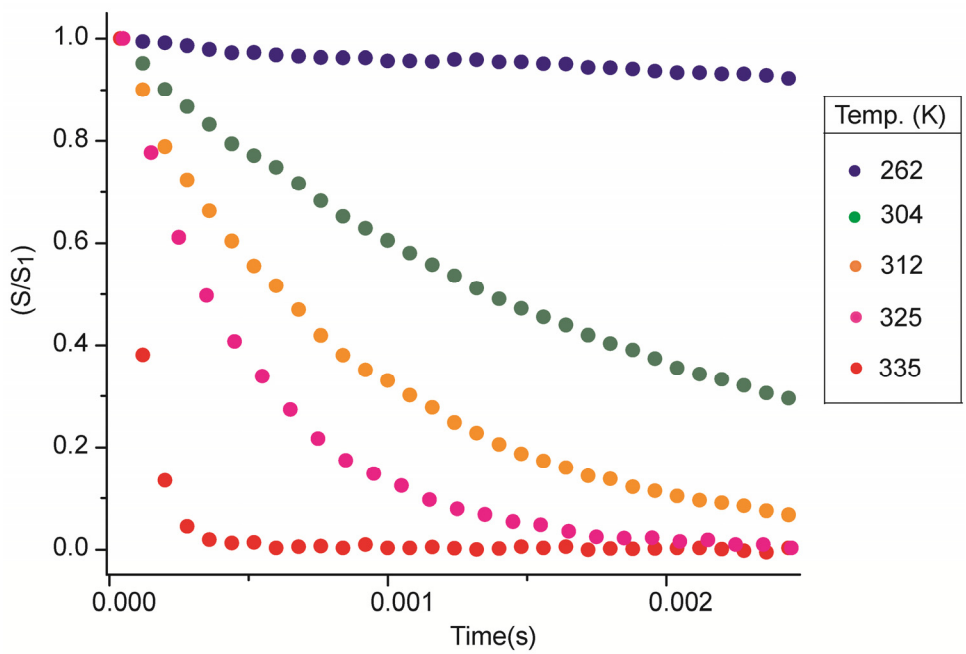

Figure 6.7. Hahn-echo ^{6}Li T_2 decay of site Li_{C2} in $Li_3V_2(PO_4)_3$. Experiments performed between 262 K and 335 K show a dramatic change in the rate of signal decay with increasing temperature.

Figure 6.8 shows the T_2 decay for Li_{C2} signal after the natural log was taken. Using the slopes of the lines, the T_2 for each temperature was calculated. It is evident that the T_2 relaxation has a strong temperature dependence, decreasing with temperature. Here, T_2 relaxation times range from 36 ± 3 ms to 0.090 ± 0.010 ms over a temperature range of 262 K to 335 K.

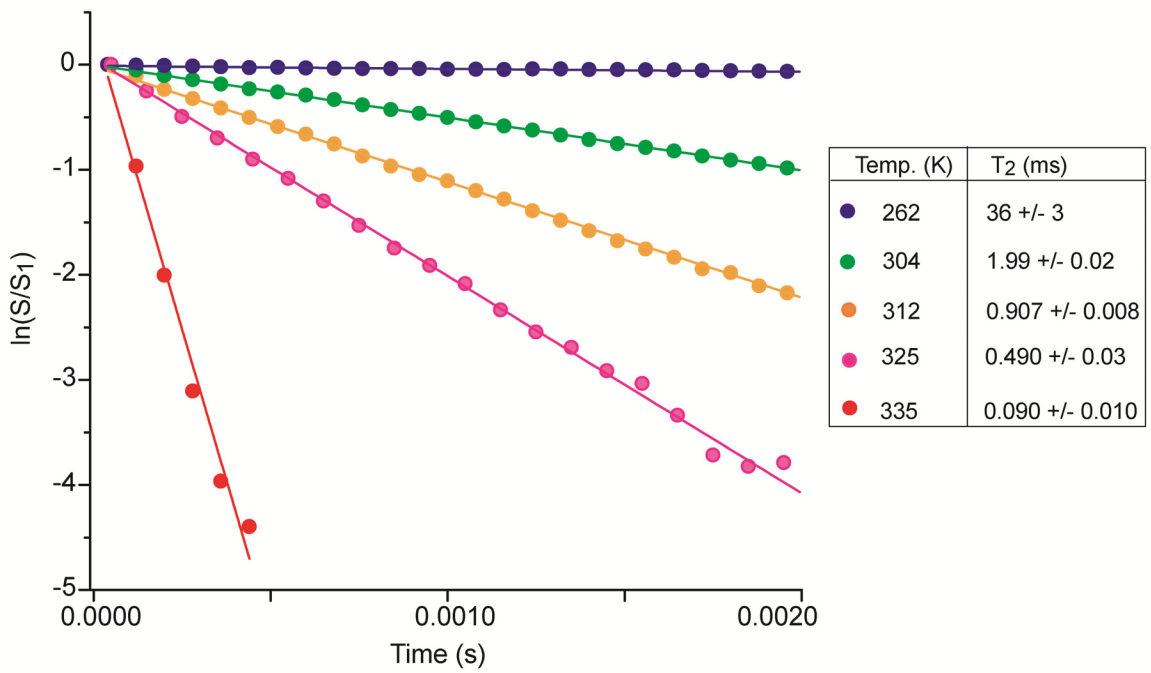

Figure 6.8. ^{6}Li T_2 relaxation of site Li_{C2} in $Li_3V_2(PO_4)_3$. Each respective value of T_2 is calculated from the slope of the line: T_2 = -1/(slope).

The temperature dependent T_2 was calculated for each of the three resonances and plotted together in an Arrhenius analysis: ln(T_2) vs. 1000/T. The goal was to calculate the activation energy for lithium ion hopping within each site. The three sites produced very similar activation energies, as shown in ***Figure 6.9.*** It should be noted that unlike the 1D selective inversion experiment, in which ion hopping between each site can be tracked separately, it is not possible to determine which sites are exchanging using T_2 studies alone.

In order to assess the validity of the results from T_2 measurements, the activation energies calculated in this experiment (42 ± 3 to 48 ± 3 kJ/mol, with an average of 45 ± 3 kJ/mol) were compared to those obtained by another member of the Goward Group, Danielle Smiley, which were measured using 1D selective inversion studies. It was found

that the current values are almost equal within error and agree with those calculated using 1D selective inversion experiments, where the selective inversion results have smaller uncertainties. ***Table 6.2*** shows a summary of the activation energies for lithium ion hopping measured using different approaches.

Table 6.2: Activation energies for lithium ion hopping in $Li_3V_2(PO_4)_3$.

T_2 Measurements (this work) (^6Li)		Selective Inversion (Danielle Smiley) (^6Li)	
Exchange Sites	Activation Energy (kJ/mol)	Exchange Sites	Activation Energy (kJ/mol)
Li_{A3}	42 ± 3	Li_{A3} - Li_{B1}	47 ± 2
Li_{B1}	44 ± 3	Li_{A3} – Li_{C2}	43 ± 2
Li_{C2}	48 ± 3	Li_{B1} – Li_{C2}	48 ± 1

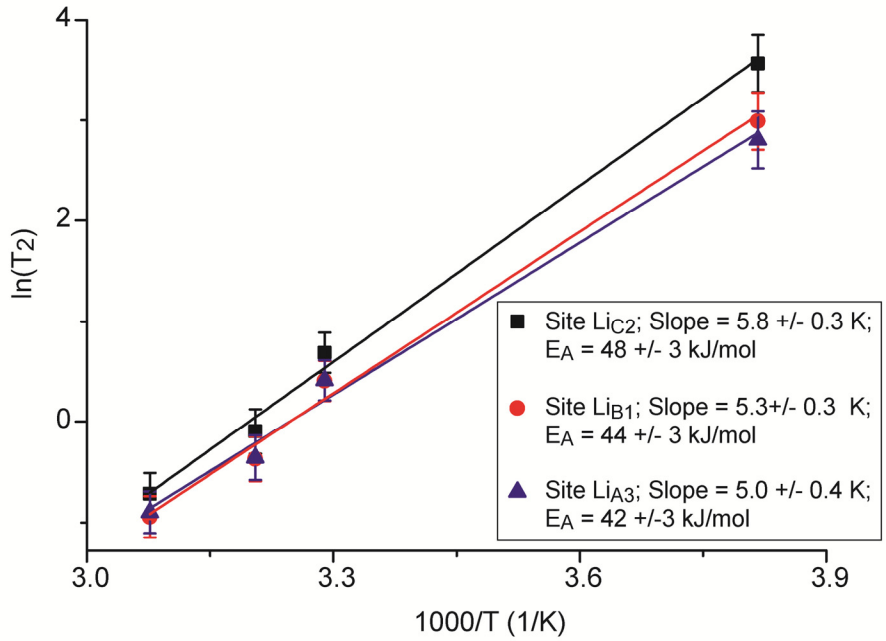

Figure 6.9. Arrhenius analysis of ^6Li sites Li_{C2}, Li_{B1} and Li_{A3} in $Li_3V_2(PO_4)_3$. The slopes for each site are similar, leading to very close values of the activation energy (E_A) for lithium hopping between sites.

In order for this data to be meaningful, it is necessary to consider what contributes to T_2 relaxation in this material. In this data set an enrichment of 50% ^{6}Li has been used, resulting in an equal distribution of ^{6}Li and ^{7}Li in the $Li_3V_2(PO_4)_3$ crystal structure. These data can be compared to the following:

a) The ^{7}Li data with 50% enrichment to determine if there is an effect from the isotope studied.
b) The case in which the ^{6}Li-^{7}Li isotope ratio is at natural abundance (with ^{7}Li at 92%) to determine if changes in the value ^{6}Li-^{7}Li dipolar coupling affect the calculated activation energy for lithium ion hopping.

Figure 6.10 shows the ^{7}Li T_2 relaxation data for $Li_3V_2(PO_4)_3$ at 50% ^{6}Li enrichment and at natural abundance, while ***Table 6.3*** shows the T_2 relaxation times for all three crystallographic sites in $Li_3V_2(PO_4)_3$ for samples with 50% ^{7}Li, 92% ^{7}Li (natural abundance). These results show that the ^{6}Li T_2 relaxation time does not vary much between the three lithium sites in this material, although the ^{7}Li T_2 times are two to three times shorter than the ^{6}Li T_2 times. The most probable cause is the difference in the gyromagnetic ratios of these nuclei. Dipolar coupling contributes significantly to the T_2 relaxation and the differences in the ^{6}Li and ^{7}Li gyromagnetic ratios ($\gamma[^7Li]/\gamma[^6Li] = 2.64$) result in different values of the respective dipolar couplings, with ^{6}Li having a smaller (homonuclear) dipolar coupling than ^{7}Li. The smaller dipolar coupling of ^{6}Li results in a longer T_2 relaxation when compared to ^{7}Li. This is a result of the relaxation mechanism in which fluctuations in the local magnetic field due to fluctuations in distance and orientation, cause nuclear relaxation.

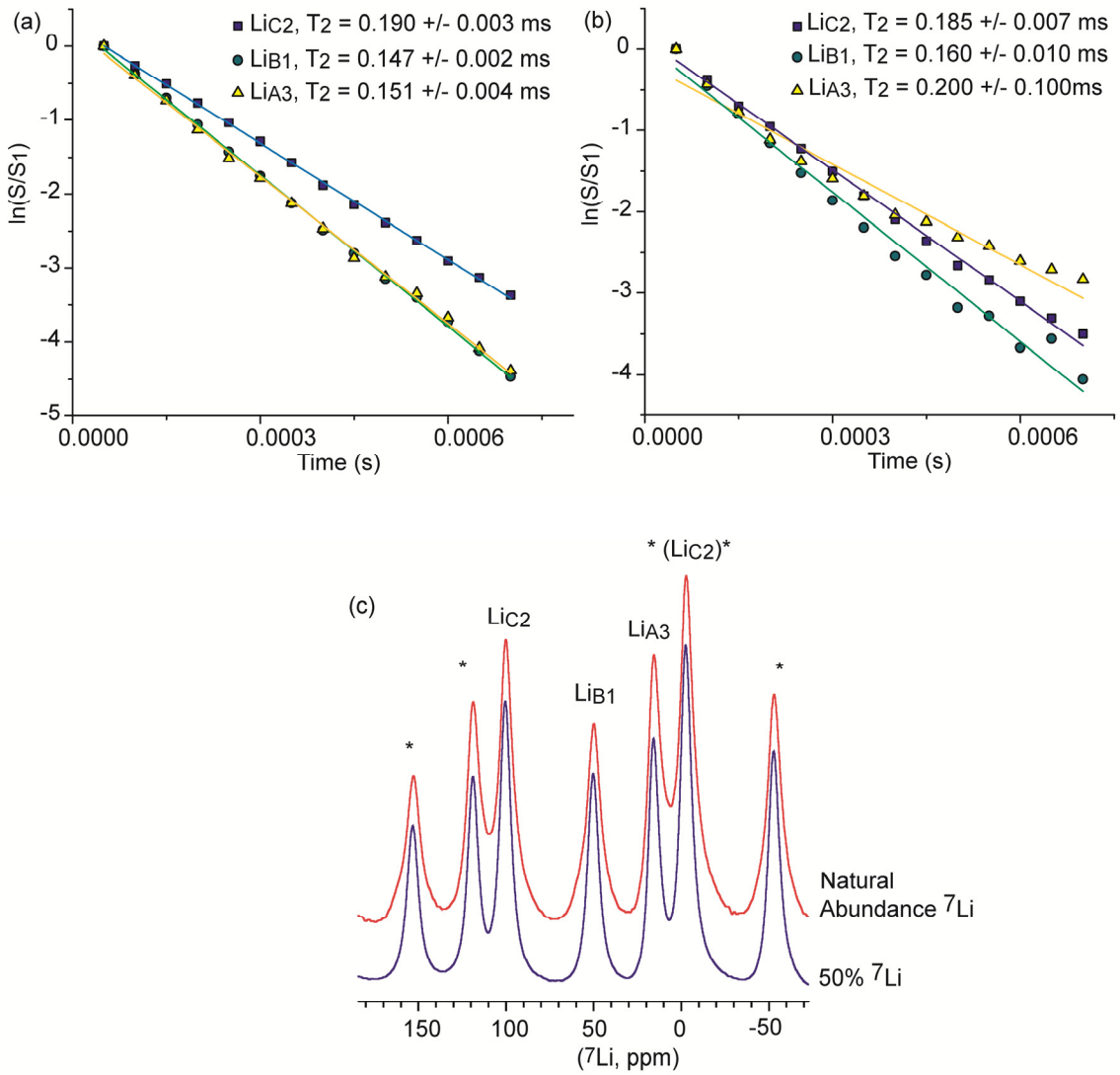

Figure 6.10. ^{7}Li T_2 decay for the three crystallographic sites in $Li_3V_2(PO_4)_3$ at room temperature. (a) Sample was 50% enriched with ^{6}Li; (b) sample was at natural isotope abundance (92% ^{7}Li). T_2 values for each site are shown and the error was calculated from the error in the slope of the best fit line. (c) ^{7}Li MAS NMR spectra of 50% enriched and naturally abundant samples. Sites Li_{A3}, Li_{B1} and Li_{C2} are shown along with the spinning sidebands. One of the low-frequency sidebands for Li_{C2} is shown and will be discussed in the text.

Table 6.3: T_2 Relaxation times for ^{6}Li and ^{7}Li in $Li_3V_2(PO_4)_3$ at 325 K with MAS 20 kHz.

Li-Site	T_2 Relaxation Time (ms)		
	^{6}Li (50% Enriched)	^{7}Li (50% Enriched)	^{7}Li (Natural Abundance)
Li_{C2}	0.490 ± 0.03	0.190 ± 0.003	0.185 ± 0.007
Li_{B1}	0.390 ± 0.03	0.147 ± 0.002	0.160 ± 0.010
Li_{A3}	0.410 ± 0.03	0.151 ± 0.004	0.200 ± 0.100

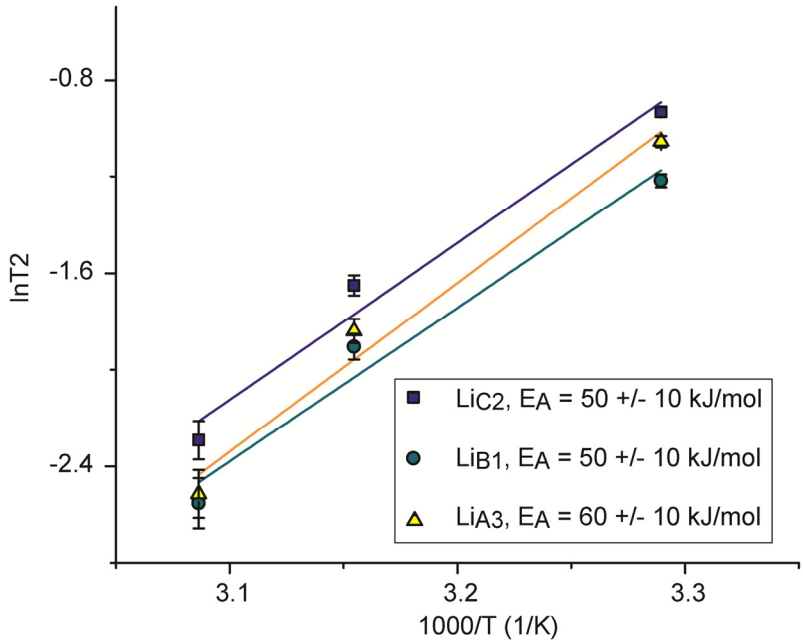

Figure 6.11. Arrhenius analysis of lithium ion hopping using ^{7}Li T_2 relaxation in 50% enriched $Li_3V_2(PO_4)_3$. Crystallographic sites Li_{C2}, Li_{B1} and Li_{A3} show equivalent values (within error) for the activation energies. These values are also in agreement with those calculated using ^{6}Li T_2 measurements.

The T_2 measurements for the 50% enriched were collected as a function of temperature and an Arrhenius analysis was performed. The resulting activation energies for each site were within error, and/or very close to those observed for the corresponding ^{6}Li study (***Figure 6.9***). ***Figure 6.11*** shows the Arrhenius analysis along with the calculated activation energies for lithium ion hopping. The activation energies for all

three sites are equivalent within error. It should be noted that error in this study is calculated from the error in the line of best fit. The larger error in this dataset, as compared to the ^{6}Li data, is due to the smaller T_2 values for ^{7}Li.

On considering the sample with natural isotope abundance, the ^{7}Li T_2 relaxation of sites Li_{C2} and Li_{B1} show little difference to the corresponding sites in the 50% ^{6}Li enriched sample. In contrast, site Li_{A3}, appears to have a longer T_2 relaxation time. This can be considered an inconclusive measurement due to the poor agreement of the line of best fit. The T_2 relaxation of this site does not appear to have a single exponential decay, and may have several contributing factors. In general there is more error in the values of T_2 for this sample when compared to those of the 50% enriched material.

An increase in the amount of ^{7}Li in the naturally abundant sample causes an increase in the homonuclear ^{7}Li-^{7}Li dipolar coupling. This leads to an increase in the line width of the central transition for all three resonances, which in turn causes a significant overlap between site Li_{A3} and one of the low-frequency spinning sidebands of Li_{C2}. ***Figure 6.10*** (c) illustrates the difference in line widths of these two spectra. In addition, ***Table 6.4*** shows the line widths (full-width at half-maximum) for each of the central transition resonances. This broadening and subsequent site overlap is the cause of the non-linear behaviour observed for Li_{A3} in ***Figure 6.10*** (b). As a result of the large error incurred by these results, an Arrhenius analysis of the sample at natural isotope abundance was not performed.

Table 6.4: Line width changes in ^{7}Li spectra of $Li_3V_2(PO_4)_3$.

Site	FWHM (Hz)	FWHM (Hz)
	50% ^{7}Li	92% ^{7}Li
Li_{A3}	1430 ± 10	1750 ± 10
Li_{B1}	1560 ± 10	1890 ± 10
Li_{C2}	1430 ± 10	1700 ± 10

These results have shown that the ^{6}Li T_2 studies resulted in the calculation of the activation energy for lithium ion hopping with more accuracy than those performed with ^{7}Li. However, it was unclear whether the absolute value of the ^{6}Li-^{7}Li dipolar coupling affected the T_2 measurements in a way that contributed to the determination of the activation energy of lithium ion hopping. Consequently, in order to use T_2 relaxation studies to gain information about ion hopping there must be a more accurate method of distinguishing between the factors that affect T_2 measurements to be certain that the temperature-dependent T_2 measurements are being solely affected by ion dynamics. In addition to dipolar coupling, there are other factors, such as paramagnetic effects, that contribute to T_2 relaxation that must also be considered.

6.4. Summary and Future Directions

T_2 relaxation is a complex and important phenomenon that can be used to detect changes in ion motion as a function of temperature in materials for lithium ion batteries. In order to use T_2 measurements for this purpose, mechanisms that contribute to T_2 relaxation must be understood, particularly those that contribute to the study of ion dynamics. T_2 measurements performed on $LiVO_3$ under static and MAS conditions

showed that homonuclear and heteronuclear dipolar coupling both contribute to T_2 relaxation and there is a prominent difference between these two contributing factors. In order to determine if the overall dipolar coupling in the system contributes to the measurement of activation energy, samples with different $^6Li/^7Li$ isotope ratios were studied. However, it was not determined if the resulting dipolar coupling had a significant effect on the calculation of activation energy due to the high error incurred in ^7Li T_2 measurements.

The dynamics of $Li_3V_2(PO_4)_3$ have been well characterized, and this study has shown that the timescale of dynamics in this system is incompatible with the REDOR experiment. The study of temperature dependent T_2 measurements offers another potential tool to evaluate dynamics in this system, provided that the timescale of dynamics matches the timescale of T_2 relaxation. This can be generalized to a wider variety of experiments, including the use of quadrupolar nuclei and heteronuclear dipolar coupling to study ion hopping, such that the timescale of the experiment must be close to the timescale of the dynamic processes of interest.

6.5. References

1. Chung, S. H.; Jeffrey, K. R.; Stevens, J. R., Dynamics of sodium ions in $NaClO_4$ complexed in poly(propylene-oxide): A Na-23 nuclear magnetic resonance study. *Journal of Chemical Physics* **1998,** 108, (8), 3360-3372.

2. Levitt, M. H., *Spin Dynamics*. John Wiley and Sons Ltd.: West Sussex, 2001; p 686.

3. A. Carrington, A. D. M., *Introduction to Magnetic Resonance with Application to Chemistry and Chemical Physics*. Harper and Row, Publishers: New York, 1967.

4. Cahill, L. S.; Kirby, C. W.; Goward, G. R., Li-6{P-31} rotational-echo, double-resonance studies of lithium ion site dynamics in $Li_3V_2(PO_4)_3$. *Journal of Physical Chemistry C* **2008,** 112, (6), 2215-2221.

5. Davis, L. J. M.; He, X. J.; Bain, A. D.; Goward, G. R., Studies of lithium ion dynamics in paramagnetic cathode materials using Li-6 1D selective inversion methods. *Solid State Nuclear Magnetic Resonance* **2012,** 42, 26-32.

6. Muller, C.; Valmalette, J. C.; Soubeyroux, J. L.; Bouree, F.; Gavarri, J. R., Structural disorder and ionic conductivity in $LiVO_3$: A neutron powder diffraction study from 340 to 890 K. *Journal of Solid State Chemistry* **2001,** 156, (2), 379-389.

7. Jian, X. M.; Tu, J. P.; Qiao, Y. Q.; Lu, Y.; Wang, X. L.; Gu, C. D., Synthesis and electrochemical performance of $LiVO_3$ cathode materials for lithium ion batteries. *Journal of Power Sources* **2013,** 236, 33-38.

8. Cahill, L. S.; Chapman, R. P.; Britten, J. F.; Goward, G. R., Li-7 NMR and two-dimensional exchange study of lithium dynamics in monoclinic $Li_3V_2(PO_4)_3$. *Journal of Physical Chemistry B* **2006,** 110, (14), 7171-7177.

9. Duer, M. J., *Introduction to Solid-State NMR Spectroscopy.* Blackwell Science, Oxford, UK: 2004; p 349.

10. Yin, S. C.; Grondey, H.; Strobel, P.; Anne, M.; Nazar, L. F., Electrochemical property: Structure relationships in monoclinic $Li_{3-y}V_2(PO_4)_3$. *Journal of the American Chemical Society* **2003,** 125, (34), 10402-10411.

11. Koller, H.; Kalwei, M., Studying ionic motion in tetrahydroxoborate sodalite by second moment analysis using Na-23{B-11} rotational echo double resonance data. *Journal of Physical Chemistry B* **2004,** 108, (1), 58-63.

Chapter 7: Summary and Outlook

7.1. Summary

This thesis has described several novel solid-state NMR spectroscopy methods that can be used to study the structural and dynamic properties of garnet-like solid-state electrolytes for lithium ion batteries. These methods aim to overcome some of the challenges inherent in studying solid-state lithium ion electrolytes. Unlike many cathode materials for lithium ion batteries, which are paramagnetic due to the presence of unpaired electrons, solid-state electrolytes are diamagnetic. The typical chemical shift range for ^{6,7}Li in diamagnetic lithium materials is -5 to +5 ppm.[1] Therefore the ^{6,7}Li resonances in solid-state electrolytes tend to be poorly resolved and overlap in many cases. In addition, garnet-like electrolytes typically exhibit lithium ion motion in a single crystallographic site and also have very long ^{6,7}Li T_1 relaxation times.[2, 3] These factors combine to make the study of solid-state lithium electrolyte materials non-trivial.

Three methods are presented in this thesis which each aim to overcome some of the challenges faced when probing the structural and dynamic properties of solid-state lithium ion electrolytes. Quadrupolar nuclei have played an important role in this work, due to the sensitivity of the electric field gradients to subtle structural details and ion dynamics. Quadrupolar nuclei can be found in the framework of many solid-state electrolyte materials. This thesis discusses the used of these framework quadrupolar nuclei to detect ion dynamics from a secondary standpoint, as opposed to the direct observation of the mobile species. EXPRESS software, created by Prof. R. Vold, was

used to simulate the ^{87}Rb quadrupolar line shape as a function of Ag^+ ion hopping rate in the solid-state electrolyte $RbAg_4I_5$, resulting in the calculation of the activation energy for Ag^+ ion hopping.

The heteronuclear dipolar coupling between ^6Li and ^7Li has been used to study dynamics in several materials.[4-6] In this thesis $^6Li\{^7Li\}$-REDOR NMR studies were used for the first time to measure the dependence of ^6Li-^7Li dipolar coupling on sample temperature in order to detect changes in ion hopping rates. Dipolar coupling between a pair of nuclei is sensitive to the rate of ion hopping and therefore can be used as a probe for changes in ion hopping when measured as a function of temperature. In addition, T_2 relaxation measurements have been used to study lithium ion dynamics as a function of temperature. T_2 relaxation times are sensitive to ion mobility and therefore can be used to study the activation energy for lithium ion hopping.

An important factor that must be considered in the methods studies in this thesis is the timescale of ion hopping as compared to that of the experiment. When quadrupolar nuclei are used to study ion hopping, the hopping rate (in Hz) must be on the timescale of the width of the quadrupolar NMR resonance (in Hz). Likewise, when heteronuclear dipolar coupling is used to study ion dynamics, the coupling constant (in Hz) must be on the same order of magnitude as the ion hoping rate (in Hz). This is also true for the rate of T_2 relaxation, which must be close in magnitude to the rate of ion hopping in order for this method to be a sensitive probe of ion dynamics. The following sections describe the work done in Chapters 3 to 6 as well as proposed future work for each project.

7.2. Intellectual Contribution and Impact of Chapters

7.2.1. Chapter 3: Structural Analysis of Garnet-Type $LaLi_{0.5}Fe_{0.2}O_{2.09}$ and Related Materials Using ^{7}Li and ^{139}La Solid-State NMR Spectroscopy

Chapter 3 focuses on the structural analysis of $Li_{3x}La_{(2/3)-x}TiO_3$, $LaLi_{0.5}Fe_{0.2}O_{2.09}$ and related materials using a combination of ^{7}Li and ^{139}La NMR spectroscopy. Initial ^{7}Li NMR studies of $LaLi_{0.5}Fe_{0.2}O_{2.09}$ indicated structural complexity that was not characterized in previous studies using powder X-ray diffraction. This chapter describes how ^{7}Li and ^{139}La NMR have been combined for the first time to extract details of the atomic level disorder that is present in $LaLi_{0.5}Fe_{0.2}O_{2.09}$. Traditionally, $^{6,7}Li$ MAS NMR is used in combination with powder X-ray diffraction to determine structural details of lithium battery materials. However, we have demonstrated here that the use of quadrupolar nuclei found in the framework of these materials can provide a significant amount of detail about structure in this class of materials.

Initial ^{7}Li MAS NMR spectroscopy studies of $LaLi_{0.5}Fe_{0.2}O_{2.09}$ and the family of materials created by changing the stoichiometric content of La, Li and Fe revealed a complex combination of spectral resonances. It was learned from T_1 studies and the analysis of the Curie-Weiss behaviour of the individual ^{7}Li resonances that the peaks in the NMR spectrum could be grouped into two categories: those arising from a series of diamagnetic lithium environments, and those with paramagnetic character. Although it is not uncommon for different resonances within a material to have different T_1 relaxation times, the existence of distinct diamagnetic and paramagnetic regions is an unusual observation.[2]

Further analysis using ^{139}La NMR spectroscopy revealed atomic-level disorder arising from the ability of lithium to move into the crystallographic site of iron. The complex environment around each lithium site created a variety of unique environments, which were seen in the ^{7}Li NMR spectra. The ^{139}La NMR spectra consisted of two distinct lanthanum resonances, with one environment showing a significant amount of broadening, which was attributed to its proximity to the structural disorder and pointed to the existence of distinct paramagnetic and diamagnetic regions within the lattice of the material.

Changes in the stoichiometric ratio of La, Li and Fe between related materials resulted in significant changes in the ^{7}Li and ^{139}La NMR spectra. The sensitivity of the lanthanum NMR spectra to the extent of structural disorder was consistent with the ^{7}Li MAS NMR, which showed that the lithium occupancy in the paramagnetic and diamagnetic regions was susceptible to the stoichiometric changes.

The results presented in Chapter 3 show that in addition to the study of the mobile ^{6,7}Li species in electrochemical materials, framework elements, such as ^{139}La, offer valuable tools that can be used to determine structural details. The sensitive electric field gradient of quadrupolar nuclei can be used to probe structure in these complex systems, offering a robust tool to study many classes of materials.

7.2.2. Chapter 4: Dynamics of Ag^+ Ions in $RbAg_4I_5$ Probed Indirectly Via ^{87}Rb Solid-State NMR Spectroscopy

Many solid-state lithium ion electrolyte materials conduct lithium through a single crystallographic site, making traditional 2D exchange studies inapplicable. Chapter 4 discusses the use of quadrupolar nuclei found in the framework of these materials to study ion dynamics indirectly. $RbAg_4I_5$ was chosen as a model material since the details of Ag^+ ion conductivity in this materials are well documented in the literature.[7, 8]

In Chapter 4 the details of Ag^+ ion motion in the solid-state electrolyte $RbAg_4I_5$ were examined using ^{87}Rb NMR spectroscopy.[6] ^{87}Rb is abundant within the framework of $RbAg_4I_5$ and the large electric field gradient makes it a sensitive probe of dynamic processes in the surrounding environment. For the first time changes in the ^{87}Rb quadrupolar NMR line shape as a function of temperature, along with simulations in EXPRESS software,[9] were used to determine the rate and activation energy of Ag^+ ion hopping. This method provides an effective means to study ion dynamics in solid-state materials and is particularly useful for cases in which the mobile species is difficult to study, such as diamagnetic electrolyte materials.

By demonstrating this method on the model material $RbAg_4I_5$, we have presented a tool that can be extended to study a variety of lithium ion conductors. The major focus will be materials that present difficulties when studying the mobile species directly. Prime examples are solid-state lithium ion electrolytes such as $Li_7La_3Zr_2O_{12}$, which has long

^{6,7}Li T_1 relaxation times, as well as significant overlap in the lithium NMR resonances and contains the quadrupolar nucleus ^{139}La in the framework.[10]

7.2.3. Chapter 5: The Use of ^{6}Li{^{7}Li}-REDOR NMR Spectroscopy to Compare the Ionic Conductivities of Solid-State Lithium Ion Electrolytes

Garnet-like solid-state lithium ion electrolytes, $Li_6BaLa_2M_2O_{12}$ (M = Ta, Nb) are qualitatively compared in Chapter 5 using ^{6}Li{^{7}Li}-REDOR NMR studies. These materials are very similar in structure, differing only in one element, which is found in the framework of the structure. They each have two crystallographic sites, of which only one is responsible for ion conductivity, making 2D exchange studies inapplicable.[2, 3] Therefore, we have made use of the sensitivity of the heteronuclear ^{6}Li-^{7}Li dipolar coupling to changes in dynamics in order to compare the ionic conductivities in these materials.

^{6}Li{^{7}Li}-REDOR studies were performed as a function of temperature for each of these materials. The initial slopes of the resulting REDOR curves were considered and it was found that with increasing temperature the slopes of the REDOR curves for both samples decreased. The Nb phase produced a more significant response and the resulting REDOR curve had an overall shallower slope than that of the Ta phase. From this data it was concluded that the Nb phase has a higher ionic conductivity than the Ta phase at every temperature, as well as a higher activation energy for lithium ion hopping. This conclusion resolved a discrepancy that came as a result of inconclusive results in the

literature, whereby several authors reported different values for ionic conductivity and activation energy for lithium ion hopping in $Li_6BaLa_2M_2O_{12}$ (M = Ta, Nb).[11, 12]

This novel method produced an effective comparison of the two materials studied, and therefore future work aims to apply this method to a wider range of materials. Other solid-state lithium electrolytes such as, $Li_{0.5}La_{0.5}TiO_3$ and $Li_7La_3Zr_2O_{12}$ are also known to conduct lithium ions in a single crystallographic site, can be studied using this method. The ability to compare ion dynamics between materials is an essential tool, as it can predict the behavior of a material when used in a battery.

7.2.4. Analysing Dynamics in Lithium Ion Conductors Using Changes in ^{6,7}Li T_2 Relaxation Times Extracted from REDOR and SEDOR Experiments

Chapter 6 discusses the use of T_2 relaxation measurements to study ion hopping in battery materials. T_2 measurements are inherent in REDOR and SEDOR experiments, and thus temperature dependent REDOR and SEDOR studies also produce the corresponding T_2 studies. The aim of this work is to target ion dynamics which corresponds to correlation times that are on the order of the T_2 relaxation, meaning that T_2 will be sensitive to these hopping mechanisms, while dipolar coupling, and the REDOR/SEDOR experiment, is not likely to be.

The mechanism of T_2 relaxations plays an important role in this study. By comparing the ^{7}Li T_2 values that were extracted from REDOR and SEDOR experiments of $LiVO_3$ it was found that there is a significant difference in the contribution of

homonuclear and heteronuclear dipolar coupling to T_2 relaxation. This interesting observation suggests that the REDOR and SEDOR experiments are sensitive to dynamics which occur on different timescales and thus, the inherent T_2 measurements will also target different timescales of dynamics.

The subsequent extraction of T_2 measurements from REDOR data can be used as an indicator of ion dynamics in ion conductors. The model material, $Li_3V_2(PO_4)_3$ has been studied and the $^{6,7}Li$ T_2 relaxation times were measured as a function of temperature. By considering the changes in T_2 an Arrhenius analysis produced values for the activation energy for lithium ion hopping for each site. These values agreed with those measured by Danielle Smiley of the Goward Group, using 1D selective inversion experiments.

The temperature-dependence of T_2 relaxation in these materials is a potential method to study ion dynamics in lithium ion conductors. At this point, it is clear that the T_2 relaxation mechanism is sensitive to dynamics in this class of materials, but the direct correlation to the rate or activation energy of lithium ion hopping need to be studied further. There are several significant factors that affect T_2 relaxation, including homonuclear and heteronuclear dipolar coupling. Therefore the next step in this project is to determine a way to extract detailed rate information from these measurements.

7.3. Conclusion

Together, the methods discussed in this thesis outline several novel techniques that can be used to study ion dynamics in solid-state electrolytes for lithium ion batteries. These approaches aim to overcome some of the typical difficulties faced when studying

the ^{6,7}Li MAS NMR of diamagnetic materials, such as poor site resolution and long T_1 relaxation times. In addition, these methods provide tools to study materials which conduct lithium within a single crystallographic site, which otherwise pose a challenge. The experiments discussed can be used to probe ion motion in a wide range of materials, and are not limited to the electrolyte family.

The solid-state electrolyte materials studied in this thesis are among the most competitive in the field. These materials are poised to replace the currently used liquid electrolytes in order to reduce the present fire risks. The measurement of ion conduction in these and other materials remains a challenge that is presently being pursued by many people. NMR spectroscopy has provided an excellent tool to study ion dynamics in lithium ion battery materials, and has been a prominent force in studying cathode and anode materials. The extension of these studies to include electrolyte materials has been non-trivial due to the challenges associated with the study of diamagnetic lithium materials. However, the techniques presented in this thesis offer novel approaches that aim to overcome some of the more common problems, allowing the study of structure and dynamics in a wide variety of competitive materials.

7.4. References

1. Xu, Z.; Stebbins, J. F., Li-6 Nuclear-Magnetic-Resonance Chemical-Shifts, Coordination-Number and Relaxation in Crystalline and Glassy Silicates. *Solid State Nuclear Magnetic Resonance* **1995,** 5, (1), 103-112.

2. O'Callaghan, M. P.; Powell, A. S.; Titman, J. J.; Chen, G. Z.; Cussen, E. J., Switching on fast lithium ion conductivity in garnets: The structure and transport properties of $Li_{3+x}Nd_3Te_{2-x}Sb_xO_{12}$. *Chemistry of Materials* **2008,** 20, (6), 2360-2369.

3. van Wullen, L.; Echelmeyer, T.; Meyer, H. W.; Wilmer, D., The mechanism of Li-ion transport in the garnet $Li_5La_3Nb_2O_{12}$. *Physical Chemistry Chemical Physics* **2007,** 9, (25), 3298-3303.

4. Spencer, L., Coomes, E., Ye, E., Terskikh, V., Ramzy, A., Thangadurai, V., Goward, G.R., *Canadian Journal of Chemistry-Revue Canadienne De Chimie* **2011,** 89, 1105-1117.

5. Spencer, T. L.; Ramzy, A.; Thangadurai, V.; Goward, G. R., Structural Complexity and Electrical Properties of the Garnet-Type Structure $LaLi_{0.5}Fe_{0.2}O_{2.09}$ Studied by (7)Li and (139)La Solid State NMR Spectroscopy and Impedance Spectroscopy. *Chemistry of Materials* **2011,** 23, (12), 3105-3113.

6. Spencer, T. L.; O'Dell, L. A.; Moudrakovski, I.; Goward, G. R., Dynamics of Ag+ Ions in $RbAg_4I_5$ Probed Indirectly via Rb-87 Solid-State NMR. *Journal of Physical Chemistry C* **2013,** 117, (19), 9558-9565.

7. Looser, H.; Mali, M.; Roos, J.; Brinkmann, D., Ag Diffusion Constant in Rbag4i5 and KAg_4I_5 Determined by Pulsed Magnetic Gradient NMR. *Solid State Ionics* **1983,** 9-10, (DEC), 1237-1240.

8. Looser, H.; Brinkmann, D.; Mali, M.; Roos, J., The Interdependence of Mobile and Stationary Ions in Rbag4i5 - an Nmr Investigation. *Solid State Ionics* **1981,** 5, (OCT), 485-488.

9. Vold, R. L.; Hoatson, G. L., Effects of jump dynamics on solid state nuclear magnetic resonance line shapes and spin relaxation times. *Journal of Magnetic Resonance* **2009,** 198, (1), 57-72.

10. Awaka, J.; Kijima, N.; Hayakawa, H.; Akimoto, J., Synthesis and structure analysis of tetragonal $Li_7La_3Zr_2O_{12}$ with the garnet-related type structure. *Journal of Solid State Chemistry* **2009,** 182, (8), 2046-2052.

11. Thangadurai, V.; Weppner, W., $Li_6ALa_2Nb_2O_{12}$ (A = Ca, Sr, Ba): A new class of fast lithium ion conductors with garnet-like structure. *Journal of the American Ceramic Society* **2005,** 88, (2), 411-418.

12. Truong, L.; Thangadurai, V., Soft-Chemistry of Garnet-Type $Li_{5+x}Ba_xLa_{3-x}Nb_2O_{12}$ (x=0, 0.5, 1): Reversible H^+ <-> Li^+ Ion-Exchange Reaction and Their X-ray, Li-7 MAS NMR, IR, and AC Impedance Spectroscopy Characterization. *Chemistry of Materials* **2011,** 23, (17), 3970-3977.

Appendix A1: SPINEVOLUTION File

SPINEVOLUTION File for $^{6}Li\{^{7}Li\}$-REDOR Curve Simulation

```
****** The System **********************************
spectrometer(MHz)  500
spinning_freq(kHz) 25
channels          Li6(73.599 1) Li7
nuclei            Li6 Li7
atomic_coords     *
cs_isotropic      0 0
csa_parameters    *
j_coupling        Jiso2
quadrupole        *
dip_switchboard   *
csa_switchboard   *
exchange_nuclei   *
bond_len_nuclei   *
bond_ang_nuclei   *
tors_ang_nuclei   *
groups_nuclei     *
******* Pulse Sequence ****************************
CHN 1
timing(usec)     (40)128      38          2       40          (40)128
power(kHz)        0           0         250        0           0
phase(deg)        0           0           0        0           0
freq_offs(kHz)    0           0           0        0           0
CHN 2
timing(usec)     (redor-9.pp)  18  2   20         redor-9.pp     (redor-9.pp)
power(kHz)        *           0   250  0           *           *
phase(deg)        *           0   0    0           *           *
```

```
freq_offs(kHz)     *          0   0    0            *          *
******* Variables ************************************
wr=25
spinning_freq=wr
tr=1000/wr
******* Options ************************************
rho0              I1x
observables       I1p
EulerAngles       zcw987
n_gamma           10
line_broaden(Hz)   *
zerofill          *
FFT_dimensions     *
options           -dw123 -re
*****************************************************
```

See another version of thhis input file in the
examples-new/dim-sections directory, and the
analytic mode version in examples-new/analyt

Appendix A2: Powder X-Ray Diffraction of Garnet-Like Electrolytes

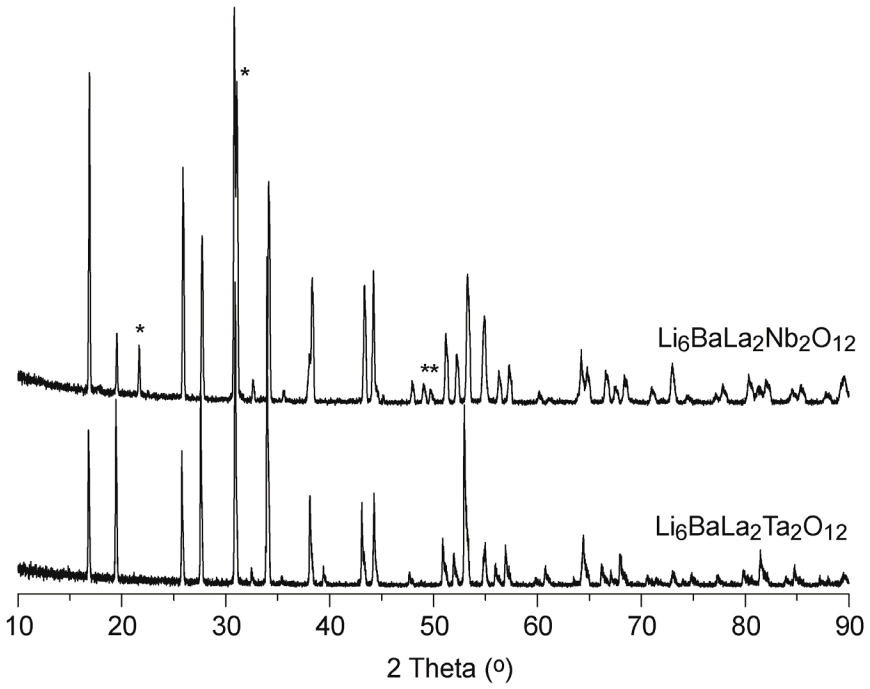

Figure A2.1. Powder X-ray diffraction patterns of $^{6,7}Li_6BaLa_2Ta_2O_{12}$ and the corresponding Nb phase. * represents an impurity phase.

Appendix A3: Powder X-Ray Diffraction Patterns of $Li_3V_2(PO_4)_3$ and $LiVO_3$

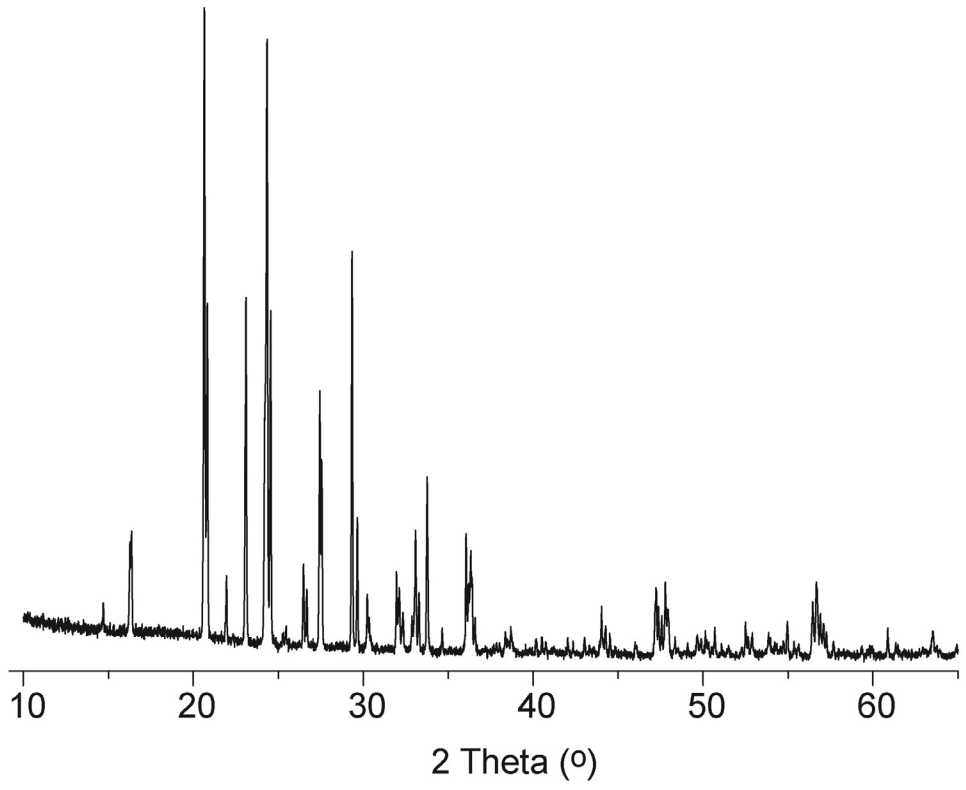

Figure A3.1. Powder X-ray diffraction patterns of $Li_3V_2(PO_4)_3$.

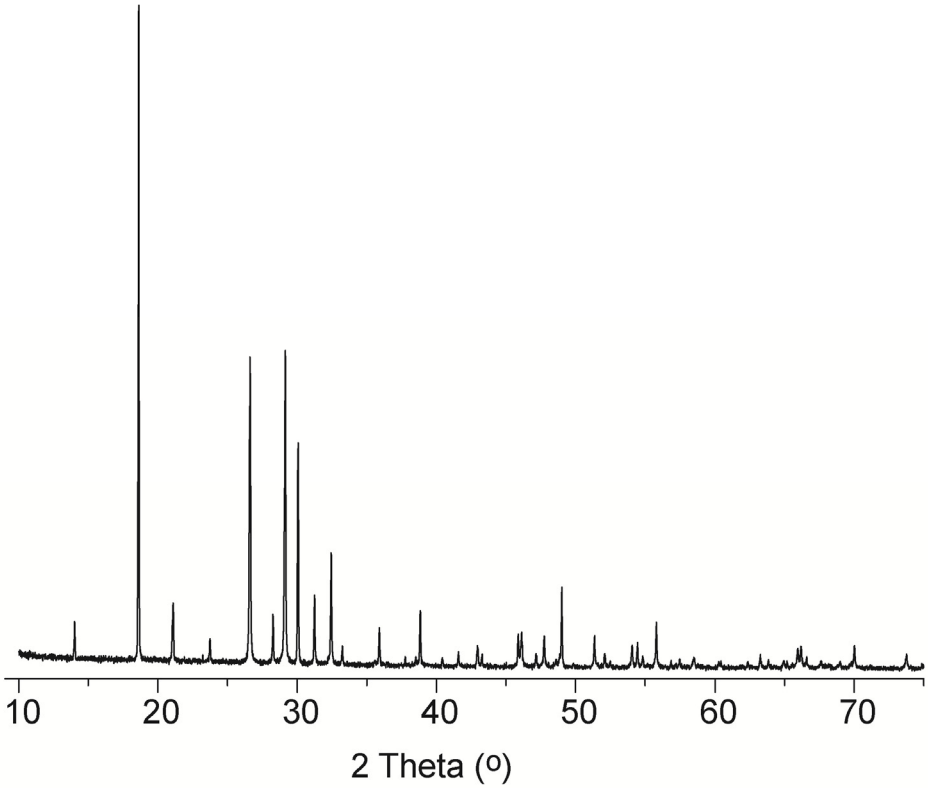

Figure A3.2. Powder X-ray diffraction patterns of $LiVO_3$.

Appendix A4: Dynamics in $Li_6BaLa_2Nb_2O_{12}$ when Li^+ is Replaced by H^+

A.4.1 Introduction

The lithium ion electrolyte material $Li_6BaLa_2Nb_2O_{12}$ possess fast lithium ion conductivity, as discussed in Chapter 5 of this thesis. Recent studies have shown that there is a possibility that Li^+ can be replaced by H^+ in similar materials, with little conclusive evidence to show the effect on the local lithium ion dynamics.[1-3] It was found that washing a garnet-structured material with water or weak acid could remove or replace the lithium ions, replacing them with hydrogen ions. Previous studies have shows that the replacement of Li^+ by H^+ in garnet like materials causes an expansion of the unit cell of the crystalline material due to the replacement of the strong Li-O bond with weaker O-H···O bond.[3]

Here, we have chosen to study the electrolyte material $Li_6BaLa_2Nb_2O_{12}$ with the goal of determining the effect of the replacement of Li^+ by H^+ on ionic conductivity using solid-state REDOR NMR. Recent success in the comparison of lithium ion conductivity in $Li_6BaLa_2M_2O_{12}$ (M=Ta, Nb), as discussed in Chapter 5, suggests that REDOR NMR methods can be used to determine the effect of the replacement of Li^+ with H^+ on the ionic conductivity in $Li_6BaLa_2Nb_2O_{12}$.

A.4.2 Experimental

$^{6,7}Li_6BaLa_2Nb_2O_{12}$ was synthesized according to the method outlined in Chapter 5. Washing was performed according to the following procedure:

H_2O Wash: 0.2 g of $^{6,7}Li_6BaLa_2Nb_2O_{12}$ was mixed with 1.33 mL H_2O and left for 1 hour. The mixture was filtered, washed with isopropanol, and allowed to dry at 60 ºC for three days. This formed $Li_{6-x}H_xBaLa_2Nb_2O_{12}$.

HCl Wash: The procedure used for the H_2O wash was performed but instead 0.01 M HCl was used. This formed $Li_{6-y}H_yBaLa_2Nb_2O_{12}$.

A.4.3 Results and Discussion

A.4.3.1 Powder X-Ray Diffraction

In order to confirm that there was no significant phase change as a result of washing, powder X-ray diffraction (PXRD) was performed and is shown in ***Figure A4.1***. The washed sampled showed a shift in the peak positions highlighted in the inset. This is consistent with previous studies, in which a change in the peak positions in the PXRD data indicated an expansion of the unit cell.[3] The PXRD data for both of the washed materials is the same. This indicates that the washing methods likely have a similar effect on the crystal structure.

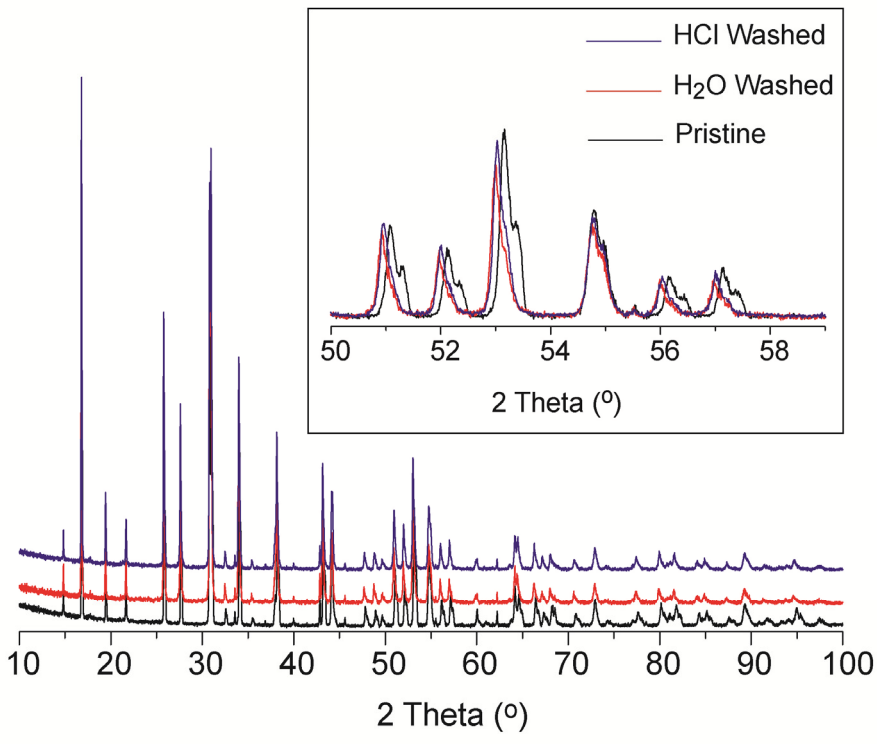

Figure A4.1. Powder X-ray diffraction of $Li_6BaLa_2Nb_2O_{12}$, in black, and the water (red) and HCl (blue) washed derivatives, $Li_{6-x}H_xBaLa_2Nb_2O_{12}$ and $Li_{6-y}H_yBaLa_2Nb_2O_{12}$, respectively. The inset shows that there is a decrease in the values of 2 Theta for peaks present in both of the washed samples, indicating an increase in unit cell size.

A.4.3.2 Solid-State ^{6}Li and ^{1}H NMR

^{6}Li MAS NMR was performed for the pristine and washed samples according to the method outlined in Chapter 5. For each spectrum, the mass of the sample in the rotor was considered and the spectrum was scaled such that the intensities reflect the relative amount of sample in each case. The NMR shows that the water and acid washing process changed the ratio of the content of lithium in each of the two crystallographic sites. ***Figure A4.2*** shows the ^{6}Li MAS NMR of the pristine $Li_6BaLa_2Nb_2O_{12}$ material as well as that of the washed materials. Clearly, there is a difference in the relative tetrahedral

(~0 ppm) and octahedral (~ 1 ppm) site occupancies. The pristine material has a larger content of lithium in the octahedral site. This is also known to be the site that is responsible for lithium ion motion in these materials. Therefore, it is consistent with the easy removal of this lithium by washing.

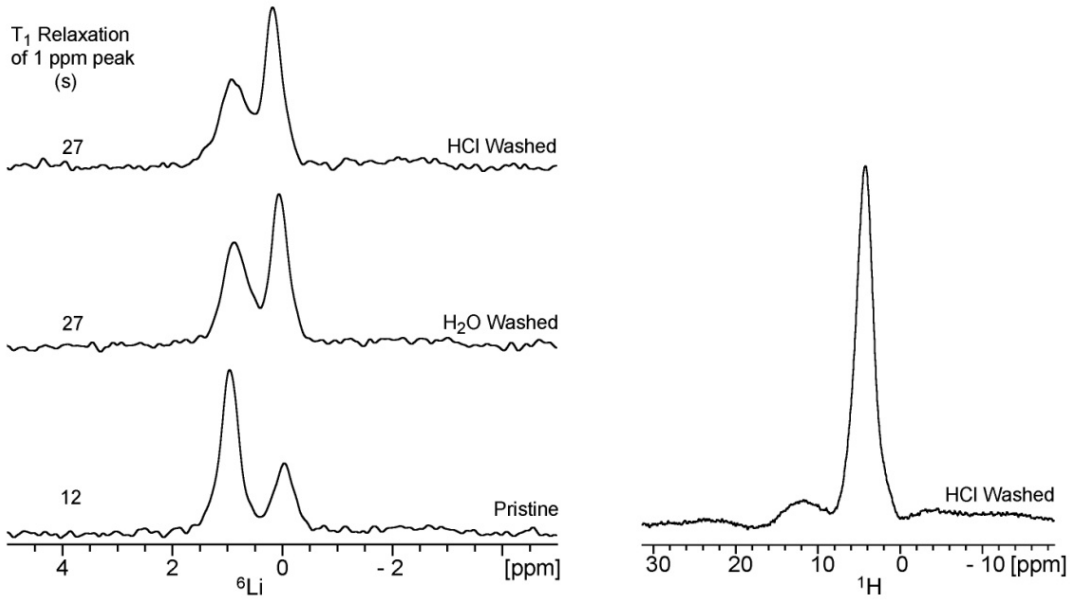

Figure A4.2. Left: ^{6}Li MAS NMR of pristine $Li_6BaLa_2Nb_2O_{12}$, and its washed derivatives. A MAS rate of 30 kHz was used, and a single transient was collected with a relaxation delay of 2 hours. On the left, T_1 relaxation times of the each octahedral site at 1 ppm sample are shown. Right: ^{1}H MAS NMR of HCl washed material. A MAS rate of 30 kHz was used in a Hahn-echo experiment with background suppression. Eight transients were collected with a recycle delay of 300 s.

Determination of the amount of lithium removed per gram was a challenging due to both the small amount of sample studied as well as the extremely long T_1 relaxation of the tetrahedral site, 0 ppm. For each of the samples a relaxation delay of 2 hours was waited before a single transient was collected to attempt to get full relaxation. However, T_1 measurements show that the tetrahedral site has a $T_1 > 100$ s, so there is a possibility that there was insufficient relaxation to perform quantitative comparison of the lithium

content in these samples. Conversely, the octahedral site, due to its greater mobility, has a measurable T_1, which changes as function of washing. Both the water and acid washed samples showed an increase in T_1, 27 s, as compared to the pristine material, 12s. This indicates firstly that the effect of washing with water and acid have similar affects on the T_1 of the octahedral site; and secondly that the changing the nature of the lithium in this site likely decreases the ionic hopping rate of lithium in this site.

A.4.3.3 Solid-State REDOR NMR

^{6}Li{^{7}Li}-REDOR NMR was performed to compare the lithium ion mobility in the pristine and washed materials and is shown in ***Figure A4.3***. Only the octahedral site is considered, as in Chapter 5. For the pristine material, the REDOR curves for high and low temperatures are shown by the triangular points in red and blue, respectively. There is a significant difference in the slopes of the REDOR curves for this material at the two measured temperatures. This is due to the difference in lithium ion hopping rate, which is faster at 325 K than at 247 K, where the ions are immobile.

The REDOR curves of the washed materials have similar slopes at 325 K, which are both steeper than that of the pristine materials at 325 K. This indicates that there is likely a difference in structure and/or ion mobility between the washed and pristine materials. Also, the REDOR curves of the washed materials show no significant difference between them, indicating that the methods have similar effects on the resulting Li distribution within the respective structures.

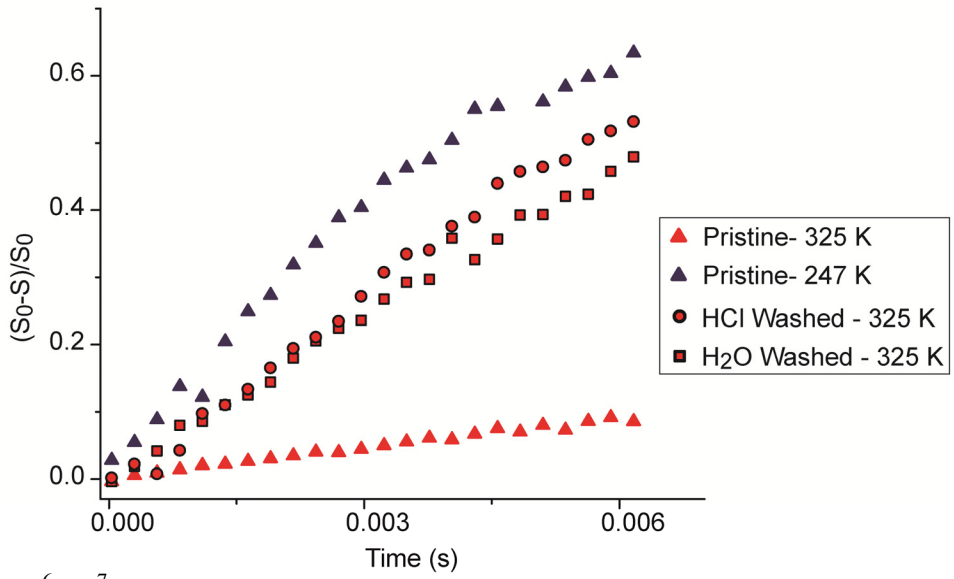

Figure A4.3. $^{6}Li\{^{7}Li\}$-REDOR of pristine and washed materials. The triangular points represent the pristine material at 325 K (red) and 247 K (blue). The square and circular points represent the H_2O and HCl washed materials.

On considering the changes in ion mobility with temperature, the $^{6}Li\{^{7}Li\}$-REDOR curves of the pristine and H_2O washed samples were compared at different temperatures, as shown in ***Figure A4.4.*** While the REDOR curve of the pristine sample changes dramatically with temperature, that of the H_2O washed sample remained the same with an increase in temperature, pointing to a lack of temperature dependent ion mobility within this temperature range. This result would suggest that the H_2O wash caused a decrease in ion conductivity. At this point the mechanism for the reduction in ion conductivity was not clear.

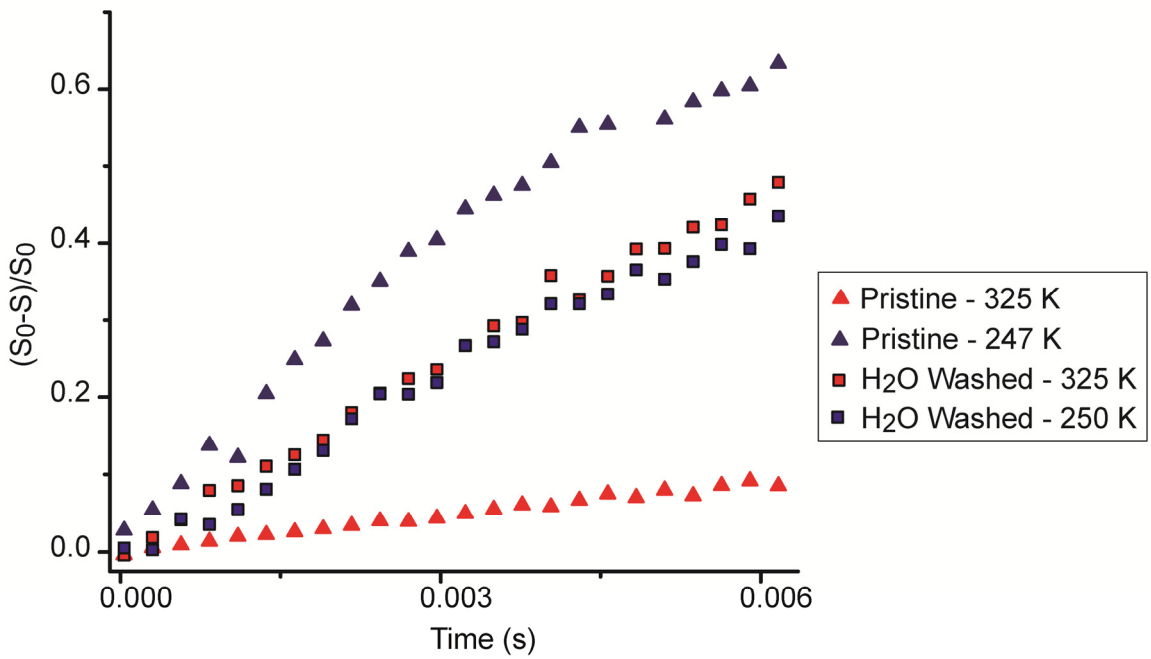

Figure A4.4. ^{6}Li{^{7}Li}-REDOR of pristine and H_2O washed materials. The triangular points represent the pristine material at 325 K (red) and 247 K (blue). The square points represent the H_2O washed material at 325 and 250 K.

Contributions to the REDOR curves of the H_2O washed sample include the distance and distribution of lithium ions within the sample, while dynamics does not play a role. This is evident for the unchanging slope at different temperatures. When the REDOR curves of the H_2O washed sample and the immobile curve of the pristine sample are compared, it is clear that there is a difference in the distance and distribution of lithium in these materials as indicated by the shallower slope of the washed sample. The increase in unit cell size, which resulted from the washing procedure, could contribute to this effect. However, the removal of lithium form the material is more likely to result in a decrease in the slope of the REDOR curve. Each of these effects would result in an increase in the average Li-Li distance. It is unclear form the ^{6}Li MAS NMR if the overall Li content of the material decreases, but the spectra in ***Figure A 4.2*** point to a change in

the location of lithium in the unit cell, which can also result in a change in the slope of the REDOR curve if this created more Li pairs with greater internuclear distances.

Although ***Figure A4.4*** suggests a significant reduction in the Li^+ conductivity, there is still the possibility of H^+ ion conductivity. Therefore the $^1H\{^7Li\}$-REDOR of the H_2O washed material was performed at 325 K and 350 K, shown in ***Figure A4.5.*** There was no change in the resulting REDOR curves within this temperature range. These results suggests that although this is a small temperature range, it is unlikely that there is significant H^+ ion conductivity, as this would result in a shallow REDOR curve.

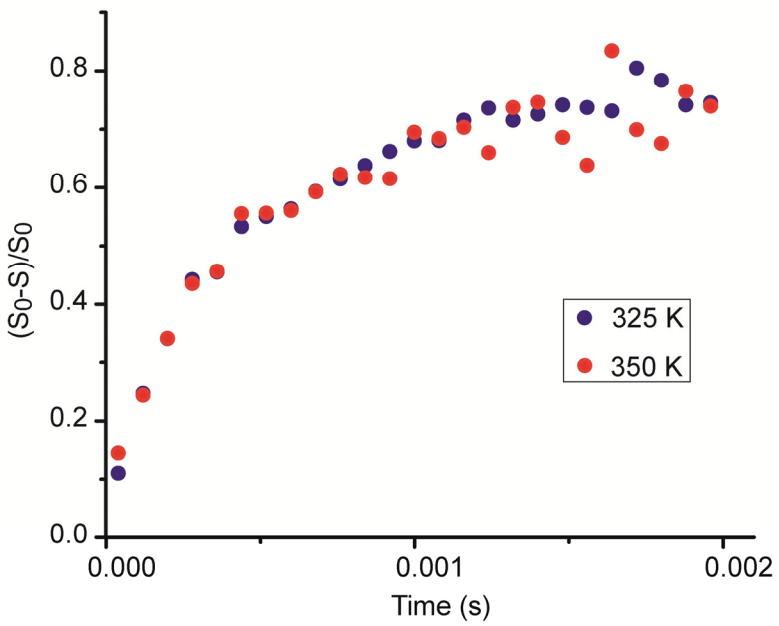

Figure A4.5. $^1H\{^7Li\}$-REDOR of H_2O washed material at 325 K (blue) and 350 K (red).

From the combination of $^6Li\{^7Li\}$-REDOR and $^1H\{^7Li\}$-REDOR NMR performed here, it would seem that washing $Li_6BaLa_2Nb_2O_{12}$ effectively decreases the lithium ion mobility in the material to a point that canot be measures using these

techniques. In addition, the presence of H^+ ions in the sample does not appear to produce any H^+ ion conductivity.

A.4.4 Summary and Outlook

The possibility of enhancing ion conductivity in lithium ion electrolyte $Li_6BaLa_2Nb_2O_{12}$ by washing with HCl and H_2O was explored using a combination of $^6Li\{^7Li\}$-REDOR and $^1H\{^7Li\}$-REDOR NMR. It was found that there was little difference in the effect of HCl or H_2O washing, and in each case some of the Li^+ was replaced by H^+. The H_2O washed sample was studies using REDOR methods and it was found that although there was an expansion in the unit cell volume (as measured using PXRD), this did not result in a change in ion mobility. Rather, there was an overall decrease in the Li^+ mobility, and no H^+ was introduced.

These puzzling results offer some clear next steps to this project:

1. High resolution ^1H NMR to determine the number of ^1H sites introduces to the material after washing. This may indicate where the ^1H is located and also which lithium sites are most affected by the washing.
2. ^1H and ^7Li cross polarization (CP) experiment may offer some insight into the rate of ion exchange in the washed materials. The measurement of dynamics in the REDOR experiment is limited to dynamics with a timescale that is on the same order as the dipolar coupling between mobile species. Conversely, the CP experiments allow the use to set the timescale of sensitivity within the experiment, allowing greater sensitivity.

Future work should aim to determine the extent of Li-H exchange that occurs as a result of washing with H_2O and/or HCl. In addition, the effect on the Li^+ and H^+ dynamics should be determined.

A.4.5 References

1. Truong, L.; Thangadurai, V. *Inorganic Chemistry* **2011**, *51*, 1222-1224.

2. Galven, C.; Fourquet, J. L.; Crosnier-Lopez, M. P.; Le Berre, F. *Chemistry of Materials* **2011**, *23*, 1892-1900.

3. Galven, C.; Dittmer, J.; Suard, E.; Le Berre, F.; Crosnier-Lopez, M. P. *Chemistry of Materials* **2012**, *24*, 3335-3345.

Appendix A5: Arrhenius Analysis of Ion Conduction

The Arrhenius analysis is typically used as a method to extract the activation energy for ion hopping from measurements of ion hopping rate, or conductivity as a function of temperature.[4] This technique is common in electrochemistry where the slope of the Arrhenius plot is used to calculate the activation energy. ***Figure A5.1*** shows an Arrhenius plot of *ln k* vs. *1/T*, where the y-intercept is *ln A* and the slope is ($-E_A/RT$). The Arrhenius relationship is shown in ***Equation A5.1***:

$$k = Ae^{-\frac{E_A}{RT}} \tag{A4.1}$$

Where k is the ion hopping rate (or ionic conductivity), A is the pre-exponential factor, E_A is the activation energy, R is the gas constant and T is the temperature.

The activation energy is determined from the slope, where a steeper slope indicates a stronger dependence of ion hopping rate on temperature. The y-intercept can be used to calculate the pre-exponential factor, also known as the frequency factor, A. This parameter represents the ion hopping rate at infinite temperature with no energy barrier.[4] The product of A and($e^{-Ea/RT}$) results in the rate of successful collisions.[5] For glass electrolytes the pre-exponential factor varies between 10 and 10^3 S/cm.[4]

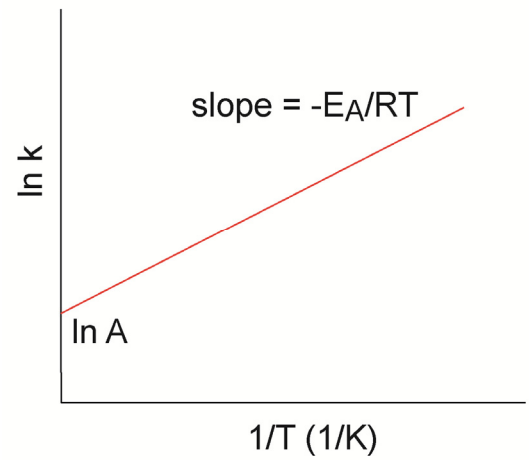

Figure A5.1. Arrhenius plot of *ln K* vs. *1/T*, where the intercept is *ln A* and the slope is ($-E_A/RT$).

The results in Chapter 5 of this thesis describe the difference in ion mobility in $Li_6BaLa_2M_2O_{12}$ (M=Ta, Nb). A pseudo-Arrhenius analysis was used (***Figure A5.2***) to determine that the Nb phase had larger activation energy for lithium ion hopping than the Ta phase, based on the steeper slope. The materials here are very similar in structure, and yet display a difference in absolute ion hopping rate and activation energy for ion hopping. From this it was determined that the reason for the difference in behaviour was the difference in the relative occupancies of the two lithium sites present in each sample. Overall it was concluded that more lithium ions in the site responsible for ion conduction lead to a higher ion hopping rate and a greater activation energy.

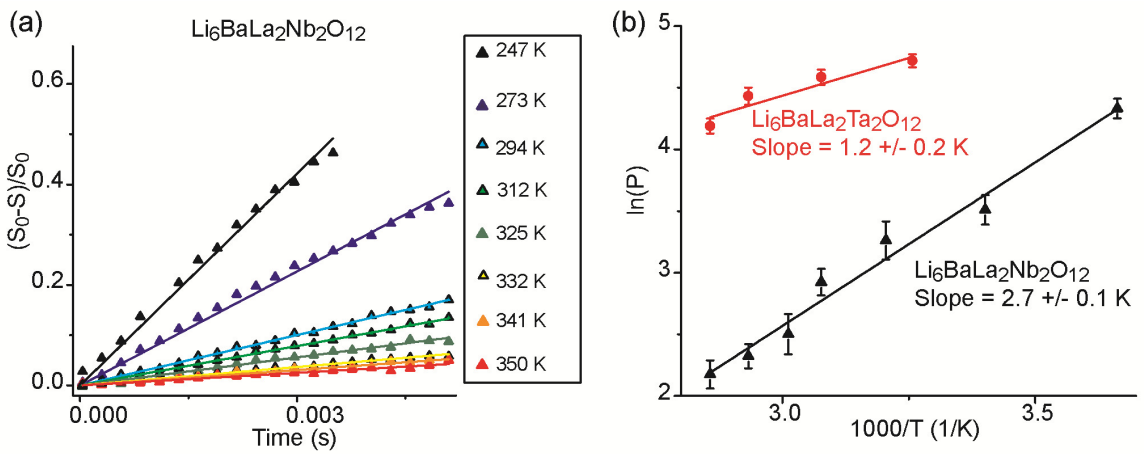

Figure A5.2. (a) ^{6}Li{^{7}Li}-REDOR curve of $Li_6BaLa_2Nb_2O_{12}$ as a function of temperature with slopes ranging from 140 ± 10 s^{-1}, for the immobile sample, to 8.3 ± 0.5 s^{-1}. (b) Pseudo-Arrhenius analysis of the REDOR curves of $Li_6BaLa_2M_2O_{12}$ (M = Ta, Nb).

In addition to different activation energies, the pre-exponential factors of each pseudo-Arrhenius plot were different. The pre-exponential factors for the Nb and Ta phases are 0.005 and 2.14, respectively, with the Nb phase having a much smaller value. ***Figure A5.2*** shows the pseudo-Arrhenius analysis of the Nb and Ta phases. The pre-exponential factors represent the y-intercepts for each of the lines, respectively. Since the pseudo-Arrhenius analysis in this case is a measure of the change in the slope of the REDOR (***Figure A5.2*** (a)) curve as a function of temperature, the pre-exponential factors obtained from this method represent the slope of the REDOR curve at infinite temperature, rather than an ion hopping rate. Here, we propose that this term could provide another value which could be used to assess the maximum ion hopping rate of an ion conductor, which may vary with the number of ions available for ion conduction.

In the case of the electrolytes $Li_6BaLa_2M_2O_{12}$ (M=Ta, Nb) the pre-exponential factors are different and it is possible that this is due to the difference in the occupancy of

the lithium sites. The Nb phase has a smaller pre-exponential factor (i.e. a more shallow REDOR curve when there is no energy barrier), which may be due to the presence of more lithium ions within the octahedral conducting site, as is known from the ^{6}Li NMR (in Chapter 5). This is a purely qualitative observation because here the y-axis of the pseudo-Arrhenius plot represents properties of a REDOR experiment, which at this point are only qualitatively related to the ion hopping properties of the electrolyte materials being studied.

Future work could be done to assess the value of the pre-exponential factor in relation to the ion conductivity or site occupancy for electrolyte materials. This is particularly interesting when considering materials which have significant partial occupancies that affect the ion mobility properties, such as the garnet-like electrolyte materials described in Chapter 5 of this thesis.

A5.1. References

1. Truong, L.; Thangadurai, V., First Total H^+/Li^+ Ion Exchange in Garnet-Type $Li_5La_3Nb_2O_{12}$ Using Organic Acids and Studies on the Effect of Li Stuffing. *Inorganic Chemistry* **2011,** 51, (3), 1222-1224.

2. Galven, C.; Fourquet, J. L.; Crosnier-Lopez, M. P.; Le Berre, F., Instability of the Lithium Garnet $Li_7La_3Sn_2O_{12}$: Li^+/H^+ Exchange and Structural Study. *Chemistry of Materials* **2011,** 23, (7), 1892-1900.

3. Galven, C.; Dittmer, J.; Suard, E.; Le Berre, F.; Crosnier-Lopez, M. P., Instability of Lithium Garnets against Moisture. Structural Characterization and Dynamics of $Li_{7-x}H_xLa_3Sn_2O_{12}$ and $Li_{5-x}H_xLa_3Nb_2O_{12}$. *Chemistry of Materials* **2012,** 24, (17), 3335-3345.

4. Bruce, P. G., *Solid State Electrochemistry*. Cambridge University Press: Cambridge, 1995; p 344.

5. Atkins, P., de Paula, J. , *Physical Chemistry - Seventh Edition*. Oxford University Press: New York, 2002; p 1139.